SAKARYA ÜNİVERSİTESİ

FEN BİLİMLERİ ENSTİTÜSÜ DERGİSİ

Sakarya University Journal of Science (SAUJS)

SAKARYA ÜNİVERSİTESİ

e-issn: 2147-835X

SAÜ Fen Bil Der/SAUJS

Cilt/Volume: 26

Sayı/Issue: 2

Nisan/April 2022

Sakarya Üniversitesi Fen Bilimleri Enstitüsü Dergisi
(Sakarya University Journal of Science)
Cilt/Volume: 26 No/ Issue:2 Nisan/April 2022

Editör Kurulu/Editorial Boards

Owner

Fatih Savaşan, Sakarya University (Turkey)

Publishing Manager

Halit Yaşar, Mechanical Engineering, Sakarya University (Turkey)

Editor-in-Chief

Davut Avcı, Pyhsics, Sakarya University (Turkey)

Associate Editors

Ihsan Hakan Selvi, Information Systems Engineering, Sakarya University (Turkey)

Ömer Tamer, Physics, Sakarya University (Turkey)

Editors

Abderrahmane Benbrik, M'Hamed Bougara University at Boumerdes (Algeria)

Abdullah Oğuz Kızılçay, Computer Engineering, Zonguldak Bülent Ecevit University (Turkey)

Ali Demir, Mathematics, Kocaeli University (Turkey)

Aligholi Niaei, Chemistry, Tabriz University (İran)

Aslı Uçar, Faculty of Health Sciences, Nutrition and dietetics, Ankara University (Turkey)

Asude Ateş, Environmental Engineering, Sakarya University (Turkey)

Bahadır Saygı, Physic, Ege University (Turkey)

Barış Yüce, Engineering Management, Exeter University, UK

Belma Zengin Kurt, Chemistry, Bezmiâlem Vakıf University (Turkey)

Benjamin Durakovic, Department of Industrial Engineering, Bosnia International University of Sarajevo (Bosnia and Herzegovina)

Berrin Denizhan, Industrial Engineering, Sakarya University (Turkey)

Can Serkan Keskin, Chemistry, Sakarya University (Turkey)

Caner Erden, International Trade and Finance, Sakarya University of Applied Sciences (Turkey)

Ceren Tayran, Physic, Gazi University (Turkey)

Cansu Akbulut, Biology, Sakarya University (Turkey)

Ece Ümmü Deveci, Environmental Engineering, Niğde Ömer Halisdemir University (Turkey)

Edgar Perez-Esteve, Food Technology, Polytechnic University of Valencia (Spain)

Elif Ağcakoca, Civil Engineering, Sakary Apllied Science University (Turkey)

Elif Eker Kahveci, Mechanical Engineering, Sakarya University (Turkey)

Fahrettin Horasan, Computer Engineering, Kırıkkale University (Turkey)

Faruk Fırat Çalım, Civil Engineering, Alparslan Türkeş University (Turkey)

Feyza Gurbuz, Industrial Engineering, Erciyes University (Turkey)

Francesco de Paulis, Electrical and Electronics Enginering, University of L'Aquila (Italy)

Gökhan Dok, Civil Engineering, Sakary Apllied Science University (Turkey)

Grazyna S Martynkova, Nanotechnology Centre, VŠB-Technical University of Ostrava · Nanotechnology Centre (Czech Republic)

Grzegorz Jaworski, Physics, Heavy Ion Laboratory, University of Warsaw (Poland)

H. F. Nied, Department of Mechanical Engineering and Mechanics, Lehigh University (U.S.A.)

Hakan Alp, Geophysical Engineering, Cerrahpaşa University (Turkey)

Hatice Esen, Industrial Engineering, Kocaeli University (Turkey)

Hüseyin Aksoy, Biology, Sakarya University (Turkey)

Ing. habil. Ali Cemal Benim, Faculty of Mechanical and Process Engineering, Duesseldorf University of Applied Sciences (Germany)

Issa Al-Harty, Civil and Architectural Engineering, Sultan Qaboos University (Oman)

İbrahim Bahadır Başyiğit, Electrical and Electronics Engineering, Isparta Apllied Science University (Turkey)

İsmail Hakkı Demir, Architecture, Sakarya University (Turkey)

Kamaruzzaman Sopian, Renewable Energy, Universiti Kebangsaan Malaysia (Malaysia)

Khalifa Al-Jabri, Civil and Architectural Engineering, Sultan Qaboos University (Oman)

Luan Thach Hoang, Mathematics, Texas Tech University (U.S.A.)

Luis A. Materon, Biology, The University of Texas Rio Grande Valley (USA)

M. Hilmi Nişancı, Electrical and Electronics Engineering, Sakarya University (Turkey)

Mahmud Tokur, Metallurgical and Materials Engineering, Sakarya University (Turkey)

Mehmet Emin Aydın, Industrial Engineering, University of Bedfordshire (UK)

Mehmet Uysal, Metallurgical and Materials Engineering, Sakarya University (Turkey)

Mesut Baran, Electrical and Computer Engineering, FREEDM Systems Center, North Carolina State University (U.S.A.)

Miraç Alaf, Metallurgical and Materials Engineering, Bilecik Şeyh Edebali University (Turkey)

Mohammad Sukri bin Mustapa, Faculty of Mechanical & Manufacturing Engineering, Universiti Tun Hussein Onn Malaysia (Malaysia)

Muhammed Fatih Adak, Computer Engineering, Sakarya University (Turkey)

Muhammed Maruf Öztürk, Computer Engineering, Süleyman Demirel University (Turkey)

Murat Güzeltepe, Mathematics, Sakarya University (Turkey)

Murat Sarduvan, Mathematics, Sakarya University (Turkey)

Murat Tuna, Chemistry, Sakarya University (Turkey)

Mustafa Akpınar, Software Engineering, Sakarya University (Turkey)

Mustafa Gülfen, Chemistry, Sakarya University (Turkey)

Nahit Gencer, Chemistry, Balıkesir University (Turkey)

Nazan Deniz Yön Ertuğ, Biology, Sakarya University (Turkey)

Necati Olgun, Mathematics, Gaziantep University (Turkey)

Nihan Akıncı Kenanoğlu, Biology, Çanakkale Onsekiz Mart University (Turkey)

Oğuz Kurt, Biology, Manisa Celal Bayar University (Turkey)

Ozan Erdinç, Electrical and Electronics Engineering, Yıldız Technical University (Turkey)

Raja Mazuir Raja Ahsan Shah, Aerospace and Automotive Engineering, Coventry University (United Kingdom)

Rıfkı Terzioğlu, Electrical and Electronics Engineering, Bolu Abant İzzet Baysal University (Turkey)

S.C. Yao, Mechanical Engineering, Carnegie Mellon University, PA (U.S.A.)

Sadık Kakaç, Mechanical Engineering, TOBB ETU (Turkey)

Selma Özçağ, Mathematics, Hacettepe University (Turkey)

Seong Jin Park, Department of Mechanical Engineering, Pohang University of Science and Technology (Korea)

Serap Coşansu Akdemir, Food Engineering, Sakarya University (Turkey)

Syed Nasar Abbas, Food Engineering, Curtin University (Australia)

Şenay Çetin Doğruparmak, Environmental Engineering, Kocaeli University (Turkey)

Tahsin Turğay, Architecture, Sakarya University (Turkey)

Tauseef Aized, Mechanical Engineering, University of Engineering and Technology (Pakistan)

Tuba Tatar, Civil Engineering, Sakarya University (Turkey)

Tuğrul Çetinkaya, Metallurgical and Materials Engineering, Sakarya University (Turkey)

Ufuk Durmaz, Mechanical Engineering, Sakarya University (Turkey)

Urvir Singh, Electrical and Electronics Enginering, Schweitzer Engineering Laboratories: SEL Inc. (U.S.A.)

Guest Editor

Aysun Eğrisöğüt Tiryaki, Mechanical Engineering, Sakarya University (Turkey)

Ertan Bol, Civil Engineering, Sakarya University (Turkey)

English Language Editor

Ömer Tamer, Physics, Sakarya University (Turkey)

Editorial Assistant

Ahmet Erhan Tanyeri, Sakarya University (Turkey)

SAKARYA ÜNİVERSİTESİ FEN BİLİMLERİ ENSTİTÜSÜ DERGİSİ
(SAKARYA UNIVERSITY JOURNAL OF SCIENCE)
İÇİNDEKİLER/CONTENTS
Cilt/Volume: 26 – No/Issue2: (NİSAN/APRİL-2022)

RESEARCH ARTICLES

SAKARYA ÜNİVERSİTESİ
FEN BİLİMLERİ ENSTİTÜSÜ DERGİSİ

Sakarya University Journal of Science
SAUJS

e-ISSN 2147-835X Period Bimonthly Founded 1997 Publisher Sakarya University
http://www.saujs.sakarya.edu.tr/

Title: Electrochemical Reduction of Lead Sulfide in NaCl-KCl and NaCl-KCl-%2Na2S

Authors: Levent KARTAL

Recieved: 2021-07-16 00:00:00

Accepted: 2022-02-08 00:00:00

Article Type: Research Article

Volume: 26
Issue: 2
Month: April
Year: 2022
Pages: 232-240

How to cite
Levent KARTAL; (2022), Electrochemical Reduction of Lead Sulfide in NaCl-KCl and NaCl-KCl-%2Na2S. Sakarya University Journal of Science, 26(2), 232-240, DOI: 10.16984/saufenbilder.972380
Access link
https://dergipark.org.tr/tr/journal/1115/issue/69580/972380

New submission to SAUJS
http://dergipark.gov.tr/journal/1115/submission/start

Sakarya University Journal of Science 26(2), 232-240, 2022

Electrochemical Reduction of Lead Sulfide in NaCl-KCl and NaCl-KCl-%2Na_2S

Levent KARTAL*[1]

Abstract

In this study, the lead production from lead sulfide (PbS) by molten salt electrolysis was investigated under potentiostatic and galvanostatic conditions using NaCl-KCl and NaCl-KCl-2%Na_2S electrolytes. Stable cell voltage and current were aimed with the addition of Na_2S to the NaCl-KCl electrolyte. Reduction experiments were carried out at constant 700 °C temperature and for 15 min. duration. The current density was set to 250 mA/cm^2 for the galvanostatic reduction experiments. It was observed that there was an increase in cell voltage in both electrolytes due to the decrease in the amount of PbS in galvanostatic experiments. In these experiments, it was determined that the reduction occurred at higher cell voltages in the NaCl-KCl electrolyte compared to the NaCl-KCl-2%Na_2S electrolyte. Although the cell voltage was aimed to remain constant with the Na_2S addition, the cell voltage decreased slightly compared to the NaCl-KCl electrolyte, but increased with the experiment duration as in the NaCl-KCl electrolyte. Potentiostatic reduction experiments carried out at a constant cell voltage of 3.0 V under the electrolyte decomposition voltage. The morphology of the cathode products was examined by SEM-EDS analysis and, the phases were examined by X-ray diffractometry. Higher current values were obtained in the NaCl-KCl-%2Na_2S electrolyte compared to the NaCl-KCl electrolyte. Current variation with electrolysis duration showed similar trends in both electrolytes. According to structural characterization, it was determined that the metallic lead mass did not contain any impurities.

Keywords: Molten salt electrolysis, electrochemical-reduction, lead extraction, lead sulfide

1. INTRODUCTION

Lead has been widely used by mankind for many years due to its features such as ease of production, low melting temperature, good formability, and high corrosion resistance. With the determination of its toxic effects thanks to the developing technology, the direct or indirect use of lead in many products have been banned or limited. However, it is still widely used in the battery manufacturing industry, insulation of underground communication cables, protection from X-rays due to its radiation-blocking properties, and ammunition production [1, 2].

The most common lead sources are galena (PbS), serousite ($PbCO_3$) ores, and waste batteries. Primary lead production is made from galena (PbS) concentrates by pyrometallurgical methods and is refined by pyrometallurgical/electrometallurgical processes and presented to the industry [3, 4]. Pyrometallurgical production is carried out in

* Corresponding author: leventkartal@hitit.edu.tr
[1] Hitit University, Faculty of Engineering, Department of Metallurgy and Material Engineering
ORCID: https://orcid.org/0000-0002-6291-8947

systems where direct melting processes (QSL, Ausmelt, Outokumpu, etc.), oxidation and reduction stages take place in the same furnace. These processes were developed to reduce the use of coke by utilizing the oxidation heat of the sulfur in the concentrate and to eliminate the costs of expensive gas cleaning, dust holding and ventilation equipment [5, 6].

In addition to oxygen and sulfur, lead concentrates generally contain iron, copper, nickel, cobalt, zinc, arsenic, antimony, tin, bismuth, selenium, tellurium, silver, gold, and these metals are collected in lead after reduction. Purification of lead from these metals is done by multi-stage pyrometallurgical, and electrometallurgical refining steps. In pyrometallurgical lead refining, copper is removed by adding S to lead, forming copper sulfide (Cu_xS_y) and withdrawing it from the surface, removal of As, Sb, and Sn by adding sodium nitrate ($NaNO_3$) to molten lead, and separating it to form sodium arsenate, antimonite, and sodium stannate compounds. Removal of Zn is accomplished by oxidation, chlorination or evaporation under vacuum. Electrometallurgical lead refining is achieved by dissolving lead anodes in fluoboric, fluosilicic and sulfamic acid-based electrolytes and depositing it at the cathode at an appropriate current density. In refining electrolysis, fluosilicic acid is generally preferred as the electrolyte due to its low price [6, 7].

Existing metallurgical processes used in metal production from sulfide ores are processes with high initial investment and operating cost. In addition, SO_2, CO, and CO_2 released in the environment during production with the traditional methods cause serious environmental problems [8]. Increasing environmental restrictions and expensive SO_2 capture systems urge researchers to develop both environmental and economic methods for sustainable metal production. The development of systems that provide stable sulfide recovery in elemental form along with metal production is of environmental and economic importance. In the production of metal from metal sulfide compounds, the most emphasized methods for the production of metal and elemental sulfur directly from metal sulfide are hydrometallurgical and electrochemical production methods. Since too much acid is consumed in the hydrometallurgical method, S forms H_2S, and an oxidant is needed to obtain elemental sulfur, it has not yet reached the stage to replace pyrometallurgical production. Although direct metal production from oxide or sulfide compounds by electrometallurgical methods has been known for many years, it gained momentum in the late 90's with the study of a group of researchers from Cambridge University on the electrochemical reduction of titanium dioxide [9]. In the process, the direct reduction of oxidized/sulfurous compounds by molten salt electrolysis, the compounds are cathodically polarized in suitable electrolytes and metal formation is provided, while the ionized O^{2-} /S^{2-} reaches the anode (usually graphite) where it is oxidized to form S_2, CO, CO_2 gases [10]. In molten salt electrolysis; electrolyte, anode material, and applied temperature are the most important components. The electrolyte is of great importance as it affects the working temperature with ion transport, and the melting temperature. In literature, NaCl-KCl is used as an electrolyte due to high S^{2-} diffusion in the reduction of sulfide compounds, while the use of $CaCl_2$ is prominent in the reduction of oxide compounds due to high O^{2-} diffusion [11, 12]. As the anode, carbon-based electrodes that are easy to mass-produce and supply are preferred. While these electrodes cause greenhouse gas (CO, CO_2) emission in the reduction of oxide compounds, carbon-based anodes act inert in the reduction of sulfide ores. Thus, with the formation of metal at the cathode and sulfur at the anode, metal production is possible with the use of a cheap anode without greenhouse gas emissions [13].

In studies on lead production by molten salt electrolysis, there are studies with chloride (LiCl-KCl), fluoridated (HBF_4), and hydroxide (NaOH) electrolytes. In chloride electrolytes, lead production was carried out at 450 °C using the LiCl-KCl-$PbCl_2$ electrolyte with graphite electrodes [14]. Doe Run and Engitec companies have developed the Engitec Flubor molten salt electrolysis process using HBF_4 electrolyte for lead generation. In the process, lead is based on ferric leaching and electrochemical reduction of

galena concentrate in a fluoroboric acid-based solution. Electro-winning is carried out in split cells using stainless steel cathodes and graphite anodes [15]. On the other hand, Buzatu et al., stated that they performed their studies in the production of Pb from wastes containing $PbSO_4$, PbO, and Pb in a NaOH based electrolyte, using stainless steel anodes and cathodes, at a current density of 600 A/m^2, at an electrolyte temperature of 35 °C [16]. Lead in powder form production at low temperature without leaching was studied by Qu et al. They stated that it is possible to produce powdered lead in 50% NaOH solutions at 120 °C, which they pelletized PbS powders [17].

In this study, lead production was carried out in one step under galvanostatic, and potentiostatic conditions at a constant temperature of 700 °C in NaCl-KCl and NaCl-KCl-2%Na_2S electrolytes. Castable lead production, which does not require extra leaching of lead sulfide and production of intermediate chloride compounds from lead sulfide, was investigated. In addition, the effects of Na_2S added to the electrolyte on cell voltage, anode, and cathode potentials under galvanostatic conditions and on current under potentiostatic conditions were examined.

2. EXPERIMENTAL

The materials used in this study are given in Table 1 along with their technical specifications.

Table 1 Materials used in electrochemical reduction experiments

Materials	Form	Specification
PbS	Powder	technical grade purity
NaCl	Powder	technical grade purity
KCl	Powder	technical grade purity
Na_2S	Powder	technical grade purity
Cathode	Graphite crucible	Ø 45 mm, h 100 mm
Anode	Graphite rod	ϕ 16 mm

NaCl-KCl constituting the electrolyte was prepared by mixing in 1:1 mole ratio considering the phase diagram. Salt mixtures, graphite crucible (65mmOD, 45mmID, 100mm height), and other graphite materials were kept in an oven at 110 °C for moisture removal. Argon gas (50 ml/min) was used as a protective atmosphere in all experiments. Pre-electrolysis was performed for 1 hour by applying a 2.7 V constant cell potential to remove electrolyte-sourced impurities. Graphite rods with a diameter of 6 mm were used as reference electrodes in the experiments. In the galvanostatic and potentiostatic reduction experiments, the heating was carried out using a medium frequency induction furnace (50 kHz, 30 kW, 40 A). In these experiments, 16 mm diameter graphite rods were used as the anode. The anode height was determined as 20 mm from the bottom of the crucible, taking into account the densities of the materials fed to the cell (electrolyte (2.05 g/cm^3), lead sulfide (7.6 g/cm^3), and lead (11.34 g/cm^3). The anode was positioned on the lead sulfide in the electrolyte to prevent short circuit formation. Fixed 3 g of PbS was used in all reduction experiments.

Characterization studies were carried out using optical emission spectrometry (OES, GNR-S7 MLP), X-ray diffractometer (XRD, Siemens D5000), scanning electron microscope with energy dispersive X-ray spectrometry (Jeol-JSM 5410).

3. RESULTS AND DISCUSSION

3.1. Electrochemical reduction of PbS

The breakdown voltages of lead sulfide (PbS) and the salts forming the electrolyte were calculated

using theoretical data. Equation 1 was used to calculate the breakdown voltages (ΔE) and the values are given in Table 2. In Equation 1, n represents the number of electrons and F represents Faraday's constant. Since the decomposition potential of lead sulfide is much lower than the decomposition voltage of NaCl, KCl, and Na_2S used in electrolyte preparation, lead sulfide reduction takes place without chlorine (Cl_2) emission.

$$\Delta E = -\Delta G/(nF) \text{ [18]} \quad (1)$$

Table 2 The standard Gibbs free energy changes along with decomposition voltages of PbS and NaCl, KCl at 700 °C

Reaction	**Gibbs Free Energy Changes ΔG°/kJ mol^{-1}**	**Theoretical Decomposition Voltage/V**
$2NaCl = 2Na + Cl_2(g)$	642.405	-3.33
$2KCl = 2K + Cl_2(g)$	688.058	-3.56
$2Na_2S=4Na+S_2(g)$	616.952	-1.6
$2PbS = 2Pb + S_2(g)$	154.416	-0.40

The variation of the standard Gibbs free energy of formation of the materials used in experimental studies with temperature is shown in figure 1. Based on these data, the variation of the decomposition potentials with temperature is given in figure 2.

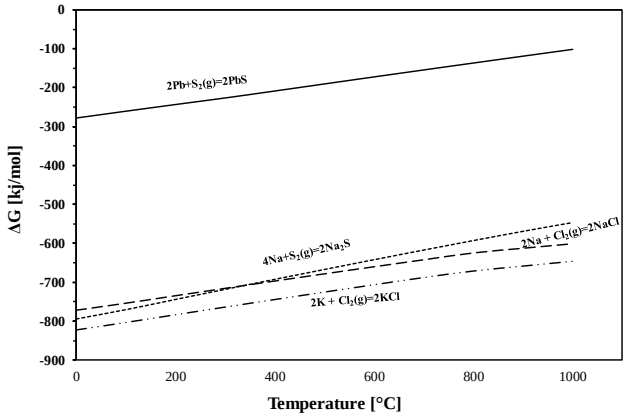

Figure 1 Change in the standard Gibbs free energy of formation of PbS, NaCl, KCl, and Na_2S as a function of temperature

It is understood that the decomposition potentials of PbS, and Na_2S, which are expected to be reduced under galvanostatic/potentiostatic experimental conditions, are much lower than the NaCl, and KCl constituting the electrolyte so that lead production can occur without harmful gas emissions (fig 2).

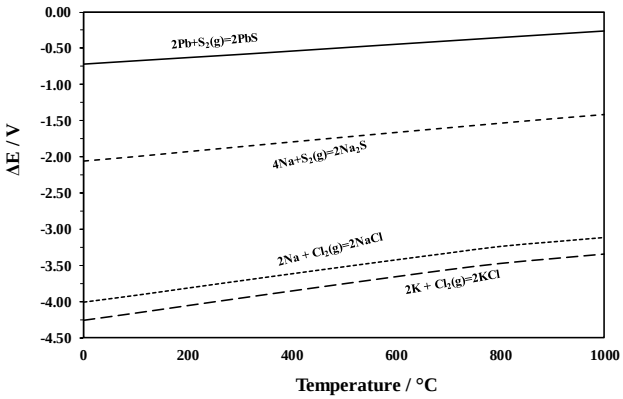

Figure 2 The decomposition potentials (ΔE°) for PbS, NaCl, KCl, and Na_2S as a function of temperature

The expected anode and cathode reactions as a result of thermodynamic investigations and calculations are given below.

$$\text{Cathode} \quad : PbS + 2e^- = Pb + S^{2-} \quad (2)$$

$$\text{Anode} \quad : S^{2-} - 2e^- = 1/2S_2(g) \quad (3)$$

$$\text{Net Reaction} \quad : PbS = Pb + 1/2S_2(g) \quad (4)$$

The lead accumulated in the cathode will collect at the bottom of the graphite crucible as a liquid and ready for casting due to the experimental operating temperature being higher than the melting temperature of lead. It is estimated that the sulfur formed at the anode leaves the system as a gas due to the operating temperature being higher than the evaporation temperature of the sulfur and condenses in cold regions.

3.2. Galvanostatic Electrolysis of PbS

The galvanostatic reduction experiments of PbS were carried out at the constant temperature of 700 °C using two different electrolytes, NaCl-KCl and NaCl-KCl-2% Na_2S. By adding Na_2S to the NaCl-KCl electrolyte, a saturation of the electrolyte with sulfur and stable cell potential was aimed. In both electrolytes, it was determined that the cell potential increased over time due to the decrease in the amount of PbS that decreased

with the electrolysis time. It was observed that the cell voltage increase was sharper in the NaCl-KCl electrolyte compared to the NaCl-KCl-2% Na_2S electrolyte and almost reached the electrolyte breakdown potential in a short experiment time of 15 minutes. Although the cell voltage in the electrolyte using NaCl-KCl-%2Na_2S was lower than the NaCl-KCl electrolyte, it started to increase at the end of the experiment due to the decrease in the amount of PbS. Yin et al. studied Sb2S3 reduction in NaCl-KCl-Na2S electrolyte and observed that the cell voltage increased from about 0.5 V to 2.25 V for 45 minutes [21].

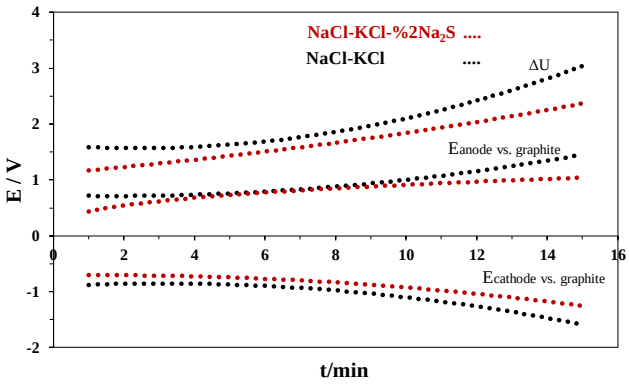

Figure 3 Variations of cell voltage at 250 mA/cm^2 in NaCl−KCl−PbS, and NaCl−KCl−%2 Na_2S-PbS melt at 700 °C

The chemical content of the cathode products produced in both electrolytes was investigated by an OES. It was observed that the lead obtained as a result of both studies did not contain any metallic impurities and high amount of sulfur residues (Table 3).

Table 3 OES results for cathode products

Electrolytes	The concentration of element *i*, *Ci* (wt.%)	
	Pb	S
NaCl−KCl	99.04	0.6
NaCl−KCl−%2 Na_2S	99.07	0.5

The products produced using NaCl−KCl, and NaCl−KCl−%2 Na_2S electrolytes were examined by SEM-EDS analysis and no impurities were detected in the metallic mass.

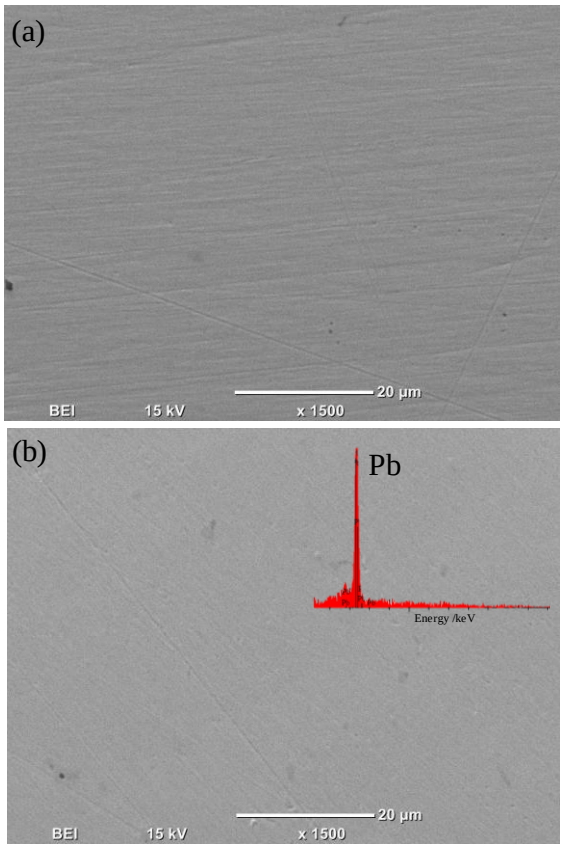

Figure 4 SEM images of the cathode products produced in (a) NaCl-KCl and (b)NaCl-KCl-Na_2S for 15 min. at 250 mA/cm^2 at 700 °C

In Figure 5, X-ray analysis results of lead produced in both electrolytes are given. It has been confirmed that the results of X-ray analysis support the results of OES and SEM-EDS analysis and that there are no oxidized/sulfurous phases in the structure. In accordance with the work of Yin et al., high purity metallic lead was obtained in the NaCl-KCl-Na_2S based electrolyte [21].

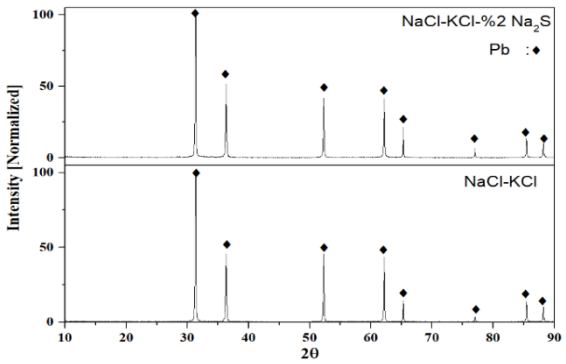

Figure 5 XRD patterns of Pb synthesized at 250 mA/cm^2 in (a) NaCl-KCl, and (b)NaCl-KCl-Na_2S melt at 700 °C

3.3. Potentiostastic Electrolysis of PbS

Lead production from PbS was also investigated under potentiostatic conditions using the same electrolytes, due to the rapid increase in the cell potential in the experiments performed under galvanostatic conditions and approaching decomposition potential of the chloride salts forming the electrolyte. Taking into account the theoretical calculations (see Table 2 and figures 1, 2), the experiments were carried out at a constant cell voltage of 3.0 V, under the breakdown voltage of the salts forming electrolyte and above the breakdown voltage of PbS. Figure 6 shows the current changes depending on the electrolysis time at a fixed cell potential of 3.0 V. The current changes obtained as a result of the experiments carried out at constant potential in two different electrolytes show a similar trend and the currents became stable after approximately 10 minutes. Qu et al. has investigated the electrochemical lead production from PbS in 50% NaOH water solution under constant voltage at 120 °C. The current behavior, similar to the study of Qu et al., the current decreased rapidly over time and continued as a flat plateau [17]. Li et al. studied the electrochemical reduction of Sb_2S_3-PbS in NaCl-KCl at 730 °C at different cell voltages [22]. Although the current values in Li and co-workers study were very different, the trend was similar to the results of Qu. The current was higher in the electrolyte containing Na_2S compared to the electrolyte without Na_2S.

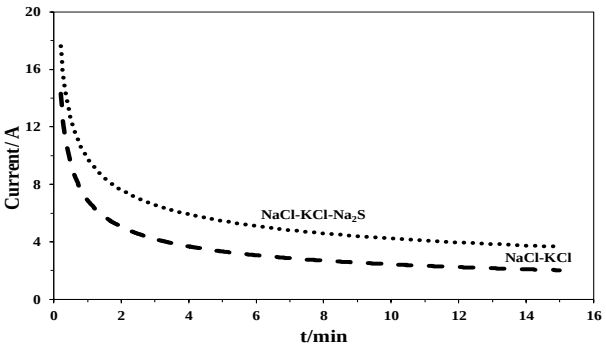

Figure 6 Current versus time at different voltages in NaCl−KCl−PbS and NaCl−KCl−%2Na_2S-PbS melt at 3.0 V, and 700 °C

The chemical content of the cathode products produced under potentiostatic conditions was examined by OES and was found that it did not contain high sulfur residues with a lead content of over 99 % (Table 4).

Table 4 Chemical analysis of cathode products

Electrolytes	The concentration of element *i*, *Ci* (wt.%)	
	Pb	S
NaCl−KCl	98.7	<0.1
NaCl−KCl−%2 Na_2S	99.2	<0.1

The obtained metallic lead was examined by SEM-EDS, and it was seen that the black spots on the surface were not sulfide residues and impurities but voids. XRD and SEM-EDS analyses also support the OES results (fig. 8, 9). Li et al. studied the electrochemical reduction of Sb_2S_3-PbS in NaCl-KCl and it is understood from XRD studies that in high purity Pb is produced at 2.2 V. The sulfide structures in metallic lead were removed with increasing time [22]. Qu et al. investigated the electrochemical lead production from PbS at different cell voltages[17]. Similar to the work of Li et al., Qu et al. also obtained high purity lead at 2.0 V and above. The highest possible voltage under the electrolyte breakdown voltage shortens the reduction time. Therefore, instead of trying different voltages, 3.0 V was applied in our study. This result is also supported by the studies of Qu and Li.

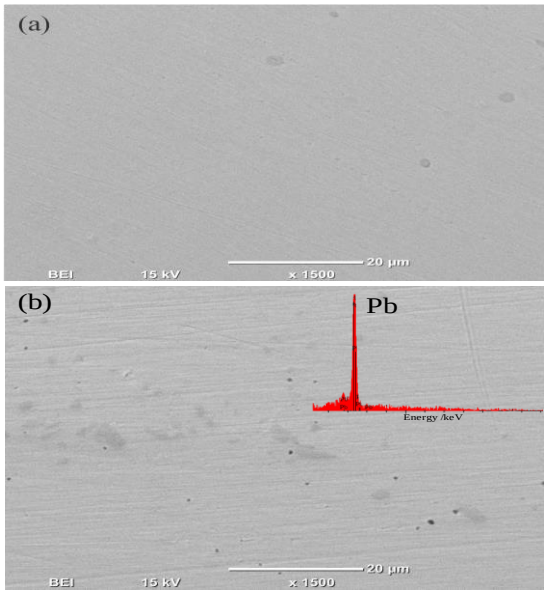

Figure 7 SEM images of the cathode products produced in (a) NaCl-KCl, and (b)NaCl-KCl-%2 Na_2S for 15 min. at 3.0 V at 700 °C

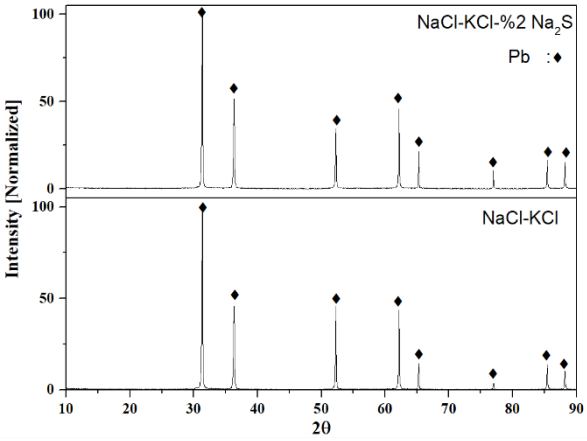

Figure 8 XRD patterns of Pb synthesized at 3.0 V in NaCl−KCl−PbS and NaCl−KCl−%2 Na_2S-PbS melt at 700 °C

Graphite is an ideal inexhaustible anode material for sulfur production as a result of the anodic oxidation of S^{2-}. This has been proven by numerous studies on the electrolysis of solid metal sulfides and dissolved metal sulfides [11, 19, 20]. The oxidized sulfur on the anode leaves the system as a gas at an operating temperature of 700 °C. While a significant part of the sulfur formed at the anode is kept in gas scrubbing bottles and it has been determined that some of it condense in cold regions.

4. CONCLUSION

In this study, lead production was investigated from lead sulfide (PbS) without SO_2 emission in NaCl-KCl, and NaCl-KCl-%2 Na_2S electrolyte at 700 °C. The key conclusions can be summarized as follows;

- In the experiments performed with NaCl-KCl electrolyte at a current density of 250 mA/cm^2 under galvanostatic conditions, it was determined that the cell voltage increased due to the decrease in the amount of PbS and reached the electrolyte breakdown voltage.
- In NaCl-KCl-%2Na_2S electrolyte, the Na_2S addition could not provide stable cell voltage, the cell potential increased over time, but the increase was slower than the NaCl-KCl electrolyte.
- In the trials carried out by applying constant 3.0 V in NaCl-KCl and NaCl-KCl-%2Na_2S electrolytes, it was observed that the current change over time was similar, and the current values were higher in the electrolyte containing Na_2S.
- Stable cell voltage and current values could not be obtained under galvanostatic and potentiostatic conditions with the addition of Na_2S to the electrolyte.
- The sulfur formed at the anode during electrolysis was collected in gas scrubbing bottles and in the cold areas of the cell.

Acknowledgments

The authors would like to acknowledge the reviewers and editors of Sakarya University Journal of Science.

Funding

The author (s) has no received any financial support for the research, authorship or publication of this study.

The Declaration of Conflict of Interest/ Common Interest

No conflict of interest or common interest has been declared by the authors.

The Declaration of Ethics Committee Approval

This study does not require ethics committee permission or any special permission.

The Declaration of Research and Publication Ethics

The authors of the paper declare that they comply with the scientific, ethical and quotation rules of SAUJS in all processes of the paper and that they do not make any falsification on the data collected. In addition, they declare that Sakarya University Journal of Science and its editorial board have no responsibility for any ethical violations that may be encountered, and that this study has not been evaluated in any academic publication environment other than Sakarya University Journal of Science.

REFERENCES

[1] P. Coleman, "Lead industry address," APPEA J., vol. 57, no. 3, pp. 41–52, 2017.

[2] J. Liu, S. Huang, K. Chen, J. Li, T. Wang, M. Mei, "Recovering metallic Pb directly from lead smelting dust by NaOH-carbon roasting process," J. Mater. Res. Technol., vol. 9, no. 3, pp. 2744–2753, 2020.

[3] D. Gregurek, Z. Peng, C. Wenzl, "Lead and zinc metallurgy," JOM, vol. 67, no. 9, pp. 1986–1987, 2015.

[4] B. Xie, T. Yang, W. Liu, D. Zhang, L. Chen, "Recovery of lead from spent lead paste by pre-desulfurization and low-temperature reduction smelting," JOM, vol. 72, no. 9, pp. 3195–3203, 2020.

[5] S. Hughes et al., "Ausmelt technology for lead and zinc processing," Lead and Zinc 2008, no. January, pp. 147–162, 2008.

[6] D. Swinbourne, "The extractive metallurgy of lead," Miner. Process. Extr. Metall., vol. 119, no. 3, pp. 182–182, 2010.

[7] I. Thornton, R. Rautiu, S. Brush, "Lead industry profile," Lead Facts, pp. 47–70, 2001.

[8] F. Habashi, "Pollution problems in the metallurgical industry: A review," JME, vol. 2, no. 1, pp. 17–26, 2011.

[9] D. J. Fray, "Reduction of titanium and other metal oxides using electrodeoxidation," Mater. Sci. Technol., vol. 20, no. 3, pp. 295–300, 2004.

[10] G. Z. Chen, "Forming metal powders by electrolysis," Advances in Powder Metallurgy: Properties, Processing and Applications, Woodhead Publishing Limited, pp. 19–41, 2013.

[11] T. Wang, H. Gao, X. Jin, H. Chen, J. Peng, and G. Z. Chen, "Electrolysis of solid metal sulfide to metal and sulfur in molten NaCl-KCl," Electrochem. commun., vol. 13, no. 12, pp. 1492–1495, 2011.

[12] K. S. Mohandas, "Direct electrochemical conversion of metal oxides to metal by molten salt electrolysis: a review," Miner. Process. Extr. Metall., vol. 122, no. 4, pp. 195–212, 2013.

[13] G. Li, D. Wang, X. Jin, G. Z. Chen, "Electrolysis of solid MoS2 in molten $CaCl_2$ for Mo extraction without CO_2 emission," Electrochem. commun., vol. 9, no. 8, pp. 1951–1957, 2007.

[14] J. E. M. and M. F. Chambers, "Production of lead metal by molten-salt electrolysis with energy-efficient electrodes. Rept. of investigations/1991." 1991.

[15] M. Free et al., "Electrometallurgy - Now and in the Future," in Electrometallurgy 2012, pp. 1–27. 2012

[16] T. Buzatu, G. Badanoiu, V. G. Ghica, and M. Buzatu, "Experimental research on lead extraction from alkaline solutions by electrolysis," Rev. Chim., vol. 66, no. 8, pp. 1147–1150, 2015.

[17] X. Qu et al., "Electrochemical Reduction of Solid Lead and Antimony Sulfides in Strong Alkaline Solutions," J. Electrochem. Soc., vol. 166, no. 2, pp. E62–E67, 2019.

[18] A. Vignes, "Electrometallurgical Extraction Processes," in Extractive Metallurgy 2, A. Vignes, Ed. LONDON: ISTE Ltd and John Wiley & Sons, Inc, 2011, pp. 87–116.

[19] M. Tan, R. He, Y. Yuan, Z. Wang, and X. Jin, "Electrochemical sulfur removal from chalcopyrite in molten NaCl-KCl," Electrochim. Acta, vol. 213, pp. 148–154, 2016.

[20] X. Ge, X. Wang, and S. Seetharaman, "Copper extraction from copper ore by electro-reduction in molten CaCl2-NaCl," Electrochim. Acta, vol. 54, no. 18, pp. 4397–4402, 2009.

[21] H. Yin, B. Chung, and D. R. Sadoway, "Electrolysis of a molten semiconductor," Nat. Commun., vol. 7, 12584, 2016.

[22] X. Li, J. Qu, Z. Zhao, Y. Zhao, H. Xie, and H. Yin, "Electrochemical desulfurization of galena-stibnite in molten salts to prepare liquid Sb–Pb alloy for liquid metal battery," J. Clean. Prod., vol. 312, 127779, 2021.

SAKARYA ÜNİVERSİTESİ
FEN BİLİMLERİ ENSTİTÜSÜ DERGİSİ

Sakarya University Journal of Science
SAUJS

e-ISSN 2147-835X Period Bimonthly Founded 1997 Publisher Sakarya University
http://www.saujs.sakarya.edu.tr/

Title: An Existing Problem for Symmetric Design: Bruck Ryser Chowla Theorem

Authors: Emek DEMİRCİ AKARSU, Safiye ÖZTÜRK

Recieved: 2021-07-06 00:00:00

Accepted: 2022-02-10 00:00:00

Article Type: Research Article

Volume: 26
Issue: 2
Month: April
Year: 2022
Pages: 241-248

How to cite
Emek DEMİRCİ AKARSU, Safiye ÖZTÜRK; (2022), An Existing Problem for Symmetric Design: Bruck Ryser Chowla Theorem. Sakarya University Journal of Science, 26(2), 241-248, DOI: 10.16984/saufenbilder.962817
Access link
https://dergipark.org.tr/tr/journal/1115/issue/69580/962817

New submission to SAUJS
http://dergipark.gov.tr/journal/1115/submission/start

Sakarya University Journal of Science 26(2), 241-248, 2022

An Existing Problem for Symmetric Design: Bruck Ryser Chowla Theorem

Emek DEMİRCİ AKARSU*[1], Safiye ÖZTÜRK[1]

Abstract

Symetric designs are interesting objects of combinatorics, and have some relations with coding theory, difference sets, geometry and finite group theory. They have applications on statistics and design experiments. In the present paper we study an existing problem for symmetric design due to Bruck, Ryser and Chowla and write an algorithm by using their theorem called BRC Theorem.

Keywords: Symmetric design, difference sets, Bruck Ryser Chowla Theorem

1. INTRODUCTION

Definition 1. Let $\mathcal{P}$ be the set of points and $\mathcal{B}$ be the set of blocks. An *incidence structure* is a triple $(\mathcal{P},\mathcal{B},\mathcal{I})$ such that $\mathcal{P}\cap\mathcal{B}=\emptyset$ and $\mathcal{I}\subseteq\mathcal{P}\times\mathcal{B}$ is an *incidence relation* between $\mathcal{P}$ and $\mathcal{B}$. For $p\in\mathcal{P}$ and $B\in\mathcal{B}$ $(p,B)\in\mathcal{I}$ mean p and B are *incidence* [1]. For instance; $\mathcal{P}$ can be the point set and $\mathcal{B}$ can be the block set in the Euclidean plane.

Let $(\mathcal{P},\mathcal{B},\mathcal{I})$ be incidence structure, $\mathcal{P}=(p_1,p_2,\dots,p_v)$ point set and $\mathcal{B}=(B_1,B_2,\dots,B_k)$ be the block set. An i*ncidence matrix* M is defined as finite incidence structure where p_i represents points, B_j represents blocks and $m_{ij}\in M$ such that

$$m_{ij}=\begin{cases}1 \text{ if } p_i\in B_j,\\ 0 \text{ otherwise.}\end{cases}$$

A symmetric (v,k,λ) design is an incidence structure $(\mathcal{P},\mathcal{B},\mathcal{I})$ for $0<k<v$ the following statements hold [2].

(i) There are v points ($|\mathcal{P}|=v$)

(ii) There are v blocks ($|\mathcal{B}|=v$)

(iii) Each point and each block are incident with k blocks and k points respectively.

(iv) Each pair of points and each pair of blocks are incident with λ blocks and λ points respectively.

If $\lambda=0$ and $\lambda=k-1$, they are called trivial symmetric designs.

Example 2. The set $\mathbb{Z}_7=\{0,1,2,3,4,5,6\}$ has a subset $D=\{1,2,3,5\}$ with four elements, if we take shifts of all the elements of D then blocks are as follows.

* Corresponding author: emek.akarsu@erdogan.edu.tr
[1] Recep Tayyip Erdoğan University, Faculty of Science and Literature, Department of Mathematics
E-mail: k.ozturk245@gmail.com
ORCID: https://orcid.org/0000-0003-4769-0830, https://orcid.org/0000-0002-6494-6175

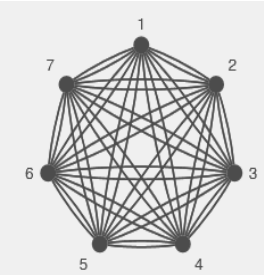

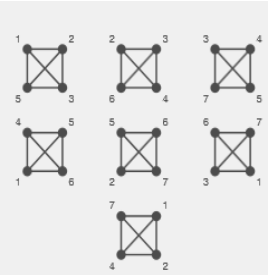

The definiton of design theory is combinatorial however there are strong connections to algebra, geometry and has applications to statistics and coding theory. Symetric designs play a key role in construction of differences sets in finite groups.

James Singer is the first person who studied difference sets by relating to topics with finite projective geometry [4]. Then the first construction of blok designs was given by [5]. In the beginning of 40's, this study became more systematic with Halls's work [6]. Levi stressed in his work that there is a close relation between finite projective geometry and affin geometry [5,7,8,9] they used equivalent matrices for these geometries in their work [8, 10, 11] in their study the theory of Bruck Ryser Chowla for (v, k, λ) parameters was given for the existence of symmetric design. In their first paper for $\lambda = 1$ the theorem was proven and this result was extended to any positive λ in the second paper. [12] was explained more simple proof of the theorem. Later so many writers worked on the related subjects [1, 12, 13, 14, 15], etc.

Difference sets link design theory to group theory because a group acts regularly on the points and the blocks of a symmetric design with the condition the group includes a difference set. Most of the examples of difference sets obtain from theory of numbers for examples squares, twin prime numbers etc. A detailed work on the difference sets and cyclotomy is given in [18].

Definition 3. Let G be a finite group with $|G| = v$. Let $\emptyset \neq D = \{d_1, d_2, \dots, d_k,\} \subseteq G$ be composed of k elements of the remaining classes in the $modulo\ v$. For $d_i, d_j \in D$, $d_i \neq d_j$ and $\alpha \in G$, $\alpha \not\equiv 1_G (\mathrm{mod}\ v)$, congruence

$$d_i - d_j \equiv \alpha (\mathrm{mod}\ v)$$

contains exactly λ pairs of solutions (d_i, d_j). Multiset of differences is expressed as follows:

$$\Delta = \{d_i - d_j |\ d_i, d_j \in D,\ d_i \neq d_j\}.$$

The parameter system (v, k, λ) in this structure expresses the difference set $D \subseteq G$. If G is a multiplicative group, difference set congruence $d_i d_j^{-1} \equiv \alpha (\mathrm{mod}\ v)$ has exactly λ solution pairs (d_i, d_j) with $d_i, d_j \in D$ and $d_i \neq d_j$. Hence the multiset is $\Delta = \{d_i d_j^{-1} |\ d_i, d_j \in D,\ d_i \neq d_j\}$ [1].

Notice that every difference set is a symmetric block design with a point set $\{0, 1, 2, \dots, v-1\}$ and a block set $\{D, D+1, \dots, D+(v-1)\}$ [13]. The most important and fundemental question of difference set is the existence problem. Does a given group have a difference set? Or can we create a difference set? To find an answer to these questions, first neccessary condition is counting of parameters of a (v, k, λ) difference set which leads the equation $k\ (k-1)\ =\ \lambda\ (v-1)$.

Another answer of the question mentioned above is Bruck- Ryser- Chowla (BRC) theorem. This theorem explains when a (v, k, λ) symmetric design does not exist, hence a (v, k, λ) difference set does not. The proof of this theorem uses incidence matrix M of the design.

2. MAIN RESULTS

Bruck-Ryser-Chowla Theorem is one of most important methods determining if a particular difference set cannot exist providing the conditons for (v, k, λ) symmetric designs' (non)- existence. This theorem also restricts the parameters of a difference set and explains how the solutions of a linear diophantine equation affects the existence of a symetric design. Bruck Ryser Chowla theory was first proven for $\lambda = 1$ [8], the writers after extend the result for any positive λ [8, 11].

$$(v, k, \lambda) = (n^2 + n + 1, n + 1, 1)$$

symmetric design is called a projective spaces where parameter n is the degree of projective

spaces. BRC theorem is used to investigate the question of existence of projective spaces with degree of non prime power n. For $n \equiv 1,2(mod\ 4)$ and $x, y \in \mathbb{Z}$ we have $n = x^2 + y^2$. The following designs are example of projective planes for degree *n=1*, *n=2* and *n=3* [16].

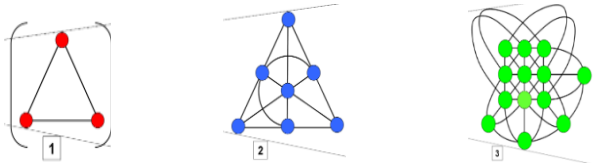

***Theorem* 4.** (*Bruck-Ryser-Chowla Theorem)* Let G be a group with degree v *and* (v, k, λ) symmetric design exists;

- If v is even then n is a perfect square.
- If v is odd, Diophantine equation $x^2 = ny^2 + (-1)^{(v-1)/2}\lambda z^2$ has a nonzero solution in integers x, y, z.

Linear diophantine equation can also be rephrased when $v \equiv 3(mod\ 4)$ or $v \equiv 1(mod\ 4)$

$$x^2 = \begin{cases} \text{If } v \equiv 3(mod\ 4), & ny^2 - \lambda z^2 \\ \text{If } v \equiv 1(mod\ 4), & ny^2 + \lambda z^2. \end{cases}$$

[8,12].

If the BRC statements become to be false for a certain set of parameters, then those parameters do not satisfy a difference set. However if the above criteria is true, we say a difference set may be possible. In addition to that it is safe to presume difference set exists whereas other tools must be used to eplore its existence.

The proof of the theorem for the case number one is straigtforward but the other case needs matrices equivalence and some arguments from linear algebra and number thoery. One can see a simplest proof of the paper in the paper of [12].

Example 5. Let us take parameter $(76, 25, 8)$. When v even, n should be perfect square. $v = 76$, $k = 25$ and $\lambda = 8$ provide $\lambda(v-1) = k(k-1)$ condition. According to Bruck Ryser Chowla Theory, since $v = 76$ is even, $n = k - \lambda$ must be perfect square in order to get a symmetric design. However, $n = 25 - 8 = 13$ is not a perfect square, there is no symmetric design with this parameter. Therefore, there is no difference set with the parameter $(76, 25, 8)$.

MATLAB applications of Linear diophantine equation

This code lists the solution triple for linear diophantine equation provided by BRC theorem. Besides, how many solutions there can be for the result is also given. This is only a sample size of the solution space.

```
function BRC_linear(v,n,l)

if (mod(v,2)==0)

   error('given value v is even. BRC holds.')

end

devir=0;

for i=1:1000

    for j=1:1000

      x=sqrt((n*i^2)+(-1)^((v-1)/2)*(l*j^2));

      if ((x^2)>0 && mod(x,1)==0)


disp(fprintf('(x,y,z)=(%1.0f,%1.0f,%1.0f)',x,i,j))

         devir=devir+1;

      end

   end

end

disp(fprintf(' For those parameters there are %1.0f triple solutions', devir))

end
```

The following result is a possible $(v, k, \lambda) = (67, 14, 2)$ difference set with $\lambda = 2, n = 12$ in group $\mathbb{Z}_{67}$. Because there are too many solutions to write of (1817) outputs, they are not given here totally.

```
>> BRC_linear(67,12,2)

(x,y,z)= (2,1,2)

(x,y,z)= (4,2,4)

(x,y,z)= (10,3,2)

(x,y,z)= (6,3,6)

(x,y,z)= (8,4,8)

(x,y,z)= (10,5,10)

(x,y,z)= (20,6,4)

          ……

(x,y,z)= (3310,993,662)

(x,y,z)= (3448,996,88)

(x,y,z)= (3320,996,664)

(x,y,z)= (3284,998,764)

(x,y,z)= (3330,999,666)

(x,y,z)= (3182,999,962)

With this paramaters there are 1817 triplet solutions.
```

The non symmetric design solution triple for $\mathbb{Z}_{67}$ is the following example. Here we have $v = 67$, $\lambda = 7$, $n = 15$, with this possible parameter $(v, k, \lambda) = (67,22,7)$ is not a difference set.

```
>>BRC_lineer(67,15,7)

With this parameters there are 0 triplet solutions.
```

The following result is a possible $(v, k, \lambda) = (73, 9, 1) -$ difference set in $\mathbb{Z}_{73}$ with $\lambda = 1, n = 8$. For other k and λ values, other possible difference sets of the group $\mathbb{Z}_{73}$ can be tested. The entire output is not shown here because there are too many solutions.

```
>>BRC_linear(73,8,1)

(x,y,z)=(273,91,91)

(x,y,z)=(387,91,289)

(x,y,z)=(663,91,611)

(x,y,z)=(276,92,92)

(x,y,z)=(414,92,322)

(x,y,z)=(561,92,497)

(x,y,z)=(759,92,713)

          ……

(x,y,z)=(2988,996,996)

(x,y,z)=(2991,997,997)

(x,y,z)=(2994,998,998)

(x,y,z)=(2827,999,89)

 (x,y,z)=(2997,999,999)

(x,y,z)=(2850,1000,350)

(x,y,z)=(3000,1000,1000)

With these parameters there are 3038 triplet solutions.
```

The following outputs are for the potential difference sets with parameters $(v, k, \lambda) = (91, 10, 1)$.

```
>> BRC_linear(91,9,1)

(x,y,z)=(12,5,9)

(x,y,z)=(9,5,12)

(x,y,z)=(24,10,18)

(x,y,z)=(18,10,24)

(x,y,z)=(36,13,15)
```

(x,y,z)=(15,13,36)

(x,y,z)=(36,15,27)

(x,y,z)=(2835,977,744)

(x,y,z)=(2880,984,648)

(x,y,z)=(2925,985,420)

(x,y,z)=(2850,986,792)

(x,y,z)=(2808,986,930)

(x,y,z)=(2835,999,972)

(x,y,z)=(2880,1000,840)

With these parameters we have 919 triplet solutions.

The non symmetric design solution triple for $\mathbb{Z}_{91}$ is $(v,k,\lambda) = (91,36,14)$ parameters, hence it is not a difference set.

```
>> BRC_linear(91,22,14)
```

With these parameters there are 0 triplet solutions.

MATLAB Application of BRC Theorem

This code is the application of the second condition of BRC Theorem. The possible solutions of the equation $x^2 = ny^2 + (-1)^{\frac{v-1}{2}}\lambda z^2$ are analayzed. That controls integers values from 1 to 1000 for y and z values. If the program results 0 output, that means there is no symmetric design. However, if the result is 1 it can be a symmetric design. When the result is 1, the existence of symmetric design should be checked by other tools.

```
function s = brc_odd(v,k,lam)
s = 0;
n = k-lam;
tic
for y= 1:1000
   for z= 1:1000
      x= sqrt((n*y^2)+((-1)^((v-1)/2))*lam*z^2);
      if floor(x)==x && x^2>0
         s = 1;
toc
         return
      end
   end
end
```

The following are the resuts of both solutions and non solutions.

```
>> brc_odd (27,13,16)        ans = 0
>> brc_odd (34,12,4)         ans = 0
>> brc_odd (46,10,2)         ans = 0
>> brc_odd (92,14,2)         ans = 0
>> brc_odd (172,19,2)        ans = 0
>> brc_odd (115,19,4)        ans = 0
>> brc_odd (117,29,7)        ans = 0
>> brc_odd (119,59,7)        ans = 0
>> brc_odd (125,32,8)        ans = 0
>> brc_odd (67,12,2)         ans = 0
>> brc_odd (137,17,2)        ans = 0
>> brc_odd (103,18,3)        ans = 0
>> brc_odd (53,13,3)         ans = 0
>> brc_odd (43,15,5)         ans = 0
>> brc_odd (77,20,5)         ans = 0
>> brc_odd (157,40,10)       ans = 0
>> brc_odd (171,85,41)       ans = 0
```

>> brc_odd (173,44,11)	ans = 0	>> brc_odd (5167,288,16)	ans = 1
>> brc_odd (181,45,11)	ans = 0	>> brc_odd (5167,820,130)	ans = 0
>> brc_odd (185,24,3)	ans = 0	>> brc_odd (5167,1107,237)	ans = 0
>> brc_odd (187,31,5)	ans = 0	>> brc_odd (5167,1477,422)	ans = 0
>> brc_odd (193,129,82)	ans = 0	>> brc_odd (5167,1764,602)	ans = 0
>> brc_odd (6271,210,7)	ans = 1	>> brc_odd (5167,2296,1020)	ans = 1
>> brc_odd (2591,260,26)	ans = 1	>> brc_odd (5167,2583,1291)	ans = 1

Table 1 The average working time for the number of solutions parameters (v,k,λ) according to (x,y,z)

(v,n,λ)	Function	The number of solutions	Average working time of the programme
(67,12,2)	BRC (v,n,l)	1817	0,22 second
(67,15,7)	BRC (v,n,l)	0	0,10 second
(73,8,1)	BRC (v,n,l)	3038	0,29 second
(91,9,1)	BRC (v,n,l)	919	0,15 second
(91,22,14)	BRC (v,n,l)	0	1,15 second

Table 2 Average working time for $(\mathrm{v},\mathrm{k},\lambda)$ parameters

(v,k,λ)	Function	1&0	Average working time of the programme
(43,15,5)	brc_odd (v,k,lam)	0	0,1 second
(53,13,3)	brc_odd(v,k,lam)	0	0,1 second
(67,12,2)	brc_odd (v,k,lam)	0	0,1 second
(77,20,5)	brc_odd (v,k,lam)	0	0,1 second
(103,18,3)	brc_odd (v,k,lam)	0	0,1 second
(115,19,4)	brc_odd (v,k,lam)	0	0,1 second
(117,29,7)	brc_odd (v,k,lam)	0	0,2 second
(119,59,7)	brc_odd(v,k,lam)	0	0,2 second
(125,32,8)	brc_odd(v,k,lam)	0	0,2 second
(137,17,2)	brc_odd(v,k,lam)	0	0,2 second
(157,40,10)	brc_odd(v,k,lam)	0	0,2 second
(171,85,41)	brc_odd(v,k,lam)	0	0,2 second
(173,44,11)	brc_odd(v,k,lam)	0	0,2 second
(181,45,11)	brc_odd(v,k,lam)	0	0,2 second
(185,24,3)	brc_odd(v,k,lam)	0	0,2 second
(187,31,5)	brc_odd(v,k,lam)	0	0,2 second
(193,129,82)	brc_odd(v,k,lam)	0	0,2 second
(2591,260,26)	brc_odd(v,k,lam)	1	0,3 second
(5167,288,16)	brc_odd(v,k,lam)	1	0,5 second
(5167,2296,1020)	brc_odd(v,k,lam)	1	0,5 second
(5167,2583,1291)	brc_odd(v,k,lam)	1	0,5 second
(5167,1477,422)	brc_odd(v,k,lam)	0	0,5 second
(5167,1764,602)	brc_odd(v,k,lam)	0	0,5 second

Acknowledgments

The work has been done mostly in here come from Öztürk's thesis under supervision of the first author [17]. The authors would like to thank the anonymous referees for necessary comments which have improved the presentation of the paper.

Funding

The authors received no financial support for the research, autorship or publication of this study.

The Declaration of Conflict of Interest/ Common Interest

No conflict of interest or common interest has been declared by the authors.

The Declaration of Ethics Committee Approval

The authors declares that this document does not require an ethics committee approval or any special permission.

The Declaration of Research and Publication Ethics

The authors of the paper declares that she complies with the scientific, ethical and quotation rules of SAUJS in all processes of the paper and that she does not make any falsification on the data collected. In addition, she declares that Sakarya University Journal of Science and its editorial board have no responsibility for any ethical violations that may be encountered, and that this study has not been evaluated in any academic publication environment other than Sakarya University Journal of Science.

REFERENCES

[1] E.S. Lander, "Symmetric Designs an Algebraic Approach," Volume 74 of London Mathematical Society, Lecture Note Series. Cambridge University, pp. 3-40, 1983.

[2] M. Hall Jr and H.J. Ryser, "Cyclic incidence matrices," Canadian Journal of Mathematics, vol. 3, pp. 495-502, 1951.

[3] D. Peifer, "Difference Set Transfers," Northfield Undergraduate Mathematics Symposium, 29 Ekim, 3-4. 2013

[4] J. Singer, "A theorem in finite projective geometry and some applications to number theory," Transactions of the American Mathematical Society, vol. 43, no. 3, pp. 377-385, 1938.

[5] R.C. Bose and K.R. Nair, "Partially balanced incomplete block designs," Sankhya: The Indian Journal of Statistics, vol. 4, no. 3, pp. 337-372, 1939.

[6] M. Hall Jr, "Cyclic projective planes," Duke Mathematical Journal, vol. 14, no. 4, pp. 1079-1090, 1947.

[7] F.W. Levi, "Groups in which the commutator operation satisfies certain algebraic conditions," The Journal of the Indian Mathematical Society, vol. 6, pp. 87-97. 1942.

[8] R.H. Bruck and H.J. Ryser, "The non existence of certain finite projective planes," Canadian Journal of Mathematics, vol. 1, no. 1, pp. 88-93, 1949.

[9] M.P. Schützenberger, "A Nonexistence Theorem for Infinite family of symmetrical block designs," Annals of Human Genetics, vol. 14, no. 1, pp. 286-287, 1949.

[10] P. Dembowski, "Finite geometries," Mathematics Subject Classification (1991): 51E, vol. 44, 1997.

[11] S. Chowla and H. J. Ryser, "Combinatorial problems," Canadian Journal of Mathe matics, vol. 2, pp. 93-99, 1950.

[12] H.J. Ryser, "The existence of symmetric block designs," Journal of Combinatorial Theory A, vol. 32, no. 1, pp. 103-105, 1982.

[13] L.D. Baumert, "Cyclic Difference Sets," California Institute of Technology Pasadane, vol. 172, pp. 1-9, 1971.

[14] D. Raghavarao, "Constructions and Combinatorial Problems in Design of Experiments," John Wiley, Newyork, 1971.

[15] R.E. Kibler, "A summary of noncyclic difference sets k<20," Journal of Combinatorial Theory A, vol. 25, no. 1, pp. 62-67, 1978.

[16] P. J. Cameron and J. H. Lint, "Desings, Graps, Codes and their Links www.maa.org/programs/maa-awards/writing-awards/the-search-for-finite-projective-plane-of-order-10," Cambridge University Press, 1991.

[17] S. Öztürk, "Fark kümelerinin varlık problemi ve Bruck Ryser Chowla Teoremi," Yüksek Lisan Tezi, Recep Tayyip Erdoğan Üniversitesi Fen Bilimleri Enstitüsü, Rize, 2020.

[18] E. Demirci Akarsu, "Almost Difference Sets and Cyclotomy," in Academic Studies in Science and Mathematics. Izmir, Turkey: Platanus Duvar Publishing, ch. 10, pp. 143–159, 2021.

SAKARYA ÜNİVERSİTESİ
FEN BİLİMLERİ ENSTİTÜSÜ DERGİSİ

Sakarya University Journal of Science
SAUJS

e-ISSN 2147-835X Period Bimonthly Founded 1997 Publisher Sakarya University
http://www.saujs.sakarya.edu.tr/

Title: A Numerical Investigation for the Effect of Environmental Conditions on the Bending Behavior of Laminated Composites

Authors: Rabi Ezgi BOZKURT, Fatih DARICIK

Recieved: 2021-04-21 00:00:00

Accepted: 2022-02-17 00:00:00

Article Type: Research Article

Volume: 26
Issue: 2
Month: April
Year: 2022
Pages: 249-261

How to cite
Rabi Ezgi BOZKURT, Fatih DARICIK; (2022), A Numerical Investigation for the Effect of Environmental Conditions on the Bending Behavior of Laminated Composites. Sakarya University Journal of Science, 26(2), 249-261, DOI: 10.16984/saufenbilder.925144
Access link
https://dergipark.org.tr/tr/journal/1115/issue/69580/925144

New submission to SAUJS
http://dergipark.gov.tr/journal/1115/submission/start

Sakarya University Journal of Science 26(2), 249-261, 2022

A Numerical Investigation for the Effect of Environmental Conditions on the Bending Behavior of Laminated Composites

Rabi Ezgi BOZKURT[1], Fatih DARICIK*[1]

Abstract

In this study, the bending behavior of fiber-reinforced laminated composites (FRCs) with a balanced and symmetric stacking sequence was investigated numerically under different environmental conditions. The numerical models of carbon/ bismaleimide, carbon/epoxy, and S-glass/epoxy laminated composites were designed and analyzed using ESAComp software. Deformation of the FRCs models was simulated with three-point bending conditions and the effects of material properties varying with environmental conditions on the flexural analysis were investigated according to the Tsai-Wu criterion and the Puck criterion. The Tsai-Wu criterion detects the failure of FRCs earlier and behaves more conservative than the Puck criterion for all environmental conditions. The flexural strength and failure mode of the laminates vary with the variation of environmental conditions. The order of the first damaged ply varied depending on the type of reinforcing fiber. Especially the presence of moisture and high temperature significantly influences the flexural strength of the laminated composites.

Keywords: Laminated composites, environmental conditions, three-point bending, failure analysis

1. INTRODUCTION

FRCs are very attractive because of their superior specific strength properties. FRCs are used in many engineering applications that contain different loads, such as static, fatigue, hygrothermal, etc. The fibers supply high strength and rigidity for in-plane properties of the FRCs. Out-of-plane properties of the FRCs are depending on the strength of matrix materials which are lower than that of the reinforcing fibers. The hygrothermal stability of the polymer matrix materials is also very low according to the fibers. Thus, the environmental conditions and thermal/hygrothermal aging directly affect the mechanical strength of the FCRS [1-5]. The surface treatment of the reinforcing material is another factor that can vary the mechanical behavior of the FCRs by changing the interface strength of the matrix and fibers [6], [7]. In recent years, studies have been carried out to increase the strength of the FCRs by strengthening them with nanoparticles [8-13]. Türkmen et al. produced glass fiber mat reinforced composite materials that have a different number of layers by the using hand lay-up method [14]. The three-point bending test method was used to determine the flexural strength of GFRP materials. Because of the test,

* Corresponding author: fatih.daricik@alanya.edu.tr
[1] Alanya Alaaddin Keykubat University, Rafet Kayış Faculty of Engineering, Machine Engineering Department
E-mail: ezgibozkurt80@gmail.com
ORCID: https://orcid.org/0000-0002-7714-1819, https://orcid.org/0000-0002-5813-1260

the maximum bending strength of 150.85 MPa was got from the manufactured materials. Bingöl et al. compared the flexural properties of glass mat reinforced composites and the woven glass fiber reinforced composite materials [15]. The research results showed that the higher fiber length of the non-woven fiberglass fabric provides higher flexural strength and the bending strength of woven glass fiber reinforced composite material is higher than that of the non-woven fiberglass fabric reinforced composites.

The physical and mechanical properties of fiber-reinforced composite materials can be improved by adding various additives. Gülşah et al investigated the flexural strength of E-glass fiber/epoxy composite materials with carbon nanotube added [16]. The experimental results have shown the addition of %0.75w carbon nanotube increased the flexural modulus and the flexural strength of the material in a ratio of %36 and %23, respectively. Kıratlı et al. reported that the graphene nanoplatelets significantly increased the flexural strength of the E-glass/epoxy laminated composites [13]. Hybrid composite structures are attracted nowadays, as many different fiber types can be used as reinforcement elements. Aydın et al. have manufactured glass fabric reinforced, carbon fabric reinforced, and hybrid glass/carbon fabric reinforced laminates and compared the flexural properties of the laminates [17]. The study presented that just carbon fiber reinforced composite structure exhibits maximum bending strength among the tested laminates.

Metal plate reinforced hybrid materials can be shown high mechanical properties. Bellini et al. investigated the flexural strength and fracture behavior of different types of aluminum carbon fibers [18]. Experimental results showed that the presence of an aluminum sheet provides an increment of the flexural strength and a slight decrease of the required energy to propagation of the crack. Furthermore, the presence of the adhesive at the composite/metal interface made the flexural strength decrease and the fracture energy increase.

The hybridization of natural fibers with their superior aging resistance and synthetic fibers relevant attention in terms of environmental impact and the durability they are provided. Calabrese et al. glass-flax/epoxy hybrid composites materials were exposed to salt–fog environmental conditions for up to 60 aging days [2]. They evidenced that adding glass fibers in flax layers positive affected flexural strength and modulus can be observed. Laminated composite materials with high fiber angles are more prone to stress concentration on the layers. Reis et al. studied stress relaxation behavior of glass/polyamide-6 composites considering different fiber directions [1], as well as exposure to NaOH and HCl solutions. Consequently, compared with the laminates with fibers at 0◦, flexural strength decreased approximately up to 50%, respectively, for the orientations of 30◦ and 45◦.

Fiber, matrix, adhesive and interface components in composite material are susceptible to degradation of Ph changed. Wang et al. GFRP composite material has been exposed to salt-water and water [3]. Consequently, the degradation was faster in saltwater than in tap water. Also, when the exposure time was increased, there has been a serious decreased in the strain values. Harrison et al. presented that seawater reduces the flexural strength of carbon/epoxy and glass/epoxy composite materials in the long term [4]. Pavan et al. showed the bending strength and damage formation of GFRP laminates composite materials under different environmental conditions [19]. They evidenced that the bending strength decreases with increasing exposure temperature. Bazli et al. investigated the flexural strength of GFRP laminated composite material under different temperature conditions [20]. Conclusion reported that as the thickness of the composite materials decreases, the flexural strength decreases when the exposure time at high temperatures increases. Meng et al. examined the CFRP from 77 K° to 298 K° and showed that the flexural strength increased as the cryogenic temperature decreased [21]. Also, has been shown that the cryogenic temperature affects the durability of the matrix and the failure mode of the layers.

In the literature examined, it has been observed that different environmental conditions affect the flexural strength of the materials. Depended on the changing environmental conditions, the change in strength values can be determined by three-point bending analysis. In this paper, Carbon fiber/bismaleimide, carbon fiber/epoxy and S-glass fiber/epoxy layered composite materials are designed with balanced symmetry and angled storied. These materials have been examined for their flexural behavior under different environmental conditions. The deformation caused by the bending load in FRC materials was investigated using the Tsai-Wu and Puck failure criteria.

2. MATERIAL AND METHOD

Three-point bending analyses were done by simulating the real test according to ASTM D790. Three different reinforced plies were considered to design FRC laminates and then to perform flexural analysis. Carbon fiber/bismaleimide (Cytek_CB) unidirectional ply, carbon fiber/epoxy (Toray_CE) unidirectional ply, and S-glass fiber/epoxy (Cytek_S-GE) unidirectional ply was employed with the material property sets that differed according to environmental conditions (Table 1). The ambient temperature 24℃ was assume as the reference for all the materials. The weight amount of moisture in the ambient was also expressed as +w%, i.e., 82℃+1w%. The laminates were designed with the symmetric and balanced stacking sequence of $[0_n/30_n/\text{-}30_n/60_n/\text{-}60_n/90_n]_s$ via ESAComp software (Figure 1). The subscript *n* is equal to 3 for 36 layers of Cytek_CB, 2 for 24 layers of Toray_CE, and 1 for 14 layers of Cytek_S-GE. However, there is an exception for Cytek_S-GE that the subscript *n* is 2 for the 0° reinforced layer. As a result of selected stacking sequences, the thicknesses of the laminates (*d*) Cytek_CB, Toray_CE, and Cytek_S-GE were 3.37 mm, 3.65 mm, and 3.30 mm respectively. The geometrical models of the three-point bending specimen were prepared with dimensions of 60 mm in the length (*L*) and 12.67 mm in the width (*b*) (Figure 2). Each laminate with different material property sets has been investigated for flexural behavior.

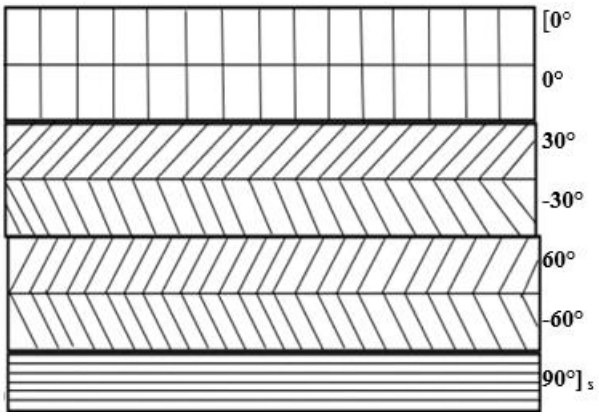

Figure 1 Stacking sequence of the laminates

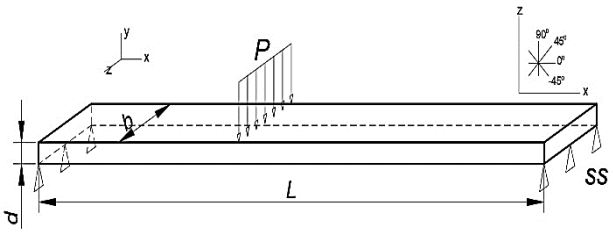

Figure 2 The dimensions of the model for bending analysis

Table 1 Mechanical Properties of FRCs Materials [22-24]

Symbol		Cytek_CB (ρ =1.568g/cm^3 V_f=60%)			Cytek_S-GE (ρ =1.839g/cm^3 V_f=49%)					Toray_CE (ρ =1.555g/cm^3 V_f=55%)			
Cond.	Temp. (°C)	-55	24	177	-54	24	66	82	82	-54	24	82	82
	Moist. (%)	0	0	1	0	0	1	0	1	0	0	0	1
Elastic Properties	E_1 (GPa)	169.00	160.00	138.00	48.81	47.99	47.13	46.88	47.37	121.00	119.00	121.00	119.50
	E_2 (GPa)	10.35	9.70	9.00	15.79	15.79	12.31	13.20	11.51	52.98	9.00	7.50	7.00
	E_3 (GPa)	10.35	9.70	9.00	15.79	15.79	12.31	13.20	11.51	52.98	9.00	7.50	7.00
	G_{12} (GPa)	5.90	5.90	2.00	4.27	4.07	3.72	3.72	2.62	5.00	4.00	4.00	3.00
	G_{31} (GPa)	5.90	5.90	2.00	4.27	4.07	3.72	3.72	2.62	5.00	4.00	4.00	3.00
	G_{23} (GPa)	3.98	3.73	3.46	5.85	5.85	4.56	4.89	4.26	4.26	3.33	2.78	2.59
	υ_{12}	0.30	0.30	0.30	0.28	0.26	0.26	0.26	0.30	0.35	0.31	0.31	0.32
	υ_{13}	0.30	0.30	0.30	0.28	0.26	0.26	0.26	0.30	0.35	0.31	0.31	0.32
	υ_{23}	0.30	0.30	0.30	0.35	0.35	0.35	0.35	0.35	0.35	0.35	0.35	0.35
Stregth Properties	X_t (MPa)	2897.00	2618.00	2278.00	1274.79	1501.20	934.52	1418.18	880.74	1682.01	2172.44	2206.66	2259.82
	Y_t (MPa)	63.00	66.00	28.00	56.54	56.54	56.40	59.64	49.71	52.98	48.86	44.23	25.91
	Z_t (MPa)	63.00	66.00	28.00	56.54	56.54	56.40	59.64	49.71	52.98	48.86	44.23	25.91
	X_c (MPa)	1620.00	1620.00	966.00	1240.16	1179.76	951.55	508.21	688.92	1396.50	1449.77	1410.32	1199.97
	Y_c (MPa)	207.00	194.00	180.00	274.27	274.27	185.68	208.57	165.13	282.44	198.67	147.72	116.43
	Z_c (MPa)	207.00	194.00	180.00	274.27	274.27	185.68	208.57	165.13	282.44	198.67	147.72	116.43
	S_{12} (MPa)	102.00	103.00	77.00	169.96	132.17	96.73	103.01	81.84	159.52	154.74	128.31	95.22
	S_{31} (MPa)	102.00	103.00	77.00	169.96	132.17	96.73	103.01	81.84	159.52	154.74	128.31	95.22
	S_{23} (MPa)	59.71	55.96	51.92	87.72	87.72	68.37	73.35	63.97	63.89	50.00	41.67	38.89

The numerical models of the bending specimens were prepared with rectangular shell elements. Longer edges of the model were divided into 120 parts and the aspect ratio for the elements was adjusted to 1. Boundary conditions for the shorter edges were set as free along the *z*-direction, as fixed along the *y*-direction. The translation of the edges along the *x*-direction was kept at *x=0* and released at *x=L*. Rotations around all of the directions were released too. Thus, the ratio of the support span to the thickness was approximately 20:1 for all the models. Then the models were loaded along the *y*-direction with a centered line load. The models were loaded until the failure was detected. In the numerical model, the value of the load causing failure was recorded.

The failure of the modeled composite materials under bending load was determined according to both the Tsai-Wu and the Puck failure criteria. According to the Tsai-Wu failure criterion, if the *f* value calculated with Equation 1is less than 1 so that the composite material is safe. The load value that makes the *f* value equal to or less than 1 was taken as failure load (P_{cr}) and the corresponding deflection (δ_{cr}) was recorded. In Equation 1, the σ_1 and σ_2 express the axial stresses along the reinforcement direction (direction-*1*) and transverse direction (direction-*2*). The term τ_{12} expresses the shear stress on the *1-2* plane. Other coefficients are the constants dependent on the material strength (Table 1).

$$f = F_1\sigma_1 + F_2\sigma_2 + F_6\tau_{12} + 2F_{12}\sigma_1\sigma_2 + F_{11}\sigma_1^2 + F_{22}\sigma_2^2 + F_{66}\tau_{12}^2 \quad (1)$$

$$F_1 = \frac{1}{X_t} - \frac{1}{X_c}, \quad F_2 = \frac{1}{Y_t} - \frac{1}{Y_c}, \quad F_6 = 0 \quad (2)$$

$$F_{11} = \frac{1}{X_t X_c}, \quad F_{22} = \frac{1}{Y_t Y_c}, \quad F_{66} = \frac{1}{S^2} \quad (3)$$

The Puck criterion dissociates the damage of the laminates into reinforcement failure (*FF*) and matrix material failure (*MF*). The criterion uses the indices *IFF* and *IMF* for fiber failure and

matrix failure, respectively. According to the criterion, reinforcement fiber failure occurs only under tensile load in the direction of the fiber and the matrix material failure is handled with three different fracture modes (Figure 3). According to Mode A failure, matrix fracture occurs on a plane parallel to the reinforcing fibers due to tensile forces transverse to the reinforcing direction. In Mode B failure, matrix fracture occurs between reinforcing fibers in the material under shear stresses and small compressive stresses. In Mode C failure, matrix cracks occur along inclined planes in the material under compression loads. Equations 4-10 are used to control each failure mode.

$$\sigma_1 > 0 \rightarrow I_{FF} = \sigma_1 / F_{1t} \tag{4}$$

$$-\sigma_1 < 0 \rightarrow I_{FF} = -\sigma_1 / F_{1c} \tag{5}$$

$$\sigma_2 \geq 0 \rightarrow$$

$$I_{MF,A} = \sqrt{\left(\frac{\sigma_6}{F_6}\right)^2 + \left(1 - p_{6t}\frac{F_{2t}}{F_6}\right)^2 \left(\frac{\sigma_2}{F_{2t}}\right)^2} + p_{6t}\frac{\sigma_2}{F_6} \tag{6}$$

$$\left.\begin{matrix} \sigma_2 < 0 \\ \left|\frac{\sigma_2}{\sigma_6}\right| \leq \frac{F_{2A}}{F_{6A}} \end{matrix}\right\} \rightarrow$$

$$I_{MF,B} = \frac{1}{F_6}\left[\sqrt{\sigma_6^2 + (p_{6c}\sigma_2)^2} + p_{6c}\sigma_2\right] \tag{7}$$

$$F_{2A} = \frac{F_6}{2p_{6c}}\left[\sqrt{1 + 2p_{6c}\frac{F_{2c}}{F_6}} - 1\right] \tag{8}$$

$$p_{2c} = p_{6c}\frac{F_{2A}}{F_6} \tag{9}$$

$$\left.\begin{matrix} \sigma_2 < 0 \\ \left|\frac{\sigma_2}{\sigma_6}\right| \leq \frac{F_{2A}}{F_{6A}} \end{matrix}\right\} \rightarrow$$

$$I_{MF,C} = -\frac{F_{2c}}{\sigma_2}\left[\left(\frac{\sigma_6}{2(1+p_{2c})F_6}\right)^2 + \left(\frac{\sigma_2}{F_{2c}}\right)^2\right] \tag{10}$$

According to Puck and Schürmann (2004), stress and strain analysis, failure criterion, and strength degradation of each layer of laminate are required to form the most realistic failure envelope [25]. However, the researchers neglected the reduced strength values that emerged with the first failure of layered composite materials under load in the failure criterion they proposed. For the failure analysis of the laminates with the Tsai-Wu and Puck criteria, when just one ply of the laminates was damaged then the entire laminates were assumed as damaged. This approach is called first ply failure (*FPF*).

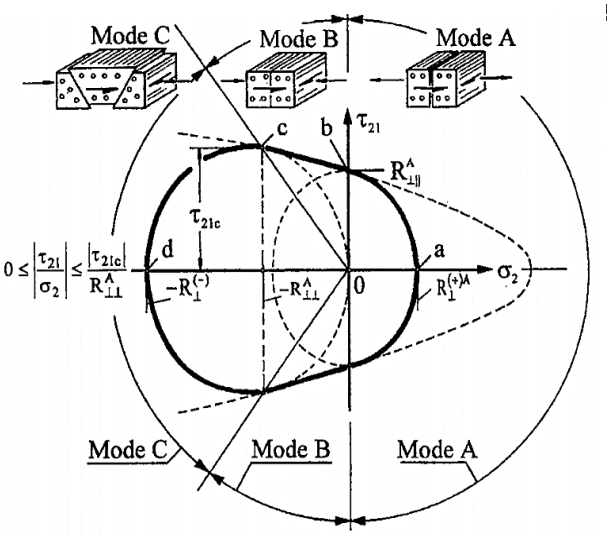

Figure 3 Formation of damage modes A, B, and C under plane stress σ_2 and τ_{21} according to the Puck criterion [24]

3. RESULT

3.1. Analysis of carbon/ bismaleimide/ composites

Variations of the P_{cr} and δ_{cr} for Cytek_CB were presented in Figures 4-5. According to both of the Tsai-Wu and Puck criteria, the bending strength of the Cytek_CB at room temperature (the reference material) is maximum, and it is slightly lower at -55°C. However, the bending strength of the Cytek_CB has been drastically reduced with the increase in temperature and the presence of moisture in the environment. According to the Tsai-Wu criterion, the bending strength of the Cytek_CB at -55°C and 177°C+1.15w% is respectively 3.61% and 57.39% lower than that of the reference material. According to the Puck criterion, the bending strength of the Cytek_CB at -55°C and 177°C+1.15w% is respectively 3.58% and 53.3% lower than that of the reference material.

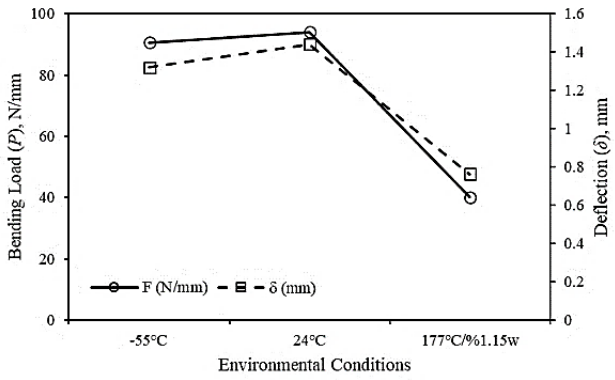

Figure 3 P_{cr} and δ_{cr} values of the Cytek_CB by the Tsai-Wu criterion

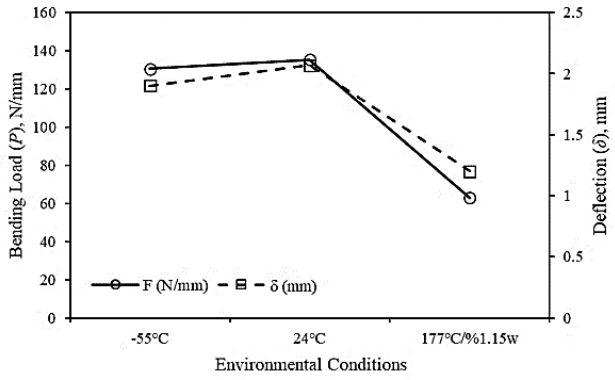

Figure 4 P_{cr} and δ_{cr} values of the Cytek_CB by the Puck criterion

The ply-wise stress (σ_1) distributions in the reference material along the fiber direction because of the P_{cr} were presented and compared (Figures 6-7). The variation of σ_1 has similar characteristics for all the environmental conditions according to both the Tsai-Wu and Puck criteria. Because of bending load, the longitudinal compressive stresses on the upper part, according to the mid plane, caused tensile σ_1 in the layers with 60°, -60°, and 90° reinforcements. The arrangement of the layers is balanced and symmetrical, so the stress distribution across the thickness of the layers is symmetric concerning the midplane.

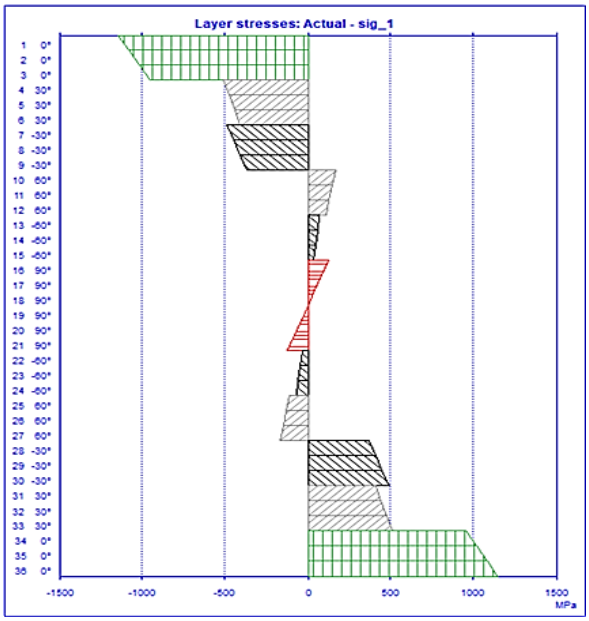

Figure 5 σ_1 values at room temperature for the Cytek_CB by the Tsai-Wu criterion

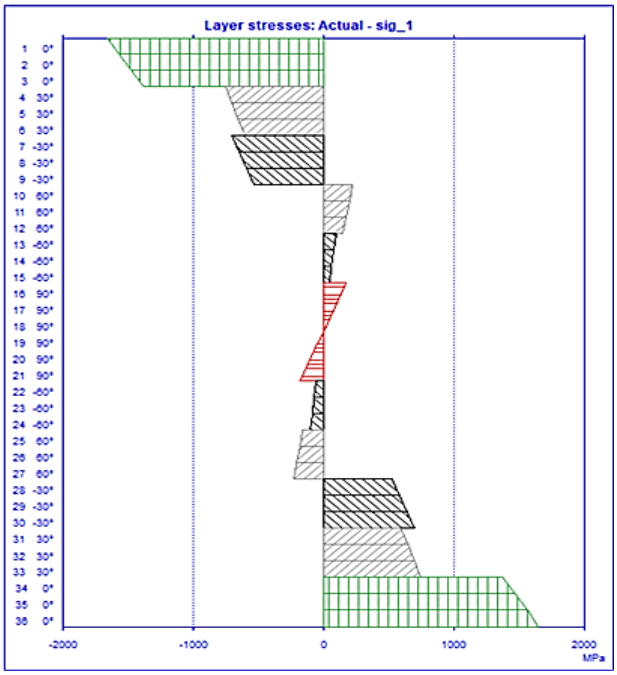

Figure 6 σ_1 values at room temperature for the Cytek_CB by the Puck criterion

The maximum stresses have occurred as tensile at 36th ply and as compression in the first layer. With the bending load applied to the Cytek_CB, the top layer has been damaged first. According to the Puck criterion, it has been observed that the damage mode is Mode A which comprises fiber failure compression (*ffc*) and planar shear stress. On the other hand, the damage is caused because

of transverse tensile (*2t*) stress, according to Tsai-Wu. The detected failure modes were valid for the failures under all environmental conditions except for the Tsai-Wu result of 177°C+1.15w%. Inverse reserve factor (*IRF*) values calculated by Tsai-Wu and Puck criterion for each layer of Cytek_CB material at room temperature has given in Figures 8-9, respectively. Because of failure loads, the Tsai-Wu criterion detects the failure of Cytek_CB early and behaves more conservative than the Puck criterion for all environmental conditions.

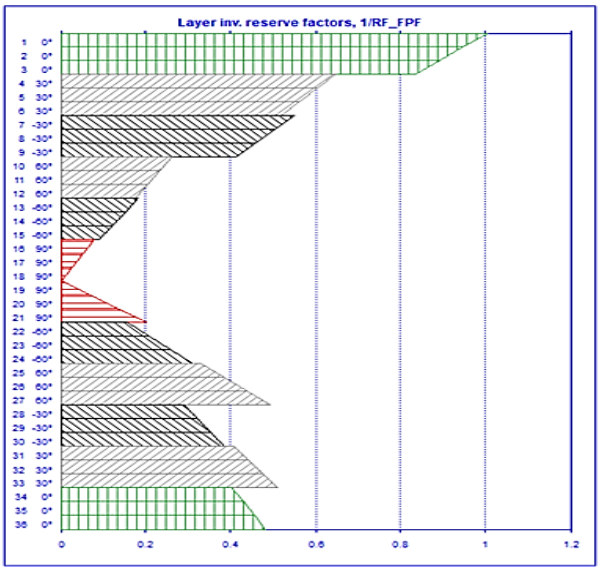

Figure 7 IRF values of the Cytek_CB layers by the Tsai-Wu Criterion

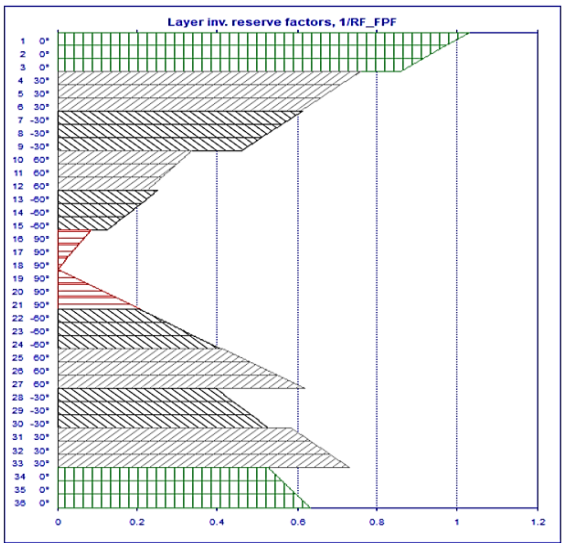

Figure 8 IRF values of the Cytek_CB layers by the Puck criterion

3.2. Analysis of carbon /epoxy / composites

P_{cr} and δ_{cr} variations for the Toray_CE in different environmental conditions were presented in Figure 10-11. According to both of the Tsai-Wu and Puck criteria, the bending strength of the Toray_CE is maximum at 82°C and it is slightly lower at -54°C and 24°C. Furthermore, the flexural strength of Toray_CE was decreased significantly with the increase in temperature and the presence of moisture. According to the Tsai-Wu criterion, the flexural strength of Toray_CE increased by 3.7% when the temperature decreased from the reference condition (room temperature) to -54°C and decreased 0.18% when it increased to 82 °C. Also, the flexural strength of Toray_CE was significantly reduced by 31.02% at the condition 82°C+1w% compared to the reference Toray_CE. According to the Puck criterion, the flexural strength of the Toray_CE increased by 2.2% when the temperature decreased from the reference condition to -54°C and decreased 0.4% when it increased to 82°C. Also, the flexural strength of Toray_CE was significantly reduced by 28.6% at the condition 82°C+1w% compared to the reference Toray_CE.

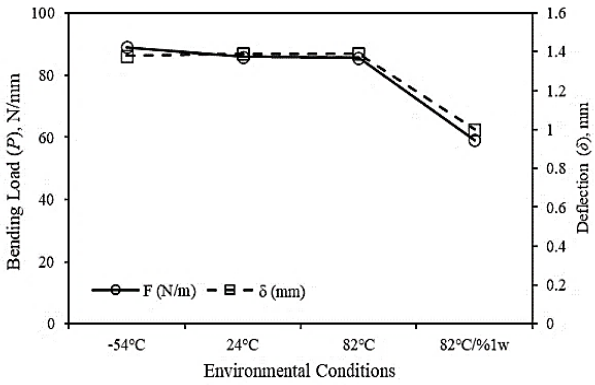

Figure 9 P_{cr} and δ_{cr} values of the Toray_CE by the Tsai-Wu criterion

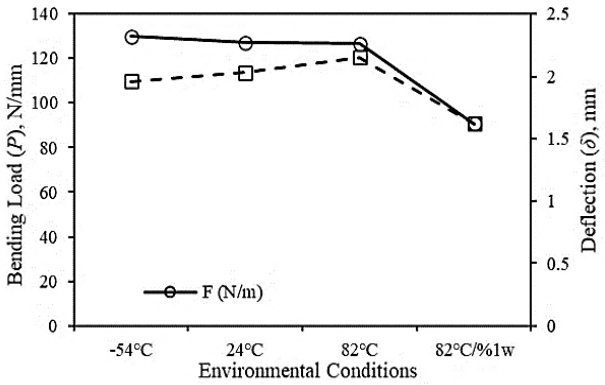

Figure 10 P_{cr} and δ_{cr} values of the Toray_CE by the Puck criterion

The ply-wise σ_1 distributions in the reference material along the fiber direction because of P_{cr} were presented in Figures 12-13. Although the planar tensile and compression strength of Cytek_CB is higher compared to Toray_CE, the flexural strength of Toray_CE is higher. This may be because of the higher shear strength of Toray_CE. The σ_1 distributions given for the Tsai-Wu and Puck damage criteria at room temperature showed similar results for all conditions. Because of bending load, the longitudinal compressive stresses on the upper part according to the mid-plane caused tensile σ_1 in the layers with 60°, -60°, and 90° reinforcements.

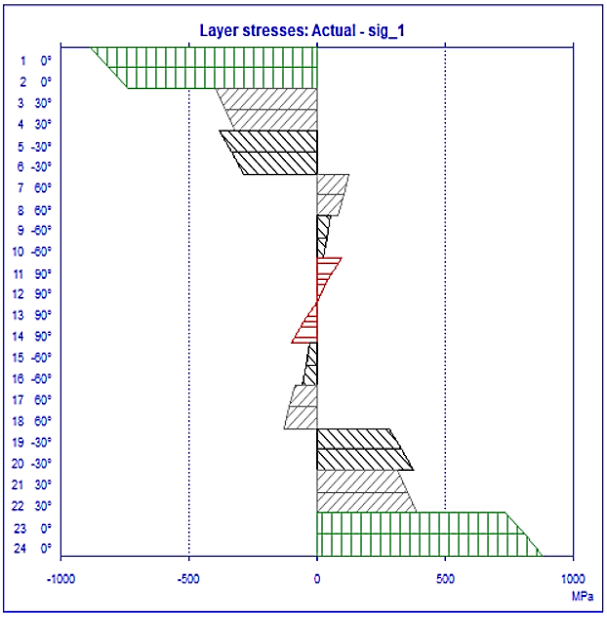

Figure 11 σ_1 values at room temperature for the Toray_CE by the Tsai-Wu criterion

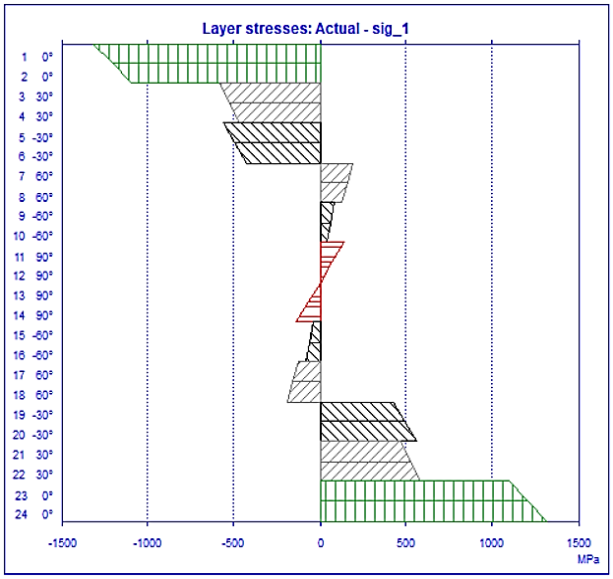

Figure 12 σ_1 values at room temperature for the Toray_CE by the Puck criterion

The maximum stresses have occurred as tensile at 24th ply and as compression in the first layer. With the bending load applied to the Toray_CE material, the top layer has been damaged first. According to the Puck criterion, it has been observed that the damage mode is Mode A. The detected failure modes according to the Puck criterion were valid for the failures of the materials under all environmental conditions. On the other hand, failure modes according to Tsai-Wu criterion could be just compression along the fiber direction (*1c*), transverse tensile (*2t*), and the combination of the first two failure modes (*1c/2t*). IRF values calculated by Tsai-Wu and Puck criterion for each layer of Toray_CE material at room temperature has given in Figures 14-15, respectively. As a result of failure loads, the Tsai-Wu criterion detects the failure of Toray_CE early and behaves more conservative than the Puck criterion for all environmental conditions.

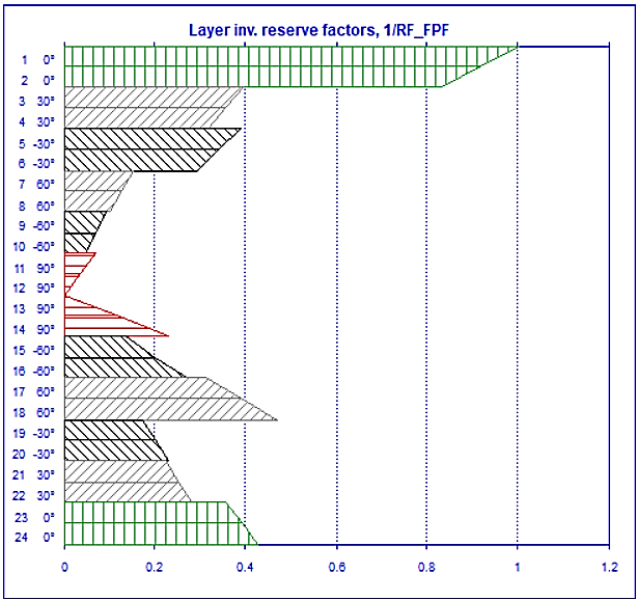

Figure 13 IRF values of the Toray_CE layers by the Tsai-Wu Criterion

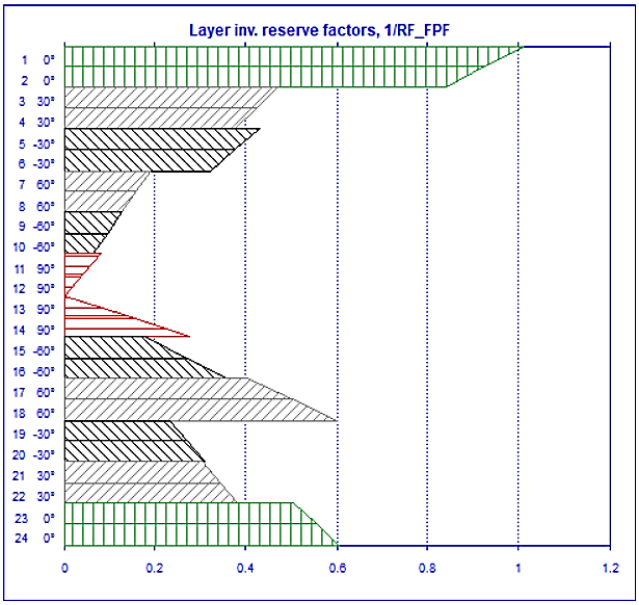

Figure 14 IRF values of the Toray_CE layers by the Puck criterion

3.3. Analysis of S-glass/epoxy/composites

For Cytek_S-GE, variations of the P_{cr} and δcr due to environmental conditions were presented in Figure 16-17. According to both of the Tsai-Wu and Puck criteria, the bending strength of the Cytek_S-GE is maximum at 66°C+0.8w%. According to the Tsai-Wu criterion, the flexural strength of Cytek_S-GE increased by 3.15% when the temperature decreased from the reference condition (room temperature) to -54 °C and decreased 0.17% when it increased to 82 °C. Besides, the flexural strength of the Cytek_S-GE increased by 15.8% at the condition of 66°C+0.8w% and decreased by 15.44% at 82°C compared to reference Cytek_S-GE. According to the puck criterion, when the temperature increased to 82°C and decreased to -54°C, the flexural strength increased by 0.83% and 14.4%, respectively compared to reference Cytek_S-GE. The flexural strength of the material at 66°C+0.8w% is 16.8% higher than the strength of reference Cytek_S-GE and it is 13.6% lower at 82°C than the reference.

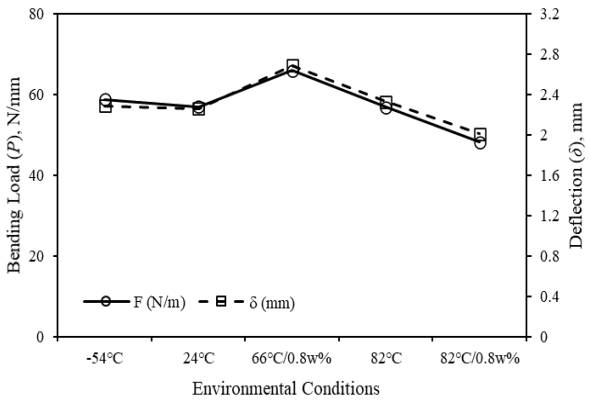

Figure 15 P_{cr} and δ_{cr} values of the Cytec_S-GE by the Tsai-Wu criterion

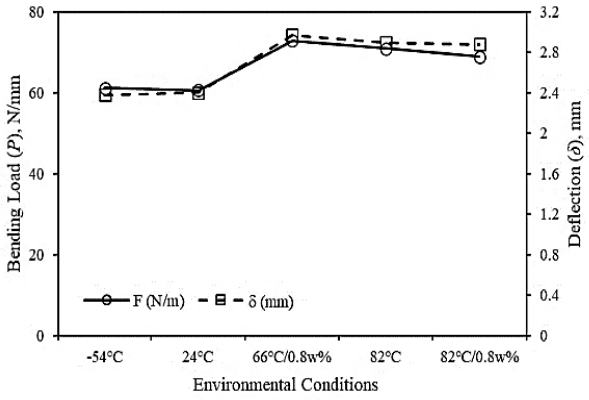

Figure 16 P_{cr} and δ_{cr} values of the Cytec_S-GE by the Puck criterion

The ply-wise σ_1 distributions in the reference material along the fiber direction due to P_{cr} were presented in Figures 18-19. The σ_1 distributions given for the Tsai-Wu and Puck damage criteria at room temperature showed similar characteristics for all conditions. Because of that,

the level of the 5th ply reinforced is just 0.24 mm higher than the 6th ply, the σ_1 at the 5th ply is tensile while the σ_1 6th ply is compressive. In addition to this, the tensile σ_1 comes up in the 90° reinforced layer on the mid-plane.

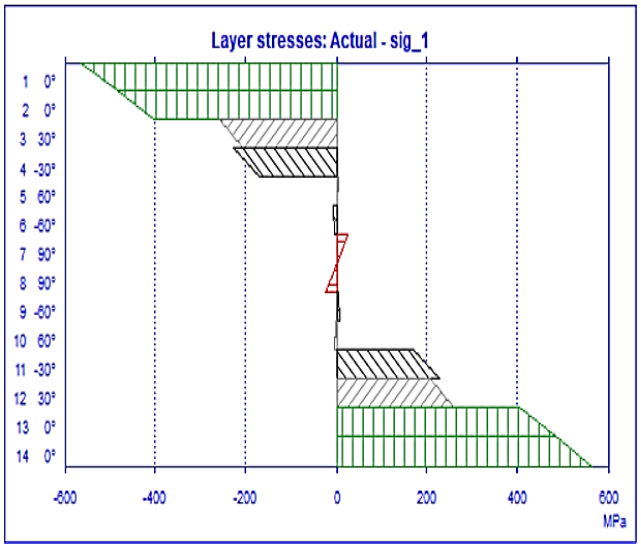

Figure 17 σ_1 values at room temperature for Cytec_S-GE by the Tsai-Wu criterion

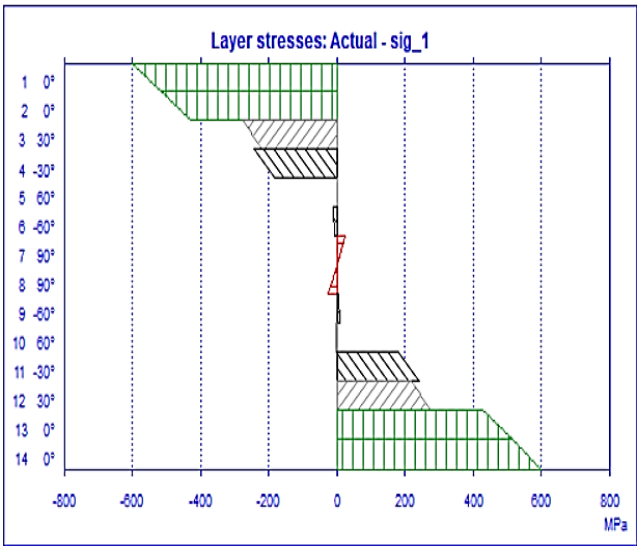

Figure 18 σ_1 values at room temperature for Cytec_S-GE by the Puck criterion

The maximum stresses have emerged as tensile at 14th ply and as compression in the first layer. With the bending load applied to the Cytek_S-GE, the 10th layer was damaged first. According to the Puck criterion, for all environmental conditions, it was observed that the damage mode is Mode A which comprises inter-fiber failure (*iff*) and planar shear stress. Also, the damage of reference material is caused by transverse tensile (*2t*) stresses according to Tsai-Wu. According to the Tsai-Wu criterion, the environmental conditions change the failure of materials. IRF values calculated by Tsai-Wu and Puck criterion for each layer of Cytek_S-GE material at room temperature were given in Figures 20-21, respectively. As a result of failure loads, the Tsai-Wu criterion detects the failure of Cytek_S-GE early and behaves more conservative than the Puck criterion for all environmental conditions.

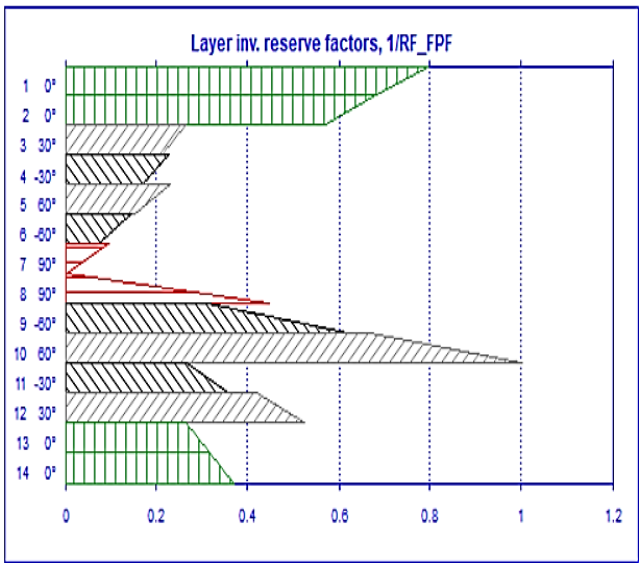

Figure 19 IRF values of the layers of the Cytec_S-GE by the Tsai-Wu Criterion

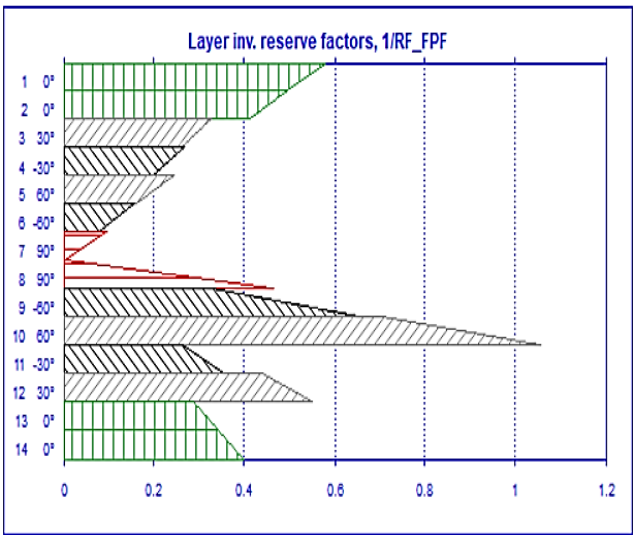

Figure 20 IRF values of the layers of the Cytec_S-GE by the Puck criterion

4. CONCLUSIONS

Numerical bending analyses of carbon/bismaleimide, carbon/epoxy, and S-glass/epoxy laminated composites were performed using ESAComp software. Materials property sets differing from environmental conditions were used for the analysis. Failure of the laminates was determined by the Tsai-Wu criterion and the Puck criterion. As a result of the analysis, the following conclusions have been obtained;

- The Tsai-Wu criterion detects the failure of FRCs earlier and behaves more conservative than the Puck criterion for all environmental conditions.
- The top layers where the line load directly affect, were damaged first in the Cytek_CB and Toray_CE laminated composites. Besides, the 10^{th} layer was damaged first in the Cytek_S-GE laminated composites.
- The variation of flexural strength differs according to the type of the laminated composite. However, high environmental temperature and moisture reduce the flexural strength.
- While the environmental conditions do not affect the damage mode according to the Puck criterion, the damage mode can change with the change of environmental conditions according to the Tsai-Wu criterion.

Funding

The authors have no received any financial support for the research, authorship, or publication of this study.

The Declaration of Conflict of Interest/ Common Interest

No conflict of interest or common interest has been declared by the authors.

Authors' Contribution

The authors contributed equally to the study.

The Declaration of Ethics Committee Approval

This study does not require ethics committee permission or any special permission.

The Declaration of Research and Publication Ethics

The authors of the paper declare that they comply with the scientific, ethical, and quotation rules of SAUJS in all processes of the paper and that they do not make any falsification of the data collected. In addition, they declare that Sakarya University Journal of Science and its editorial board have no responsibility for any ethical violations that may be encountered and that this study has not been evaluated in any academic publication environment other than Sakarya University Journal of Science.

REFERENCES

[1] A. M. Amaro, P. N. B. Reis, and M. A. Neto, “Experimental study of temperature effects on composite laminates subjected to multi-impacts,” Compos. Part B Eng., vol. 98, pp. 23–29, 2016.

[2] L. Calabrese, V. Fiore, T. Scalici, and A. Valenza, “Experimental assessment of the improved properties during aging of flax/glass hybrid composite laminates for marine applications,” J. Appl. Polym. Sci., vol. 136, no. 14, pp. 1–12, 2019.

[3] J. Wang, H. GangaRao, R. Liang, D. Zhou, W. Liu, and Y. Fang, “Durability of glass fiber-reinforced polymer composites under the combined effects of moisture and sustained loads,” J. Reinf. Plast. Compos., vol. 34, no. 21, pp. 1739–1754, 2015.

[4] P. Ghabezi and N. Harrison, “Mechanical behavior and long-term life prediction of carbon / epoxy and glass / epoxy composite laminates under artificial seawater environment,” Mater. Lett., p. 127091, 2019.

[5] F. Daricik and S. Kiratli, “Farklı Çevresel Ş artlarda İki Eksenli Yüklemelere Maruz

Tabakalı Kompozit Malzemelerin Hasarı Damage of Laminated Composite Materials Exposed to Biaxial Loads in Different," vol. 36, no. March, pp. 219–233, 2021.

[6] P. Kiss, J. Glinz, W. Stadlbauer, C. Burgstaller, and V. Archodoulaki, "The effect of thermally desized carbon fibre reinforcement on the flexural and impact properties of PA6 , PPS and PEEK composite laminates : A comparative study," Compos. Part B, vol. 215, no. March, p. 108844, 2021.

[7] P. Kiss, J. Schoefer, W. Stadlbauer, C. Burgstaller, and V. M. Archodoulaki, "An experimental study of glass fibre roving sizings and yarn finishes in high-performance GF-PA6 and GF-PPS composite laminates," Compos. Part B Eng., vol. 204, no. October 2020, p. 108487, 2021.

[8] C. L. Chiang, H. Y. Chou, and M. Y. Shen, "Effect of environmental aging on mechanical properties of graphene nanoplatelet/nanocarbon aerogel hybrid-reinforced epoxy/carbon fiber composite laminates," Compos. Part A Appl. Sci. Manuf., vol. 130, no. November 2019, p. 105718, 2020.

[9] A. Ramesh, K. Ramu, M. A. Ali Baig, and E. D. Guptha, "Influence of fly ash nano filler on the tensile and flexural properties of novel hybrid epoxy nano-composites," Mater. Today Proc., vol. 27, pp. 1252–1257, 2020.

[10] A. K. Srivastava, V. Gupta, C. S. Yerramalli, and A. Singh, "Flexural strength enhancement in carbon-fiber epoxy composites through graphene nano-platelets coating on fibers," Compos. Part B Eng., vol. 179, no. August, p. 107539, 2019.

[11] F. Daricik and A. Topcu, "Theoretical Analysis on the Thermal and Electrical Properties of Fiber Reinforced Laminates Modified with CNTs Karbon Nanotüp ile Modifiye Edilmiş Fiber Takviyeli Laminelerin Isıl ve Elektriksel Özelliklerinin Teorik Analizi," vol. 35, no. December, pp. 925–936, 2020.

[12] R. Keshavarz, H. Aghamohammadi, and R. Eslami-Farsani, "The effect of graphene nanoplatelets on the flexural properties of fiber metal laminates under marine environmental conditions," Int. J. Adhes. Adhes., vol. 103, no. August, p. 102709, 2020.

[13] S. Kıratlı and Z. Aslan, "Flexural Behavior of Graphene Nanoplatelets Reinforced Cross-Ply E- glass/epoxy Laminated Composite Materials Sakine," Cumhur. Sci. J., vol. 39, no. 2, pp. 531–542, 2018.

[14] I. Türkmen and N. S. Köksal "Investigation of mechanical properties and impact strength depending on the number of fiber layers in glass fiber," vol. 2, pp. 17–30, 2013.

[15] M. Bingöl and K. Çavdar, "Effects of Different Reinforcements for Improving Mechanical Properties of Composite Materials," Uludağ Univ. J. Fac. Eng., vol. 21, no. 2, p. 123, 2016.

[16] G. Öner, H. Y. Ünal, and Y. Pekbey, "Karbon nanotüp katkılı camlifi -epoksi kompozitlerin termal ve eğilme özelliklerinin araştırılması," no. 232, pp. 805–816, 2017.

[17] M. R. Aydın, V. Acar, F. Yapıcı, K. Yıldız, M. V. Topcu and Ö. Gündoğdu, "Influence of Fiber Stacking Sequence in Inter-ply Hybrid Composites Structures on the Mechanical and Dynamics Properties," vol. 8, no. 3, pp. 255–263, 2018.

[18] V. Di Cocco, F. Iacoviello, and L. Sorrentino, "Failure energy and strength of Al / CFRP hybrid laminates under flexural load," no. October, pp. 1–6, 2019.

[19] G. Pavan, K. K. Singh, and Mahesh, "Elevated thermal conditioning effect on flexural strength of GFRP laminates: An

experimental and statistical approach," Mater. Today Commun., vol. 26, no. November 2020, p. 101809, 2020.

[20] M. Bazli, H. Ashrafi, A. Jafari, X. L. Zhao, H. Gholipour, and A. V. Oskouei, "Effect of thickness and reinforcement configuration on flexural and impact behaviour of GFRP laminates after exposure to elevated temperatures," Compos. Part B Eng., vol. 157, pp. 76–99, 2019.

[21] J. Meng et al., "Mechanical properties and internal microdefects evolution of carbon fiber reinforced polymer composites : Cryogenic temperature and thermocycling effects," Compos. Sci. Technol., vol. 191, no. November 2019, p. 108083, 2020.

[22] Solvay Technical Data Sheet Cycom® 381 Prepreg 2021. https://catalogservice.solvay.com/downloadDocument?fileId=MDkwMTY2OWM4MDU1YmZmNg==&fileName=CYCOM381_CM_EN.pdf&base=FAST

[23] J. Tomblin, J. Mckenna, Y. Ng, and K. S. Raju, "Advanced General Aviation Transport Experiments B – Basis Design Allowables for Epoxy – Based Prepreg Fiberite 8-Harness Graphite Fabric," 2001.

[24] J. Tomblin, J. Sherraden, W. Seneviratne, and K. S. Raju, "A - Basis and B - Basis Design Allowables for Epoxy Based Prepreg," 2002.

[25] A. Puck and H. Schürmann, "Failure analysis of FRP laminates by means of physically based phenomenological models," Compos. Sci. Technol., vol. 62, no. 12-13 SPECIAL ISSUE, pp. 1633–1662, 2002.

SAKARYA ÜNİVERSİTESİ
FEN BİLİMLERİ ENSTİTÜSÜ DERGİSİ

Sakarya University Journal of Science
SAUJS

e-ISSN 2147-835X Period Bimonthly Founded 1997 Publisher Sakarya University
http://www.saujs.sakarya.edu.tr/

Title: Quasi-Resonant Half-Wave Buck Converter with Non-Isolated High-Side Switching Techniques

Authors: Burak GÖRDÜK, Elif TOPUZ, Deniz YILDIRIM

Recieved: 2021-11-03 00:00:00

Accepted: 2022-02-18 00:00:00

Article Type: Research Article

Volume: 26
Issue: 2
Month: April
Year: 2022
Pages: 262-272

How to cite
Burak GÖRDÜK, Elif TOPUZ, Deniz YILDIRIM; (2022), Quasi-Resonant Half-Wave Buck Converter with Non-Isolated High-Side Switching Techniques. Sakarya University Journal of Science, 26(2), 262-272, DOI: 10.16984/saufenbilder.1018283
Access link
https://dergipark.org.tr/tr/journal/1115/issue/69580/1018283

New submission to SAUJS
http://dergipark.gov.tr/journal/1115/submission/start

Sakarya University Journal of Science 26(2), 262-272, 2022

Quasi-Resonant Half-Wave Buck Converter with Non-Isolated High-Side Switching Techniques

Burak GÖRDÜK*[1], Elif TOPUZ[1], Deniz YILDIRIM[1]

Abstract

Power density of the power converters became one of the most important parameters in many applications. Power density is increased by reducing the losses through use of better performing components and circuit topologies. It can be increased further by reducing the size of filter components through increasing the switching frequency. In hard-switching converters however, losses due to switching will eventually render this method not applicable. Instead, resonant converters are utilized in many high-frequency switched power supplies. Soft-switching feature of these converters provide increased efficiency due to decreased switching losses. Such converters exploit the resonance of the specific inductors and capacitors in the circuit called as resonant tank elements. Resonance behavior is used in order to eliminate turn-on or turn-off losses. Existing power converter topologies can be modified to create the resonance during switching period. Such converters are called as quasi-resonant converters. This paper presents analysis and design of Zero Current Switching (ZCS) half-wave quasi-resonant buck converters. In this topology, high-side switching is required. Two different non-isolated high-side switching techniques are utilized. Experimental results are obtained for light load to full load operation. Both techniques are compared in detail.

Keywords: Half-wave Buck Converter, high-side switching, quasi-resonant converters, Zero-Current Switching.

1. INTRODUCTION

The working principle of the conventional pulse width modulated (PWM) converters are based on transferring the energy using capacitors and inductors with the help of semiconductor elements. These semiconductor elements are operated as switches either in fully on or off mode connecting energy transfer elements to source and load. Output voltage can be adjusted by the duty cycle of control signal. Unlike linear power supplies, switched-mode converters tend to generate ripple at their output due to switching action. This ripple can be reduced by increasing the switching frequency or increasing the size of filter elements. The latter is least demanded because of the increased cost and size of the converter [1].

The MOSFETs are semiconductor switching elements that are used in low to mid-range power

* Corresponding author: burakgorduk@gmail.com
[1] Istanbul Technical University, Faculty Of Electrical and Electronics, Department of Electrical Engineering
E-mail: topuzelifn@gmail.com, yildiri1@itu.edu.tr
ORCID: https://orcid.org/0000-0002-2333-0649, https://orcid.org/0000-0001-8575-2305, https://orcid.org/0000-0001-6216-6290

supplies. They are suitable for high frequency operation up to couple of MHz depending on the ratings. However, increased switching frequency means increased switching losses due to the hard-switching behavior of the PWM converters. To overcome this issue, switched-mode power conversion technologies are transformed from simple PWM converters to resonant converters [2]. Beside low switching losses compared to PWM converters, they can eliminate electromagnetic interference (EMI) problems because of sinusoidal variations; they do not have sharp rising voltage/current waveforms [3]. The resonant converters were found out in early 1980s [4].

Many different configurations of resonant converters are available and quasi resonant converters are one of them. Quasi-resonant converters are derived from the conventional PWM converters, where, resonant tank elements are added to the circuit. Since quasi-resonant converters include LC tank circuit, it is possible to obtain zero current (ZCS) or zero voltage switching (ZVS) in semiconductor elements. While ZCS is used for eliminating turn-off losses of the switching element, ZVS is used for turn-on switching losses [5].

ZCS Quasi resonant converters are used in bidirectional battery equalizers to minimize switching loss. It is seen that efficiency is higher than around 20%~30% unlike conventional battery equalizers [6]. Quasi resonant converters can be half-wave or full-wave configuration. Analysis of the ZCS quasi-resonant converters is studied in [7, 8]. In ZCS quasi-resonant buck converter, high side switching is necessary because of buck converter topology. There are couples of techniques for high side switching [9]. For example, using of a P-channel switch or isolated gate drive circuitry.

On the other hand, ZVS quasi-resonant buck converter is also studied in [10, 11]. In [11], a 3 kW quasi-resonant buck converter is developed and maximum 98.7% efficiency is obtained using ZVS. Also, steady state analysis of ZVS quasi-resonant converter is studied in [12].

In this study, ZCS quasi-resonant (half-wave) buck converter is investigated, analyzed and experimentally verified. Two circuit boards are produced with different approaches on non-isolated high-side switching. Based on the experimental results, performances of these circuits are investigated.

2. HALF WAVE QUASI RESONANT ZCS BUCK CONVERTERS

The half-wave ZCS buck converter depicted in Fig. 1 is a type of quasi-resonant converter in which an LC resonant tank is added to switch element. L_r and C_r are resonant elements and the series diode D_1 prevents inductor current becoming negative. Since output filters L_f and C_f are large in value the output part can be represented by a current source with a value equals to load current as given in Fig. 2.

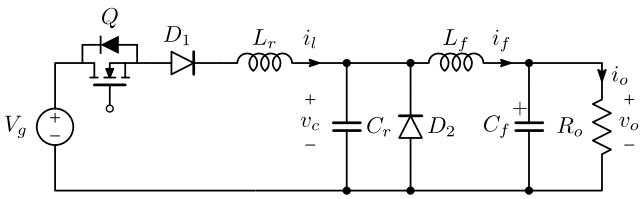

Figure 1 Half-wave ZCS buck converter

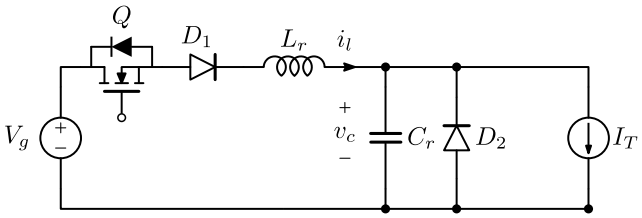

Figure 2 Half-wave ZCS buck converter with constant current source

2.1. Steady State Analysis of The Half Wave ZCS Buck Converter

In order to get an understanding of the relationship between input and output voltage with certain operating conditions of the circuit, the steady state analysis must be done. This analysis is done by normalizing voltage and inductor current equations. For the normalization approach, notations used are given in equations 1 to 8.

$$V_T = V_g \quad (1)$$

$$V_{base} = V_T \quad (2)$$

$$I_{base} = \frac{V_T}{R_0} \quad (3)$$

$$R_0 = \sqrt{\frac{L_r}{C_r}} \quad (4)$$

$$j_L = \frac{i_L}{I_{base}} \quad (5)$$

$$J_T = \frac{I_T}{I_{base}} \quad (6)$$

$$m_c = \frac{v_c}{V_{base}} \quad (7)$$

$$F = \frac{f_s}{f_o} \quad (8)$$

Where, f_s is the switching frequency, f_o is the resonant frequency, and F is normalized frequency, R_0 is effective load resistance, m_c, j_L, and J_T are the normalized capacitor voltage, inductor current, and load current respectively.

The first interval of the operation starts by turning on the switch Q. Before this interval, load current I_T is flowing through diode D_2. In this interval, series diode D_1 and freewheeling diode D_2 are also conducting. Equivalent circuit is given in Fig. 3.

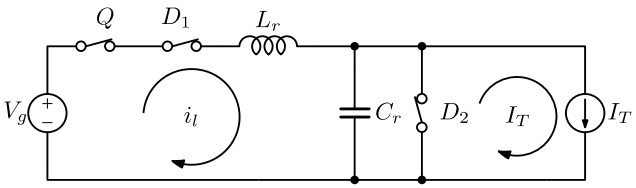

Figure 3 Equivalent circuit of interval I

Current flowing through the resonant inductor rises linearly from zero to steady state output current value. Interval I ends when inductor current reaches to steady state output current value. Therefore, interval I is called as inductor charging mode [5]. The normalized state equation is given in equation (9).

$$\frac{1}{\omega_0}\frac{dj_L}{dt} = 1 \quad (9)$$

With the initial condition of shown in equation (10).

$$j_L(0) = 0 \quad (10)$$

The interval has a length of angle α. When iL equals to IT, D2 turns off and interval ends. By solving the initial condition problem, final values are obtained in equations (11) to (13).

$$j_L(\omega_0 t) = \omega_0 t \quad (11)$$

$$m_c(\omega_0 t) = 0 \quad (12)$$

$$\alpha = J_T \quad (13)$$

Second interval is the ringing interval of the resonant tank. Equivalent circuit belongs to the second interval is given in Fig. 4. State equations are given in equations (14) and (15).

$$\frac{1}{\omega_0}\frac{dj_L}{dt} = 1 - m_c \quad (14)$$

$$\frac{1}{\omega_0}\frac{dm_c}{dt} = j_L - J_T \quad (15)$$

These equations belong to a circle with the center (1, J_T) in the state plane trajectory. This circle has the initial point of (0, J_T) and the final point of (Mc_1, 0). This interval lasts for the angle β and ends when inductor current goes to zero and hence series diode D_1 turns off.

The switch is turned off at third interval because of the inductor current being zero. In this interval series diode D_1 and freewheeling diode D_2 are also off, output current I_T discharges the tank capacitor linearly. Corresponding equivalent circuit is given in Fig. 5.

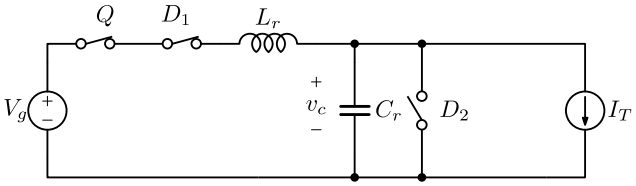

Figure 4 Equivalent circuit of interval II

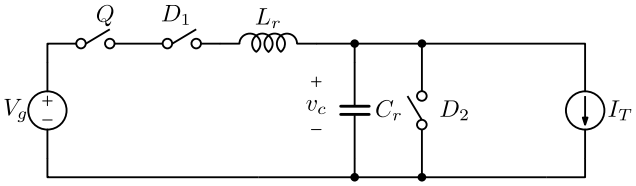

Figure 5 Equivalent circuit of interval III

Normalized state equation and initial conditions are given in equations (16) to (18).

$$\frac{1}{\omega_0}\frac{dm_c}{dt} = -J_T \tag{16}$$

$$m_c(\alpha+\beta) = M_{c1} \tag{17}$$

$$m_c(\omega_0 t) = M_{C1} - J_T(\omega_0 t - a - \beta) \tag{18}$$

Third interval lasts for an angle δ and ends when the resonant tank capacitor voltage goes to zero, and Interval IV begins as freewheeling diode D_2 turns on and output current flows through on it. Equivalent circuit is given in Fig. 6.

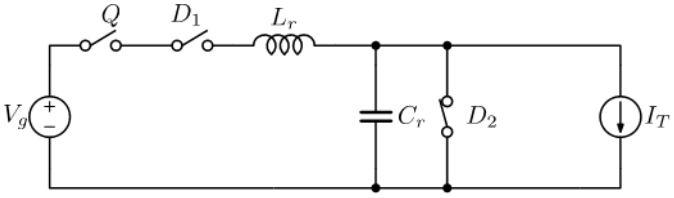

Figure 6 Equivalent circuit of interval IV

Both the capacitor voltage and the inductor current are zero. This interval lasts for the angle ξ and ends when switch Q is turned on again at the start of the first interval. For the whole switching period T_S waveforms of gate signals, resonant capacitor voltage and resonant inductor current along with the interval numbers and angles are given in Fig 7.

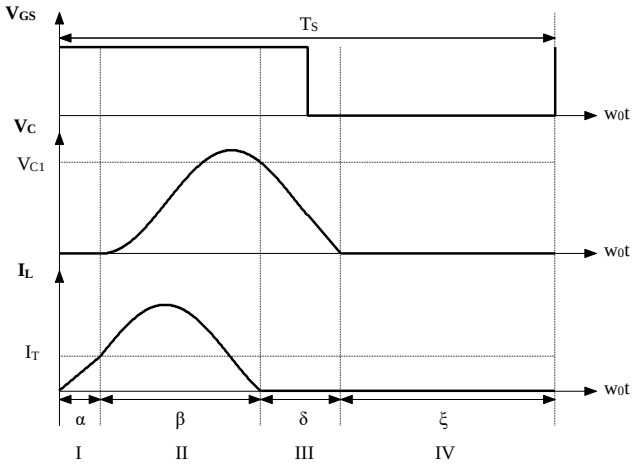

Figure 7 Waveforms for the half-wave ZCS quasi resonant buck converter

The state plane trajectory for these four intervals is given in Fig. 8.

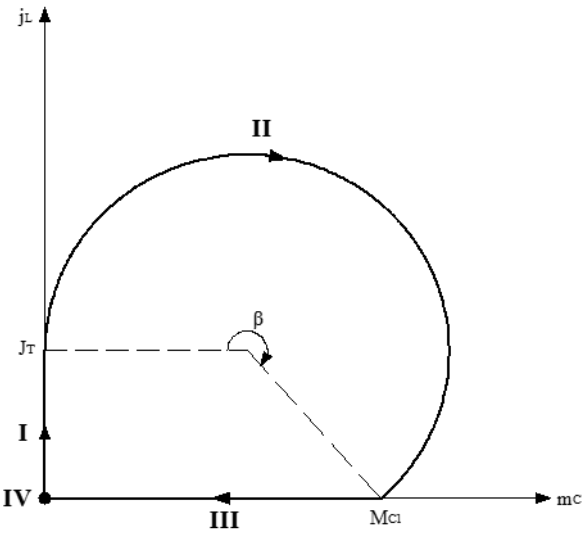

Figure 8 State plane trajectory of the converter

The conduction angles α, β, δ and ξ compose the switching period. Using state plane trajectory and circuit averaging techniques, conversion ratio of the converter can be expressed as given in equation (19).

$$\langle m_c \rangle = F\frac{1}{2\pi}[\frac{1}{2}J_T + \pi + \sin^{-1}J_T + \frac{1}{J_T}(1+\sqrt{1-J_T{}^2})] \quad (19)$$

Conversion ratio is controllable by F, but it also depends on J_T. Function of load current dependency is plotted in Fig. 9.

2.2. Mode Boundaries

Consequently, to obtain ZCS condition, some boundary conditions are shown in equations (20) to (23).

$$J_{out} < 1 \quad (20)$$

$$\xi > 0 \quad (21)$$

$$\langle m_c \rangle \le 1 - \frac{J_{out}F}{4\pi} \quad (22)$$

$$F << 1 \quad (23)$$

According to these mode boundaries, design parameters are determined.

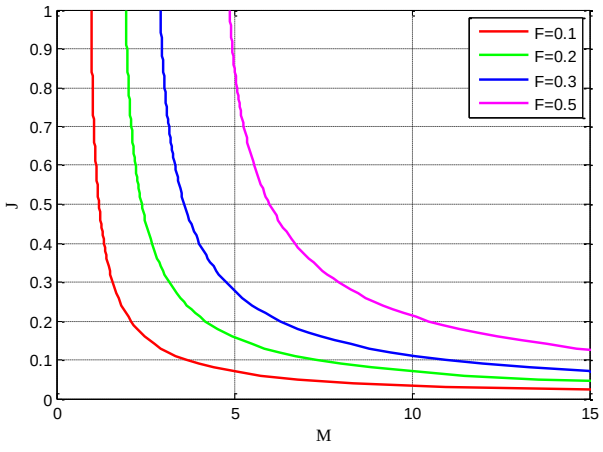

Figure 9 Load current dependency of M for different frequencies

3. DESIGN PARAMETERS

According to specification of the ZCS buck converter given in Table I, resonant elements' parameters (resonant inductance, resonant capacitance, and resonant frequency) are calculated. To calculate resonant elements' parameters two conditions given in equations (24) and (25) must be considered. Firstly, to obtain zero current switching, switching frequency must be much lower than the resonant frequency, and secondly normalized load current value must be lower than 1.

$$f_s << f_o \quad (24)$$

$$(J = \frac{I}{I_{base}} = \frac{I}{V_{in,\min}/R_o}) < 1 \quad (25)$$

Normalized load current value assumed as 0.85 for the worst-case scenario which is minimum input voltage (43V) because lower J_{out} value leads to higher peak resonant inductor current which is undesired for the converter. Using conversion ratio formula and normalized current, resonant tank inductor and capacitor values are calculated and nearest standard values are chosen.

With this equation, resonant frequency is then calculated as 677 kHz. Resonant frequency can be expressed using L_r and C_r as given in equation (26).

$$f_0 = \frac{1}{2\pi\sqrt{L_r C_r}} = 677kHz \quad (26)$$

By using these equations, J_{Tmax} can also be expressed in terms of L_r and C_r as given in equation (27).

$$J_{T\max} = \frac{I_T}{I_{base\min}} = \frac{I_T}{\frac{V_{\min}}{R_0}} = \frac{I_T R_0}{V_{\min}} = \frac{5}{43}\sqrt{\frac{L_r}{C_r}} = 0.85 \quad (27)$$

By using these equations, L_r and C_r are calculated as follows.

$$L_r = 1.72\mu H$$

$$C_r = 32.2nF$$

Standard values of 1.8µH and 33nF are selected as resonant tank elements.

With the resonant elements selected, steady-state simulation of the converter was made in order verify ZCS ability. Circuit model shown in Fig. 10, is implemented in PSIM environment. Open-loop simulation is done with nominal input voltage and 60W output power at 168 kHz switching frequency. From the simulation results shown in Fig. 11, ZCS ability of the converter and the voltage conversion ratio is verified.

Table 1 Specifications of the designed converter

Parameter	Unit	Value
Input voltage range	[V]	48 ± 10%
Output voltage	[V]	12
Rated output power	[W]	60
Switching frequency	[kHz]	150 - 200

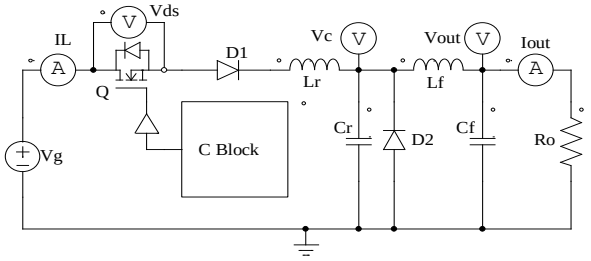

Figure 10 PSIM model of the converter

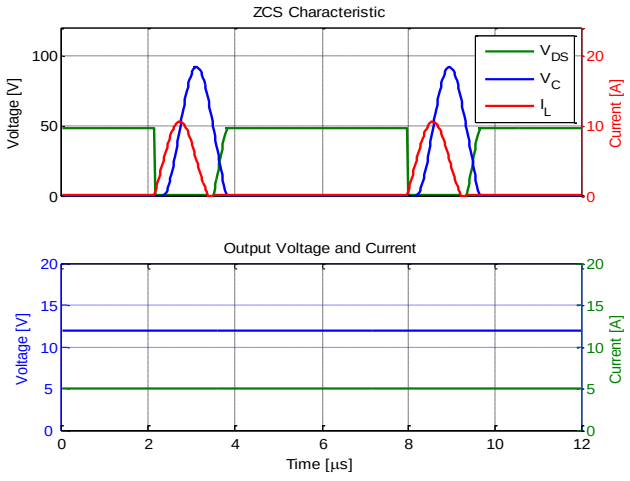

Figure 11 Simulation results at V_g = 48 V, R = 2.4Ω, f_s = 168 kHz

Since the designed converters will be controlled digitally by microcontrollers, closed-loop operation of the converter is also simulated. Necessary compensation function was implemented in "C Block" inside PSIM environment. Closed-loop operation of the system is then verified with the step changes in output load. It is observed that the system outputs the desired output voltage of 12V with no stability problems. Fig. 12 shows the converter response to no-load start and switch to full load when time equals to 40 ms. Transient loading caused output voltage to undershoot about 30% of the rated output voltage and it is recovered in 2 ms by the controller.

Actual implementation of the closed loop control is done for the MKL03Z32VFK4 microcontroller. Embedded software for this microcontroller is developed as a finite state machine with three states. Initialization state starts after power-on-reset. In this state, microcontroller peripherals are set according to the application. Then run state begins. Run state starts the operation of the converter. Voltage is controlled with 200 kHz control loop frequency. Run state flow diagram is given in Fig. 13. Fault state is the last state and it is activated only if the input voltage or current is out of the limits.

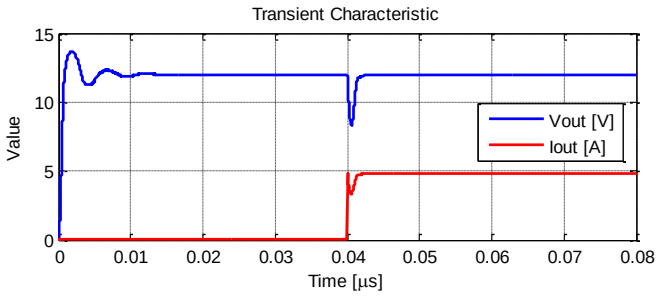

Figure 12 Step response of no load to full load condition

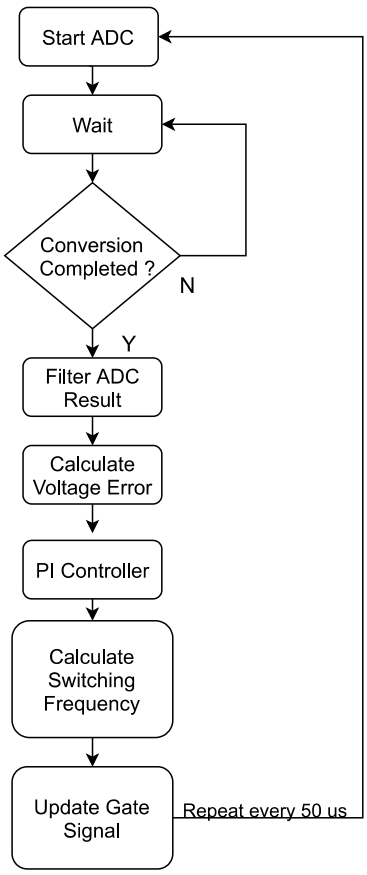

Figure 13 Run state flowchart diagram

4. GATE CIRCUIT DESIGN

After the open-loop and closed-loop operation of the converter is verified in simulation, necessary circuit boards were designed for experimental results. In the buck converter topology, switch element is placed at the high side, meaning that the drain pin of the MOSFET is directly connected to supply voltage. This causes the source pin to be floating. Thus, the applied gate-source voltage has to be floating with reference to ground as well. Two different high-side switching approaches are used in this study.

4.1. High-side Switching Design I

In the first circuit a half-bridge driver IC is used. These drivers have a channel for high side N channel switch. The source pin connection of the driver is floating with reference to ground. Gate-source drive voltage is generated using bootstrap method. However, in order to generate this bootstrapped voltage, source connection of the switch should have a direct reference to ground. In ZCS quasi-resonant buck converter topology, due to series diode and resonant inductor this is not the case. Thus, it can be problematic to use such technique because of possible charge – discharge issues of the bootstrap capacitor. Instead, an isolated DC-DC converter module is used as the floating switch voltage supply. In this topology, gate driver and the microcontroller are placed on the power ground. This provides a simple feedback path from the output by using only one voltage divider. The circuitry is given in block diagram in Fig. 14.

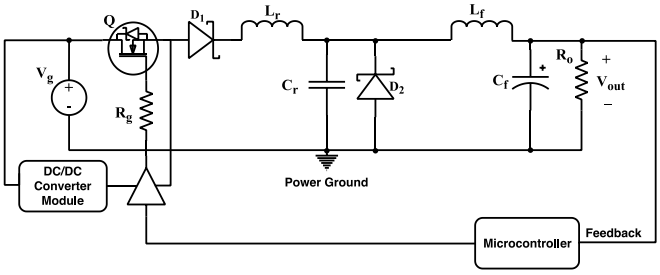

Figure 14 Circuit diagram of design I

4.2. High-side Switching Design II

For the second circuit a different approach is used to eliminate the need of a high side gate driver. Instead, a low side gate driver is used with its ground connected directly to the source pin of the N-channel switch and supplied from an auxiliary 12V input. Supply of the microcontroller is also referenced to this ground providing simple connection between the controller and the gate driver. This placement of the microcontroller ground has a drawback as well. Output voltage is floating with reference to the ground of the microcontroller. Moreover, the voltage difference between these two points is negative, making it not possible to measure the output voltage directly via microcontroller. Instead, an isolated amplifier is used to transfer output voltage with reference to floating ground point. The circuitry is given in block diagram in Fig. 15. Designed circuit boards are shown in Fig. 16. Both PCBs are designed to have a high-power density.

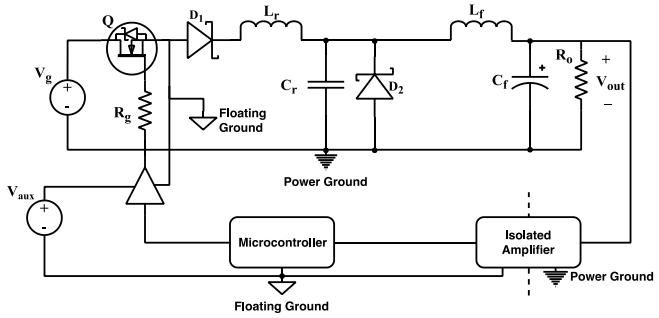

Figure 15 Circuit diagram of design II

a)

b)

Figure 1 (a) Converter I, (b) Converter II

5. EXPERIMENTAL RESULTS

Designed and assembled converter circuits are investigated in experimental operation. Both of the circuits were evaluated for open-loop and closed-loop operation at the nominal operation range. From the first results, a couple of adjustments had to be made. One of which is related to first topology. It is observed that under certain conditions like light load and low switching frequency, the converter works fine. Increasing the load and the switching frequency however, causes the gate driver to fail and get permanent damage on the output side. Reason for this is found as negative voltage spikes on the source pin caused by the parasitic inductance due to semiconductors and PCB layout. Source-to-ground voltage measurement on this point is given in Fig. 17. It can be seen that negative voltage spikes were as high as 6.8V in amplitude. Since there was no direct reference to ground at this point, these spikes were able to cause latch-up on the driver, which specified the maximum repetitive transients as -5V. In order to solve the problem, gate resistor is moved from gate path to source path of the driver. D_3 and D_4 are two schottky diodes placed in order to clamp the negative voltage spikes. Revised topology is given in Fig. 18. With these adjustments, converter was able to work for the whole operation range.

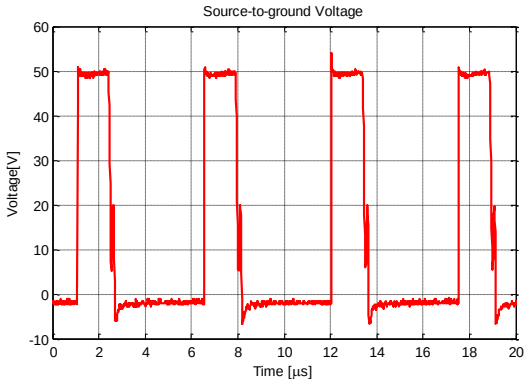

Figure 17 Negative voltage spikes on source connection

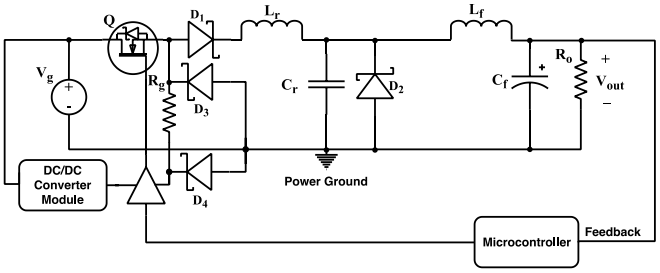

Figure 18 Modified circuit diagram of design I

The second switching topology was far smoother and easier regarding the switching and transients. The only issue was that the microcontroller is placed to the floating ground point that is actually the source connection of the switch. This ground reference has a lot of switching noise and analog measurements are highly affected from these

noises. This made the stable closed loop operation hard to achieve. In order to overcome this issue, embedded software in the microcontroller has adjusted accordingly. Analog Digital Conversion (ADC) is started every PWM cycle. Timing of the ADC is controlled via trigger output from PWM timer. Trigger point is adjusted to ensure conversions start when the switch is fully turned off. Therefore, switching noises could be eliminated from ADC results. First order digital low-pass filter is used to further smoothen voltage measurement. Fig. 19 shows the closed loop response of the system to zero load to full load transition.

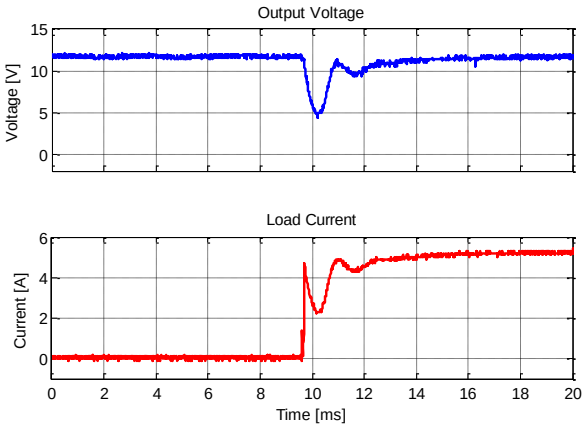

Figure 19 Closed loop response of zero load to full load transition

In the Fig. 20, full load operation waveforms of both converters are given. It can be seen that both converters operate in ZCS.

a)

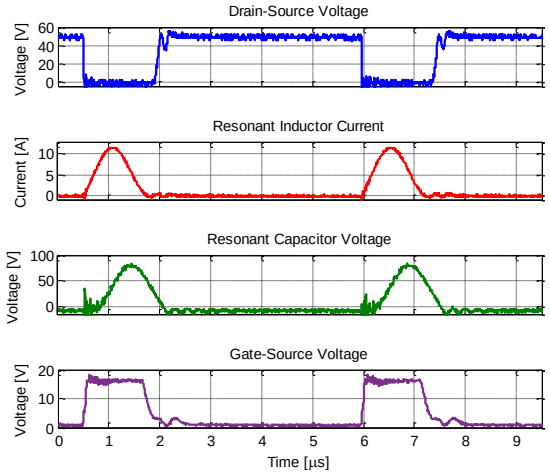

b)

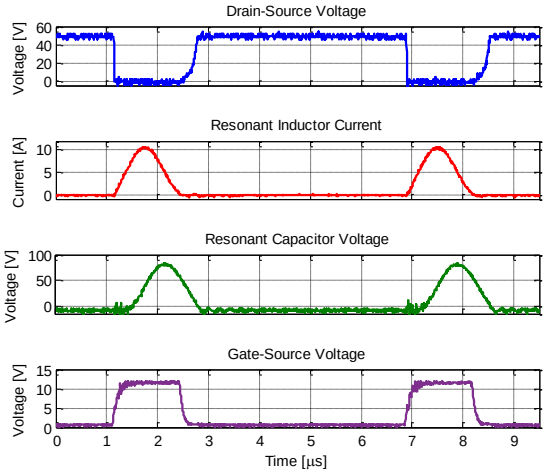

Figure 20 Full load operation waveforms of converter I (a) and converter II (b)

Gate-source and drain-source voltage of the first converter also indicates that the additional diodes placed on the circuit created a path for the circulating energy when the switch is off. Although this does not affect the operating properties of the converter, it decreases the overall efficiency. Especially in the light load operation, low frequency oscillations due to MOSFET's output capacitance and resonant inductance cause undesired currents to flow from the clamping diodes. This drawback can be seen in Fig. 21 that shows the efficiency graphs of both designs.

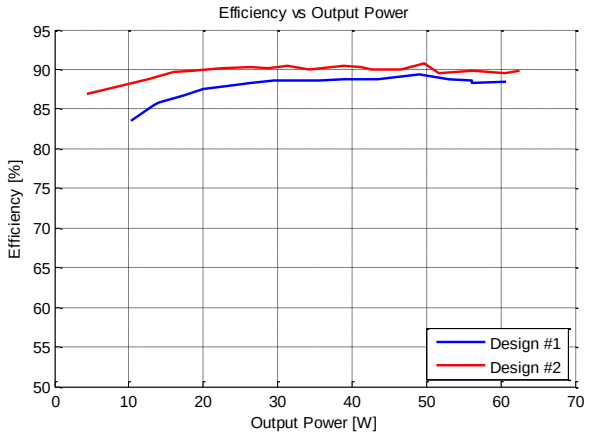

Figure 21 Efficiency curves of the designed converters

6. CONCLUSION

Zero current switching half-wave buck converters are investigated in this study. Steady-state

analysis of the converter is done for a 48V to 12V, 60W step down converter. Resonant tank element values are calculated and selected from standard values in order to provide the given conversion ratio and output power. Closed loop operation of the converter is done by designing a PI controller with the help of the small signal model. Digital type PI controller is simulated in PSIM environment. Two different approaches of non-isolated high side switching technique are utilized. Necessary circuit schematics and printed circuit boards were designed and manufactured. Embedded software for the MKL03Z32VFK4 microcontroller is developed. Experimental results show that both of the converters are able to supply 60W power up to 90% efficiency, having a peak power density of 13.66 W/in^3 zero current switching capability.

Funding

The author (s) has no received any financial support for the research, authorship or publication of this study.

The Declaration of Conflict of Interest/ Common Interest

No conflict of interest or common interest has been declared by the authors.

Authors' Contribution

Authors contributed equally to the study.

The Declaration of Ethics Committee Approval

This study does not require ethics committee permission or any special permission.

The Declaration of Research and Publication Ethics

The authors of the paper declare that they comply with the scientific, ethical and quotation rules of SAUJS in all processes of the paper and that they do not make any falsification on the data collected. In addition, they declare that Sakarya University Journal of Science and its editorial board have no responsibility for any ethical violations that may be encountered, and that this study has not been evaluated in any academic publication environment other than Sakarya University Journal of Science.

REFERENCES

[1] M. K. Kazimierczuk, D. Czarkowski, “Resonant Power Converters,” Wiley-IEEE Press, Second Edition, 2011.

[2] M. V. Sudarsan, S. Babu1, L. Satyanarayana, and S. Suresh, “Design and Analysis of Zero Current Switching Based DC to DC Buck Converter,” Journal of Automation & Systems Engineering, pp. 108-121, 2014.

[3] R. W. Erickson, D. Maksimovic, “Fundamentals of Power Electronics,” University of Colorado, Second Edition, 2001.

[4] I. Jamil, J. Zhao, “Analysis, Design and Implementation of Zero Current-Switching Resonant Converter DC-DC Buck Converter,” International Journal of Electrical and Electronics Engineering (IJEEE), vol. 2, Issue 2, 2013.

[5] S. Ang, A. Oliva, “Power Switching Converters,” Second Edition, Boca Raton, FL : Taylor & Francis, 2005.

[6] Y. Lee and G. Cheng, "Quasi-Resonant Zero-Current-Switching Bidirectional Converter for Battery Equalization Applications," in IEEE Transactions on Power Electronics, vol. 21, no. 5, pp. 1213-1224, 2006.

[7] İ. Özdemir and A. B. Yildiz, "Time-domain analysis of full-wave quasi-resonant zero-current switching buck converter by modified nodal analysis," 2018 5th International Conference on Electrical and Electronic Engineering (ICEEE), pp. 23-26, 2018.

[8] A. V. Dymerets, R. D. Yershov, A. N. Gorodny, Y. O. Denisov, S. Boiko and V. Kuznetsov, "Dynamic Characteristics of Zero-Current-Switching Quasi-Resonant

Buck Converter under Variation of Resonant Circuit and Load Parameters," 2020 IEEE 40th International Conference on Electronics and Nanotechnology (ELNANO), pp. 848-853, 2020.

[9] M. Wendt, L. Thoma, B. Wicht and D. Schmitt-Landsiedel, "A Configurable High-Side/Low-Side Driver With Fast and Equalized Switching Delay," in IEEE Journal of Solid-State Circuits, vol. 43, no. 7, pp. 1617-1625, 2008.

[10] F. Doub, K. Yeferni, S. Rahmani and K. Al-Haooao, "Experimental Evaluation of a Zero-Voltage-Switched Quasi-Resonant Buck Converter," 2018 15th International Multi-Conference on Systems, Signals & Devices (SSD), pp. 326-331, 2018.

[11] J. Wang, F. Zhang, J. Xie, S. Zhang and S. Liu, "Analysis and design of high efficiency Quasi-Resonant Buck converter," 2014 International Power Electronics and Application Conference and Exposition, pp. 1486-1489, 2014.

[12] L. Li, Y. Gao and P. K. T. Mok, "A more accurate steady state analysis of zero-voltage switching quasi-resonant converters," 2016 IEEE International Symposium on Circuits and Systems (ISCAS), pp. 1606-1609, 2016.

SAKARYA ÜNİVERSİTESİ
FEN BİLİMLERİ ENSTİTÜSÜ DERGİSİ

Sakarya University Journal of Science
SAUJS

e-ISSN 2147-835X Period Bimonthly Founded 1997 Publisher Sakarya University
http://www.saujs.sakarya.edu.tr/

Title: Identification of Lactic Acid Bacteria in Fermented Cornichon Pickles Produced with Acid Whey and Vinegar

Authors: Semanur CEBECİ AVUNCA, Özlem ÖZTÜRK ÇETİN, Arzu ÇAĞRI MEHMETOĞLU, Mustafa ÖZTÜRK

Recieved: 2022-01-03 00:00:00

Accepted: 2022-02-18 00:00:00

Article Type: Research Article

Volume: 26
Issue: 2
Month: April
Year: 2022
Pages: 273-282

How to cite
Semanur CEBECİ AVUNCA, Özlem ÖZTÜRK ÇETİN, Arzu ÇAĞRI MEHMETOĞLU, Mustafa ÖZTÜRK; (2022), Identification of Lactic Acid Bacteria in Fermented Cornichon Pickles Produced with Acid Whey and Vinegar. Sakarya University Journal of Science, 26(2), 273-282, DOI: 10.16984/saufenbilder.1052803
Access link
https://dergipark.org.tr/tr/journal/1115/issue/69580/1052803

New submission to SAUJS
http://dergipark.gov.tr/journal/1115/submission/start

Sakarya University Journal of Science 26(2), 273-282, 2022

Identification of Lactic Acid Bacteria in Fermented Cornichon Pickles Produced with Acid Whey and Vinegar

Semanur CEBECİ AVUNCA[1], Özlem ÖZTÜRK ÇETİN[1],
Arzu ÇAĞRI MEHMETOĞLU[1], Mustafa ÖZTÜRK*[1]

Abstract

The purpose of this study is to isolate, identify and compare lactic acid bacteria responsible for fermentation from pickles produced with vinegar and acid whey (AW). For this reason, fermented cornichon pickles were produced by using AW and vinegar as brine media. Colonies with different morphologies were selected and isolated at the 0, 7, 14, 21, 35, 49, 77 and 105th days of fermentation. A total of 139 isolates were obtained. Salt, acidity and pH values of brine and cornichon were followed on each analysis day. Growth and gas formation from glucose of isolates at different temperatures (10, 45, and 50 ^{o}C), salt concentrations (2, 4.5, and 10% (w/w)), different pH values (3, 4.5, and 9.6), were analyzed. Eight isolates were determined as heterofermentative according to their ability to produce CO_2 from glucose. The isolates were observed to show the highest growth at 10 ^{o}C, and a very few isolates developed at 45 ^{o}C and 50 ^{o}C. No isolates were able to grow at pH 9.6, 25 of the isolates were able to grow at pH 4, and only 4 isolates were able to grow at pH 3. Only one isolate was able to show resistance to 10% salt concentration. Almost all isolates grew at 2% and 6.5% salt concentrations. 48 selected isolates were identified with API 50 CHL. 19 isolates were determined as *Lactobacillus pentosus* (8 vinegar, 11 AW) and 29 isolates as *Lactobacillus plantarum* (16 vinegar, 13 AW). As a result, *L. plantarum* and *L. pentosus* species were the dominant bacteria for cornichon pickles produced with AW and vinegar. Microbial flora in the pickles produced with two different brines were similar. The results show that AW can be successfully used for pickle production.

Keywords: Lactic acid bacteria, identification, acid whey, cornichon pickle

1. INTRODUCTION

By pickling, foods can be preserved for longer and consumed even when little or no available [1]. Lactic acid fermentation and salt are two important factors in pickle production. In pickle fermentation, the lactic acid bacteria in the natural flora come from the raw material. Lactic acid fermentation inhibits the development of pathogenic microorganisms, provides protection against the growth of microorganisms that cause degradation and toxin formation, and also increases the nutritional value of the product [2].

* Corresponding author: ozturkm@sakarya.edu.tr
[1] Sakarya University, Faculty of Engineering, Department of Food Engineering
E-mail: semanur.cebeci@ogr.sakarya.edu.tr, ozlem.ozturk10@ogr.sakarya.edu.tr, acagri@sakarya.edu.tr
ORCID: https://orcid.org/0000-0001-7873-2226, https://orcid.org/0000-0002-5280-3257, https://orcid.org/0000-0001-6967-7288, https://orcid.org/0000-0002-3919-897X

The success of the lactic acid fermentation is significant for pickle quality [3].

Greek yogurt is a fermented milk product in which the serum part of yogurt is filtered and removed. The demand for Greek yogurt has increased rapidly in recent years. Thus, acid whey (AW), a by-product of Greek yogurt manufacture, also increased. Approximately 2-3 kg of AW emerges from the production of 1 kg of Greek yogurt [4]. In the USA, approximately 4 million tons of acid whey was produced as by product of Greek yogurt manufacture in 2015 [5]. Acid whey is difficult to powder as it contains high levels of lactic acid and calcium [6]. The presence of high amounts of lactic acid reduces the commercial value of AW, limits potential food applications, making it very difficult to process [7]. However, AW can cause serious environmental problems if not properly disposed of. Various evaluation methods have been investigated in order to increase the value of AW and to eliminate its harm to the environment [5, 8].

Lactic acid bacteria (LAB) is very important for fermented foods with its ability to inhibit pathogens and spoilage microorganisms. Organic acids, hydrogen peroxide, exopolysaccharides, antimicrobial and aromatic compounds synthesized by LAB during fermentation contribute to the texture, shelf life, flavor and aroma development of foods [9]. In addition, it has a protective effect by lowering the pH of the environment with the organic acids it produces [10]. Lactic acid bacteria are resistant to gastric acid and pancreatic secretions in the stomach. Lactic acid bacteria that are resistant to conditions in the digestive system and survive are probiotic [11, 12].

The amount of LAB in cornichons is very low. But when cornichons meet with brine, the existing LAB adapt quickly to the environment and begin to develop rapidly. Coliform group bacteria coming from the raw material are inhibited with increasing acidity during fermentation. Another undesirable microorganism is yeasts, competing with LAB for fermentable sugars [2]. The dominant LAB in the pickled environment are listed as *Leu. mesenteroides*, *Stp. faecalis*, *P. pentosaceus*, *L. brevis*, *L. plantarum*. *P. pentosaceus*, *L. brevis*, *L. plantarum* are generally used in commercial fermentation [13].

Some phenotypic and genotypic tests are used to identify LAB. Phenotypic tests determine the characteristics of bacteria such as growth at different temperatures, resistance to high acidity and salt concentrations, gas formation from glucose, cell morphology, and thus identification from family to genus can be provided [14, 15]. API 50 CHL can identify the species and subspecies by examining the carbohydrate fermentation characteristics of bacteria. Genotypic tests are aimed at determining the DNA characters of bacteria [16, 17].

In this study, our objective was to isolate and identify LAB responsible for fermentation of cornichon pickles produced by using vinegar and AW as brine.

2. MATERIALS AND METHODS

2.1. Pickle samples

Three independent batches of cornichon pickles were manufactured with brines produced from AW and vinegar. Cornichons were washed with water, 290-300 g cornichons were placed in 600 cc glass jars and plastic pressure apparatus were placed on top to keep cucumbers in brine. Vinegar used in the production was obtained from a local market and diluted with distilled water until the titration acidity was 1% (w / w). The AW was obtained from a local dairy plant and was kept at room temperature until the titration acidity reached 1% (w / w). The final salt concentration of the brines were adjusted to 8% by using coarse salt. Acid whey was boiled at 100^{o}C for 10 minutes, and coagulated proteins (if any) were removed by filtering with a cloth. Pickles were placed for fermentation in an incubator set at 25 ° C. Chemical and microbiological analysis were conducted on the 0, 7, 14, 21, 35, 49, 77, 105th days of fermentation. At each analysis point, two jars of pickles (one jar of pickle manufactured with AW and one jar pickle manufactured with vinegar) were opened and used for analysis.

2.2. Chemical and microbiological analysis of pickle samples

The pH of brine samples was measured by a pH meter (Inlab® solid pro; Mettler Toledo, Columbus, OH, ABD). Titration acidity (947.05; AOAC 2007) and salt analysis (975.20; AOAC, 2007) of all samples taken from the brine were measured. Colonies of lactic acid bacteria were isolated from pickled samples at the 0, 7, 14, 21, 35, 49, 77, 105th days of fermentation.

10 ml of pickle brine was taken under aseptic conditions, and necessary dilutions were made with sterile peptone water. 0.1 µL of brine sample from each dilution was inoculated into petri plates containing MRS (DeMan, Rogosa and Sharpe Agar) and M17 agar. Petri plates were incubated for 48 hours at 30°C. Petri plates containing MRS agar were incubated under anaerobic conditions.

2.3. Isolation of lactic acid bacteria

Colonies with different morphologies were taken from MRS and M17, then inoculated on MRS agar. Petri plates were incubated for 48 hours at 30°C. After incubation, a single colony was taken with a loop and dipped into tubes containing MRS Broth, incubated at 30°C for 48 hours. When the incubation was over, the liquid medium was homogenized with vortex and inoculated again on MRS agar and MRS Broth. The pure cultures with sterile glycerol (30%) were kept as frozen culture at -80°C until the day of identification analysis.

2.4. Identification of lactic acid bacteria

The isolates kept at -80°C were transferred to 10 mL MRS Broth for revival. Gram stain and cell morphologies of 18-24 hour fresh cultures grown at 30°C were examined under the microscope. The shapes of the bacteria were determined as cocci or bacilli. The catalase reaction was investigated by dripping 3-4 drops of %30 H_2O_2 solution on the colonies developed for 24 hours at 30 °C in MRS agar and observing the gas evolution. Gram-positive and catalase-negative bacteria were assumed as LAB.

To test CO_2 production; samples from the activated culture were inoculated into MRS Broth containing a Durham tube and incubated at 30 ^{O}C for 7 days. It was evaluated as heterofermentative if CO_2 formation was detected and homofermentative if CO_2 formation was not detected [18, 19].

To observe the activities of bacterial cells at different temperatures, pH and salt concentration; they were incubated in MRS broth at three different temperatures (10ºC, 15ºC and 45ºC for 5 days), in MRS broth adjusted different pH conditions using lactic acid (3, 4.5 and 9.6 for 3 days, 30°C) and at different salt concentrations (2%, 6.5% and 10% NaCl (w/v) for 3 days, 30°C) [18, 19].

Carbohydrate fermentation patterns were determined using API 50 CHL test strips according to manufacturer's instructions (BioMérieux, Marcy l'Etolie, France). API 50 CH kit (BioMérieux, Marcy l'Etolie, France) was used to determine the isolates at the species level.

3. RESULTS AND DISCUSSION

3.1. Chemical and microbiological characteristics of pickle samples

Salt, acidity and pH analyzes of the brines were made to have information about the general condition of the pickles. The titration acidity values increased from 0.61 to 1.06% and 0.71 to 1.85% and at the end of fermentation for the pickles with vinegar and AW, respectively.

The pH values were between 3.59 and 3.34 in brines produced with vinegar, and between 4.21 and 3.48 in brines produced with AW at the manufacture and at the end of fermentation, respectively. The initial and final pH of the vinegar brines was lower than the brine produced with AW.

Table 1 pH, titration acidity and salt values of pickle brines

Fermantation	pH		Titration Acidity (%)		Salt (%)	
Day	AW	Vinegar	AW	Vinegar	AW	Vinegar
0	4.21±0.04	3.59±0.11	0.71±0.07	0.61±0.01	4.93±0.12	4.53±0.48
7	3.71±0.03	3.53±0.08	1.32±0.03	0.79±0.05	3.58±1.46	4.68±0.44
14	3.64±0.02	3.58±0.29	1.49±0.11	0.80±0.17	5.07±0.81	4.69±1.05
21	3.62±0.03	3.36±0.30	1.71±0.16	1.06±0.22	5.47±0.45	4.79±0.20
35	3.61±0.06	3.52±0.28	1.78±0.16	0.93±0.25	4.97±0.53	4.78±0.31
49	3.57±0.01	3.55±0.14	1.85±0.16	0.95±0.12	5.30±0.54	4.41±0.21
77	3.48±0.02	3.52±0.33	1.84±0.19	0.94±0.24	5.18±0.52	4.51±0.19
105	3.53±0.04	3.49±0.31	1.75±0.13	0.97±0.22	5.21±0.51	4.57±0.26

The titration acidity of pickles produced with AW increased at a higher rate compared to pickles produced with vinegar. The higher numbers of lactic acid bacteria and also lactose content in pickles produced with AW may have caused the higher titration acidity. Although the titration acidity of pickles produced with AW was about twice of the pickles produced with vinegar at the end of fermentation, the pH values of both pickles were found to be similar. Calcium salts and/or protein in the AW may have caused buffering effect, preventing pH decrease and causing observing similar pH values with pickles produced with vinegar.

Salt concentrations are between 4.41 and 4.79 in brine produced with vinegar, and between 3.58 and 5.30 in brine produced with AW. It has been stated that the salt ratio in vegetable fermentations should be in the range of 1-8%. Excessive salt content inhibits the growth of lactic acid bacteria [20].

3.2. Identification results of lactic acid bacteria

It is known that all LAB are Gram-positive bacteria. According to gram stain results of 139 isolates, 109 isolates were defined as Gram-positive. Gram-negative bacteria (30) were eliminated because they did not show the characteristic of LAB. Lactic acid bacteria are catalase negative. All 109 of Gram-positive bacteria also gave catalase negative results.

53 isolates were obtained from pickles produced with vinegar: 16 cocci and 37 bacilli. 56 isolates were obtained from pickles produced with AW: 14 cocci and 42 bacilli.

Many studies report cultures grown on MRS agar as lactobacilli and on M17 agar as lactococci [21, 22]. This information is incomplete and can cause confusion. Polysorbate, acetate and magnesium in the composition of MRS agar are supportive factors for the development of Lactobacilli. MRS agar does not show a feature such as inhibiting the growth of other microorganisms. Other bacteria and yeasts can also grow on MRS agar. M17 agar promotes the development of lactic streptococci by increasing the buffering capacity of the medium, due to β-glycerophosphate it contains. Similar to MRS agar, there is no selective additive to inhibit the growth of other microorganisms in M17 agar, only the growth of Lactococci is supported. As a result, MRS is the most suitable medium for the growth of Lactobacillus. However, defining all the bacteria that develop in MRS as Lactobacillus is incorrect, the fact is we do not know for sure without further analyses. This is also the case for M17 agar [1, 23].

Gas formation of lactic acid bacteria by utilization of glucose usage was monitored with Durham tubes. In total, 8 heterofermentative bacteria were detected: 3 in pickles produced with AW, and 5 in pickles produced with vinegar. In cucumber pickles, it is desirable that CO_2 formation is as low as possible during fermentation as it causes swelling problems. Therefore, heterofermentative lactic acid bacteria are less desirable than homofermentative lactic acid bacteria [24].

The isolates, activated twice, were incubated for 5 days at three different temperatures, 10 °C, 45 °C and 50 °C. Bacteria obtained from the pickles produced with vinegar, 14 isolates grew at 10 °C, 11 isolates at 45°C and 4 isolates at 50 °C. From

the bacteria isolated from pickles produced with AW, 13 isolates grew at 10 ^{o}C, 5 isolates at 45 ^{o}C, and 3 isolates at 50 ^{o}C. The optimum growth temperature of lactic acid bacteria in cucumber fermentations was determined as 16-32 °C [24].

After the isolates were activated, they were incubated for 3 days at three different pH values; 3, 4.5 and 9.6. At pH 3, 4 isolates, and at pH 4.5, 20 isolates were able to grow. No growth was observed at pH 9.6 for pickles manufactured with vinegar. A similar situation exists in the isolates of pickles produced with AW. Four isolates obtained from pickles produced with AW showed growth at pH 3.0, and 26 isolates at pH 4.5. No isolate showed growth at pH 9.6.

The ability of bacterial isolates to grow at three different salt concentrations were evaluated at 2%, 6.5% and 10% salt concentrations. There are a total of 53 isolates from the pickles produced with vinegar. 50 isolates showed growth at 2% concentration, 44 isolates at 6.5% concentration. Two isolates were able to grow at 10% salt concentration. Most of the isolates obtained from pickles produced with AW showed growth at 2% and 6.5% concentrations. There are a total of 56 isolates obtained from AW brine. 55 isolates were able to show growth at 2% salt concentration and 50 isolates at 6.5% salt concentration. No isolates obtained from AW brine could grow at 10% salt concentration.

Table 2 Phenotypic characteristics of LAB isolated from pickles and identification result with API 50 CHL test kit

Brine Type	Isolate No.	GFG	Morf.	pH			T (ºC)			NaCl (%)			LAB identification	%
				3	4,5	9,6	10	45	50	2	6,5	10		
Vinegar	112	-	Bacil	-	-	-	-	-	-	++	++	-	*L.plantarum*	99.8
	131	-	Bacil	-	+	-	-	-	++	+	+	-	*L.pentosus*	97.4
	141	-	Bacil	-	+	-	-	-	-	+	+	-	*L.plantarum*	99.9
	152	-	Bacil	-	-	-	-	-	-	++	+	-	*L.pentosus*	98.6
	162	-	Bacil	-	+	-	+	+	-	-	++	-	*L.plantarum*	99.9
	172	+	Bacil	-	+	-	+	++	-	+	++	+	*L.plantarum*	99.1
	183	-	Bacil	-	+	-	+	-	-	++	++	-	*L.plantarum*	99.9
	184	-	Bacil	+	+	-	-	-	-	++	++	-	*L.plantarum*	99.8
	313	-	Bacil	-	-	-	-	++	-	++	+	-	*L.plantarum*	99.6
	331	-	Bacil	-	-	-	-	-	-	+	+	-	*L.plantarum*	99.9
	363	-	Cocci	-	-	-	-	-	-	+	+	-	*L.pentosus*	60.7
	381	-	Bacil	-	+	-	-	++	-	-	-	-	*L.plantarum*	99.9
	721	-	Bacil	-	-	-	-	-	-	+	+	-	*L.plantarum*	999
	761	-	Cocci	-	-	-	-	-	-	+	+	-	*L.pentosus*	98.6
	X152	-	Bacil	-	-	-	-	-	-	+	++	-	*L.plantarum*	99.9
	X183	-	Bacil	-	+	-	-	-	-	+	+	-	*L.plantarum*	99.9
	X323	-	Cocci	-	+	-	-	-	-	+	++	-	*L.plantarum*	99.9
	X354	-	Bacil	-	-	-	-	-	-	++	+	-	*L.pentosus*	97.2
	X361	+	Bacil	-	+	-	-	-	-	++	+	-	*L.pentosus*	98.6
	X362	+	Bacil	-	+	-	-	-	-	++	-	-	*L.pentosus*	97.4
	X711	-	Cocci	+	-	-	++	++	+	+	+	-	*L.pentosus*	88.7
	X751	-	Bacil	-	-	-	+	-	-	++	++	-	*L.plantarum*	99.8
	X753	-	Cocci	-	-	-	-	-	-	++	++	-	*L.plantarum*	66.6
	X771	-	Bacil	-	-	-	++	-	-	+	++	-	*L.plantarum*	99.9
AW	241	-	Bacil	-	-	-	-	-	-	+	+	-	*L.pentosus*	97.4
	263	-	Cocci	-	+	-	-	+	-	+	+	-	*L.plantarum*	99.9
	272	-	Cocci	+	-	-	-	-	-	++	+	-	*L.plantarum*	99.9
	411	-	Cocci	-	-	-	-	-	-	+	+	-	*L.plantarum*	99.9
	432	-	Bacil	-	-	-	-	-	-	+	+	-	*L.pentosus*	99.8
	444	-	Bacil	-	+	-	-	-	-	+	+	-	*L.pentosus*	98.6
	463	-	Cocci	-	-	-	-	-	-	+	++	-	*L.pentosus*	91.6
	474	-	Bacil	-	-	-	+	-	+	+	++	-	*L.plantarum*	99.2

482	-	Bacil	-	+	-	-	-	-	+	+	-	*L.plantarum*	99.9
483	-	Bacil	-	+	-	++	++	+	++	++	-	*L.plantarum*	99.6
823	-	Bacil	-	+	-	-	-	-	++	++	-	*L.plantarum*	99.9
831	+	Bacil	-	-	-	+	-	-	++	-	-	*L.pentosus*	98.6
833	-	Bacil	-	-	-	-	-	-	++	-	-	*L.plantarum*	99.9
881	-	Bacil	-	+	-	+	+	-	++	+	-	*L.plantarum*	99.9
X221	-	Bacil	-	+	-	-	-	-	++	+	-	*L.plantarum*	99.9
X253	-	Bacil	-	-	-	-	-	-	++	+	-	*L.pentosus*	99.9
X273	-	Bacil	+	+	-	++	-	-	+	+	-	*L.pentosus*	51.5
X281	-	Bacil	-	+	-	-	-	-	-	-	-	*L.pentosus*	99.9
X283	-	Bacil	-	+	-	+	-	++	++	+	-	*L.pentosus*	99.8
X452	-	Bacil	-	-	-	-	-	-	+	-	-	*L.plantarum*	99.9
X472	-	Cocci	-	+	-	-	-	-	+	+	-	*L.pentosus*	97.4
X481	-	Bacil	-	-	-	-	-	-	+	+	-	*L.plantarum*	99.9
X862	+	Cocci	-	-	-	++	-	-	+	++	-	*L.plantarum*	99.9
X874	+	Bacil	-	+	-	+	-	-	++	++	-	*L.pentosus*	98.6

-: negatif reaction, +: positive reaction, ++: strong positive reaction
GFG: Gas from glucose, T: Temperature, NaCl: Salt concentration

3.3. Carbohydrate Fermentations

Isolates were grouped according to the results of phenotypic analysis. 48 bacteria with different phenotypic characteristics were selected and identified with API 50 CH test kit. Selection of bacteria was carried out based on their resistance to high acidity, high salt concentrations, and their behavior at different temperatures. *L. plantarum* appeared to be the dominant microorganism for both brine types.

L. plantarum and *L. pentosus* species isolated from the pickles produced with vinegar were identified with high percentage (~99%). Only two species were identified with 60%. We observed that *L. planturum* species was dominant in pickles produced with vinegar. Bacteria isolated from M17 agar turned out to be *L. pentosus* species and bacteria isolated from MRS agar, *L. plantarum* species were dominant.

L. plantarum and *L. pentosus* species were isolated from the pickles produced with AW. Unlike the pickles produced with vinegar, *L.pentosus* species seems to be more dominant in pickles manufactured with AW. Similarly, *L.pentosus* species were dominant in the isolated samples from M17 agar.

According to API test results, genus characteristics of some species are inconsistent with previously determined cell morphologies. Although samples 323, 761, X323, X711, X753, X771 isolated from the pickles produced with vinegar and samples 263, 272, 411, 463, X472, and X862 were isolated from pickles produced with AW were determined as cocci, they were identified as Lactobacilli according to API test results.

Lactic acid bacteria that classified as heterofermentative according to the gas formation test were identified as *L. plantarum* and *L. pentosus*. These two bacteria were reported as "facultative heterofermentative", and they may exhibit gas-forming abilities [25, 26].

L. plantarum and *L. pentosus* are in the Streptobacterium group from Lactobacilli. The optimum growth temperature these species are 30-35 ^{o}C, and they are able to grow at 15 ^{o}C but mostly not at 50 ^{o}C. Growth test at different temperatures showed that *L. plantarum* and *L. pentosus* showed characteristics growth at temperatures studied, and several isolates were able to grow at 45 and 50 ^{o}C. The ability to grow at 10 ^{o}C was found to be higher for both bacteria. Şimşek (2003) reported that *L. plantarum* species isolated from pickles were able to grow at 15 ^{o}C, but only 1 isolate could grow at 45 ^{o}C [27].

L. plantarum and *L. pentosus* species seem to show the best growth at pH 4.5. The growth characteristics of both species at different pHs are quite similar. At pH 3, bacteria showed poor growth and at pH 9.6 no bacteria could grow. Even though *L. plantarum* and *L. pentosus* species were weakly able to grow at pH 3, and their acid resistance were quite high. Elmacı et al. [28] stated that *L. plantarum* bacteria isolated from cucumber pickle samples showed low growth at pH 3 and showed no growth at pH 9. However, they reported that *L. plantarum* showed the best growth at pH 4. In another study, *Lactobacillus* strains isolated from pickles showed growth at the level of 6.2-7.7 log cfu/mL at pH 3 [29].

Growth tests of different salt concentrations showed that most of the isolated LAB were able to grow at 2 and 6.5% salt concentrations (only 3 and 6 LAB were unable to grow at 2% and 6.5% salt concentrations, respectively). 10% salt concentration inhibited the growth of all isolated species except one bacterium (sample 172). Çetin [3] examined the growth conditions of the LAB isolated from pickles at 6.5%, 10% and 12% salt concentrations. They reported majority of the species isolated were *L. plantarum* showing growth at 6.5% concentration. They also reported that the growth ability of bacteria decreased considerably with the increase in salt concentration. In another study, *L. plantarum* bacteria isolated from cucumber pickles showed very good growth at 3% and 6.5% salt concentrations, while the growth level was very low level at 10% salt concentration [28].

The utilization of carbohydrates by the isolates exhibited similar results in the API test. All of the isolates were able to ferment D-ribose, D-fructose, D-glucose and D-mannose but not glycogen, xylitol. Especially the ability to use D-xylose and L-arabinose was definitive for identification.

L. plantarum and *L. pentosus* species show great similarity to each other in terms of phenotype. The biggest feature distinguishing *L.pentosus* from *L. plantarum* is that *L.pentosus* can ferment both xylose and arabinose [30]. We have observed similar results at the phenotypic tests for *L. plantarum* and *L. pentosus*. When the API test kit results were examined, samples showed a positive reaction by fermenting the D-xylose in microtube 6 were defined as *L. pentosus*.

Dursun [31] performed identification analyzes of LAB isolated from 15 different pickled cucumber samples, and stated that *L. plantarum*, *L. brevis*, and *L. acidophilus* species were dominant. Alan and Dığrak [32] isolated LAB from the pickled cucumber samples they produced and performed their identification analysis. According to the results of the analysis, they stated that the majority of the isolates were *L. plantarum* species. Tamminen et al. [33] stated that *L. plantarum* and *L. pentosus* constituted most of the bacteria they isolated from pickled cucumbers.

4. CONCLUSION

Isolates obtained from the pickles produced with two different brines prepared with vinegar and AW showed that *L.plantarum* and *L.pentosus* bacteria were the dominant flora. It was observed that the microbial flora of the pickles produced with two different brines were similar. Isolated bacteria from both brines exhibited similar resistance to acidity and salt concentration during fermentation, and their phenotypic characteristics were also quite similar. Some LAB isolated from both brines such as X273, 483, X884 and 184 exhibited growth at high acid and salt concentrations, which may indicate possible probiotic potential. The fact that the pickles produced with AW have a similar flora to the pickles produced with vinegar supports the conclusion that AW can be used successfully in pickle production.

Funding

The authors would like to thank to The Scientific and Technological Research Council of Turkey (TÜBİTAK) (Grant no: 118O999) for the financial support.

The Declaration of Conflict of Interest/ Common Interest

No conflict of interest or common interest has been declared by the authors.

Authors' Contribution

The authors contributed equally to the study.

The Declaration of Research and Publication Ethics

The authors of the paper declare that they comply with the scientific, ethical and quotation rules of SAUJS in all processes of the paper and that they do not make any falsification on the data collected. In addition, they declare that Sakarya University Journal of Science and its editorial board have no responsibility for any ethical violations that may be encountered, and that this study has not been evaluated in any academic publication environment other than Sakarya University Journal of Science.

REFERENCES

[1] N. Aktan, U. Yücel, and H. Kalkan, Turşu Teknolojisi, Ege Üniversitesi Ege Meslek Yüksekokulu Yayınları, no. 23, 1998.

[2] M. Tokatlı, D. Dursun, N. Arslankoz, P. Şanlıbaba, and F. Özçelik, "Turşu üretiminde laktik asit bakterilerinin önemi," Akad. Gıda Derg., vol. 10, no. 1, pp. 70–76, 2012.

[3] B. Çetin, "Turşu fermantasyonunda kullanılabilecek laktik asit bakterilerinin belirlenmesi ve probiyotik turşu üretimi için uygun suşların seçimi," 2017.

[4] P. Menchik and C. I. Moraru, "Nonthermal concentration of liquid foods by a combination of reverse osmosis and forward osmosis. Acid whey: A case study," J. Food Eng., vol. 253, no. February, pp. 40–48, 2019.

[5] M. J. Lindsay, T. W. Walker, J. A. Dumesic, S. A. Rankin, and G. W. Huber, "Production of monosaccharides and whey protein from acid whey waste streams in the dairy industry," Green Chem., vol. 20, no. 8, pp. 1824–1834, 2018.

[6] S. Talebi, F. Suarez, G. Q. Chen, X. Chen, K. Bathurst, and S. E. Kentish, "Pilot study on the removal of lactic acid and minerals from acid whey using membrane technology," ACS Sustain. Chem. Eng., vol. 8, no. 7, pp. 2742–2752, 2020.

[7] J. Chandrapala et al., "Properties of acid whey as a function of pH and temperature," J. Dairy Sci., vol. 98, no. 7, pp. 4352–4363, 2015.

[8] E. M. Silva and S. T. Yang, "Kinetics and stability of a fibrous-bed bioreactor for continuous production of lactic acid from unsupplemented acid whey," J. Biotechnol., vol. 41, no. 1, pp. 59–70, 1995.

[9] J. P. Salminen, T. Roslin, M. Karonen, J. Sinkkonen, K. Pihlaja, and P. Pulkkinen, "Seasonal variation in the content of hydrolyzable tannins, flavonoid glycosides and proanthocyanidins in oak leaves," J. Chem. Ecol., vol. 30, no. 9, pp. 1693-1711, 2004.

[10] E. Yang, L. Fan, Y. Jiang, C. Doucette, and S. Fillmore, "Antimicrobial activity of bacteriocin-producing lactic acid bacteria isolated from cheeses and yogurts," AMB Express, vol. 2, no. 1, pp. 1–12, 2012.

[11] H. Rodríguez et al., "Food phenolics and lactic acid bacteria," Int. J. Food Microbiol., vol. 132, no. 2–3, pp. 79–90, 2009.

[12] G. Klein, A. Pack, and G. Reuter, "Antibiotic resistance patterns of enterococci and occurrence of vancomycin-resistant enterococci in raw minced beef and pork in Germany," Appl. Environ. Microbiol, vol. 64, pp. 1825–1830, 1998.

[13] C. S. Pederson and M. N. Albury, "Effect of temperature upon bacteriological and chemical changes in fermenting cucumbers," N. Y. Agr. Expt. Sta. Bull, p. 744, 1950.

[14] E. Çetinkaya and K. Ayhan, "Mikrobiyolojide Kullanılan Bazı Moleküler Teknikler Molecular Technics Used in Microbiology," Karaelmas Fen ve Mühendislik Derg., vol. 2, no. 1, pp. 53–62, 2012.

[15] F. Kıran and Ö. Osmanağaoğlu, "Laktik asit bakterilerinin (LAB) identifikasyonunda/tiplendirmesinde kullanılan moleküler yöntemler," Erciyes Üniversitesi Fen Bilim. Enstitüsü Derg., vol. 27, no. 1, pp. 62–74, 2011.

[16] E. Papamanoli, N. Tzanetakis, E. Litopoulou-Tzanetaki, and P. Kotzekidou, "Characterization of lactic acid bacteria isolated from a Greek dry-fermented sausage in respect of their technological and probiotic properties," Meat Sci., vol. 65, no. 2, pp. 859–867, 2003.

[17] O. Yerlikaya, "Laktik asit bakterilerinin tanılanmasında kullanılan başlıca fenotipik ve moleküler yöntemler," Gıda ve Yem Bilim. Teknol. Derg., vol. 14, pp. 8–22, 2014.

[18] J. Yu, W. Goa, M. Qing, Z. Sun, W. Wang, W. Liu, L. Pan, T. Sun, H. Wang, N. Bai, and H. Zhang, "Identification and characterization of lactic acid bacteria isolated from traditional pickles in Sichuan," China. J. Gen. Appl. Microbiol., vol. 58, no. 3, pp. 163–172, 2012.

[19] S. Bağder Elmacı, M. Tokatlı, D. Dursun, F. Özçelik, ve P. Şanlıbaba, "Phenotypic and genotypic identification of lactic acid bacteria isolated from traditional pickles of the Çubuk region in Turkey," Folia Microbiologica, vol. 60, no. 3, pp. 241–251, 2015.

[20] M.G. Başdoğan, "Geleneksel olarak üretilen turşulardan izole edilen laktik asit bakterilerinin probiyotik potansiyelinin belirlenmesi," Ege Üniversitesi, 2020.

[21] B. Şimşek and O. Sağdıç, "Isparta ve yöresinde üretilen dolaz (tort) peynirinin bazı kimyasal ve mikrobiyolojik özellikleri," Süleyman Demirel Üniversitesi Fen Bilim. Enstitüsü Derg. vol. 10, no. 3, pp. 346-351, 2006.

[22] P. Ertürkmen, Z. Öner, "Beyaz peynir örneklerinden izole edilen laktik asit bakterilerinin başlatıcı (starter) kültür özelliklerinin biyokimyasal yöntemlerle belirlenmesi," Süleyman Demirel Üniversitesi Fen Bilim. Enstitüsü Derg. vol. 19, no. 3, pp. 9-16, 2015.

[23] K. Halkman and Ö. Sağdaş, Mikrobiyoloji El Kitabı. 2014.

[24] M. A. Daeschel and H. P. Fleming, "Selection of lactic acid bacteria for use in vegetable fermentations," Food Microbiol., vol. 1, no. 4, pp. 303–313, 1984.

[25] G. Bustos, A. B. Moldes, J. M. Cruz, and J. M. Domínguez, "Influence of the metabolism pathway on lactic acid production from hemicellulosic trimming vine shoots hydrolyzates using Lactobacillus pentosus," Biotechnol. Prog., vol. 21, no. 3, pp. 793–798, 2005.

[26] L. Axelsson, "Lactic Acid Bacteria: Classification and Physiology. in: Salminen, S.von Wright, A. and Ouwehand A. (Eds.), Lactic Acid Bacteria: Microbiological and Functional Aspects". 3rd rev. and exp. ed. Marcel Dekker, Inc., New York, pp.1-66, 2004.

[27] B. Şimşek, "Koyun Sütünden İşlenen Beyaz Peynirlerde İnek Sütü Varlığını Saptama Düzeyinin Belirlenmesi," 2003.

[28] S. Bağder Elmacı, M. Tokatlı, D. Dursun, F. Özçelik, and P. Şanlıbaba, "Phenotypic and genotypic identification of lactic acid bacteria isolated from traditional pickles of the Çubuk region in Turkey," Folia Microbiol. (Praha)., vol. 60, no. 3, pp. 241–251, 2015.

[29] A. A. Boricha, S. L. Shekh, S. P. Pithva, P.

S. Ambalam, and B. R. Manuel Vyas, “In vitro evaluation of probiotic properties of Lactobacillus species of food and human origin,” LWT, vol. 106, pp. 201–208, 2019.

[30] M. C. Curk, J. C. Hubert, and F. Bringel, “Lactobacillus paraplantarum sp. nov., a new species related to Lactobacillus plantarum,” Int. J. Syst. Bacteriol., vol. 46, no. 2, pp. 595–598, 1996.

[31] D. Dursun, “Ankara çubuk yöresi turşularından izole edilen laktik asit bakterilerinin tanımlanması ve toplam hücre protein profillerinin belirlenmesi,” Ankara Üniversitesi, 2010.

[32] Y. Alan and M. Dığrak, “Doğal turşulardan izole edilen lactobacillus plantarum suşlarının İzolasyonu ve Tanımlanması,” KSÜ Doğa Bilim. Derg., vol. 15, no. 2, pp. 46–49, 2012.

[33] M. Tamminen et al., “Screening of lactic acid bacteria from fermented vegetables by carbohydrate profiling and PCR-ELISA,” Lett. Appl. Microbiol., vol. 39, no. 5, pp. 439–444, 2004.

SAKARYA ÜNİVERSİTESİ
FEN BİLİMLERİ ENSTİTÜSÜ DERGİSİ

Sakarya University Journal of Science
SAUJS

e-ISSN 2147-835X Period Bimonthly Founded 1997 Publisher Sakarya University
http://www.saujs.sakarya.edu.tr/

Title: Theoretical Investigation of the W(CO)6 and CO Selenization Process

Authors: Nadire NAYİR

Recieved: 2021-12-18 00:00:00

Accepted: 2022-02-19 00:00:00

Article Type: Research Article

Volume: 26
Issue: 2
Month: April
Year: 2022
Pages: 283-291

How to cite
Nadire NAYİR; (2022), Theoretical Investigation of the W(CO)6 and CO Selenization Process. Sakarya University Journal of Science, 26(2), 283-291, DOI: 10.16984/saufenbilder.1038357
Access link
https://dergipark.org.tr/tr/journal/1115/issue/69580/1038357

New submission to SAUJS
http://dergipark.gov.tr/journal/1115/submission/start

Sakarya University Journal of Science 26(2), 283-291, 2022

Theoretical Investigation of the $W(CO)_6$ and CO Selenization Process

Nadire NAYİR*[1]

Abstract

Detailed atomic-level insight into the mechanism of $W(CO)_6$ and CO selenization is essential for the fabrication of cheap and environmentally benign transition metal chalcogenides such as MoS_2 and WSe_2. Earlier discussions in literature have focused mainly on the CO methanation by sulfur and its derivatives but H_2Se mediated CO methanation at the atomic level is yet to be explored. First-principles calculations and ReaxFF-based molecular dynamics simulations are conducted here to explore the relative stabilities of intermediates formed during the gas-phase interactions of $W(CO)_6$ and H2Se, determined associated reaction energies and kinetic barriers. The methanation of CO, which is released from the organometal, by H_2Se is further investigated. The results indicate that the chain reactions of $W(CO)_6$ and H_2Se lead to the formation of a thermodynamically stable end product of $W(SeH)_2Se_2$. Depending on the temperature, $W(HSe)_2Se_2$ is expected to go through a last uphill reaction by releasing H2Se into the environment and evolving into a WSe_3 molecule. Additionally, the dehydrogenation of organometallic molecules is thermodynamically feasible but kinetically controlled, requiring a significant activation energy. When all CO groups are released from the W atom, the H_2 release from W-compund becomes nearly barrierless. Since CO radical groups are dominant byproducts formed during the MOCVD chain reactions but in a chalcogen rich environment, this work also shed light into the CO selenization during the growth of transition metal diselenides (e.g., WSe_2, $MoSe_2$, $CrSe_2$) and discusses the formation of potential products such as CSe_2, CH_4, H_2Se, CO, H_2O, Se_2.

Keywords: Density functional theory, ReaxFF molecular dynamics, $W(CO)_6$ and H_2Se interactions, CO methanation.

1. INTRODUCTION

Transition metal dichalcogenides (TMD) which belong to the emerging family of two-dimensional layered materials are a promising platform for a new generation of electronic and optoelectronic devices because of their unique physicochemical, optical, and electronic properties [1-6]. TMD is composed of layers that are coupled by weak van der Waals forces but have strong covalent bonds between the in-plane atoms. There are many techniques to fabricate such materials, e.g., atomic layer deposition [7-9], chemical vapor deposition/metal-organic chemical vapor deposition (MOCVD) [2, 10, 12], and molecular beam epitaxy [13-16]. Among them, MOCVD is a common method that is utilized for the synthesis of TMD materials.

* Corresponding author: nnayir@kmu.edu.tr
[1] Karamanoğlu Mehmetbey University, Kamil Özdağ Faculty of Science, Pyhsics Department
ORCID: https://orcid.org/0000-0002-3621-2481

Because it allows for control of the precursor ratio and flux and provides flexibility in precursor selection, it consequently enables the fabrication of high-quality, nearly single-crystalline TMD materials. MOCVD uses volatile metal-organic and chalcogen precursors that are injected into the chamber through separate inlets. This leads to complex physicochemical processes that initiate the deposition of TMD materials onto substrate. Even though this technique reduces the need for source heating because of the relatively high vapor pressures of hydrides, the elevated temperature is still required during growth to overcome energy barrier necessary to eliminate residual carbon from the metal precursors and promote chemisorption of metal and chalcogen by surface [2, 10, 11].

Despite tremendous progress on the MOCVD growth technique, the synthesis of large-scale, defect-free TMD materials with controllable thickness is still challenging for reasons such as the fact that the synthesis and characterization are costly and relatively slow, precursors are expensive and toxic, and the selection of substrate is restricted. This has therefore triggered theoretical modeling to shed new light on the design and fabrication of TMD-based devices at the atomistic level. To date, Xuan et. al [17] developed a multiscale framework as a combination of ReaxFF empirical potential and continuum fluid dynamics methods for the gas-phase kinetics of the MOCVD growth of WSe_2 from the gas precursors $W(CO)_6$ and H_2Se. However, to the best of the author's knowledge, there is no report yet on a detailed mechanism of the $W(CO)_6$ selenization at the DFT level and the CO selenization process has yet to be explored. In this study, the selenization of $W(CO)_6$ and CO is investigated using DFT and ReaxFF methods. A series of DFT calculations are conducted to extract a thermodynamically allowable pathway from $W(CO)_6$ and H_2Se gas-phase precursors to WSe_3. ReaxFF atomistic simulations are also performed to explore the impact of temperature on the adduct formation besides end-product derived from the $W(CO)_6$ and H_2Se chain chemical interactions. Following the results obtained at DFT and ReaxFF level, the CO methanation by H_2Se is further studied to provide insight into the relative stabilities of adducts formed during the MOCVD growth of WSe_2.

2. METHOD OF CALCULATIONS

Jaguar calculations: Nonperiodic QM calculations are performed via Jaguar[18] using the B3LYP functional and the LACV3P**++ effective core potential. **ReaxFF MD simulations:** Molecular dynamics (MD) simulations are performed using ReaxFF/ADF [19] based on the ReaxFF force field developed by Xuan et al [17]. A comprehensive review of the ReaxFF formalism can be found in Chenoweth et al.[20] The models in the figures are visualized using VESTA [21].

3. RESULTS AND DISCUSSION

3.1. Impact of H_2 formation on MOCVD growth of TMD growth

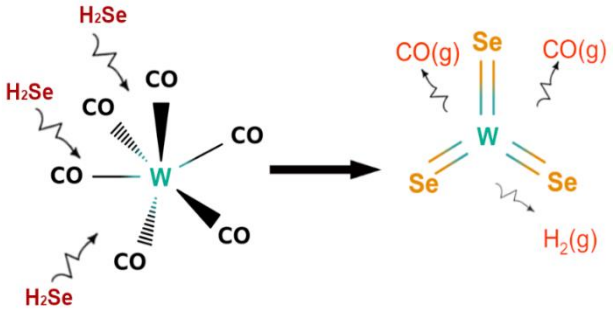

Figure 1 The initial and final product of MoCVD gas-phase reactions.

MOCVD gas-phase kinetic of TMD materials from volatile organometal and chalcogen precursors is a complicated process and heavily relies on numerous chemical reactions. In this study, the DFT calculations are conducted to track the chemical and structural evolution of the vaporized $W(CO)_6$ and H_2Se precursors to the end product of WSe_3 and to lay out the full picture of the thermodynamically favorable MOCVD reaction pathway (Figures 1-3). The chemical reactions are classified into three main groups: (i) CO dissociation from (ii) H_2Se binding to and (iii) H_2 elimination from $W(CO)_x(H_2Se)_y(HSe)_zSe_m$ molecule where x, y, z, m=0, 1, 2, 3, 4 (Figure 1), as also reported by Xuan et al. [17]

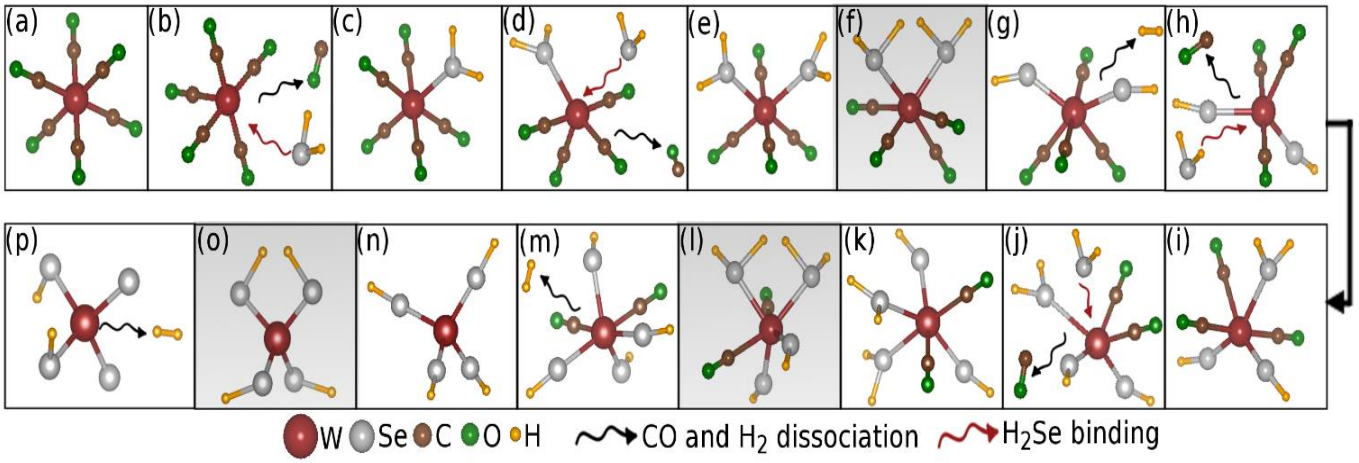

Figure 2 Ball-and-stick representations of the proposed MOCVD reaction pathway starting from (a) the dissociation of CO from $W(CO)_6$ and leading to (p) the thermodynamically stable end product, $W(SeH)_2Se_2$. (f, l, o) The three key transition states for H_2 formation are highlighted with a gray background.

As shown in Figure 2a-c, the MOCVD gas-reaction chain initiates with the loss of the first CO group from the $W(CO)_6$ molecule with dissociation energy of 1.79 eV, and then, continues with H_2Se binding to the W-metal. Losing the second CO group creates a new empty site for binding of the second H_2Se to the metal (Figure 2d,e), which leads to the bimolecular elimination of H_2 from $W(CO)_4(H_2Se)_2$ (Figure 2f,g). Then, the $W(CO)_4(HSe)_2$ molecule goes through two consecutive carbonyl dissociations, binds two more H_2Se (Figure 2h-j) molecules, and results in $W(CO)_2(HSe)_2(H_2Se)_2$ (Figure 2k). The presence of two hydrides weakly bonded to metal triggers the evolution of the $W(CO)_2(HSe)_2(H_2Se)_2$ molecule to $W(CO)_2(HSe)_4$. To reach this stable conformational state of $W(CO)_2(HSe)_4$, the $W(CO)_2(HSe)_2(H_2Se)_2$ molecule passes through a second transition state by releasing an H_2 molecule (Figure 2l,m). Subsequently, the resulting $W(CO)_2(HSe)_4$ molecule, loses the last two CO groups and degrades into $W(HSe)_4$ (Figure 2n). This molecule releases further an H_2 molecule (Figure 2o), finally evolving to the thermodynamically stable end product of $W(HSe)_2Se_2$ (Figure 2p). Figure 3a illustrates the proposed MOCVD reaction pathway starting from the gas-phase precursors $W(CO)_6$ and H_2Se and leading to the thermodynamically stable end product of $W(SeH)_2Se_2$ at the DFT level. Then, depending on the temperature, $W(HSe)_2Se_2$ goes through a last uphill reaction by releasing H_2Se into the chamber and evolves into the WSe_3 molecule with a net additional energy of 0.52 eV by following the reaction pathway shown in Figure 3b.

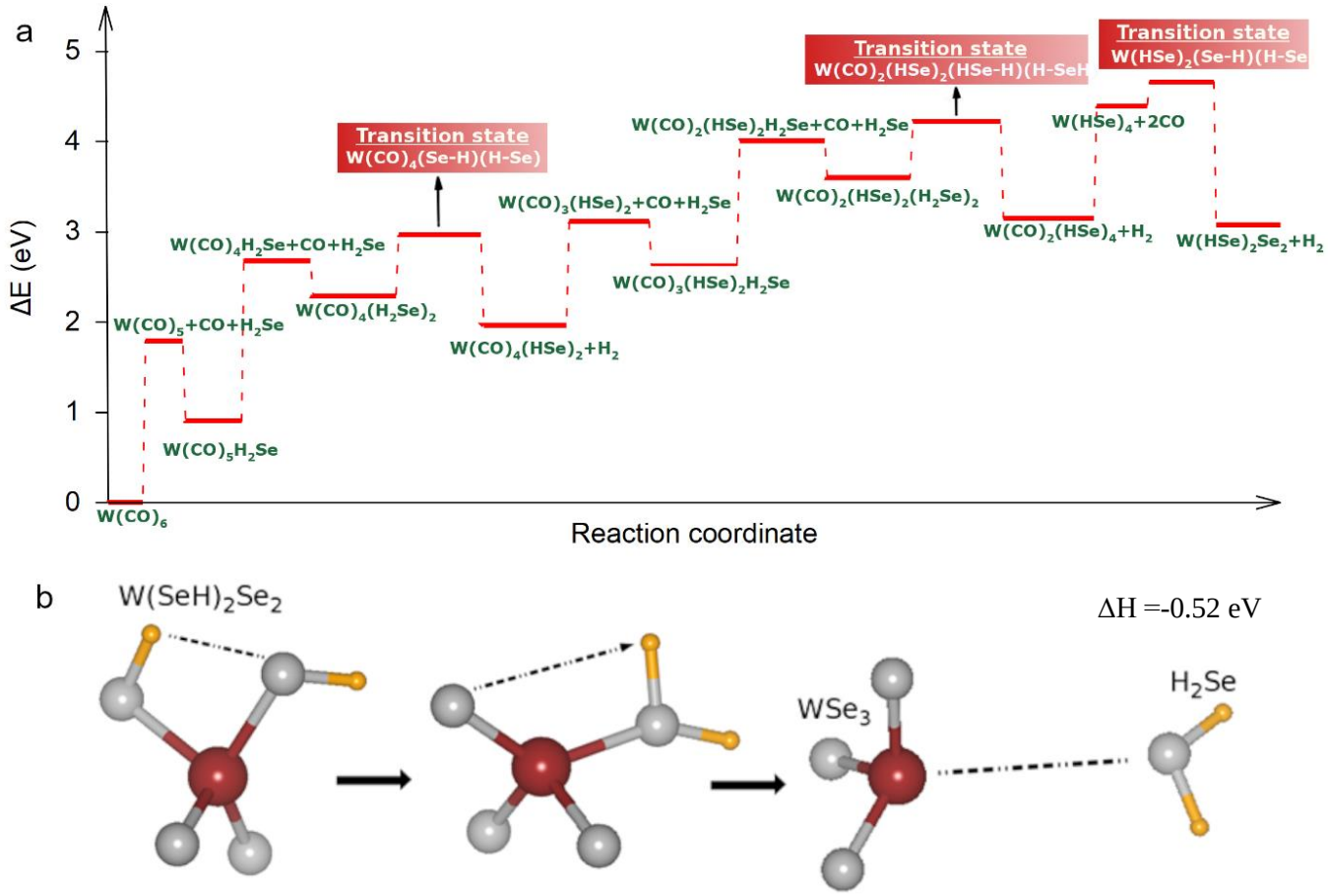

Figure 3 (a) DFT-based reaction pathways for MOCVD growth of WSe_2, starting from the gas precursors $W(CO)_6$ and H_2Se and leading to the thermodynamically stable end-product of $W(H_2Se)Se_2$. (b) Chemical evolution of WSe_3 and H_2Se from $W(SeH)_2Se_2$ with an entalphy energy of 0.52 eV, where dark red, gray and gold atoms are W, Se and H, respectively.

Additionally, as seen from Figure 3a, the H_2 elimination is an exothermic chemical event - in case that at least two H_2Se or HSe bind to a W metal, three key transition states are expected for H_2 release in the thermodynamically proposed MOCVD reaction pathway illustrated in Figures 2 and 3:

$$W(CO)_4(H_2Se)_2 \rightarrow W(CO)_4(HSe)_2 + H_2$$

$$\Delta H = -0.33 \text{ eV}, \quad E_a = 0.68 \text{ eV} \qquad (1)$$

$$W(CO)_2(H_2X)_2(HX)_2 \rightarrow W(CO)_2(HSe)_4 + H_2$$

$$\Delta H = -0.45 \text{ eV}, \quad E_a = 0.62 \text{ eV} \qquad (2)$$

$$W(HSe)_4 \rightarrow W(HSe)_2Se_2 + H_2$$

$$\Delta H = -1.32 \text{ eV}, \quad E_a = 0.27 \text{ eV} \qquad (3)$$

where ΔH and E_a are enthalpy and activation energies of the reactions above. These transition reactions result in thermodynamically more stable products of $W(CO)_4(HSe)_2$, $W(CO)_2(HSe)_4$ and $W(HSe)_2Se_2$ than the reactants of $W(CO)_4(H_2Se)_2$, $W(CO)_2(H_2Se)_2(HSe)_2$ and $W(HSe)_4$, suggesting that 2D-WSe_2 growth is thermodynamically favored. However, the results also show that dehydrogenation of organic molecule is kinetically hindered, requiring activation energy of 0.6 − 0.7 eV (Eqs. 1-2) to overcome the kinetic barrier for the H_2 elimination, indicating that the MOCVD growth of WSe_2 requires external energy (e.g., temperature and/or pressure) to accelerate the chemical reactions. Additionally, the reaction of

$$W(CO)_2(HSe)_2(H_2Se)_2 \rightarrow W(CO)_2(HSe)_2(Se{-}H)(H{-}Se)^{TS}$$

is considered as a rate-limiting reaction governing the MOCVD growth kinetics since the W-organic molecule encounters the highest energy barrier of 0.68 eV during the H_2 release. The willingness of the Se atom to lose the H atom decreases with the decrease of the number of CO ligands bound to a W atom. In case of losing all CO groups from the W atom, the H_2 release from the W-compund becomes nearly barrierless (0.27 eV in Eq. 3).

The combustion of $W(CO)_6$ with H_2Se molecules increase the CO concentration in the environment. Therefore, the CO methanation by H_2Se and potential intermediates are also expected to form during the MOCVD growth of WSe_2 and other transition metal diselenides such as $MoSe_2$, $CrSe_2$. Table 1 summarizes the proposed reactions for adduct formation and corresponding energies. Additionally, the proposed thermodynamically favored reaction pathway for CO methanation by H_2Se is as follows:

$$SeCO \rightarrow H_3CSeH \rightarrow CH_4 \rightarrow CSe_2 \quad (4)$$

CSe_2 formation from the CO selenization is expected to realize in four stages:

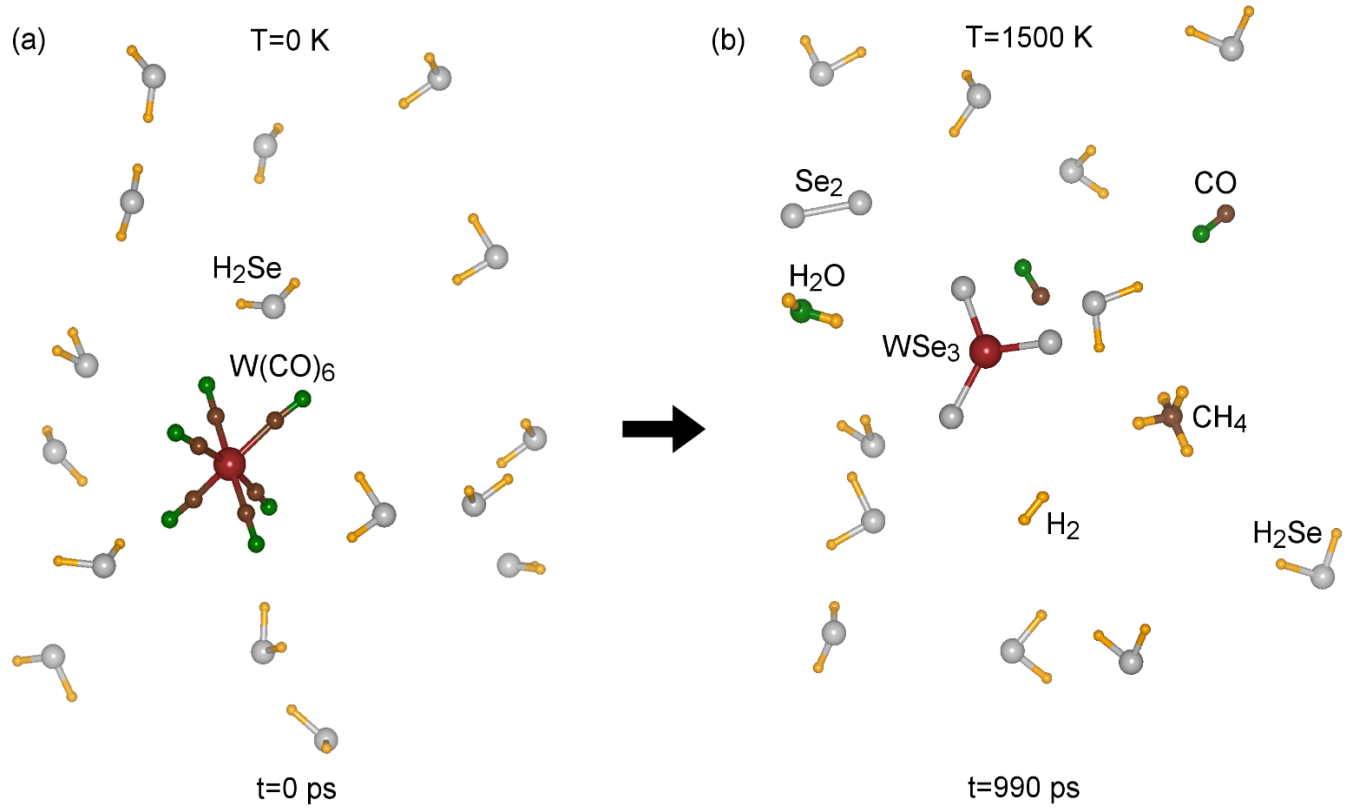

Figure 4 MOCVD gas-phase kinetic at 1500 K obtained from CVHD implemented ReaxFF-MD simulations. (a) The initial configuration of the simulation box which includes the gas-phase precursors $W(CO)_6$ and H_2Se and (b) the end- and by-products formed at 1500 K.

I) The pathway in Eq. 4 is expected to initiate with the attack by Se radical present on CO to form SeCO, which is thermodynamically favored.

$$CO + Se \rightarrow SeCO \qquad \Delta H = -3.62 \text{ eV}$$

Note that the HSe formation is catalyzed by organometal with vacancies, then two HSe molecules come together and form H_2Se and Se radical as seen below:

$$-W{=}Se + H_2Se \rightarrow -W{-}SeH + HSe$$

$$HSe + HSe \rightarrow H_2Se + Se$$

The SeCO formation by Se_2 and HSe manifest endothermic behavior. Additionally, even though the selenization reaction of CO by H2Se exhibits a slightly exothermic character (-0.07 eV), this is also kinetically hindered which requires

activation energy of 1.96 eV to release an H_2 molecule.

$CO + Se_2 \rightarrow SeCO + Se$ $\Delta H = 1.14$ eV

$CO + HSe \rightarrow SeCO + H$ $\Delta H = 1.18$ eV

$CO + H_2Se \rightarrow OC{-}H_2Se\ (TS) \rightarrow SeCO + H_2$

$\Delta H = -0.07$ eV, $Ea = 1.96$ eV

Table 1 Reaction and associated energies in eV.

Reaction	Energy (eV)	Reaction	Energy (eV)
$SeCO + H_2Se \rightarrow SeCSeHOH$	0.66	$CO+H_2Se \rightarrow OCH_2Se\ (TS)$	1.96
$SeCO + 3H_2 \rightarrow H_3CSeH + H_2O$	-1.27	$OCH_2Se\ (TS) \rightarrow SeCO + H_2$	-2.03
$CO + Se_2 \rightarrow SeCO + Se$	1.14	$SeCOH + HSe \rightarrow SeCO + H_2S$	-3.22
$CO + Se \rightarrow SeCO$	-3.62	$CH_4 + Se_2 + CSe_2 + 2H_2$	4.01
$SeCO + H_2Se + CSe_2 + H_2O$	0.54	$CO + H_2Se + SeCO + H_2$	-0.07
$SeCSeHOH \rightarrow CSe_2 + H_2O$	2.90	$SeCO + H_2Se \rightarrow SeCOH + HSe$	3.22
$CO + HSe \rightarrow SeCOH$	0.90	$CO + H_2Se \rightarrow OCH + HSe$	2.42
$H_3CSeH + H_2 \rightarrow CH4 + H_2Se$	-0.90	$CO+HSe \rightarrow SeCO + 1/2H_2$	1.18
$SeCOH + HSe \rightarrow SeCSeHOH$	-2.56	$CH_2 + H_2Se \rightarrow CH_3+HSe$	-1.58
$CH3_3 + HSe \rightarrow H_3CSeH$	-2.65	$CH_3+ H_2Se \rightarrow CH_4+HSe$	-1.30
$CH_4 + 2H_2Se \rightarrow CSe_2+ 4H_2$	6.34	$CH_4 + 2Se_2 \rightarrow CSe_2 + 2H_2Se$	3.24

II) Then, SeCO interacts with H_2 gases and converts to

$SeCO + 3H_2 \rightarrow H_3CSeH + H_2$

III) Then H_3CSeH degrades to CH_4 by releasing water and H_2 gases to the environment.

$H_3CSeH + H_2 \rightarrow CH_4+ H_2Se$

IV) At elevated temperatures, CSe_2 is expected to form in the presence of CH_4 and Se_2.

$CH_4 + 2Se_2 \rightarrow CSe_2 + 2H_2Se$

In the case of the methane interaction with Se radical, the two consecutive insertion reactions of Se in the H-C bond, followed by two H_2 releases (Eqs. 5-6) can also lead to the CSe_2 formation but this pathway is kinetically hindered because of a fairly high energy barrier:

$CH_4 + Se \rightarrow HSe\text{-}CH_3 \rightarrow Se{=}CH_2 + H_2$ (5)

$Se{=}CH_2 + Se \rightarrow Se{=}CH(SeH) \rightarrow CSe_2 + H_2$ (6)

Lastly, H_2 molecules released during the CO methanation can hydrogenate Se-atoms to form H_2Se.

$2H_2 + 2Se \rightarrow 2\ H_2Se$

As a result, all these DFT results together suggest the formation of the stable byproducts of CSe_2, H_2, H_2Se, HSe, H_2O, CH_4 during the MOCVD reactions

3.2. By-products derived from chemical reactions of the precursors $W(CO)_6$ and H_2Se using ReaxFF simulations

In this section CVHD method is combined with ReaxFF-MD simulations to shed a light on the elementary reaction pathways and the kinetics of the byproducts formed during the MOCVD growth from the gas precursors $W(CO)_6$ and H_2Se. Molecular dynamics (MD) simulations are highly effective in capturing detailed chemical events, reaction pathways, and product formation during gas-phase simulations. However, the MD timescale is usually restricted to nanoseconds, but the occurrence of meaningful reactions encountered during experiments usually require a timescale of about seconds to minutes [22]. Therefore, the traditional MD method employs high temperature to accelerate molecular collisions and successful reaction events. To address this discrepancy between the temperature used in MD simulations and experimental conditions, several accelerated molecular dynamics methods have been developed [23]. Collective Variable-driven Hyperdynamics or

CVHD [24, 25] is one of these methods which combines hyperdynamics and metadynamics to accelerate reactive events. Using this method, the MD simulation is performed by adding a bias potential $\Delta V(\eta)$ to the true potential energy surface to overcome the energy barrier in low-temperature simulations. The bias is constructed dynamically and is a function of collective variables (CVs) based on a distortion function described as $\chi_i = (r_i - r_i^{min})/(r_i^{max} - r_i^{min})$ where r_i is the length of every pair of bonds and $r_i^{min}$and r_i^{max} denotes the bond length of pair $i$at the beginning and end of a reaction event. The effective simulation time which is referred to as 'hypertime', is the multiplication of boost factor with the MD simulation time: $t_{hyper} = t_{MD} \times Boost = t_{MD} \times \langle e^{\beta \Delta V(\eta)} \rangle$ where $\beta = 1/k_B T$ and k_B is the Boltzmann constant.

The simulation box consisted of 1 $W(CO)_6$ and 20 H_2Se with the dimensions of 30x30x30 $Å^3$ (Figure 4a). The system energy was minimized and heated up to the target temperature of 1500 K with a heating rate of 50K/ps and an increment of 100 K with a time step of 0.1 fs. Each temperature increment was followed by an equilibration of 100ps. CVs are based on the distortion of local bond lengths and this study included three types of bonds for constructing CVs. The first one is W-Se bond with parameters $r_i^{min} = 2.10Å$ and $r_i^{max} = 3.05Å$ and the second pair is the H-Se bond with $r_i^{min} = 1.50Å$and $r_i^{max} = 2.80Å$ and C−O bond with $r_i^{min} = 1.20Å$and $r_i^{max} = 2.50Å$. The $r_i^{min}$and r_i^{max} values are based on the potential energy versus bond scan data available in Ref.17. Gaussian hills of width δ=0.025 and height ω = 0.25 kcal/mol were deposited at an interval of 1000 iterations (t_i = 0.1ps) and the waiting time to check if a reaction occurred is 1ps as suggested in the reference.

As shown in Figure 4b, the chain reactions of the volatile $W(CO)_6$ and H_2Se precursors lead to the formation of the end product of WSe_3 at 1500 K. Additionally, based on the ReaxFF results, the stable by-products of CH_4, H_2Se, CO, H_2O, Se_2 and H_2 are expected to form during the MOCVD growth process (Figure 4b). It is noteworthy that the current ReaxFF potential does not completely capture the interaction between C and Se for the CSe_2 formation because this potential is not trained against the associated DFT data [17].

4. CONCLUSIONS

DFT and ReaxFF simulations have been conducted to explore details of the atomistic mechanism of $W(CO)_6$ and CO hydroselenization. The DFT results propose a thermodynamically favorable MOCVD reaction pathway which initiates from $W(CO)_6$ and H_2Se, and leads to the WSe_3 end product. Furthermore, both DFT and ReaxFF results show that the conversion of $W(SeH)_2Se_2$ to WSe_3 is entropy driven, meaning that such conversion needs elevated temperatures (e.g. heating system at elevated temperature) to eliminate H_2Se from the energetically more stable $W(SeH)_2Se_2$. H_2 release reactions are also expected to play a crucial role in the MOCVD growth of WSe_2. The results presented here indicate that H_2 elimination from $W(CO)_4(H_2Se)_2$ requires the highest activation energy, and as such is considered as a rate-limiting reaction governing the MOCVD growth kinetics. Both ReaxFF and DFT results suggest the formation of stable byproducts of CSe_2, H_2, H_2Se, HSe, H_2O, CH_4 besides the end product of WSe_3 during the MOCVD chemical reactions at elevated temperatures. Since understanding the MOCVD gas-phase kinetics is critical to fabricate large-area single crystal transition metal diselenide thin film, this work can provide valuable thermodynamic and kinetic insight into the $W(CO)_6$ and CO hydroselenization in chalcogen rich environment.

Acknowledgments

This work was financially supported by the National Science Foundation (NSF) through the Pennsylvania State University 2D Crystal Consortium−Materials Innovation Platform (2DCC-MIP) under the NSF cooperative agreement DMR-1539916. The author also thanks Prof. Adri van Duin for the fruitful discussions

REFERENCES

[1] A. Eftekhari, "Tungsten Dichalcogenides (WS_2, WSe_2, and WTe_2): Materials Chemistry and Applications," J. Mater. Chem. A, vol. 5, no. 35, pp. 18299–18325, 2017

[2] T.H. Choudhury, X. Zhang, Z.Y.A. Balushi, M. Chubarov, J.M. Redwing, "Epitaxial Growth of 2D Layered Transition Metal Dichalcogenides," ArXiv190903502 Cond-Mat 2019.

[3] H. Qin, Q.-X. Pei, Y. Liu, Y.-W. Zhang, "The Mechanical and Thermal Properties of MoS2–WSe2 Lateral Heterostructures," Phys. Chem. Chem. Phys., vol. 21, no. 28, pp. 15845–15853, 2019.

[4] W. Choi, N. Choudhary, G.H. Han, J. Park, D. Akinwande, Y.H. Lee, "Recent Development of Two-Dimensional Transition Metal Dichalcogenides and Their Applications," Mater. Today, vol. 20, no. 3, 116–130, 2017.

[5] D. Andrzejewski, H. Myja, M. Heuken, A. Grundmann, H. Kalisch, A. Vescan, T. Kümmell, G. Bacher, "Scalable Large-Area p–i–n Light-Emitting Diodes Based on WS2 Monolayers Grown via MOCVD," ACS Photonics, vol. 6, no. 8, pp. 1832–1839, 2019.

[6] X. Zhang, F. Zhang, Y. Wang, D.S. Schulman, T. Zhang, A. Bansal, N. Alem, S. Das, V.H. Crespi, M. Terrones, J.M. Redwing, "Defect-Controlled Nucleation and Orientation of WSe_2 on HBN: A Route to Single-Crystal Epitaxial Monolayers," ACS Nano, vol. 13, no. 3, pp. 3341–3352, 2019.

[7] B.D. Keller, A. Bertuch, J. Provine, G. Sundaram, N. Ferralis, J.C. Grossman, "Process Control of Atomic Layer Deposition Molybdenum Oxide Nucleation and Sulfidation to Large-Area MoS_2 Monolayers," Chem. Mater., vol. 29, no. 5, pp. 2024–2032, 2017.

[8] W. Hao, C. Marichy, C. Journet, "Atomic Layer Deposition of Stable 2D Materials," 2D Mater., vol. 6, no. 1, 012001, 2018.

[9] G.-H. Park, K. Nielsch, A. Thomas, "Atomic Layer Deposition: 2D Transition Metal Dichalcogenide Thin Films Obtained by Chemical Gas Phase Deposition Techniques (Adv. Mater. Interfaces 3/2019)," Adv. Mater. Interfaces, vol. 6, no. 3, 1970024, 2019.

[10] X. Zhang, Z.Y. Al Balushi, F. Zhang, T.H. Choudhury, S.M. Eichfeld, N. Alem, T.N. Jackson, J.A. Robinson, J.M. Redwing, "Influence of Carbon in Metalorganic Chemical Vapor Deposition of Few-Layer WSe_2 Thin Films," J. Electron. Mater., vol. 45, no. 12, pp. 6273–6279, 2016.

[11] T.H. Choudhury, H. Simchi, R. Boichot, M. Chubarov, S.E. Mohney, J.M. Redwing, "Chalcogen Precursor Effect on Cold-Wall Gas-Source Chemical Vapor Deposition Growth of WS_2," Cryst. Growth Des., vol. 18, no. 8, pp. 4357–4364, 2018.

[12] Y. Gong, X. Zhang, J.M. Redwing, T.N. Jackson, "Thin Film Transistors Using Wafer-Scale Low-Temperature MOCVD WSe_2," J. Electron. Mater., vol. 45, no. 12, pp. 6280–6284, 2016.

[13] L. Jiao, H.J. Liu, J.L. Chen, Y. Yi, W.G. Chen, Y. Cai, J.N. Wang, X.Q. Dai, N. Wang, W.K. Ho, M.H. Xie, "Molecular-Beam Epitaxy of Monolayer MoSe2: Growth Characteristics and Domain Boundary Formation," New J. Phys., vol. 17, no. 5, 053023, 2015.

[14] Y. Zhang, T.-R. Chang, B. Zhou, Y.-T. Cui, H. Yan, Z. Liu, F. Schmitt, J. Lee, R. Moore, Y. Chen, H. Lin, H.-T. Jeng, S.-K. Mo, Z. Hussain, A. Bansil, Z.-X. Shen, "Direct Observation of the Transition from Indirect to Direct Bandgap in Atomically Thin Epitaxial $MoSe_2$," Nat. Nanotechnol., vol. 9, no. 2, pp. 111–115, 2014.

[15] H.J. Liu, L. Jiao, L. Xie, F. Yang, J.L. Chen, W.K. Ho, C.L. Gao, J.F. Jia, X.D. Cui, M.H. Xie, "Molecular-Beam Epitaxy of Monolayer and Bilayer WSe_2: A Scanning Tunneling Microscopy/Spectroscopy Study and Deduction of Exciton Binding Energy," 2D Mater., vol. 2, no. 3, 034004, 2015.

[16] M. Nakano, Y. Wang, Y. Kashiwabara, H. Matsuoka, Y. Iwasa, "Layer-by-Layer Epitaxial Growth of Scalable WSe_2 on Sapphire by Molecular Beam Epitaxy," Nano Lett., vol. 17, no. 9, pp. 5595–5599, 2017.

[17] Y. Xuan, A. Jain, S. Zafar, R. Lotfi, N. Nayir, Y. Wang, T.H. Choudhury, S. Wright, J. Feraca, L. Rosenbaum, JM Redwing, V. Crespi, A.C.T. van Duin, "Multi-Scale Modeling of Gas-Phase Reactions in Metal-Organic Chemical Vapor Deposition Growth of WSe_2," J. Cryst. Growth, vol. 527, 125247, 2019.

[18] A.D. Bochevarov, E. Harder, T.F. Hughes, J.R. Greenwood, D.A. Braden, D.M. Philipp, D. Rinaldo, M.D. Halls, J. Zhang, R.A. Friesner, "Jaguar: A High-Performance Quantum Chemistry Software Program with Strengths in Life and Materials Sciences," Int. J. Quantum Chem., vol. 113, no. 18, pp. 2110–2142, 2013.

[19] Amsterdam Modeling Suite Making Computational Chemistry Work For You https://www.scm.com/ (accessed 2020 -11 -10).

[20] K. Chenoweth, A.C.T. van Duin, W.A. Goddard, "ReaxFF Reactive Force Field for Molecular Dynamics Simulations of Hydrocarbon Oxidation," J. Phys. Chem. A, vol. 112, no. 5, pp. 1040–1053, 2008.

[21] K. Momma, F. Izumi, "VESTA 3 for Three-Dimensional Visualization of Crystal, Volumetric and Morphology Data," J. Appl. Crystallogr., vol. 44, no. 6, pp. 1272–1276, 2011.

[22] S.M. Eichfeld, L. Hossain, Y.-C. Lin, A.F. Piasecki, B. Kupp, A.G. Birdwell, R.A. Burke, N. Lu, X. Peng, J. Li, A. Azcatl, S. McDonnell, R.M. Wallace, M.J. Kim, T.S. Mayer, J.M. Redwing, J.A. Robinson, "Highly Scalable, Atomically Thin WSe2 Grown via Metal–Organic Chemical Vapor Deposition," ACS Nano, vol. 9, no. 2, pp. 2080–2087, 2015.

[23] K.L. Joshi, S. Raman, A.C.T. van Duin, "Connectivity-Based Parallel Replica Dynamics for Chemically Reactive Systems: From Femtoseconds to Microseconds," J. Phys. Chem. Lett., vol. 4, no. 21, pp. 3792–3797, 2013.

[24] K.M. Bal, E.C. Neyts, "Merging Metadynamics into Hyperdynamics: Accelerated Molecular Simulations Reaching Time Scales from Microseconds to Seconds," J. Chem. Theory Comput., vol. 11, no. 10, pp. 4545–4554, 2015.

[25] K.M. Bal, E.C. Neyts, "Direct Observation of Realistic-Temperature Fuel Combustion Mechanisms in Atomistic Simulations," Chem. Sci., vol. 7, no. 8, pp. 5280–5286, 2016.

SAKARYA ÜNİVERSİTESİ
FEN BİLİMLERİ ENSTİTÜSÜ DERGİSİ

Sakarya University Journal of Science
SAUJS

e-ISSN 2147-835X Period Bimonthly Founded 1997 Publisher Sakarya University
http://www.saujs.sakarya.edu.tr/

Title: Reliability Analysis of Sakarya Area Electricity Distribution System

Authors: Adem TAŞIN, Türker Fedai ÇAVUŞ

Recieved: 2021-05-03 00:00:00

Accepted: 2022-02-27 00:00:00

Article Type: Research Article

Volume: 26
Issue: 2
Month: April
Year: 2022
Pages: 292-299

How to cite
Adem TAŞIN, Türker Fedai ÇAVUŞ; (2022), Reliability Analysis of Sakarya Area Electricity Distribution System. Sakarya University Journal of Science, 26(2), 292-299, DOI: 10.16984/saufenbilder.932219
Access link
https://dergipark.org.tr/tr/journal/1115/issue/69580/932219

New submission to SAUJS
http://dergipark.gov.tr/journal/1115/submission/start

Sakarya University Journal of Science 26(2), 292-299, 2022

Reliability Analysis of Sakarya Area Electricity Distribution System

Adem TAŞIN*[1], Türker Fedai ÇAVUŞ[1]

Abstract

Power system reliability is an important issue for providing minimal loss of service to each user. It is accepted that almost 90% of power outages are caused by failures in the Electricity Distribution System. In this study, the reliability analysis of the Alancuma feeder belonging to the Sakarya distribution system was aimed. The reliability assessment of the feeder was made using the analytical approach, Monte Carlo simulation (MCS) technique and ETAP (Electrical Transient and Analysis Program) software, and the results were observed to be close to each other. The most commonly used SAIFI and SAIDI system indices were evaluated according to the Turkey average and the reasons for the interruption for the feeder were investigated.

Keywords: Reliability, Monte Carlo Method, distribution system.

1. INTRODUCTION

Although there are many definitions of reliability, the widely accepted view is that the device/system will be able to fulfill the purpose expected of it under operating conditions for a certain period of time [1].

Reliability techniques for future design, planning, control and Operation help to evaluate electrical power systems [2].

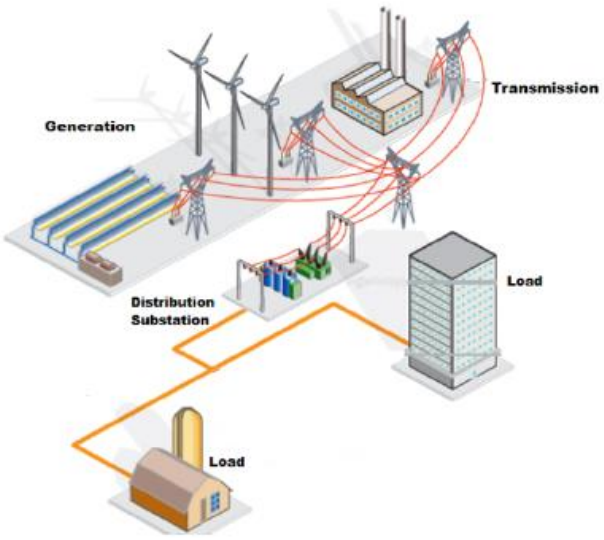

Figure 1 Structure of a Power System

* Corresponding author: ademtasin@gmail.com
[1] Sakarya University, Faculty of Engineering, Electrical-Electronics Engineering
E-mail: tfcavus@sakarya.edu.tr
ORCID: https://orcid.org/0000-0002-6222-9842, https://orcid.org/0000-0003-1399-8044

Considering the electrical energy system as a whole, it can be divided into three basic parts: generation, transmission and distribution [3].

Since electrical energy systems are large and complex, as well as reliability indices and types of failures for each level vary, reliability analysis for the entire system is very difficult

Therefore, electrical energy systems are divided into 3 hierarchical levels at the point of reliability evaluation. The first level is related to the production phase and the ability to meet demand power. The second level examines the situation in which energy can be produced and delivered to the main reducer substations to cover the production and transmission stages. The third level evaluates all stages of generation, transmission and distribution [4-5].

The effect of Index results obtained at the second level on load point indices is explained by statistics that it is around 1%. Therefore, both the impact of indices obtained from the first and second level regions on the analysis of customer load point indices is negligible, as well as the large and complex size of the system, which includes all three levels, when evaluating reliability at the distribution level, the indices of generation and transmission levels are omitted [6].

2. DISTRUBITION SYSTEM RELIABITIY

Distribution system reliability analysis is performed by calculating the necessary indices for user load points. The classic concept uses three basic indices parameters for reliability indices. These indices are commonly referred to in Billiton's book [3] as the average failure rate (λ), the average outage time (r), and the average annual outage time (U). It is also worth noting that these indices are expected or average values, not deterministic values [3].

2.1. Distribution Reliability İndices

In a research project of EPRI (Electric Power Research Institute), it has been determined that customer-indexed reliability indices are the most commonly used indices [4].

In general, these indices in the literature;

1. Customer-oriented indices,
2. Load and energy-oriented indices,
3. Cost-oriented and other indices.

It is divided into groups as [7].

2.1.1. Customer Oriented İndices

SAIFI (System Average Interruption Frequency Index)

$$\text{SAIFI}=\frac{\sum \lambda_i N_i}{\sum N_i} \quad \textit{(Interruption/customer yr.)} \qquad (1)$$

Where λ_i is the failure rate and *Ni* is the number of customers of load point *i.*

SAIDI (System Average Interruption Duration Index)

$$\text{SAIDI}=\frac{\sum U_i N_i}{\sum N_i} \textit{ (hour/customer.year)} \qquad (2)$$

Where U_i is the annual outage time and *Ni* is the number of customers of load point *i.*

CAIDI (Customer Average Interruption Duration Index)

$$\text{CAIDI}=\frac{\sum U_i N_i}{\sum \lambda_i N_i} \textit{ (Hour/customer interruption)} \qquad (3)$$

(Hour/customer interruption)

ASAI (Average Service Availability Index)

$$\text{ASAI}=\frac{\sum N_i*8760-\sum U_i N_i}{\sum N_i*8760} \textit{ (p.u)} \qquad (4)$$

ASUI (Average Service Un-availability Index)

$$\text{ASUI} = 1 - \text{ASAI}=\frac{\sum U_i N_i}{\sum N_i*8760} \textit{ (p.u)} \qquad (5)$$

Where 8760 shows the total time (hour) value in a calendar year.

2.1.2. Load and Energy Oriented İndices

ENS (Energy Not Supplied Index)

$$ENS = \sum L_{a(i)} U_i \quad (KWh/yr.) \tag{6}$$

Where $L_{a(i)}$ is the average load connected to load point i.

AENS (Average Energy Not Supplied Index)

$$AENS = \frac{\sum L_{a(i)} U_i}{\sum N_i} \quad (KWh/customer\ yr.) \tag{7}$$

2.2. Methods for Distribution Reliability Analysis

2.2.1. Analytical Approach

In the study, it was accepted that system components are connected to each other in series when calculating indices. In this method, the average failure rate, the average repair time and the average annual outage time indices for each load point are given by the following equations [4].

$$\lambda_s = \sum \lambda_i \tag{8}$$

$$U_s = \sum \lambda_i . r_i \tag{9}$$

$$r_s = \frac{U_s}{\lambda_s} = \frac{\sum \lambda_i . r_i}{\sum \lambda_i} \tag{10}$$

2.2.2. Monte Carlo Simulation (MCS) Method

Monte Carlo simulation method is a simulation technique using probabilistic distributions [8].

This simulation technique is generally based on three basic levels. First, a set of random numbers is created in the specified range, and second, according to the desired method of probabilistic distribution of these numbers (Exponential distribution) probabilistic distribution is made, third, the results are obtained by repeating the targeted number of operations.

For the time-sequential simulation technique, realistic artificial working/repair history of the relevant system elements are needed [11]. This artificial history is generated using the random number generator and the probability distribution of the error and repair parameters of the element. The reliability indices of the system and the probabilistic distribution of these indices are obtained from the artificial history of the system [9].MCS helps in building an artificial history for each component operation for a simulation time, which was set in this work to be 10000 years.

Roy BILLINTON and his team compared the reliability indices results [8] found by applying analytical methods to the RBTs test system with the results found by Monte Carlo simulation method in their study, and showed that he achieved results close to analytical results.

2.2.3. Reliability Assessment Tool in ETAP

ETAP (Electrical Power System Analysis & Operation Software) is a simulation program in which analysis is performed and reported in different modules within the scope of IEC and ANSI standards in electrical power systems [10].

Load flow analysis module, short circuit analysis module, harmonic analysis module, etc. in addition to its modules, there is a reliability assessment module. With the reliability module in the program, the reliability indices of the system created in a one-line diagram can be calculated.

Reliability analysis studies are also available with different software such as ETAP. For example the effect of automatic reclosers on distribution network system was examined using [12] analytical technique. This application is made with DISREL software. And 11kV Karberey-Ramety Feeder-II DIgSILENT software was used for reliability analysis of the electrical power distribution system [13].

3. RESEARCH METHODOLOGY

The purpose of this research work reliability analysis of the Alancuma feeder of the Kozluk (Figure 2) region belonging to the Sakarya distribution system.

First, an analytical calculation of the reliability analysis of the selected feeder is performed, second, a simulation calculation is performed with MCS, and third, the feeder is modeled in the ETAP, and the reliability analysis of the feeder is performed, and then the results found are compared.

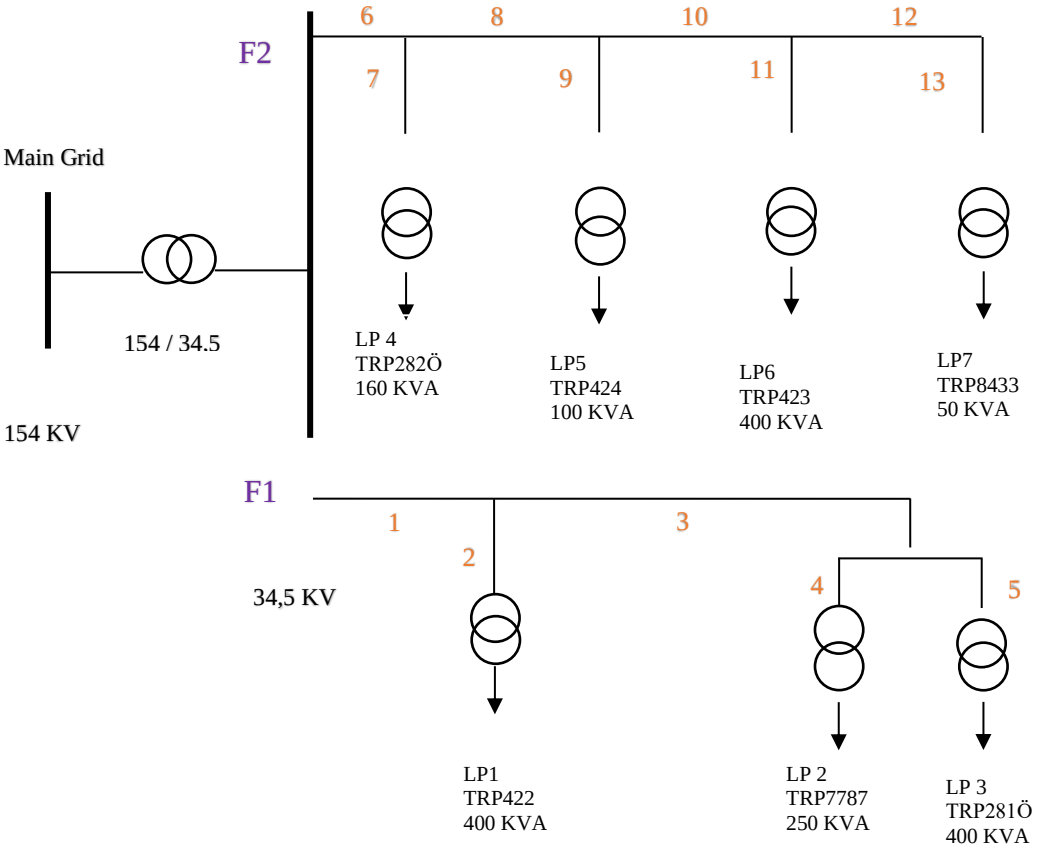

Figure 2 One-Line Diagram of Alancuma Feeder

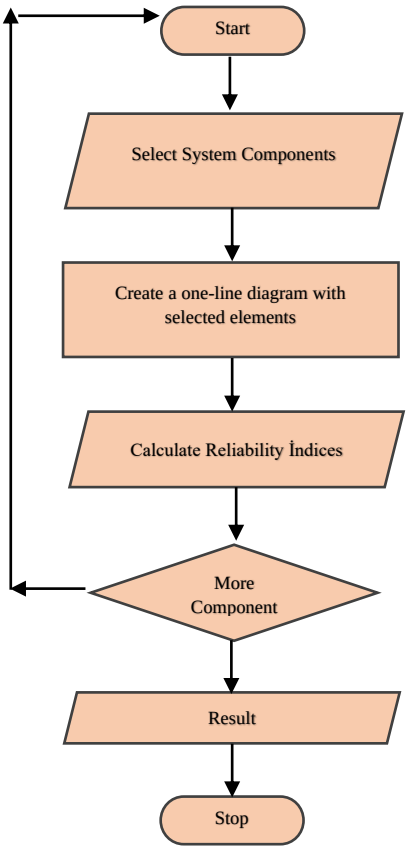

Figure 3 Flow Chart for Calculation of Reliability

Figure 3 shows the flowchart of the feeder in the ETAP software.

From SEDAŞ data [14], the average failure rate, average outage time and average annual unavailability are calculated from the last five-year interruption occurrences and outage durations of Alancuma feeder.

Table 2 shows the average failure rate, average downtime and average annual unavailability indices calculated according to Table 1 and SEDAŞ data [14].

Table 1 Details of the system of Fig. 2

Load Point	Number of Customers	Average load demand (kW)
LP 1	203	368
LP 2	1	225
LP 3	1	372
LP 4	1	139,2
LP 5	112	92
LP 6	20	296
LP 7	7	32,7

Table 2 Reliability parameters for system of Fig. 2

F1				
Component Section	Length (km)	λ (f/yr)	r (hours)	U (hours/yr)
1	0,0579	0,4016	0,1141	0,0458
2	0,0270	0,1875	0,0533	0,0100
3	0,2073	1,4373	0,4086	0,5873
4	0,0781	0,5416	0,1539	0,0833
5	0,0767	0,5317	0,1511	0,0803
F2				
Component Section	Length (km)	λ (f/yr)	r (hours)	U (hours/yr)
6	0,2276	1,5782	0,4486	0,7080
7	0,0638	0,4423	0,1257	0,0556
8	0,7743	5,3673	1,5257	8,1892
9	0,0173	0,1200	0,0341	0,0040
10	0,4000	2,7728	0,7882	2,1856
11	0,1361	0,9437	0,2682	0,2532
12	0,6656	4,6137	1,3115	6,0510
13	0,3455	2,3951	0,6808	1,6307

From the indices in Table 1, the complete reliability indices of the system have calculated.

Table 3 shows the reliability indices of the system calculated by analytical, MCS and ETAP.

Table 3 System Indices

System Indices	Analytical	MCS	ETAP
SAIFI	21,33	21,3359	21,3282
SAIDI	19,88	19,8554	19,9023
CAIDI	0,932	0,93061	0,933
ASAI	0,9977	0,99773	0,9977
ASUI	0,0022	0,00226	0,00227
ENS	30322	30277,4	30371
AENS	87,89	87,76	90,7

SAIFI- (interruption/cust.yr) ENS- (kWh/yr)
SAIDI- (hours/cust.yr) AENS- (kWh/cust.yr)
CAIDI- (hours/cust..interp.) ASAI (p.u)

The study showed that analytical, simulation and modeling results are very close to each other.

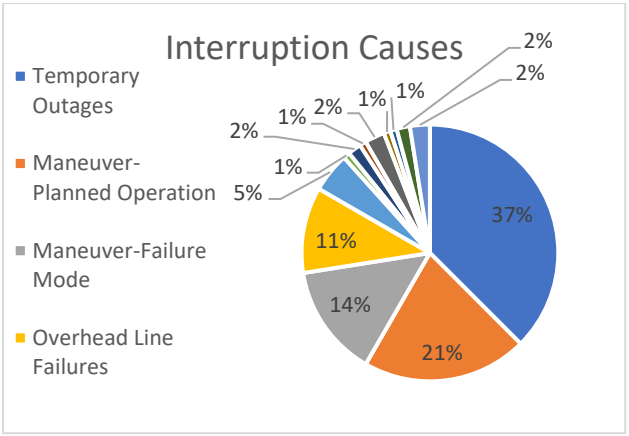

Figure 4 Interruption Causes of Alancuma Feeder

It is seen that the highest reason for interruption is temporary outages with 37%. This is followed by planned maintenance work with 14%.

4. CONCLUSION

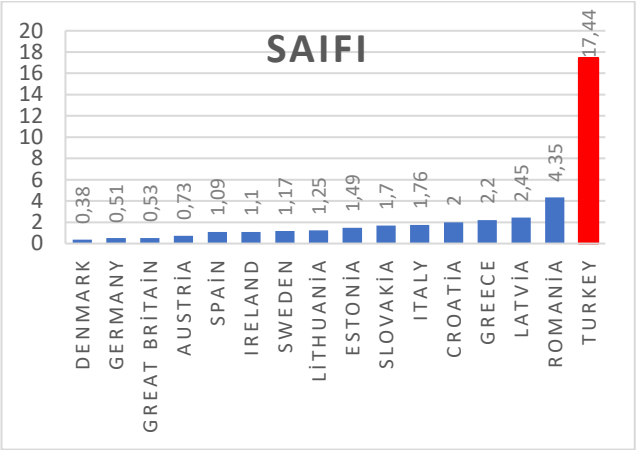

Figure 5 2019 SAIFI values of Turkey and Other Countries [15].

TEDAŞ 2019 activity report [15] on Turkey and other European countries compared SAIFI and SAIDI values. As shown in the Figure 5 and Figure 6, the values of SAIFI and SAIDI which the two most used indices are higher in our country compared to other countries.

It was observed that the SAIFI value of the Alancuma feeder was above the average of Turkey, and the SAIDI value was below the average.

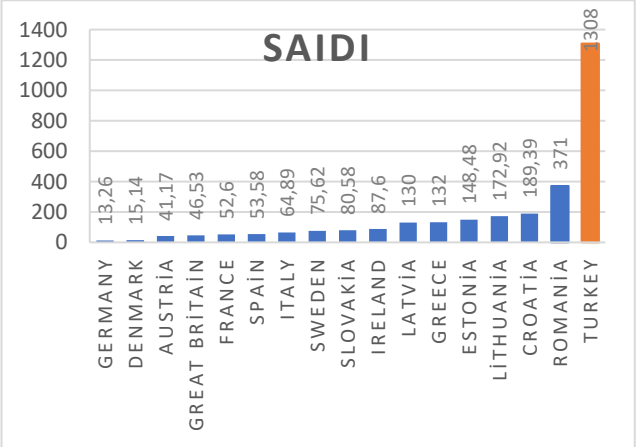

Figure 6 2019 SAIDI (minutes/customer yr.) Values of Turkey and Other Countries [15].

Acknowledgments

The authors would like to thank the valuable managers and employees of SEDAŞ Technical Academy Department for their assistance in obtaining and using the data used in the paper.

Funding

The authors has no received any financial support for the research, authorship or publication of this study.

The Declaration of Conflict of Interest/ Common Interest

No conflict of interest or common interest has been declared by the authors.

The Declaration of Ethics Committee Approval

This study does not require ethics committee permission or any special permission.

The Declaration of Research and Publication Ethics

The authors of the paper declare that they comply with the scientific, ethical and quotation rules of SAUJS in all processes of the paper and that they do not make any falsification on the data collected. In addition, they declare that Sakarya University Journal of Science and its editorial board have no responsibility for any ethical violations that may be encountered, and that this study has not been evaluated in any academic publication environment other than Sakarya University Journal of Science.

REFERENCES

[1] R. Billinton, and R.N. Allan “Reliability evaluation of engineering systems: concepts and techniques,” 2nd ed. New York: Plenum Press, xvi, pp. 6–7, 1992.

[2] Isa S. Qamber, “Power systems control and reliability: electric power design and enhancement” Apple Academic Press, 2020

[3] R.E., Brown, "Electric power distribution reliability," 2nd ed. Power engineering. New York: Marcel Dekker, xvi, pp.17–19, 2009.

[4] R.N., Allan, "Reliability evaluation of power systems," 2nd ed. Springer Science & Business Media, pp. 10–13, 2013.

[5] R., Billinton, and L. Goel. Overall adequacy assessment of an electric power system. in IEE Proceedings C (Generation, Transmission and Distribution), " IET. Vol. 139, Issue 1, pp. 57– 63, 1992.

[6] R. Billinton and R. N. Allan, Reliability Assessment of Large Electric Power System. Boston: Kluwer Academic Publishers, 1988.

[7] Transmission and Distribution Committee. (2003). IEEE Guide for Electric Power Distribution Reliability Indices. *IEEE Std*, *1366*, 2003.

[8] Faulin, J., et al., "Simulation methods for reliability and availability of complex systems," Springer Science & Business Media, 2010.

[9] R. Billinton, and P.J.I.T.o.P.S. Wang, "Teaching distribution system reliability evaluation using Monte Carlo simulation," 14(2): pp. 397-403, 1999.

[10] ETAP 11.1 User Guide, pp.30/1–30/45 January 2012.

[11] C., Bhargava, & P. S. R. . Murty, Reliability evaluation of radial distribution system using analytical and time sequential techniques. In *2016 7th India International Conference on Power Electronics (IICPE)* IEEE, pp. 1-6, 2016.

[12] T. M., Aljohani, & M. J. Beshir, "Distribution system reliability analysis for smart grid applications," Smart Grid and Renewable Energy, 8(7), pp. 240-251, 2017.

[13] K. R., Puri, A. B. Subba, K. Pelden,, & R. Chhetri, "Reliability Assessment of Distribution System through Cost Analysis," International Journal of Scientific Research and Engineering Development (IJSRED), vol. 3,pp. 560-565, 2020.

[14] https://www.sedas.com/tr-tr/Bilgi_Danisma/Pages/Tablo1.aspx [Accessed-25-April- 2021]

[15] https://ww.tedas.gov.tr/sx .web.docs/tedas/docs/Stratejikplan/2019_Turkiye_Dagitim_Sektor_Raporu_16430543.pdf [Accessed-26-April- 2021]

SAKARYA ÜNİVERSİTESİ
FEN BİLİMLERİ ENSTİTÜSÜ DERGİSİ

Sakarya University Journal of Science
SAUJS

e-ISSN 2147-835X Period Bimonthly Founded 1997 Publisher Sakarya University
http://www.saujs.sakarya.edu.tr/

Title: Changes in Food Supply and Consumption Practices of People in Turkey During the COVID-19 Pandemic

Authors: Hatice SIÇRAMAZ, Güliz HASKARACA, Yusuf ARSLAN

Recieved: 2021-09-22 00:00:00

Accepted: 2022-02-28 00:00:00

Article Type: Research Article

Volume: 26
Issue: 2
Month: April
Year: 2022
Pages: 300-312

How to cite
Hatice SIÇRAMAZ, Güliz HASKARACA, Yusuf ARSLAN; (2022), Changes in Food Supply and Consumption Practices of People in Turkey During the COVID-19 Pandemic. Sakarya University Journal of Science, 26(2), 300-312, DOI: 10.16984/saufenbilder.999233
Access link
https://dergipark.org.tr/tr/journal/1115/issue/69580/999233

New submission to SAUJS
http://dergipark.gov.tr/journal/1115/submission/start

Sakarya University Journal of Science 26(2), 300-312, 2022

Changes in Food Supply and Consumption Practices of People in Turkey During the COVID-19 Pandemic

Hatice SIÇRAMAZ[1], Güliz HASKARACA*[1], Yusuf ARSLAN[2]

Abstract

The COVID-19 pandemic has had social and economic impacts on every country in the world and has caused significant changes in human nutrition. In this study, changes in the food supply chain and consumption practices before and after the controlled normalization of people living in Turkey were examined, with a survey of 1087 people. The results revealed that people focused on a healthier diet during the pandemic. The increase in dietary supplement consumption has not been too high, only 11% of people started to take dietary supplements, but fast food consumption had a sharp fall. The packaging has become more critical. People continued to use take-out services from supermarkets and fast-food restaurants. Although normalization has begun, most of them (90%) reduced or did not think about eating out until COVID-19 will over. This study revealed the effects of the pandemic on human nutrition and showed which direction the food supply should go.

Keywords: Pandemics, coronavirus, nutritional supplements, consumption habits

1. INTRODUCTION

The new coronavirus disease (COVID-19) is a highly transmittable and pathogenic viral infection caused by severe acute respiratory syndrome coronavirus 2 (SARS-CoV-2) that has started to affect the whole world in the last months of 2019 and still continues [1]. This disease was declared a pandemic on March 11, 2020 [2]. Many business sectors have been affected positively or negatively by the COVID-19 pandemic depending on sector and region [3, 4]. However, the literature data obtained from google searches, sectoral communications, unemployment rates, and surveys have shown that the COVID-19 pandemic has had significant adverse effects on the economy of countries [5-9]. Within that period, the food sector was one of the most negatively affected sectors by the COVID-19 pandemic. Restaurants and fast food points were closed and were only permitted take-out services with the curfews. Besides, education was paused in education units, and many workplaces switched to remote work. As expected, with a change in the daily hassle and "staying at home" calls people's eating routines changed. Individuals who had previously eaten their meals outside started to prepare their meals at home. On the

* Corresponding author: gyaldirak@sakarya.edu.tr
[1] Sakarya University, Faculty of Engineering, Department of Food Engineering
E-mail: haticesicramaz@sakarya.edu.tr
ORCID: https://orcid.org/0000-0002-5943-9566, https://orcid.org/0000-0002-4641-886X,
[2] Sakarya University, Faculty of Busines, Management Department
E-mail: yusufarslan@sakarya.edu.tr
ORCID: https://orcid.org/0000-0002-1873-7567

other hand, the first wave of the COVID-19 pandemic was a situation that the current generation encountered for the first time. This emerging situation has created an unusual situation for both Turkey and other countries in the world [10, 11]. In the face of this sudden situation, the media frequently published nutritional suggestions which are necessary or helpful to avoid the disease. And not only do people tend to obey these instructions, but also, they spread them from social media accounts to be beneficial to others. But, how are this information and instructions affect people? How were food consumption habits affected by this chaotic environment? Studies seeking answers to these questions from many countries have started to be published. The current study aimed to contribute to the studies on the subject and to reveal the changes in the food supply chain and food consumption habits of individuals living in Turkey.

Food consumption habits of people have changed during the pandemic. For example, a study carried out by Marty et al. [12] revealed that during the curfews in France, people's moods in food choices were much more critical than in the previous periods. Out of 48% of the 938 people who participated in their study pointed out that the convenience of preparing meals was less important now. In addition, in the same survey, 26% and 29% of participants reported that a healthy diet and not gaining weight were more important comparing the previous, respectively. To understand the change in consumption habits before and after the COVID-19 pandemic in underdeveloped countries of Africa, two other researches were carried out in Sudan in 2017 and 2020. The results had shown that while cereal and milk were preferred on day and night before 2020, fish and other seafood were started to be preferred in 2020. Similar results were obtained in research on Tanzania [13, 14]. In Italy, one of the countries most affected by the COVID-19, it was observed that people did not eat breakfast but had a late snack before the COVID-19 pandemic, however in 2020, most people prefer a healthy breakfast enriched with green vegetables [15, 16].

On the other hand, fast food is one of the most consumed ready-to-eat meals among young people, especially those between the ages of 18-35. The survey conducted by Mediabrands Insight company with 2500 participants stated that fast-food consumption was caused by starving [17]. Within the daily routine, people were eating fast foods in order to save time and reach or eat food in a very short time period as soon as possible. However, with the effects of curfews, the closure of restaurants and fast-food points, and a slowing of daily bustle, it is estimated that there is a sharp decrease in the consumption of ready meals. Determining the level of these decreases is of great importance both for determining the effects of the pandemic on the fast-food sector and for determining the changes in consumers' eating tendencies.

According to a survey of Turkish Statistical Institute [18], before the pandemic, the most commonly consumed food group in Turkey was bread and other cereals with a proportion of 19.9%, followed by vegetables (18.8%) and protein-rich foods - meat, fish and other seafood (17.3%). However, with the COVID -19 pandemic, the food consumption habits of Turkish adults may have changed, as in other countries. On the other hand, although people's eating and food supply habits have changed during the COVID-19 pandemic, an investigation by Sheth [19] revealed that governments' normalization steps brought back eating out habits. In line with this knowledge, our study aimed to evaluate Turkish people's food supply and food consumption practices before and after the COVID-19 pandemic and assess the extent of this change. Evaluating the study results will contribute to the roadmap to be followed in the food consumption chain during the pandemic period.

2. MATERIAL AND METHODS

In the current study, a questionnaire study was administered to determine the changes in food supply and consumption practices of people living in Turkey during the COVID-19 pandemic. For that purpose, an online method was used for the data-gathering processes. An online survey

was created using Google Forms, forms and the questionnaire link was disseminated through the connections of the authors. Links were restricted so that they cannot be accessed twice from the same IP. People who had the link were also asked to feel free to share it with their friends and family so that the sample would have maximum diversity. As expected, it was not possible to reach people face to face during the lockdown period, so the study was carried out with people who can be reached online. An online survey was carried out with the approval of the Sakarya University Ethics Committee between the 20th and 27th of July 2020 in Turkey, with the attendance of 1087 usable questionnaires, for people over the age of 18. In total, 32 different questions (including both multiple-choice questions and open-ended questions) were asked to the participants to determine the demographical information of the sample group, changes in consumption practices, weight changes during pandemic, hygienic rules followed during purchase, use of take-out services, consumption advices of World Health Organization [20]. The questions asked to the participants within the scope of the study are given in Table 1. The data were analyzed through descriptive statistics and chi-square analyses by using the IBM SPSS version 20 statistic program (IBM Corporation, Armonk, NY) (IBM Corp, 2011).

Table 1 Questions in the survey

	Questions
Demographical Information	What is your gender?
	How old are you?
	What is your marital status?
	What is your educational status?
	Where do you live in?
	How do you evaluate your economic status?
Questionnaire	Was there any change in your food consumption practices during the pandemic COVID-19?
	If there were changes, can you describe?
	Did you gain weight in the last 5 months? Please choose the appropriate option.
	Did you take supplements during the pandemic?
	Please choose the option that best reflects your preference to purchase packaged food products from the market before the COVID-19 outbreak.
	Has your preference for purchasing packaged food products changed after the COVID-19 outbreak (during and after the pandemic)?
	During the COVID-19 pandemic, did you pay attention to purchase your bread in packages?
	Choose the answer that best reflects your opinion about your bread purchases during the COVID-19 pandemic.
	During the COVID-19 pandemic, did you pay attention to the packaging of the meat and meat products that you purchase?
	Choose the answer that best reflects your opinion on meat and meat product purchases during the COVID-19 pandemic.
	Were there any products you suspected while consuming during the pandemic?
	Which product and / or products did you suspect?
	Is there a food group that you have difficulty to obtaining during the pandemic?
	If yes, what is the category of this product?
	Are there any food product(s) you gave up buying during the COVID-19 outbreak?
	If there are product(s) you gave up, what are they?
	What is your reason for giving up?
	Do you take care to choose corporate, well-known brands in the products you will purchase during COVID-19?
	Have you used take-out services on food products before the normalization process started?
	If you have used the services, which product group(s) did you prefer?
	Have you used take-out services in your food shopping after the normalization process started?
	If so, which product(s) did you prefer?
	Do you care about the compliance with the hygiene rules while choosing the opened cafes, restaurants, etc.?
	Please mark the option that best reflects your opinion about eating in food consumption areas (cafe, restaurant, etc.) considering the COVID-19.
	Have you read the 'healthy eating recommendations for adults' published by the World Health Organization (WHO) during the COVID-19 pandemic?
	How carefully did you pay attention to these published suggestions?

3. RESULTS AND DISCUSSION

3.1. Participants' demographical information

The results of a survey with 1087 participants living in Turkey were evaluated in this study. The gender distribution of the people participating in the study was 641 women and 446 men. The percentage of the age group of the participants was 44% for 18-25, 29% for 26-35, 17% for 36-45, 8% for 46-55, and 2% for 56 and above. A great majority of the participants, with 75%, had a university or higher degree. Half of them were living in the metropolis, and 95% of these people

described their economic situation as a medium, good or excellent.

3.2. Changes in eating habits of participants and preferences of packaged foods

The COVID-19 pandemic has caused significant changes in daily life. These necessarily experienced changes have brought about adaptation problems in many areas. The most important of these changes is eating habits [21]. During the quarantine period, factors such as stress, anxiety, anger, low mood, insomnia, and restrictions on access to food have changed the eating habits of individuals. The hypothalamic-pituitary-adrenal axis, which regulates stress responses, also regulates nutritional responses because the neural circuits that regulate food intake converge in the paraventricular nucleus. Since the systems controlling food intake and stress responses share the same anatomy, each system can affect the other. It is known that stress changes nutritional responses in both an increase and a decreasing manner [22].

Out 46% of 1087 participants reported that their eating habits were not affected by the COVID-19 pandemic, while 54% of them said that their eating habit was affected. When our survey results were examined according to the Chi-Square test, it was seen that there is a statistically significant relationship between the gender of the participants and the change in their eating habits within the COVID-19 period ($\chi 2(1) = 35.659$, $p<0.001$). According to these results, it can be said that, within the COVID -19 period, there has been a greater chance for female participants (61.6%) than the male participants (43.3%) in terms of their eating habits.

The change in eating habits is shown in Figure 1. In total, 37% of the participants consumed a healthier and more balanced diet, while 21% started to eat more pastries. The outbreak oriented most people to a more nutritious diet, but a large group opted for a less healthy, carbohydrate-heavy unbalanced diet. Eftimov et al. [23] concluded that frequencies of salt, fat/oil, and sweet products have decreased and consumption of fruits and vegetables has increased during the quarantine in almost all countries. McAtamney et al. [24] conducted a study to determine the effects of emotional dysregulation on eating habits during COVID-19 in the United Kingdom. As a result of that study, it was found that the majority of the participants (58.1%) did not change the amount of food they ate compared to before COVID-19, 16.2% ate less on average, and 25.7% ate more [24]. Conformably, Chenarides et al. [25] reported that 60% of the participants ate the same amount of food as compared before while 13% of them ate less, and 20% of them ate more, among the 861 people living in the United States. Besides, 4 % of the participants reported that they started to consume more junk food than compared in the period before the pandemic. Some of the people with uncontrolled free time at home may be addicted to junk food. This situation may have occurred because people had to stay at home for a long time against their will and did not know how to spend time at home. On the other hand, junk food consumption could be changed according to country, even within the same country. Some of the literature data conducted during the Covid-19 period have revealed that junk food consumption of people has varied during the lockdown. In these studies, between 19-45 % of the consumers reported that their junk food consumption increased, while 10-28 % of the consumers reported that their junk food consumption decreased during lockdown [26-35].

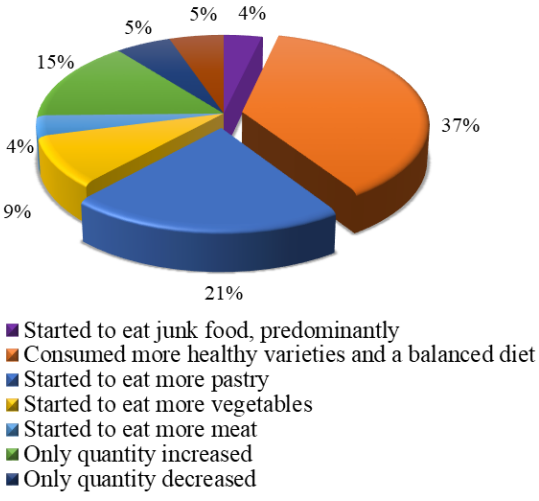

Figure 1 Change in diet during the COVID-19 pandemic

When the relationship between eating habits and age was examined according to the Chi-Square test, there was a statistically significant relationship between the age group of the participants and the change in their eating habits within the COVID-19 period ($\chi2(4) = 23.590$, $p<0.001$). According to Tamhane's T2 test results, the most important changes were observed between the "18-24" and "56 and above" groups (mean dif =0.323, $p<0.05$). There was also a statistically significant relationship between the subjective income level of the participants and the change in their eating habits within the pandemic ($\chi2(4) = 15.705$, $p <0.05$) according to the Chi-Square test results. Tamhane's T2 test results revealed that the significant changes were between the "very low" income group and all the other groups (Respectively; Low: mean dif= 0.550; $p<0.001$ / Middle: mean dif=0.561; $p<0.001$ / Good: mean dif=0.533; $p<0.001$ / Very good: mean dif=0.346; $p<0.05$).

An unbalanced and carbohydrate-heavy diet is expected to result in higher calorie intake and weight gain. During the outbreak, while 40% of the participants stated that they kept their weight, 38% gained 1-3 kg, and 18% gained 4-7 kg in the first three-month period after the pandemic started. There are more reasons to gain weight than eating, but the results in Figure 1 and the weight gaining quantities confirm each other; a balanced diet helps maintain weight. Al-Domi et al. [36] reported that, as a result of a survey that is carried out in Jordan with the attendance of 4473 responders (obese (n = 1135), normal body weight (n = 1561), and underweight (n = 116)), a significant increase was observed in the bodyweight of Jordanians. According to the study, 12.9% of underweight, 28.5% of the normal body weight, 36.4% of the overweight' and 41.1% of the obese participants gain weight during the COVID-19 quarantine.

Our results were also in accordance with the results of a study carried out by Fancourt et al. [37]. According to the study conducted by University College London with 90,000 panelists to assess the situation in the 14th week of the pandemic, it was revealed that 17% of the panelists ate more than usual, 23% of them ate healthier than usual, 40% of them gain weight while 40% of them did not gain weight. Young people and women have been most likely to change their eating habits [38].

Food supplements are sources of nutrients in concentrated forms and are regulated by the directive 2002/46/EC of the European Council [39]. Supplements do not substitute a balanced diet, but it can be concluded that those who take supplements are healthier and more conscious [40]. The nutritional supplement intake status of participants was researched in this survey. It was observed that 11% of them started to consume nutritional supplements during the pandemic, and 5% were already using supplements. According to the Chi-Square test results, there is a statistically significant relationship between the gender of the participants and their supplementary food consumption situation within the pandemic period ($\chi2(4) = 9.965$, $p <0.05$). 12.6% of the female participants stated that they started to use supplementary food, while only %9.9 of male participants said so. The ratio was also greater for females (5.9%) than males (2.5%) for the period before the pandemic. No relationship was found between the age group of the participants and their supplementary food consumption during the pandemic. ($\chi2(8) = 9.502$, $p=0.302$). The participants' educational levels did not affect their supplementary food consumption habits during the pandemic ($\chi2(6) = 6.634$; $p=0.356$). Their income levels were likewise determined to be ineffective ($\chi2(8) = 4.671$, $p=0.792$). Al-Domi et al. [37] reported that 32.7% of people did not want food intake or supplements containing antioxidants while 46% of them wanted to take, among the 4473 responders that attended their survey.

Packaging is one of the main tools to ensure food safety. It has been used for centuries and protects the product from physical, chemical, and biological damage. In the survey, participants' preferences to purchase packaged food products before the pandemic was investigated. 80% of people preferred packaged foods, and 17% did not pay attention to whether it was packaged. Of course, food safety was not the only reason to choose to package; living in the metropolis also

brought supermarkets to replace small grocery stores, which required packaging. According to the data, it was observed that most of the participants maintained their packaging preferences during the pandemic. Changes, if any, were in the direction of packaging preference. These results are shown in Table 2.

Table 2 Preferences for purchasing packaged food products after the pandemic

Has your preference for purchasing packaged food products changed after the COVID-19 outbreak (during and after the pandemic)?	**Percentage of people (%)**
No, it has not changed, I still only buy packaged food products.	50
No, it has not changed, I still only buy unpackaged food products.	8
Yes, it has changed, I started to pay attention that all the food products I buy are packaged.	37
Yes, it has changed, and I started to prefer unpackaged products.	5

3.3. Preferences for bread

Bread is the primary foodstuff in daily nutrition. Turkey is among the first countries in the world with high consumption of bread such that 199.6 kg/year consumption per person was recorded in the book Guinness World Records in the year 2000 [41]. Demirtas et al. [42] revealed in 2018 a bread consumption of 101.5 kg/year for people living in Turkey. Considering these statistics, it can be concluded that bread was the primary nutrient during the pandemic. Turkish Ministry of Agriculture and Forestry has required the use of packaging in bread in March 2020 [43]. While 60% of the participants paid attention to only buying packaged bread during the COVID-19 outbreak, the remaining 40% packaged themselves after purchasing. In Figure 2, the considerations of participants about bread packages were given in detail. The data collected showed that 13% of people did not care whether the bread was packed or not. The gender of this 13% group was 53% male and 47% female. According to the Chi-Square test results, there is a statistically significant relationship between the gender of the participants and their packed bread buying behavior habits within the COVID-19 period ($\chi2(1) = 8.452$, $p < 0.05$). According to these results, it can be said that, within the COVID-19 period, there has been a greater demand for female participants (63.5%) than the male participants (54.7%) in terms of their preference for packed bread. The ages of participants also affected their preferences for packaged bread consumption habits ($\chi2(4) = 17.150$, $p < 0.05$). The effect of the pandemic on packaged bread purchase was most seen in the 18-25 and 46-55 age groups (mean dif=0.209, $p<0.05$). The education level of the participants had no effect on the bread packaging preferences ($\chi2(3) = 3.544$, $p= 0.315$). However, the economic situation had a significant impact on this decision ($\chi2(4) = 9.595$, $p<0.05$). According to Tamhane's T2 test results, the only significant difference occurred between the "very low" and "very high" income groups (mean dif= 0.466, $p<0.05$).

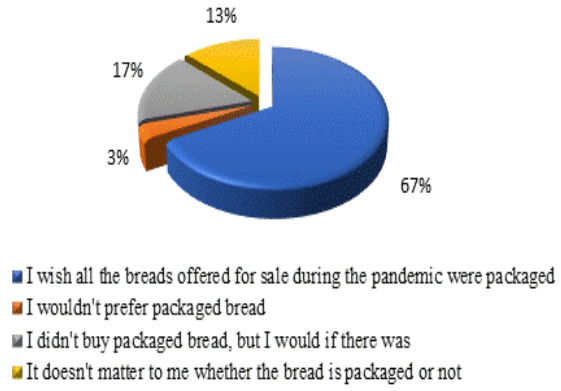

Figure 2 Considerations of the participants while purchasing bread

3.4. Preferences for meat

Meat and meat products are exposed to direct contact with butchers. They can be considered risky in terms of contamination, but fortunately, they are mostly consumed after cooking. Even so, packaging was preferred by 60% of participants in meat and meat product supply as in bread. According to Figure 3, 70% of participants preferred packaged meat and meat products,

while 10% complained that they could not find the packaged product.

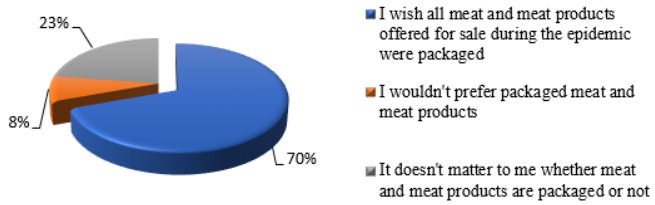

Figure 3 Considerations of the participants while purchasing meat and meat products

When the effect of demographic data on packaged meat consumption was examined, it was seen that while the gender ($\chi2(1) = 34.699$, $p<0.001$), age ($\chi2(4) = 20.071$, $p <0.001$), and education level ($\chi2(3) = 8.206$, $p <0.05$) of the participants significantly affected their consumption of packaged meat, economic income level ($\chi2(4) = 3.584$, $p=0.465$) did not. According to the Chi-Square test results, it can be said that, within the COVID-19 period, there has been a greater demand for female participants (67.6%) than the male participants (49.8%) in terms of their preference for packed meat. As a result of Tamhane's T2 test, the most significant differences were seen in the 18-25 and 26-35 age groups (mean dif=0.131, $p<0.05$). In addition, "high school graduate" and "post-graduate" participants revealed the most significant differences (Tamhane's T2 test -mean dif=0.164, $p<0.05$).

3.5. Cases of suspicion and access to food

58% of 1087 surveyed people suspected some products during the pandemic. Table 3 shows which product(s) it was. Bakery and pastry products, as well as fruits and vegetables, were found suspicious due to the possibility of direct contact. According to the Chi-Square test results, there was a statistically significant relationship between the gender of the participants and their suspicion of certain products ($\chi2(1) = 5.500$, $p <0.05$). The suspicion was higher for female participants (60.7%) than the male participants (52.9%). There was no effect of age on suspicion ($\chi2(4) = 6.961$, $p=0.138$). Educational background has had a significant effect ($\chi2(3) = 9.810$, $p <0.05$) on suspicion for "primary educated" and "post-graduate" participants (mean dif=0.241, $p<0.05$).

Table 3 Suspected food groups

Which product(s) did you suspect?	**Number of people**
Bakery products (bread and bagel)	347
Meat and meat products	206
Milk and dairy products	157
Fruits and vegetables	387
Pastry products (other than bread)	267
Others (fast foods, foreign foods, etc.)	10

Food supply is an essential factor in survival, and any inaccessibility to food during the pandemic can bring significant problems. The survey revealed an 87% availability rate of food supply during the COVID-19 outbreak. The difficultly obtained food group names are given in Table 4. The leading group was bakery products, although, in Turkey, bakeries are served at home on curfew days. However, due to the change in the order that people are accustomed to, when they went to the market, they tried to supply a large amount of flour and yeast at a time and tried to make their own bread at home. Many individuals who participated in the survey also stated that they could not find bread yeast in the market for a while.

Table 4 Difficultly supplied food groups

What is the category of difficultly obtained food during the pandemic?	**Number of people**
Bakery products (bread, bagel)	32
Meat and meat products	10
Milk and milk products	10
Fruits and vegetables	32
Nuts	6
Pastry products	15
Other (legume, yeast for bread making, etc.)	35

During the COVID-19 outbreak, 61% of the people participating in the survey did not give up purchasing any product. Fast food products were

at the top of the product groups that the remaining 421 people gave up on purchasing. The reason for this is thought to be the closure of restaurants and food supply centers during the pandemic process. Bakery products followed fast food products (Table 5). When the participants were asked about their reasons for giving up purchasing, the most given answer was observed as the suspicion of possible hygiene neglect.

Table 5 Categories of food products that were given up to purchase during the pandemic

What was the category of food product you gave up to purchase?	Number of people
Fast food products	328
Snack products	180
Bakery products (bread, bagel)	93
Meat and meat products	24
Milk and milk products	18
Fruits and vegetables	36
Nuts	52
Pastry products	209
Sugary drinks and foods	119
Tea and coffee products	20
Other	9

3.6. Preferences for the corporate status of the production and sales area and use of take-out services

Well-known companies did not lose customers due to the confidence that the risk of contamination was well managed. 81% of the surveyed people paid attention to purchasing products from corporate companies during the COVID-19 pandemic.

Before the "controlled normalization process" started, the number of participants using take-out service was 347 (32%). Fast food was the most preferred product group for take-out, as illustrated in Figure 4. It was followed by bakery and pastry products with 24%. The 16% group that marked "the other" option stated "all supermarket needs" in the explanation part of the survey. The gender ($\chi2(1) = 3.511$, $p > 0.05$) and age ($\chi2(4) = 3.947$, $p > 0.05$) of participants were not effective on these preferences. However, education level was an important factor in their preference for well-known brands during the pandemic ($\chi2(3) = 12.587$, $p < 0.05$). The most significant differences were obtained for "high school graduate" and "post-graduate" participants (mean dif=0.146, $p<0.05$).

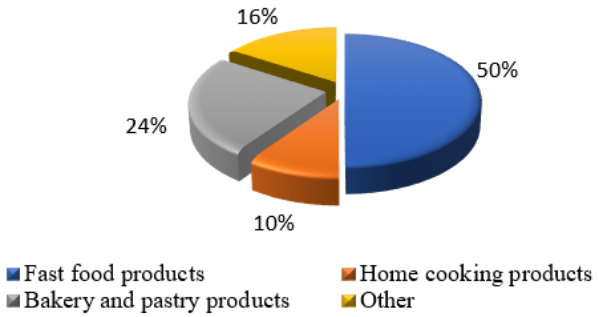

Figure 4 Take-out service product groups preferred by participants before the normalization process begin

With controlled normalization, people mostly returned to their social lives, restaurants were opened, and the demand for take-out service decreased from 32% to 29%. During the controlled normalization period, it was observed that the interest in fast food continued to a rise (Figure 5).

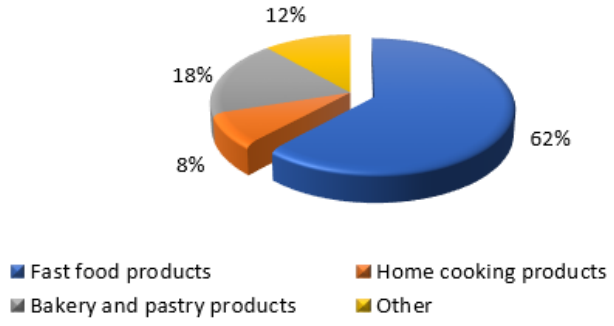

Figure 5 Take-out service product groups preferred by participants after the normalization began

3.7. Observing the effects of compliance with hygiene rules

Most of the participants (94%) paid attention to the compliance to hygiene rules of food consumption areas opened with normalization. In fact, the possibility of foodborne transmission of COVID-19 is considered negligible yet [43]. However, 66% of the participants stated that they

did not consider eating out during the pandemic (Figure 6). According to analyses, there was a statistically significant relationship between the gender of the participants and their consideration of hygiene policies while choosing between the restaurants ($\chi2(2) = 14.060$, $p < 0.05$). It was observed that hygiene was a more important factor for female participants (86.4%) than the male participants (77.8%) in terms of their restaurant preferences. However, the age ($\chi2(8) = 10.050$, $p > 0.05$) and educational background ($\chi2(6) = 5.373$, $p > 0.05$) did not have a significant effect.

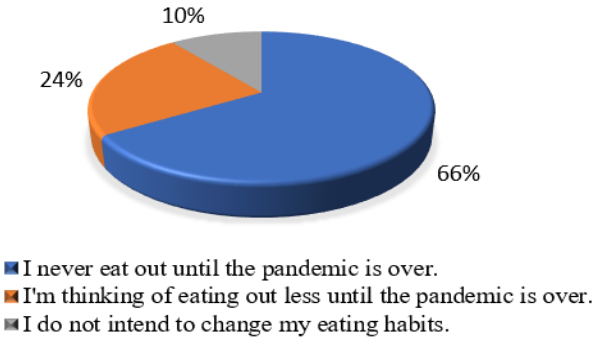

Figure 6 Decision about eating in food consumption areas due to the COVID-19 pandemic

3.8. Attention to the guidelines of WHO about eating habits

Butler & Barrientos [44] summarized the impact of diet on COVID-19 and claimed that a healthy diet reduces the possibility of getting COVID-19 disease. WHO has published practical advice on maintaining a healthy diet to reduce the susceptibility of COVID-19. However, 68% of the participants stated that they did not hear these recommendations. Besides, only 42% of those who are aware of the recommendations practiced them. Also, as demonstrated in Section 3.2 and in Figure 1, 37% of the surveyed people stated that they started to consume healthier foods and take care of eating a healthy diet after the covid-19 period. The gender ($\chi2(1) = 1.414$, $p > 0.05$) and education level ($\chi2(3) = 0.929$, $p > 0.05$) of the participants did not affect the results. However, their age ($\chi2(4) = 12.622$, $p < 0.05$) and economic status ($\chi2(4) = 10.119$ $p<0.05$) had important effects on their attention to WHO's suggestions regarding healthy nutrition during the COVID-19 pandemic.

4. CONCLUSIONS

The survey with 1087 participants living in Turkey revealed that, during the COVID-19 pandemic, there were no vast problems with the food supply. The survey revealed that take-out services were used generally for fast food products before the pandemic. The consumption of fast food decreased significantly during the COVID-19 pandemic, but still, the services were used to purchase. The total take-out service usage was 32% of participants during the pandemic, and the rate decreased to 29% in the controlled normalization period.

Although most people were not aware of the recommendations of WHO, they focused on a healthier diet by regulating daily nutrients. Also, most of them did not take any additional dietary supplements. While 30% of the participants stated that they gave up fast food consumption, 19% left pastry products, 17% left snacks, and 11% left sugary products. There has been an increasing trend in packaged product purchases.

It was also exhibited that, although normalization has begun, most people do not consider eating outside until the pandemic is over. The study revealed the food supply and consumption practices of people in Turkey during the COVID-19 pandemic. It is estimated that the results will demonstrate the current situation and guide the precautions to be taken.

Acknowledgments

We thank to Betül Kutanis, Ebubekir Genc, Eda Nur Samancı, Ercan Kurtaran, Feyza Sağlam, Harbin Shantır and Rümeysa Sevindik for their helps in collecting survey data.

Funding

The author (s) has not received any financial support for the research, authorship, or publication of this study.

The Declaration of Conflict of Interest/ Common Interest

No conflict of interest or common interest has been declared by the authors.

REFERENCES

[1] M. A. Shereen, S. Khan, A. Kazmi, N. Bashir and R. Siddique. "COVID-19 infection: Origin, transmission, and characteristics of human coronaviruses", J Adv Res., vol. 16, no. 24, pp. 91-98. 2020.

[2] World Health Organization (WHO). "WHO Director-General's opening remarks at the media briefing on COVID-19", Retrieved Juy 25, 2020, from https://www.who.int/dg/speeches/detail/who-director-general-s-opening-remarks-at-the-media-briefing-on-covid-19---11-march-2020.

[3] C. Ang. "The Economic Impact of COVID-19, According to Business Leaders", Visualcapitalist, Published on December 29, 2020. Retrieved from: https://www.visualcapitalist.com/economic-impact-covid-19/. 2020.

[4] World Economic Forum. "The economic effects of COVID-19 around the world. Written by: Rosamond Hutt, 17 Febuary 2020", Retrieved from: https://www.weforum.org/agenda/2020/02/coronavirus-economic-effects-global-economy-trade-travel/. 2020.

[5] A. Goolsbee and C. Syverson. "Fear, lockdown, and diversion: Comparing drivers of pandemic economic decline", Journal of Public Economics, 193, 104311. 2020.

[6] L. Hensvik, T. L. Barbanchon and R. Rathelot. "Job search during the COVID-19 crisis", Journal of Public Economics, vol. 194, 104349, 2021.

[7] R. Padhan and K. P. Prabheesh. "The economics of COVID-19 pandemic: A survey", Economic Analysis and Policy, vol. 70, pp. 220-237. 2021.

[8] K. A. Abay, K. Tafere and A. Woldemichael. "Winners and Losers from COVID-19: Global Evidence from Google Search", World Bank Policy Research Working Paper No. 9268, Retrieved July 20, 2020 from https://ssrn.com/abstract=3617347. 2020.

[9] N. Fernandes. "Economic Effects of Coronavirus Outbreak (COVID-19) on the World Economy", IESE Business School Working Paper No. WP-1240-E, Available at SSRN: https://ssrn.com/abstract=3557504. 2020.

[10] N. Gencer. "Being elderly in COVID-19 process: Evaluations on curfew for 65-year-old and over citizens and spiritual social work", Turkish Journal of Social Work Research, vol. 4, no. 1, pp. 35–42, 2020.

[11] F. Tang, J. Liang, H. Zhang, M. M. Kelifa, Q. He and P. Wang. "COVID-19 related depression and anxiety among quarantined respondents", Psychology Health, vol. 36, no. 2, pp. 164-178, 2021.

[12] L. Marty, B. de Lauzon-Guillain, M. Labesse and S. Nicklaus. "Food choice motives and the nutritional quality of diet during the COVID-19 lockdown in France", Appetite, vol. 157, 105005, 2021.

[13] F. A. Khalid, A. K. M. Ali, S. A. Ali, Z. Y. A. Mosmar, S. S. M. Salih, T. K. Salman, M. A. Desogi, M. A. Soghaier, E. E. Mohammed and A. A. Mohammed. "Households' dietary habits and food consumption patterns in Hamishkoreib locality, Kassala State, Sudan", Journal of Ethnic Foods, vol. 4, no 3, pp. 181-186. 2017.

[14] N. Bundala, J. Kinabo, T. Jumbe, C. Rybak and S. Sieber. "Does homestead livestock production and ownership contribute to consumption of animal

source foods? A pre-intervention assessment of rural farming communities in Tanzania", Scientific African, vol. 7, e00252, 2020.

[15] E. Ruggiero, M. Bonaccio, A. di Castelnuovo, A. Bonanni, S. Costanzo, M. Persichillo, F. Bracone, C. Cerletti, M. B. Donati, G. de Gaetano, L. Iacoviello and INHES Study Investigators. "Consumption of whole grain food and its determinants in a general Italian population: Results from the INHES study", Nutrition, metabolism, and cardiovascular diseases, vol. 29, no. 6, pp. 611–620, 2019.

[16] G. Maugeri, P. Castrogiovanni, G. Battaglia, R. Pippi, V. D'Agata, A. Palma, M. di Rosa and G. Musumeci. "The impact of physical activity on psychological health during Covid-19 pandemic in Italy", Heliyon, vol. 6, no. 6, e04315, 2020.

[17] Anonymous. The news about a survey of Mediabrands Insight. Retrieved August 9, 2020, from https://www.marketingturkiye.com.tr/haberler/turkiyede-fast-food-sektoru/, 2017.

[18] Anonymous. Information of year 2019 from Turkish Statistical Institute. Retrieved August 30, 2020, from http://www.tuik.gov.tr/UstMenu.do?metod=kategorist, 2019

[19] J. Sheth. "Impact of Covid-19 on consumer behavior: Will the old habits return or die?", Journal of Business Research, vol. 117, pp. 280-283, 2020.

[20] World Health Organization (WHO). "World Health Organization Regional Office for the Eastern Mediterranean. Nutrition advice for adults during the COVID-19 outbreak", Retrieved Juy 31, 2020, from http://www.emro.who.int/nutrition/nutrition-infocus/nutrition-advice-for-adults-during-the-covid-19-outbreak.html. 2020.

[21] J. L. Wilkins. "Challenges and Opportunities Created by the COVID-19 Pandemic", Journal of Nutrition Education and Behavior, vol. 52, no. 7, pp. 669-670. 2020.

[22] J. Maniam and M. Morris. "The link between stress and feeding behaviour", Neuropharmacology, vol. 63, no. 1, pp. 97-110, 2012.

[23] T. Eftimov, G. Popovski, M. Petković, B. K. Seljak and D. Kocev. "COVID-19 pandemic changes the food consumption patterns", Trends in Food Science Technology, vol. 104, pp. 268-272, 2020.

[24] K. McAtamney, M. Mantzios, H. Egan and D. J. Wallis. "Emotional eating during COVID-19 in the United Kingdom: Exploring the roles of alexithymia and emotion dysregulation", Appetite, vol. 161, 105120, 2021.

[25] L. Chenarides, C. Grebitus, J. L. Lusk and I. Printezis. "Food consumption behavior during the COVID-19 pandemic", Agribusiness, vol. 37, no. 1, pp. 44-81, 2020.

[26] D.Caso, M. Guidetti, M. Capasso, N. Cavazz. "Finally, the chance to eat healthily: Longitudinal study about food consumption during and after the first COVID-19 lockdown in Italy" Food Quality and Preference, vol. 95, 104275, 2022.

[27] A. Constant, D.F. Conserve, K. Gallopel-Morvan, J. Raude. "Socio-cognitive factors associated with lifestyle changes in response to the COVID-19 epidemic in the general population: results from a cross-sectional study in France" Front Psychol, vol. 11, 579460, 2020.

[28] M. Górnicka, M.E. Drywień, M.A. Zielinska, J. Hamułka. "Dietary and lifestyle changes during covid-19 and the subsequent lockdowns among polish adults: a cross-sectional online survey

plifecovid-19 study" Nutrients, vol. 12, pp. 1-23, 2020.

[29] V. Kriaucioniene, L. Bagdonaviciene, C. Rodríguez-Pérez. "Associations between changes in health behaviours and body weight during the COVID-19 quarantine in Lithuania: the Lithuanian COVIDiet study" p. 12, 2020.

[30] D.C. Malta, C.L. Szwarcwald, S.M. Allard, R. Knight, D.A. Sweeney, A.D. Swafford. "The COVID-19 Pandemic and changes in adult Brazilian lifestyles: a cross-sectional study, 2020" medRxiv : Preprint Server Health Science, vol. 29, e2020407, 2020.

[31] V.M. "The impact of COVID-19 on the dietary habits of middle-class population in mulund" Clinical Nutrition and Dietetics, Mumbai, India, 2020.

[32] M. Pellegrini, V. Ponzo, R. Rosato, E. Scumaci, I. Goitre, A. Benso, et al. "Changes in weight and nutritional habits in adults with obesity during the "lockdown" period caused by the COVID-19 virus emergency" Nutrients, vol. 12, pp. 1-11, 2020.

[33] C. Rodríguez-Pérez, E. Molina-Montes, V. Verardo, R. Artacho, B. García-Villanova, E.J. Guerra-Hernández, et al. "Changes in dietary behaviours during the COVID-19 outbreak confinement in the Spanish COVIDiet study" Nutrients, vol. 12, pp. 1-19, 2020.

[34] E. Sánchez-Sánchez, G. Ramírez-Vargas, Y. Avellaneda-López, J.I. Orellana-Pecino, E. García-Marín, J. Díaz-Jimenez. "Eating habits and physical activity of the Spanish population during the covid-19 pandemic period" Nutrients, vol. 12. pp. 1-12, 2020.

[35] F. Scarmozzino, F. Visioli. "Covid-19 and the subsequent lockdown modified dietary habits of almost half the population in an Italian sample" Foods, vol. 9, no. 5, p. 675, 2020.

[36] H. Al-Domi, A. Al-Dalaeen, S. Al-Rosan, N. Batarseh and H. Nawaiseh. "Healthy nutritional behavior during COVID-19 lockdown: A cross-sectional study", Clinical nutrition ESPEN, vol. 42, pp. 132–137, 2021

[37] D. Fancourt, F. Bu, H. W. Mak and A. Steptoe. "Covid-19 social study week 14. Publish date: 25th June 2020", Retrived from https://www.covidsocialstudy.org/results. 2020.

[38] Anonymous. "European Council Directive No. 2002/46/EC, relating to food supplements", Retrieved July 20, 2020, from https://eur-lex.europa.eu/legal-content/EN/ALL/?uri=celex%3A32002L0046, 2002

[39] R. Beitz, G. B. Mensink, S. Rams and A. Döring. "Use of vitamin and mineral supplements in Germany", Bundesgesundheitsblatt – Gesundheitsforschung – Gesundheitsschutz, vol. 47, no. 11, pp. 1057-1065, 2004.

[40] Anonymous. "The largest bread consumption per capita records of Guinness World Records book", Retrieved August 21, 2020, from https://www.guinnessworldrecords.com/world-records/largest-bread-consumption-per-capita. 2000.

[41] B. Demirtas, A. Kaya and E. Dagistan. "Consumers' bread consumption habits and waste status: Hatay/Turkey example", Turkish Journal of Agriculture - Food Science and Technology, vol. 6, pp. 1653-1661, 2018.

[42] Anonymous. "Republic of Turkey, Ministry of Agriculture and Forestry. Notice for the sale and consumption of

bakery products to be followed during the COVID-19 pandemic", Retrieved September 1, 2020, from https://www.tarimorman.gov.tr/Sayfalar/Detay.aspx?SayfaId=52. 2020.

[43] M. Rizou, I. M. Galanakis, T. M. S. Aldawoud and C. M. Galanakis. "Safety of foods, food supply chain and environment within the COVID-19 pandemic", Trends in Food Science Technology, vol. 102, pp. 293-299, 2020.

[44] M. J. Butler and R. M. Barrientos. "The impact of nutrition on COVID-19 susceptibility and long-term consequences", Brain, Behavior, and Immunity, vol. 87, pp. 53-54, 2020.

SAKARYA ÜNİVERSİTESİ
FEN BİLİMLERİ ENSTİTÜSÜ DERGİSİ

Sakarya University Journal of Science
SAUJS

e-ISSN 2147-835X Period Bimonthly Founded 1997 Publisher Sakarya University
http://www.saujs.sakarya.edu.tr/

Title: Real-Time Encrypted Traffic Classification with Deep Learning

Authors: Deniz Tuana ERGÖNÜL, Onur DEMİR

Recieved: 2021-11-23 00:00:00

Accepted: 2022-03-08 00:00:00

Article Type: Research Article

Volume: 26
Issue: 2
Month: April
Year: 2022
Pages: 313-332

How to cite
Deniz Tuana ERGÖNÜL, Onur DEMİR; (2022), Real-Time Encrypted Traffic Classification with Deep Learning. Sakarya University Journal of Science, 26(2), 313-332, DOI: 10.16984/saufenbilder.1026502
Access link
https://dergipark.org.tr/tr/journal/1115/issue/69580/1026502

New submission to SAUJS
http://dergipark.gov.tr/journal/1115/submission/start

Sakarya University Journal of Science 26(2), 313-332, 2022

Real-Time Encrypted Traffic Classification with Deep Learning

Deniz Tuana ERGÖNÜL*[1], Onur DEMİR[1]

Abstract

Confidentiality requirements of individuals and companies led to the dominance of encrypted payloads in the overall Internet traffic. Hence, traffic classification on a network became increasingly difficult as it must rely on only the packet headers. Many vital tasks such as differential pricing, providing a safe Internet for children, and eliminating malicious connections require traffic classification, even if the payload contents are encrypted. Encrypted traffic is harder to classify as packet content becomes unreadable. In this work, we aim to provide an insight into traffic classification using encrypted packets in terms of both accuracy and packet processing time. LSTM (Long Short-Term Memory) architecture is a good candidate for this problem as it can handle sequences. Each flow can be modeled as a sequence and patterns of the sequences can provide valuable information. We compare the performance of LSTM with other methods in both real-time and offline experiments. Compared to a machine learning method both online and offline LSTM excelled with precision and recall differences up to 50%. Average accuracy with LSTM was measured as 97.77% offline and 91.7% in real-time. Average packet processing time in real-time was recorded as 0.593 msec which is 5 times faster than a recent work that uses LSTM method.

Keywords: Deep learning, neural networks (Computer), computer communication networks, classification

1. INTRODUCTION

In traffic classification, the principal aim is to recognize and name different groups of packets using the information available at the network level. Identifying the class of a network packet can be used for running predefined rules on it, such as ensuring the quality of service promised to the customer, detecting malicious user activities, or dropping certain content for parental control [1]. Classification can be in terms of the application, protocol, or category of a packet [2]; for example, WhatsApp Web application, HTTPS protocol, chat category; Skype application, TLS protocol, VoIP category. The need for classification comes from different reasons such as offering specialized internet packages according to customer needs (prioritizing online gaming traffic and reducing latency in the game for an online gamer), setting a special discount for social media platforms (e.g., Facebook, Twitter), or managing traffic of protocols that use too much bandwidth such as BitTorrent. Mostly, it is the focus of ISPs (Internet Service Provider) and

* Corresponding author: dtergonul@gmail.com
[1] Yeditepe University, Faculty of Engineering
E-mail: odemir@cse.yeditepe.edu.tr
ORCID: https://orcid.org/0000-0003-2945-0833, https://orcid.org/0000-0002-1088-6461

defense industry units of countries; however, every institution can benefit from a dedicated solution whether it is online or offline [3]. Labeling of pre-captured network packets is called offline classification; online classification is when they are labeled one after another in real-time [4].

Classification is usually performed on bidirectional flows instead of a single packet. A flow is a set of packets exchanged between two distinct networks, using the same transport protocol (e.g., TCP, UDP) and port numbers. What identifies a flow is called a five-tuple: transport protocol, source IP, destination IP, source port, destination port. In a bidirectional flow, packets that have their IP and port pairs reversed also counts. Once a flow is labeled, any packet that belongs to that flow can be labeled as the same.

The oldest and easiest method of classifying a flow is querying for its port numbers in IANA's (Internet Assigned Numbers Authority) Service Name and Transport Protocol Port Number Registry [5]. Although practical in respect of time and effort, this technique is not very reliable. The applications can pick other ports to communicate with each other rather than using the standard ports. Usage of nonstandard ports jeopardizes the reliability of this method. There is even a term called port obfuscation [6]. Protocols using obfuscation (e.g., VPNs) willingly avoid using the standards to hide their identity.

A somewhat more advanced way to classify flows is to do deep packet inspection (DPI), in other words, to analyze all layers of packets, including packet payload. An unencrypted payload can give a clear idea of what protocol a packet uses. Some protocols have unique patterns (signatures) which can be directly used to label packets. Regular expression databases are generated to store this information. However, maintaining such a database is a tedious job. On the other hand, payload encryption got popular over the years. As an example, Google Transparency Report [7] (Figure 1) shows that the preference for HTTPS over HTTP has increased significantly in the last seven years, from 48% in 2014 to 95% in 2021. Encryption changes the content of packets in such a way that they are no longer human-readable. For this reason, it becomes very challenging to find an easily recognizable pattern in the payload.

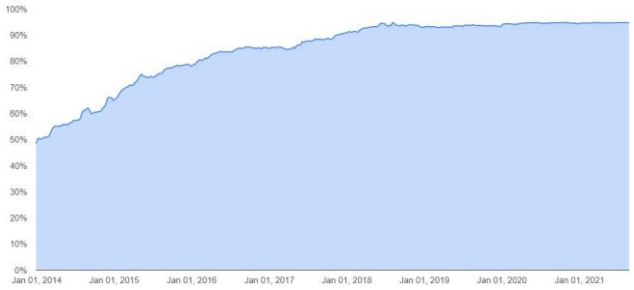

Figure 1 Encrypted traffic across Google

Statistical flow classification is another valid method that uses features such as average packet inter-arrival times, packets per second, byte frequencies, etc. [6].

In recent years, research on machine learning and deep learning models intensified, since the accumulation and storage of data has become easier and cheaper. The advantages of these models are that they can be trained offline with an abundant amount of training data. As it is for many learning problems, feature selection may be considered a tedious task, but it is possible to make a model learn how to do that on its own. Deep learning is a relatively new technology for flow classification. There are not many research papers yet, especially with an LSTM model, and the existing ones usually do offline classification [8]. Thus, the elapsed time, a critical performance measure for online classification, does not get mentioned.

One of the challenges of traffic classification is data, as it is for almost all learning problems. Tools such as Wireshark [9] can collect live traffic into packet capture (PCAP) files. The difficulty here is that the collected data is often noisy. The packets which do not fall in any of the main categories are noise. The operating system, services running in the background, other applications, or services that applications use might be the reason for the noise. It is crucial to feed learning models with clean data since any noise might cause them to make incorrect connections, leading them to deduct unreliable

knowledge. Thankfully, there is a very common public dataset named ISCXVPN2016 (UNB ISCX Network Traffic Dataset) [10] that is used prevalently in this area. However, it is worth noting that a model trained with data obtained from a particular network may not perform well on a different network [11].

This work aims to classify flows, even if they contain encrypted packets, as to their categories, in real-time. Encryption adds a new difficulty level since the packet payload becomes indecipherable to infer a piece of information from it without decryption. This difficulty has no effect on the proposed solution because the solution does not require the examination of packet payloads. Crucial metrics for this work include accuracy, and elapsed time for processing (analyzing and classifying) a single packet. The biggest goal of the study is to examine the performance of an LSTM model named LSTM-FS (LSTM with Flow Sequences) for the categorization problem both offline and online, to find out accuracies, to observe the number of packets processed per second in the online environment, and the processing time of a single network packet.

Here is the list of questions this study intends to shed some light on:

- Why is LSTM a good candidate for the traffic classification problem?
- How to model this problem for LSTM?
- How does LSTM perform both accuracy and timewise?

The reason for choosing LSTM is that it has a memory where earlier sequences of packets can be remembered. LSTM, a variant of RNN (Recurrent Neural Network), can store information for a while and use this information for future predictions. It has structures called gates which let information be stored or forgotten. This approach allows LSTM to perform well with data sequences. For instance, LSTM has been used for NLP (Natural Language Processing) problems because words in a paragraph are somehow related, and LSTM can figure out these relationships. Similarly, network packets also have temporal information thus can be handled in sequences. What is inside an encrypted network packet is often a mystery; it is not straightforward how to obtain information from them with techniques such as DPI. It is both challenging and time-consuming for the human eye to find consistent patterns for each label when payloads are encrypted. However, LSTM can make deductions from data that are not directly visible.

There are four scenarios to test LSTM-FS. The first scenario is to detect whether the traffic is VPN or not. In the second scenario, six non-VPN categories (chat, email, file transfer, P2P, streaming, VoIP) exist to label the given data. The third scenario only includes VPN versions of these six categories. In the last scenario, with the second and third scenarios combined, labeling is made among six non-VPN and six VPN categories. Along with offline tests, online simulations also exist for each scenario of LSTM-FS. LSTM-FS gave good results with respect to speed and accuracy.

Section 2 includes briefs of 11 studies in the traffic classification field. At the end of it, there is a table that summarizes the big picture. The problem is explained along with the presented solution in Section 3. Section 4 introduces the environment in which the tests ran, the test scenarios, the data and its usage, and the parameters; it contains test results. Inferences made following the tests are shared in Section 5; possible improvements and new ideas for future work are also discussed.

2. BACKGROUND

In this section, we tried to compile a comprehensive list of related studies to our work. One of the studies included in this section is a purely statistical method, while three of them consist of machine learning models trained with statistical features. There is a survey paper about deep learning methods that also underlines the difficulties of encrypted traffic classification. The remaining works are all deep learning methods, and two of which are LSTM. Most of the classification involves grouping based on protocols, applications, or other categories. Only

the last study mentions real-time classification. ISCXVPN2016 [10] stands out as the major dataset used.

Statistical Protocol Identification (SPID) [12-14] is an open-source project that accepts PCAP files as input to generate protocol models by examining flow and payload statistics. Before any classification can be performed, the user must initiate training by feeding pre-labeled PCAP files to SPID. At the training phase, for each flow in a pre-labeled PCAP, a protocol model is generated. SPID stores the generated models in a database. If there exists another model with the same label, the two models get merged. At the testing phase, a new model is generated that corresponds to the current session; then, it is compared with the models in the database. SPID algorithm uses packets with payload in a session to calculate some features (attribute meters). A protocol model is made of these meters. There are 34 available, 7 of them are flow-level, and 27 are payload-level. Each one has a counter vector of size 256 that has a unique meaning for the meter. For example, ByteFrequency is a payload-level meter that interprets this vector as a list of ASCII characters where index 65 corresponds to the 'A' character. Each meter calculation returns a list of indices for the meter's counter vector. The elements at these indices are increased by 1. The researchers got an average of 100% precision and 92% recall when tested with BitTorrent, eDonkey, HTTP, SSL, and SSH flows.

Characterization of Encrypted and VPN Traffic Using Time-Related Features [15] is a significant study for two reasons: they provide a public dataset named ISCXVPN2016 which has been used by many researchers through the years, and they present a machine learning approach for flow classification. The dataset consists of various PCAPs, and it is 26.2 GB large. The files can be grouped into 14 different categories: chat, email, file transfer, P2P, streaming, VoIP, VPN chat, VPN email, VPN file transfer, VPN P2P, VPN streaming, VPN VoIP, Tor (The Onion Router) browsing, Tor streaming. They calculate a total of 24 time-based, statistical features to perform classification. The main features include flow duration, the time between two successive packets (in the forward, backward, and both directions), the time a flow is active and idle, flow bytes per second, and flow packets per second. Other features are the minimum, maximum, average, and standard deviation of these features. They employed four flow timeout values 15, 30, 60, and 120; to find out 15 is the most accurate. They had accuracy levels above 80%.

Yamansavascilar et al. [11] used machine learning algorithms J48 (also known as C4.5), Random Forest, k-Nearest Neighbors (k-NN), and Bayes Net to identify popular consumer applications such as Facebook, Twitter, and Skype. Just as we do in this paper, the ISCXVPN2016 dataset is made use of along with an internal dataset. For applications that are available on mobile phones, they captured cellular traffic as well.

The datasets contain 15,462 and 3,748 flows, respectively. They chose 111 features, but the selection procedure of these features is not unclear. Accuracy varies between 85.44%-93.94% for the external dataset and 69.90%-90.87% for the internal. Using evaluators, they succeeded in decreasing the number of features as down as 12; while maintaining the accuracy levels. They realized that the misclassified samples are often in the same category. Therefore, category classification before application identification can be considered as future work.

Bagui et al. [16] compared the performance of six supervised machine learning techniques: Logistic Regression, Support Vector Machine (SVM), Naive Bayes, kNN, Gradient Boosting Trees, and Random Forest, in terms of accuracy, precision, sensitivity, and specificity. They utilized the same 24 time-related features in [15] along with the ISCXVPN2016 dataset. Separately for each category (browsing, chat, email, file transfer, P2P, streaming, VoIP), they did binary classification to identify if traffic is VPN encrypted or non-VPN encrypted. The sample distribution within each category is well-balanced (almost 50%-50%). Sample amounts range between 1,113 and 10,000, not enough to try out deep neural networks, as they state. Gradient Boosting Tree and Random Forest outperformed the other methods in respect

of all metrics with values around 94%. Aiming for high accuracy and low overfitting, they used grid search to find an optimal, work-for-all set of hyperparameters which increased the values by a few percent. Additionally, through feature selection, they ordered a minimum set of features by importance for each category. Although feature selection deteriorates accuracy results to 90%, they claim that it can be advantageous where speed matters more, but they did not present any experiment results backing this assumption.

One-dimensional Convolutional Neural Network (1-D CNN) is a model for traffic identification and classification. Wang et al. [17] claimed network traffic as sequential data. They argue that solution becomes more prone to get stuck at a local minimum when a problem is divided into sub-problems. Consequently, they present an end-to-end solution where feature extraction, feature selection, and classifier are one [16]. In other words, their model takes raw data and learns features on its own. They used the ISCXVPN2016 dataset, excluded capture files that are vague. (e.g., Both browsing and streaming is a suitable label for "Facebook_video.pcap", they say.) To do data pre-processing, they adopted a toolkit of their team named USTC-TK2016 [19] which transforms capture files into images. Wang et al. noticed that the images generated for same-class flows looked very similar. They observed that bidirectional flows yield higher accuracy than unidirectional ones; and as opposed to using only the application layer of a packet, using all layers is better. Since CNN accepts equally long data, they employed only the first 784 bytes of each flow. How many samples they had for each category is not addressed in the paper. However, they did mention an imbalance in the dataset as a future concern. They did four experiments: binary classification between VPN and non-VPN data, category classification among non-VPN, VPN, and mixed data. Best accuracy results were respectively 99.9%, 83%, 98.6% and 86.6%. They also pointed out that 1-D CNN delivers better performance than two-dimensional.

Rezaei and his team [8] provided a survey paper about traffic classification with deep learning techniques, namely, Multi-Layer Perceptron (MLP), CNN, RNN, Autoencoder, and Generative Adversarial Network. They emphasized the challenging aspects of this field, such as data collection. They state that other than ISCXVPN2016 and a few others, there is not a publicly available and widely used dataset. Researchers tend to capture data on their own, specific to their needs. Because of background traffic caused by routers, operating systems, et cetera, collecting noiseless capture files is far from an easy task. Another issue is that a model trained with a particular network's data might perform way worse when tested on another network or even on the same network but under different circumstances (i.e., high congestion). They also stressed how to tackle encrypted traffic. For example, time-series features such as inter-arrival time are not changed by encryption, because they do not depend on packet payloads. Using the payload of the first TCP packets may still be convenient since the handshake stays unencrypted. However, the authors also pointed out that newer encryption protocols such as QUIC and TLS 1.3 remain open for investigation. Other problems they discussed are zero-day applications (classes the model has not seen yet), multi-label classification (one flow carrying multiple classes), middle flow classification (classification using packets from the middle of the flow), transfer learning, and multi-task learning.

Deep Packet [20] can identify the protocol or application to which a packet belongs (by 98% recall), label it by its category while differentiating VPN from non-VPN (94%). Lotfollahi et al. used the ISCXVPN2016 dataset by dividing it into 17 application classes for the first experiment: 6 VPN, 6 non-VPN category classes for the second. Instead of flows, they work with packets, and the packet distribution within each set of classes is highly imbalanced. (e.g., 5K AIM vs. 7872K FTPS, 13K VPN email vs. 5120K VoIP) To handle this matter, they did under-sampling; they excluded samples from dominant classes. Their model consists of two parts: stacked autoencoders and 1-D CNN. The autoencoders take care of feature extraction automatically, eliminating the need for an expert. Since inputs fed into a NN must be fixed length, they decided

on 1500 bytes after examining packet length histogram. Some pre-processing steps are padding UDP headers (so they become equal length with TCP), discarding TCP handshake and DNS packets (bring no useful information), and masking IP addresses (causes over-fitting). They explain how their model can classify encrypted packets with the following hypothesis: although encrypted, packets of the same application may still contain consistent patterns. This hypothesis is also how they justify why their model failed to classify Tor categories.

Parchekani et al. [21] adopted the ISCXVPN2016 dataset and a local ISP's data to classify five non-VPN (chat, email, FTP, streaming, VoIP), and one VPN class which symbolizes all kinds of VPN traffic. They fed each flow's first 784 bytes into their models. The models consist of MLP and RNN layers. To receive the best precision values (above 80%), they tried two approaches: score and distance. Their study reveals that distance is a better metric than score. Both include a definition of a threshold parameter to either accept or reject a label. For the given input, in the first approach, each candidate non-VPN label gets a score. If the one with the maximum score is less than the threshold, it gets rejected. In the second approach, candidates get a distance value; and if the label with the minimum distance is more than the threshold, it is not accepted. In both cases, rejection means classification as VPN. Accepted ones go through a second phase where their category decision becomes finalized. To accomplish this, they use other thresholds to decide if another classification is necessary.

With his team, Zhou [22] combined entropy estimation with traditional machine learning methods SVM, Random Forest, Naive Bayes, and Logistic Regression along with a NN, to distinguish VPN from non-VPN on the ISCXVPN2016 dataset. Compared with metrics from past works, results improved by 1% to 7%, with Random Forest remaining the best method (98%). Additionally, they built a NN which takes 23 statistical features (from [15]) as input to classify Tor data (ISCXTor2016 [23]) into 8 categories, as opposed to 7 seen in prior works. (Streaming is divided into two labels: audio and video) With this model, they improved some of the previous studies' metrics by nearly 30%. They also examined the 23 features using principal component analysis and found that it is possible to eliminate half of the features without significantly sacrificing accuracy.

Network traffic classifier by Lopez-Martin et al. [24] integrated LSTM on top of CNN to classify a dataset from RedIRIS [25], which contains 266,160 flows with 108 applications. They used nDPI [26], an open-source DPI library, to label the data. Label distribution is quite imbalanced; almost half of the data is HTTP, followed by DNS with 20% and SSL with 15%. After trying out a few combinations, they settled on five features: source port, destination port, payload length, TCP window size, and packet direction. (96% accuracy) They observed that adding timestamp as a feature did not enhance the results. Before further experiments, they set the sequence length as 20 packets. For each flow, they discarded the packets after the 20th; and if the flow was not long enough, they employed padding. Later they realized that a length of 5 to 15 is sufficient for good results. Among models CNN-only, RNN-only, and CNN with LSTM, the latter performed the best with an accuracy of 96%.

Byte Segment Neural Network is a model by Liu et al. [27] based on RNN variants LSTM and GRU (Gated Recurrent Unit) to classify protocols and applications DNS, BitTorrent, PPLive, QQ, SMTP, 360, Amazon, Yahoo, Cloudmusic, and Foxmail. The real-world data they used consisted of 2,516 (DNS) to 55,576 (Cloudmusic) samples/datagrams. All header information (Ethernet, IP, TCP/UDP) got removed from datagrams. The segment generator splits the payload into equally length byte segments. According to their experiments, the most practical length is 8, against 3, 5, and 10. Compared to nDPI and a binary classifier named Securitas [28], they got better results for 5 of the applications considering recall, precision, and F-score. They have an average F-score of 95.82%. In the training phase, it takes 43 msec on average to prepare input, and 20 epochs of training take 123 minutes, whereas, in the testing phase, processing a datagram takes 2.97 msec.

Table 1 Related Work

Paper	Classification	Method	Features
Statistical Protocol IDentification with SPID: Preliminary Results [14]	Protocol	Statistical	7 flow-level, 27 payload-level
Characterization of Encrypted and VPN Traffic Using Time-Related Features [15]	Category	k-NN, C4.5 (J48)	24 time-based
Application Identification via Network Traffic Classification [11]	Application	J48, Random Forest, k-NN, Bayes Net	111 (Reduced to 12)
Comparison of machine-learning algorithms for classification of VPN network traffic flow using time-related features [16]	Category	Logistic Regression, SVM, Naive Bayes, k-NN, Gradient Boosting Trees, Random Forest	24 time-based
End-to-end Encrypted Traffic Classification with One-dimensional Convolution Neural Networks [17]	Category	1-D CNN	First 784 bytes of a flow
Deep Packet: A Novel Approach for Encrypted Traffic Classification Using Deep Learning [20]	Protocol, Application, Category	Stacked autoencoders + 1-D CNN	First 1500 bytes of a packet
Classification of Traffic Using Neural Networks by Rejecting: A Novel Approach in Classifying VPN Traffic [21]	Category	MLP + RNN	First 784 bytes of a flow
Practical evaluation of encrypted traffic classification based on a combined method of entropy estimation and neural networks [22]	Category	Entropy estimation + (SVM, Random Forest, Naive Bayes, Logistic Regression, NN)	23 time-based
Network Traffic Classifier with Convolutional and Recurrent Neural Networks for Internet of Things [24]	Protocol, Application	CNN, RNN, CNN + LSTM	5
Byte Segment Neural Network for Network Traffic Classification [27]	Protocol, Application	LSTM, GRU	Equal length byte segments

Table 1 consists of all the studies summarized except Deep Learning for Encrypted Traffic Classification [8], a survey paper. Classification is usually done based on protocol, application, or category. The methods used include purely statistical methods as well as decision tree solutions with statistical features. Tree-based machine learning methods have gradually started to be replaced by deep learning methods. Features used include both flow-level and payload-level information. Specifically, the use of time-based features is quite common. All studies except the last take place offline.

Unquestionably, the work of Draper-Gil et al. stands out in this area. Noise-free data is a big problem in traffic classification as in almost every field; Draper-Gil and his team present a quality dataset that is used by many researchers after them. This dataset is quantitatively full enough to be used even for deep learning solutions; plus, it consists of popular applications (such as YouTube, Netflix, Skype, etc.). Besides, it can easily be seen that the 24 time-based features they offer inspired many studies.

The five features used by the penultimate study, one of the 2 studies that use LSTM, are taken directly from the packets as in this study (LSTM-FS). Unlike that study, there are 23 features defined in LSTM-FS. They use flows of length 20 as sequences, any flow longer gets its packets discarded, and any flow shorter gets padded. On the contrary, the length of 10 is used in LSTM-FS, and no packets get discarded; instead, they are handled in new sequences. The other LSTM-

based study only checks payloads, which is different than in LSTM-FS. They are the only researchers who shared elapsed time results. They report 2.97 msec as the average datagram processing time; our proposed solution LSTM-FS performs 5 times faster than their solution.

3. METHODOLOGY

In this section, our proposed solution for traffic classification, LSTM with Flow Sequences (LSTM-FS), is described. The section is divided into five subsections for flow generation (3.1.), feature extraction (3.2.), creating train and test data (3.3.), model generation (3.4.), and testing offline/online classification (3.5.).

Our solution operates with PCAP files; and includes libpcap [29], a C/C++ library for network traffic capture operations. Wireshark [9], which is a well-known opensource network packet analyzer, also utilizes this library. The solution supports Ethernet as data link layer (Layer 2, L2) protocol; IPv4 as network layer protocol (Layer 3, L3); TCP and UDP as transport layer (Layer 4, L4) protocols. Raw IP packets which do not involve a data link layer at all are not supported directly. Instead, these PCAPs are modified with a tool named tcprewrite [30] so that their packets have fake Ethernet layers.

3.1. Flow Generation

The first step of our solution for the traffic classification problem is bidirectional flow generation; in other words, identifying the packets with the same endpoints and ports so that they are associated with the same flow. Since its five-tuple uniquely describes a flow, after a given packet is analyzed, it is grouped with the others which have the same L4 protocol, source-destination port, and IP pairs. In our design, a flow is strictly related to at least one non-dummy packet (A dummy packet's all features appear as -1.), and a classification label.

3.2. Feature Extraction

In our solution, packets hold almost everything one can obtain from a network packet except the payload. We exclude capture length, MAC addresses, IP addresses, IP Identification, fragmentation-related IP fields, and checksums since these are not used for classification. Other left-out fields are Ethernet type, IP version, and Protocol field of IP header, as these are identical for all packets (IPv4, 4, TCP/UDP, respectively).

Packet fields shown in Table 2 directly correspond to features to feed into the learning model. Valid packet directions are forward and backward. TCP fields are all set to 0 for UDP packets and vice versa. It is important to note that packets lined up in a PCAP file may not represent their actual order. That is why epoch time is a more reliable reference since it indicates when a packet is captured.

Table 2 Packet fields

Field	Definition
direction	Packet direction
actualLength	Length on wire, frame length
arrivalTime	Epoch time
ipHeaderLength	IP header length (IHL)
ipTypeOfService	Type of Service (TOS) field of IP header
ipTotalLength	IP header length + IP data length (datagram length)
ipTimeToLive	Time to Live (TTL) field of IP header
tcpSrcPort	TCP source port
tcpDestinationPort	TCP destination port
tcpSeqNumber	Sequence number field of TCP header
tcpAckNumber	Acknowledgement number field of TCP header
tcpHeaderLength	TCP header length (HLEN, data offset)
tcpReserved	Reserved field of TCP header
tcpFlags	Flags field of TCP header
tcpWindowSize	Sliding window size field of TCP header
tcpUrgentPointer	Urgent pointer field of TCP header
udpSrcPort	UDP source port
udpDestinationPort	UDP destination port
udpLength	UDP header length (8 bytes) + UDP data length

3.3. Creating Train and Test Data

To create training and testing data, we first examine PCAP files under subdirectories of a given directory. Subdirectory names get

interpreted as labels. After all the PCAPs get examined, sample creation will take place, as shown in Figure 2.

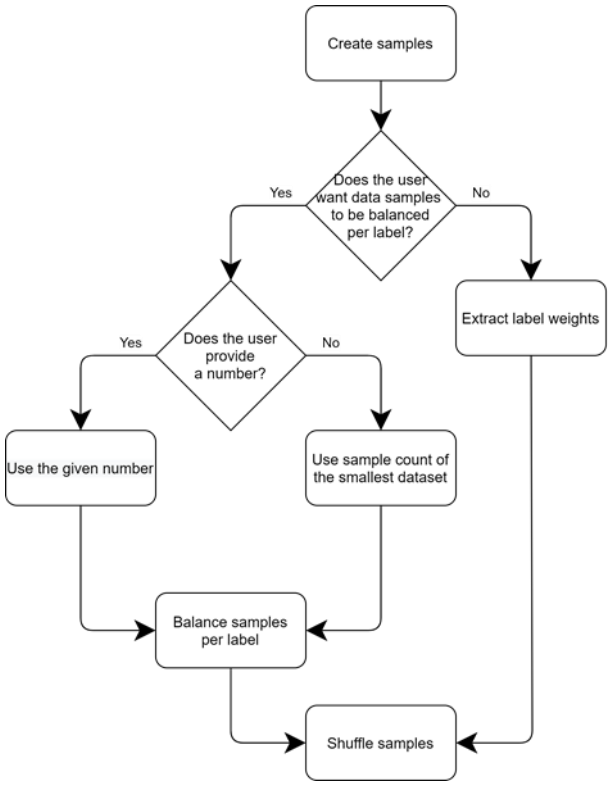

Figure 2 Sample creation flowchart

For each flow, a set of samples get created. A sample is a flow sequence which is part of a flow and consists of at least one non-dummy packet. Sequences have a preset length of 10. Thus, flows with fewer packets get padded with dummy packets (Figure 3). On the other hand, for flows with more packets, extra samples are created. To be exact, every 10 consecutive packets in a flow becomes a sample (Figure 4). Users can choose whether they want the data to be balanced per label or not. This way, any deprivation an imbalanced dataset may cause (e.g., over-fitting) can be prevented by under-sampling. If no balancing should occur, the algorithm will output label weights for the learning model to use. After samples are created, (optionally) balanced, then shuffled, 85% of them are training data, and the rest is testing data. It is crucial to emphasize that packets in a sequence must be in order. So, shuffling samples only means swapping ten packets in bulks.

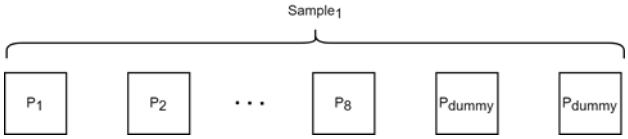

Figure 3 Sample creation when the number of packets in flow is less than 10

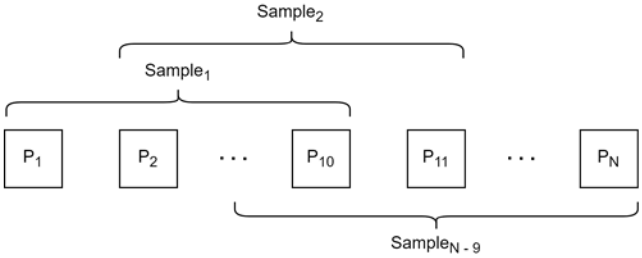

Figure 4 Sample creation when the number of packets in flow is greater than 10

Samples go through one more step before being written to the relevant file; feature scaling. Equation 1 shows min-max normalization (rescaling) formula where x_i is the original value for i^{th} sample, and x_i^0 is the normalized value. This requires finding the minimum and maximum values for each feature. Note we only consider TCP packets for the calculation for TCP-related features. Naturally, the same applies to UDP as well. Dummy packets are not considered for scaling. Next, invalid features are determined. If the minimum and maximum values are equal or if at least one of them is undefined, the feature is invalid. Invalid features will not appear in training and testing files.

$$x_i' = \frac{x_i - \min(x)}{\max(x) - \min(x)} \quad (1)$$

One of the goals of this work is to come up with a feasible solution for online classification. To properly test this solution, an online environment or a realistic simulation is required. Our outputs are training and test datasets as CSV files; the test data is also extracted as a single PCAP file (dummy packets excluded) where its packets are shuffled using Algorithm 1. This mixed data is more representative of an online setting than data in which flow sequences come in sizes of 10 one after another. Function nextPacketID ensures that packets stay in order in their flows (Figure 5). The

new packet series gets dumped to a PCAP file beside a text file for each packet label.

1: **function** shufflePackets
2: *packets* ← []
3: *availableFlowCount* ← *size*(*flows*)
4: **while** *availableFlowCount* > 0 **do**
5: *f* ← *random*(*availableFlowCount*)
6: *p* ← *nextPacketID*(*f*)
7: **if** *ID*(*p*) ≠ −1 **then**
8: Add *p* to *packets*
9: **else** ► End of flow
10: *availableFlowCount* ← *availableFlowCount* – 1
11: Remove *f* from *flows*
12: **end if**
13: **end while**
14: **end function**

Algorithm 1 Algorithm to shuffle packets retaining order in their flows

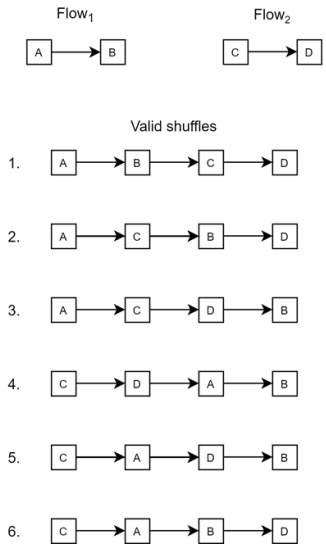

Figure 5 Valid shuffle examples

3.4. Model Generation

Our solution includes a Python program that uses TensorFlow [31] and Keras [32] libraries. The program builds a learning model, trains it with given data, and serializes it. The serialized model is imported through an API named CppFlow [33]. Its first layer, the masking layer, helps disregard dummy values, such as values of dummy packets. The second layer, LSTM, is the heart of the model. LSTM is an RNN variant that utilizes gates to decide what to remember and forget from information learned so far. Considering its success with modeling sequential data, series of consecutive packets are also expected to fit in this model. Packets of a flow are never entirely independent from each other. LSTM might be able to figure out dependencies and different kinds of relations among data. Dropout is a reasonable parameter for an LSTM layer that combats with over-fitting by dropping some of the gathered information. Last is the dense layer; it has a unit for each label, and its activation function is SoftMax. This function will assign probability values for each unit stating how likely is it for this label to be correct. The probabilities will add up to 1. Model compilation configuration is given in Table 3.

Table 3 Model compilation configuration

Optimizer	Learning Rate	Loss Function	Metrics
Adam	0.001	Sparse Categorical Crossentropy	Sparse Categorical Accuracy

As the LSTM layer of Keras library requires data to be in a 3D shape where x is the number of samples, y is timesteps or sequence length (10), and z is feature count, the input gets reshaped accordingly. It is worth noting that the LSTM layer can be structured to take varying lengths of sequences by setting the input shape parameter's first value as none. However, batch training, which reduces training time with the help of parallelism, must still contain equal length samples. For this reason, padding can be used. The batch count parameter for the LSTM layer and is set to 128. The output should contain a

single label for each sequence instead of each packet.

Large datasets might take a lot of memory and other resources of computers. Chunk size is an advantageous parameter for this case. It is set to 1 million, and the model's fit function runs for each chunk. This means 1 million rows are processed at a time; for example, if there are 10 million rows in total, they are processed in 10 iterations. The critical point here is to set the chunk size to such a number so that there is enough RAM to handle that many rows. Any number higher will result in an insufficient memory error. The lower the number is, the more the iterations. An optimal number can be found by experiment. Another parameter for fit is class weight. A class weight map associates each label with a coefficient. If data is imbalanced, these may help underrepresented labels to get noticed more often. The required coefficients are outputted during train and test data creation. Other than fit, Keras provides three more functions for the model: compile, predict, and evaluate. Compile builds the model based on a given configuration. Evaluate assesses the model using the provided test input and output. For adequate evaluation, test data should be completely different from train data. Finally, predict function takes a single input sequence and returns the model's prediction.

3.5. Testing Offline/Online Classification

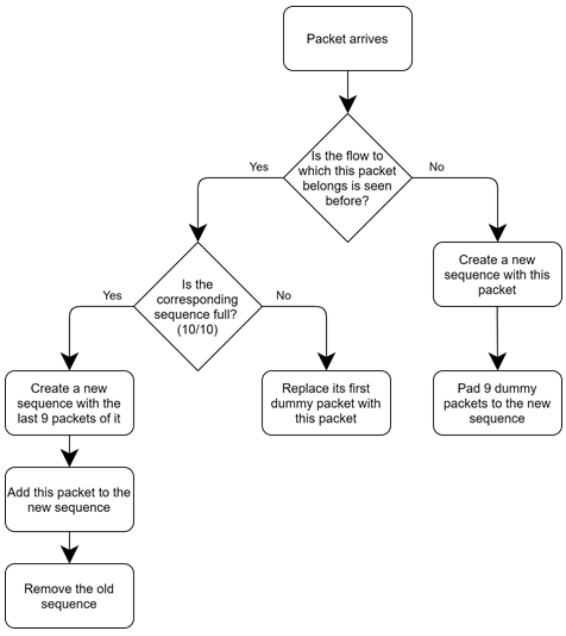

Figure 6 Sequence (sample) creation when testing

For this case, our solution accepts a single PCAP file as an input; and three text files: one for each packet's actual/expected label, another for feature validities, and valid feature values required for normalization. We utilize actual packet labels for accuracy calculations, comparing expectations with predictions, and creating a confusion matrix. Since the learning model learns with a subset of features, the same subset must be obtained during testing. Similarly, the same scaling technique must be applied to data with the values obtained when training. Moreover, for normalization, any packet value less than the relevant min value will be elevated to the min, and a value more than the max will be lowered to the max. Unlike when train and test data creation take place, sequences are created during analysis, not after all packets are seen (Figure 6). Thus, each packet can be directly sent to the classification model right after being analyzed.

We let the user pick a number which will be the number of packets to wait to get a classification result. Since the model works with sequences of (10) packets, it makes sense to assign this number to at least 2. Any sequence having less than this number of non-dummy packets will get skipped. There is also a limit calculation for probability found by the model (Equation 2, L is the number of labels.). Packets with predicted results with less will be labeled as unknown. This parameter can be used to decrease the number of false positives. Misclassifications are prevented by setting a confidence limit; any prediction with lower probability will be classified as unknown, instead of accepting the predicted label no matter how low the probability is. For instance, for 2 labels (L = 2) we required the model to be more than 50% ($1/L$) confident with its prediction. Thus 1.5 is selected as the coefficient.

$$probabilityLimit = \frac{1}{L}1.5 \quad (2)$$

3.5.1. Thread Utilization

A key factor for online traffic classification simulation is packet sender-receiver threads. Two threads run throughout the program, one being the

sender and the other is the receiver. The threads work with a shared variable which is a fixed-size buffer where packets are stored. The executable uses lock mechanisms to prevent race conditions. The sender's job is to fill the buffer until there is no packet left. It goes back to the beginning of the buffer if the buffer is full and overwrites the old content. It also lets the reader know where to start reading and how many packets to read. This number strictly cannot be greater than the buffer size since this implies a packet drop. After every sent packet the sender sleeps for 100 nanoseconds which is the interpacket gap for a link speed of 1 Gigabit/second. An interpacket gap defines the minimum await time between two packets. On the other hand, the reader waits until the buffer is nonempty. When it can acquire the lock, it copies the relevant part of the buffer pointed by the sender. It then forwards the copied packets for classification. Thread organization helps answer questions such as how many packets can be classified in a limited amount of time; how this number is related to buffer size, and how much time it takes to process a single packet.

Although sender-receiver threads synchronize well, it is nearly impossible to measure the time elapsed for a single thread on a Windows machine. This study is only interested in the reader's performance, how fast it can process a packet and how many packets it can process in a time frame. For this reason, to remove the sender from the equation, a distribution is generated of sent packet amounts from different program runs. The type of distribution (e.g., normal, exponential) is decided by examining these amounts, and the related calculations are made (e.g., mean and standard deviation for normal, rate parameter for exponential). The runs are done with all available cores (12). Random packet amounts are generated using the distribution until no packet is left. Up to the number of available cores, for each random amount, a reader will be spawned. For optimization, each thread will be assigned to a specific core. Since the external library class to represent the model may not be thread-safe, each reader has its copy of the model.

4. TESTS AND RESULTS

This section describes the dataset used in this work and how it is utilized, test scenarios, and hardware features; test results for LSTM-FS (LSTM with Flow Sequences) are given. Comparisons were made among different studies.

4.1. Dataset

The experiments use the ISCXVPN2016 dataset [10]. The dataset contains all encrypted packets: non-VPN, VPN, and Tor samples. Tor is ruled out from tests for the sake of simplicity. There exist six non-VPN and six VPN categories for chat, email, file transfer, P2P, streaming, VoIP. As opposed to Draper-Gil et al. [15], this work does not include the "browsing" label since the others match better with the PCAPs. For the transport layer, TCP and UDP are supported, the program ignores ICMP and IGMP packets. PCAPs with raw IP packets, almost all VPN data, are padded with Ethernet headers. Doing this provides a way to merge multiple PCAPs with different link types.

4.2. Test Scenarios

The study by Draper-Gil et al. [15] has four test scenarios: A-1, A-2 non-VPN, A-2 VPN, and B, as summarized in Table 4. The same scenarios are built for the method LSTM-FS to make meaningful comparisons. In the first part of Scenario A (A-1), the researchers split the dataset into two labels, non-VPN and VPN, to feed into Weka (Figure 7). In the second part of Scenario A (A-2 non-VPN and A-2 VPN), they divide each label's data into six categories and handle both separately (Figure 8 and Figure 9). In Scenario B, this study uses 12 labels (six non-VPN and six VPN categories) to perform classification in one step. All experiment scenarios ran both offline and online for LSTM-FS.

Table 4 Test scenarios

Scenario	Labels
A-1	non-VPN, VPN
A-2 non-VPN	chat, email, file transfer, P2P, streaming, VoIP

A-2 VPN	VPN chat, VPN email, VPN file transfer, VPN P2P, VPN streaming, VPN VoIP
B	chat, email, file transfer, P2P, streaming, VoIP, VPN chat, VPN email, VPN file transfer, VPN P2P, VPN streaming, VPN VoIP

Figure 7 Input directory structure for Scenario A-1

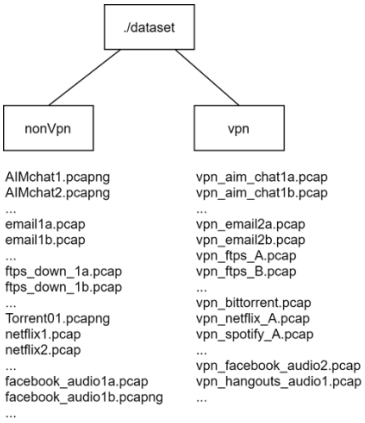

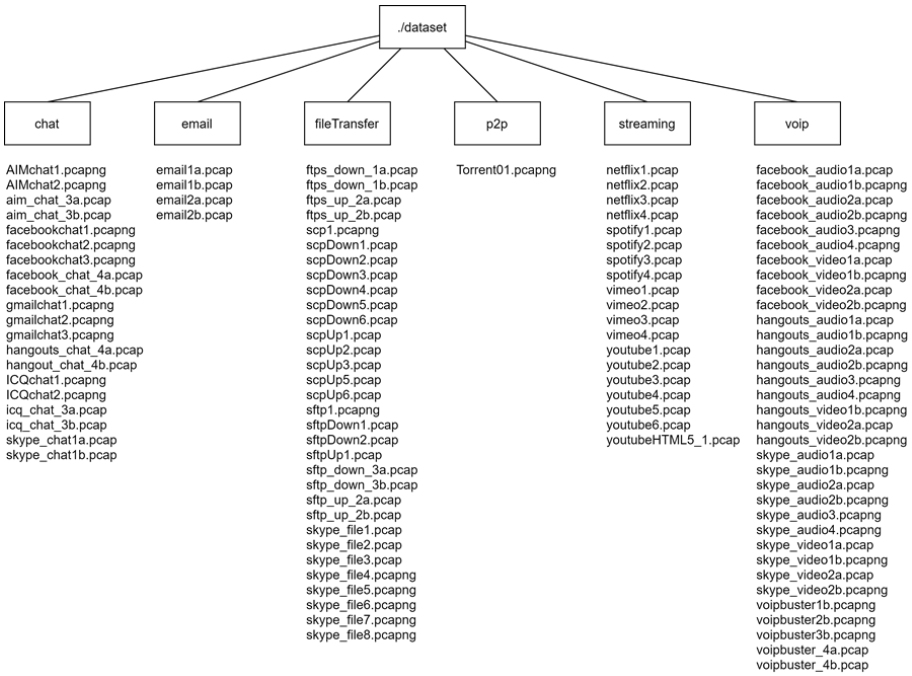

Figure 8 Input directory structure for Scenario A-2 non-VPN

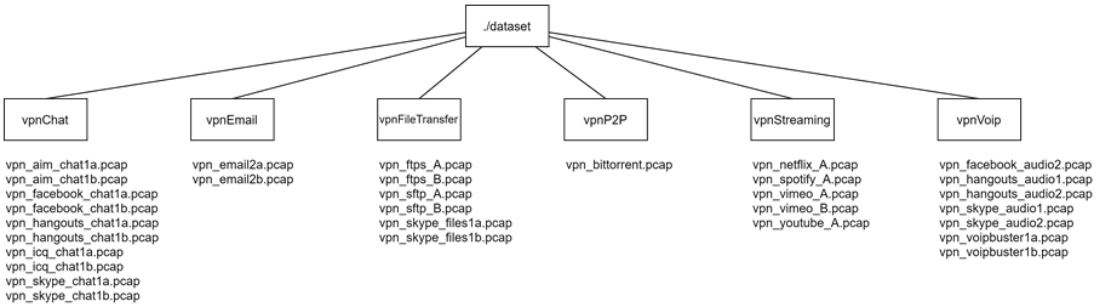

Figure 9 Input directory structure for Scenario A-2 VPN

4.3. Experimental Setup

4.3.1. Hardware Specifications

All tests are executed on a commercial PC with Intel Core i7-8750H CPU @ 2.20GHz and 16 GB RAM. The CPU has 12 cores.

4.3.2. Data Sampling

Since it takes too long to process millions of data (See Tables 5, 6, 7), LSTM-FS creates sub-datasets. For every scenario, 10,000 data is chosen randomly per label (Figure 10), in a way that packet order in sequences is preserved. For its tests, it repeats this process five times to generate five models.

Table 5 Scenario A-1 sample distribution before sampling

Label	Number of Samples
nonVpn	20,998,396
vpn	4,796,577

Table 6 Scenario A-2 non-VPN sample distribution before sampling

Label	Number of Samples
chat	91,509
email	18,329
fileTransfer	10,736,535
p2p	105,031
streaming	729,343
voip	7,459,544

Table 7 Scenario A-2 VPN sample distribution before sampling

Label	Number of Samples
vpnChat	80,497
vpnEmail	20,132
vpnFileTransfer	372,354
vpnP2P	419,646
vpnStreaming	1,510,282
vpnVoip	2,393,401

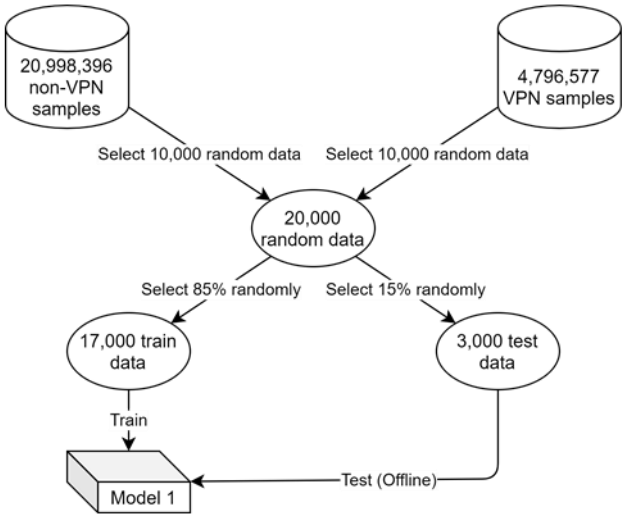

Figure 10 Model generation example (Scenario A-1)

4.3.3. Parameters

All LSTM-FS models use the same 17 features. Features ipHeaderLength and tcpUrgentPointer are discarded by the algorithm since they are the same for all chosen samples. The feature scaling method is normalization. Dropout is 0.1. The sequence length is 10. 75% of the data is used to train, 15% to validate, and 10% to test. Class weight optional parameter is unused since there already exists an equal amount of data per label. Chunk size is 1 million, the batch count is 128. Epoch count is 1. For scenarios A-2 non-VPN and B, Adam learning rate was changed to 0.01 from 0.001. (This had an impact on accuracy around 3%.) For online classification, 1 sender and 11 reader threads test each model first. The goal is to decide on an appropriate distribution type for sent packet amounts to replace the sender thread. The packet buffer is made large enough to prevent packet drops. 10 tests run to get average accuracy and time results. There is no restriction on how many packets LSTM-FS should see before classification; every sample immediately enters the classification model. A sample is classified as unknown if the best probability is under a limit which a formula given in Section 3 calculates.

4.4. Test Results

Average accuracy results, and average elapsed times are shared for all test scenarios. Time values presented are in seconds; averaged results denote

that the related test ran five times. Accuracy column corresponds to correctly classified instances percentage; precision, recall, and F-measure are weighted averages.

4.4.1. Offline Classification

Table 8 exhibits the average accuracy results of offline classification with LSTM-FS for all scenarios. Table 9 shows the average elapsed times.

Table 8 LSTM-FS (Offline) average accuracy results

Scenario	Accuracy	Precision	Recall	F-Score
A-1	99.818	0.9982	0.9982	0.9982
A-2 non-VPN	97.988	0.9804	0.9799	0.9799
A-2 VPN	96.828	0.9691	0.9683	0.9683
B	96.43	0.9658	0.9643	0.9644

Table 9 LSTM-FS (Offline) average elapsed times

Scenario	Data Generation	Training	Testing
A-1	562.73	12.68	2.39
A-2 non-VPN	291.39	25.96	3.54
A-2 VPN	26.62	28.08	3.73
B	432.17	68.29	7.36

4.4.2. Online Classification

After five runs for the first model, as can be seen from Figure 11 that the sender tends to send a low number of packets rather than a high number. In other words, the sender rarely holds the CPU for long and sends a high number of packets at once; on the contrary, it releases the CPU quite often, resulting in a lower number of piled-up packets. The mean and standard deviation is 81.3062 and 497.534, respectively. The exponential distribution fits this data. The rate parameter (λ) is 0.0122 ($1/\mu$).

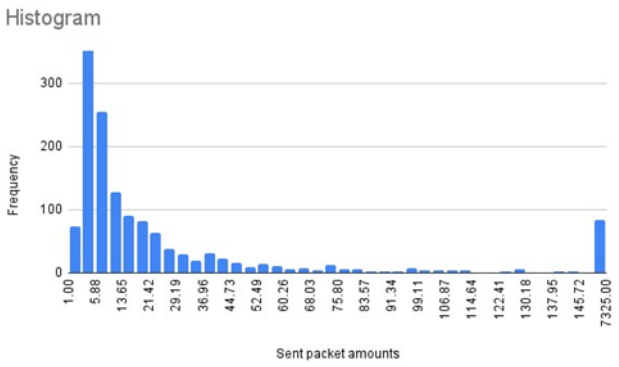

Figure 11 LSTM-FS (Online) Scenario A-1 model 1 sent packet amounts histogram

The maximum amount of sent packets is 7,970. However, the packet buffer size is decided as 25,000 since further experiments showed that sometimes each reader gets a few packets, then the remaining packets are received by the one who finishes reading first.

Table 10 exhibits the average accuracy results of online classification with LSTM-FS for all scenarios. Table 11 shows the average elapsed times.

Table 10 LSTM-FS (Online) average accuracy results

Scenario	Accuracy	Precision	Recall	F-Score	Unknown (%)
A-1	99.8554	0.9986	0.9986	0.9986	6.93
A-2 non-VPN	94.8119	0.9551	0.9515	0.9506	0.65
A-2 VPN	83.8309	0.8477	0.8346	0.8319	5.6
B	88.3211	0.9098	0.8849	0.8874	0.1

Table 11 LSTM-FS (Online) average elapsed times

Scenario	Testing	Packet/Second	Packet Processing Overhead (msec)
A-1	14.45	1,856.99	0.5398
A-2 non-VPN	60.81	1,355.75	0.7477
A-2 VPN	35.73	2,466.01	0.4058
B	116.89	1,529.62	0.6786

4.5. Evaluation

In the following charts (Figure 12, 13, 14, 15, 16, 17, 18, 19); LSTM-FS (Offline), LSTM-FS (Online) precision and recall values are shown together with the work (C4.5) by Draper-Gil et al. [15]. They did flow-based classification. They got the best accuracy with the C4.5 algorithm. The purple columns in the charts correspond to their work; the values are from their paper, but there may be slight differences as they did not share the exact values. The blue columns represent offline LSTM results, while the green ones are online LSTM results. The reason for choosing precision and recall metrics is that Draper-Gil et al. only presented these values. They displayed the values per label: BRW (browsing), CHAT, STR (streaming), MAIL, VOIP, P2P, and FT (file transfer). Label BRW is left out from the graphs since our work does not contain this label. It can be generalized that offline LSTM performs the best, followed by online LSTM. Please note that the comparison between our method and Draper-Gil et al.'s could be fairer if we used the same labeling. Even though we used the same dataset, this was not possible since they did not share how they labeled each PCAP file. For example, it is unclear which PCAPs they associated with the label BRW.

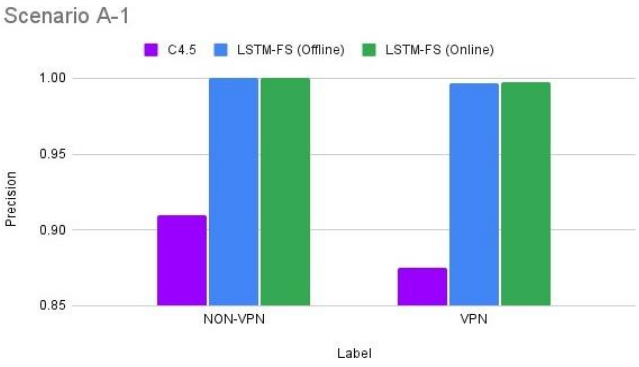

Figure 12 Precision comparison of [15], LSTM-FS (Offline), LSTM-FS (Online) for Scenario A-1

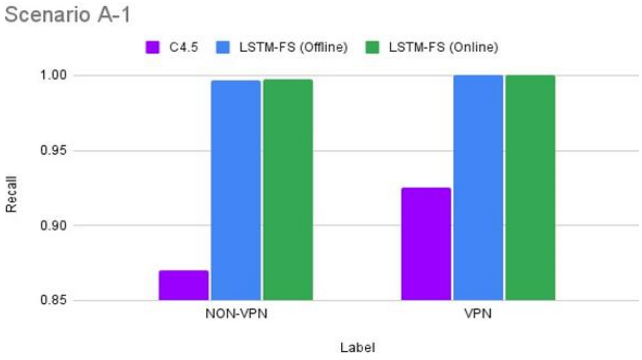

Figure 13 Recall comparison of [15], LSTM-FS (Offline), LSTM-FS (Online) for Scenario A-1

For scenario A-1, this study gives much better results than theirs, and there is not much difference between offline/online LSTM. As precision is related to false positives, we can infer that all three algorithms are prone to mislabeling as VPN where the actual label is non-VPN. On the other hand, a higher recall means a lower number of false negatives, which suggests that all three algorithms are better at identifying VPN traffic than non-VPN. Since there are only two labels for this scenario, precision and recall gave similar meaning results.

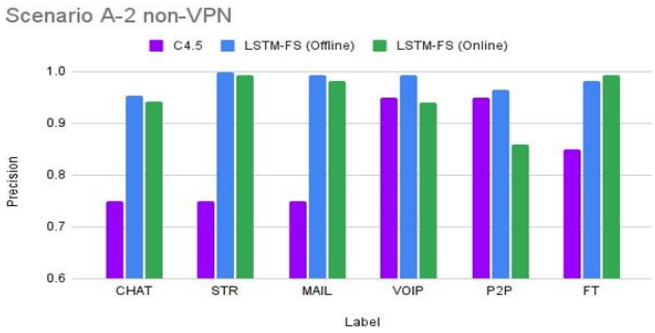

Figure 14 Precision comparison of [15], LSTM-FS (Offline), LSTM-FS (Online) for Scenario A-2 non-VPN

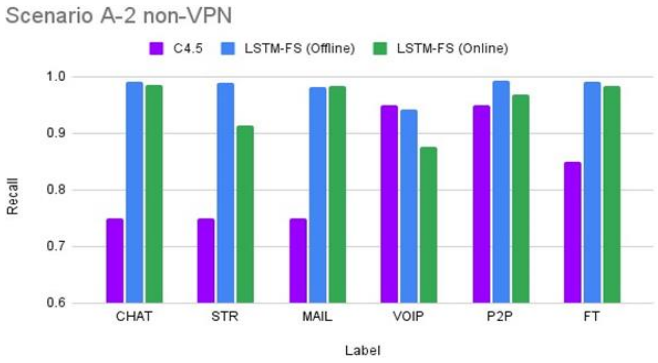

Figure 15 Recall comparison of [15], LSTM-FS (Offline), LSTM-FS (Online) for Scenario A-2 non-VPN

Scenario A-2 precision results show that except for VOIP and P2P our both algorithms excelled (especially for CHAT, STR, and MAIL). Offline LSTM is generally better than online; for FT, online LSTM has the best result. The difference between both algorithms stands out for VOIP and P2P. Furthermore, for P2P, C4.5 performs better than online LSTM. Label CHAT seems to have more false positives than the other labels for all algorithms. Regarding recall results, online LSTM now beat C4.5 for P2P. It means that even though C4.5 gives fewer false positives, it gives more false negatives for P2P. Interestingly, for VOIP, C4.5's recall result is better than both of our algorithms'. C4.5 is especially good at differentiating VOIP among other non-VPN labels.

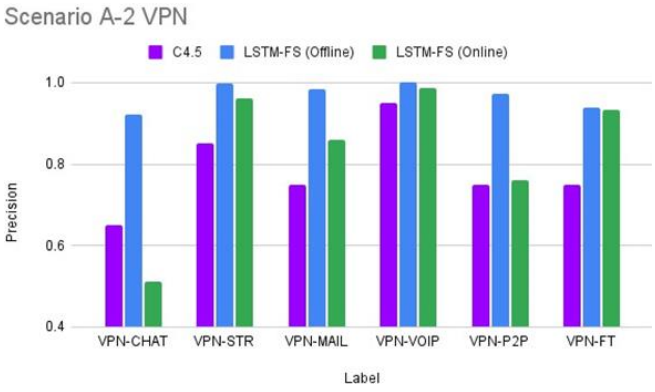

Figure 16 Precision comparison of [15], LSTM-FS (Offline), LSTM-FS (Online) for Scenario A-2 VPN

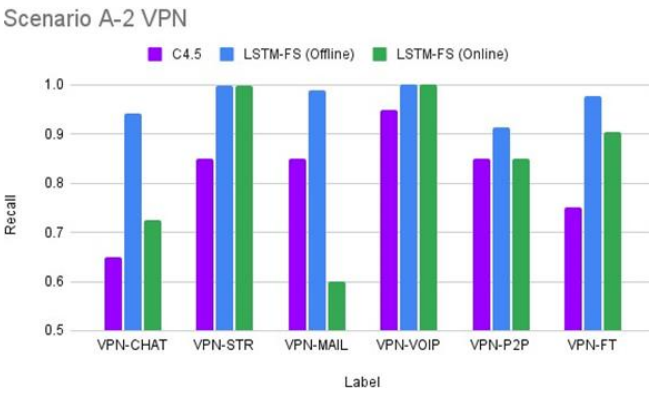

Figure 17 Recall comparison of [15], LSTM-FS (Offline), LSTM-FS (Online) for Scenario A-2 VPN

Offline LSTM stands out for its Scenario A-2 VPN-CHAT precision result, whereas online LSTM performed the worst. For the rest of the labels, our algorithms performed much better than C4.5. However, VPN-VOIP results are close. VPN-MAIL recall result for online LSTM is especially low.

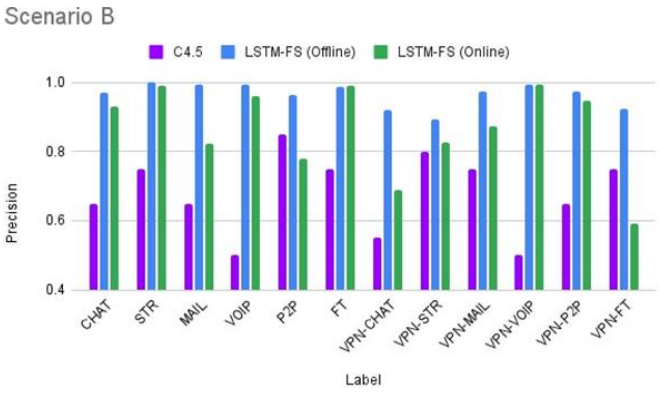

Figure 18 Precision comparison of [15], LSTM-FS (Offline), LSTM-FS (Online) for Scenario B

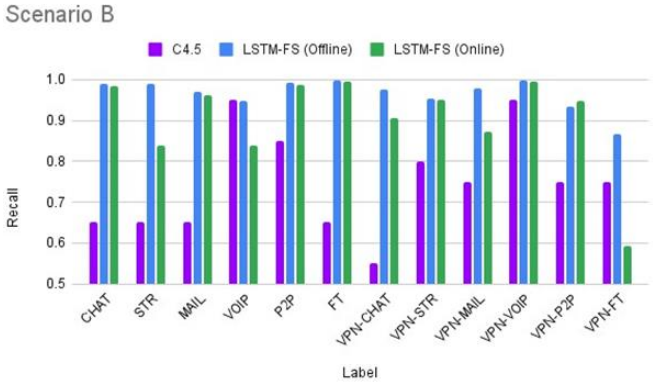

Figure 19 Recall comparison of [15], LSTM-FS (Offline), LSTM-FS (Online) for Scenario B

C4.5 VOIP and VPN-VOIP precision performance are surprisingly not good for Scenario B, even though it excelled for Scenario A-2 non-VPN and VPN. It can be said that when non-VPN and VPN labels are mixed C4.5 struggles to identify correctly. Both algorithms seem to be better at this. Online LSTM especially struggles with P2P and VPN-FT. C4.5 VOIP and VPN-VOIP recall results are still good; however, none of the recall results beat our algorithms.

Byte Segment Neural Network [27] spends 43 msec for each data sample at the training phase, and the total training time is 123 minutes. On average, training takes at most 68.29 seconds with LSTM-FS for Scenario B. Thus, processing overhead per sample is 0.5 msec, since Scenario B consists of 120,000 data. On the other hand,

they measured the average time to deal with a sample during online classification as 2.97 msec and shared that for Securitas [28] this is 7.01 msec. Packet processing overhead is at most 0.7477 msec with LSTM-FS for Scenario A-2 non-VPN.

5. CONCLUSION

The problem we tried to attack is to classify encrypted packets using the packet headers. An LSTM deep learning model trained with features that can be taken directly from a network packet is presented in this study. The method yields valid results regarding both its speed and accuracy, outperforming a well-known machine learning study. Compared to the only paper that shared its online classification results [27], the LSTM model presented in this paper gave better results in terms of speed. We are confident that this model can be used for real life situations.

The design presented in this study can be easily used not only for categorization but also for other types of traffic classification (e.g., protocol or application classification). All that needs to be done is to pre-label the input data correctly and introduce these labels to the algorithm. In addition, a new feature can be easily added to the algorithm, or an existing feature can be removed. For these reasons, it can be said that this study will be instrumental in paving the way for many future studies such as intrusion detection systems.

Funding

The authors have not received any financial support for the research, authorship or publication of this study.

The Declaration of Conflict of Interest/Common Interest

No conflict of interest or common interest has been declared by the authors.

The Declaration of Ethics Committee Approval

This study does not require ethics committee permission or any special permission.

The Declaration of Research and Publication Ethics

The authors of the paper declare that they comply with the scientific, ethical and quotation rules of SAUJS in all processes of the paper and that they do not make any falsification on the data collected. In addition, they declare that Sakarya University Journal of Science and its editorial board have no responsibility for any ethical violations that may be encountered, and that this study has not been evaluated in any academic publication environment other than Sakarya University Journal of Science.

Authors' Contribution

The authors contributed equally to the study.

REFERENCES

[1] H. Tahaei, F. Afifi, A. Asemi, F. Zaki and N. B. Anuar, "The rise of traffic classification in IoT networks: A survey," Journal of Network and Computer Applications, vol. 154, 102538, 2020.

[2] O. Salman, I.H. Elhajj, A. Kayssi et al., "A review on machine learning-based approaches for Internet traffic classification," Annals of Telecommunications, vol. 75, no. 11, pp. 673-710, 2020.

[3] Z. J. Al-Araji, S. S. S. Ahmad, M. W. Al-Salihi, H. A. Al-Lamy, M. Ahmed, W. Raad and N. M. Yunos, "Network Traffic Classification for Attack Detection Using Big Data Tools: A Review," Lecture Notes in Networks and Systems, pp. 355-363, 2019.

[4] M. AlSabah, K. Bauer and I. Goldberg, "Enhancing Tor's performance using real-time traffic classification," ACM conference on Computer and communications security, pp. 73-84, 2012.

[5] IANA. Service Name and Transport Protocol Port Number Registry [Online]. Available: https://www.iana.org/assignments/service-names-port-numbers/service-names-port-numbers.xhtml. [Accessed April 27, 2022].

[6] J. Khalife, A. Hajjar and J. Diaz-Verdejo, "A multilevel taxonomy and requirements for an optimal traffic-classification model," International Journal of Network Management, vol. 24, no. 2, pp. 101-120, 2014.

[7] Google. HTTPS encryption on the web [Online]. Available: https://transparencyreport.google.com/https/overview?hl=en. [Accessed April 27, 2022].

[8] S. Rezaei and X. Liu, "Deep Learning for Encrypted Traffic Classification: An Overview," IEEE Communications Magazine. vol. 57. no. 5. pp. 76-81, 2019.

[9] Wireshark [Online]. Available: https://www.wireshark.org. [Accessed April 27, 2022].

[10] UNB. VPN-nonVPN dataset (ISCXVPN2016) [Online]. Available: https://www.unb.ca/cic/datasets/vpn.html. [Accessed April 27, 2022].

[11] B. Yamansavascilar, A. Guvensan, A. Yavuz, and E. Karsligil, "Application identification via network traffic classification," International Conference on Computing, Networking and Communications (ICNC), pp. 843-848, 2017.

[12] E. Hjelmvik. SPID Statistical Protocol Identification [Online]. Available: https://sourceforge.net/projects/spid. [Accessed April 27, 2022].

[13] E. Hjelmvik. The SPID Algorithm Statistical Protocol IDentification. 2008.

[14] E. Hjelmvik and W. John, "Statistical Protocol IDentification with SPID: Preliminary Results," Swedish National Computer Networking Workshop. vol. 9. pp. 4-5, 2009.

[15] A. H. Lashkari, G. Draper-Gil, M. S. I. Mamun, and A. A. Ghorbani, "Characterization of Encrypted and VPN Traffic Using Time-Related Features," In Proceedings of the 2nd international conference on information systems security and privacy (ICISSP), pp. 407-414, Feb. 2016.

[16] S. Bagui, X. Fang, E. Kalaimannan, S. C. Bagui, and J. Sheehan, "Comparison of machine-learning algorithms for classification of VPN network traffic flow using time-related features," Journal of Cyber Security Technology. vol. 1. no. 2. pp. 108-126, 2017.

[17] W. Wang, M. Zhu, J. Wang, X. Zeng, and Z. Yang, "End-to-end encrypted traffic classification with one-dimensional convolution neural network," IEEE International Conference on Intelligence and Security Informatics (ISI), pp. 43-48, 2017.

[18] echowei. Deep Learning models for network traffic classification [Online]. Available: https://github.com/echowei/DeepTraffic. [Accessed April 27, 2022].

[19] yungshenglu. USTC-TK2016 [Online]. Available: https://github.com/yungshenglu/USTC-TK2016. [Accessed April 27, 2022].

[20] M. Lotfollahi, R. S. H. Zade, M. J. Siavoshani, and M. Saberian, "Deep Packet: A Novel Approach For Encrypted Traffic Classification Using Deep Learning," Soft Computing, vol. 24. no. 3, pp. 1999-2012, 2020.

[21] A. Parchekani, S. N. Naghadeh, and V. Shah-Mansouri, "Classification of Traffic

Using Neural Networks by Rejecting: a Novel Approach in Classifying VPN Traffic," Jan. 2020. arXiv preprint arXiv:2001.03665.

[22] K. Zhou, W. Wang, C. Wu, and T. Hu, "Practical evaluation of encrypted traffic classification based on a combined method of entropy estimation and neural networks," ETRI Journal, vol. 42, no. 3, pp. 311-323, 2020.

[23] UNB. Tor-nonTor dataset (ISCXTor2016) [Online]. Available: https://www.unb.ca/cic/datasets/tor.html. [Accessed April 27, 2022].

[24] M. Lopez-Martin, B. Carro, A. Sanchez-Esguevillas, and J. Lloret, "Network Traffic Classifier With Convolutional and Recurrent Neural Networks for Internet of Things," IEEE Access, vol. 5, pp. 18042-18050, 2017.

[25] RedIRIS. Welcome to RedIRIS [Online]. Available: https://www.rediris.es. [Accessed April 27, 2022]

[26] L. Deri, M. Martinelli, T. Bujlow, and A. Cardigliano, "nDPI: Open-source high-speed deep packet inspection," International Wireless Communications and Mobile Computing Conference (IWCMC). pp. 617-622, 2014.

[27] R. Li, X. Xiao, S. Ni, H. Zheng, and S. Xia, "Byte Segment Neural Network for Network Traffic Classification," IEEE/ACM 26th International Symposium on Quality of Service (IWQoS). pp. 1-10, Jun. 2018.

[28] X. Yun, Y. Wang, Y. Zhang, and Y. Zhou, "A Semantics-Aware Approach to the Automated Network Protocol Identification," IEEE/ACM Transactions on Networking. vol. 24. no. 1. pp. 583-595, 2016.

[29] tcpdump. TCPDUMP/LIBPCAP public repository [Online]. Available: https://www.tcpdump.org. [Accessed April 27, 2022].

[30] tcpreplay. tcprewrite [Online]. Available: https://tcpreplay.appneta.com/wiki/tcprewrite. [Accessed April 27, 2022].

[31] Abadi et al. TensorFlow: Large-scale machine learning on heterogeneous systems [Online]. Available: tensorflow.org. 2015. [Accessed April 27, 2022].

[32] F. Chollet et al. Keras [Online]. Available: https://keras.io. 2015. [Accessed April 27, 2022].

[33] serizba. CppFlow [Online]. Available: https://github.com/serizba/cppflow. [Accessed April 27, 2022].

SAKARYA ÜNİVERSİTESİ
FEN BİLİMLERİ ENSTİTÜSÜ DERGİSİ

Sakarya University Journal of Science
SAUJS

e-ISSN 2147-835X Period Bimonthly Founded 1997 Publisher Sakarya University
http://www.saujs.sakarya.edu.tr/

Title: CFD Analysis of Convection Heat Transfer in Corrugated Channels for Different Inclination Angle

Authors: Haydar KEPEKÇİ, Erman ASLAN

Recieved: 2022-02-07 00:00:00

Accepted: 2022-03-08 00:00:00

Article Type: Research Article

Volume: 26
Issue: 2
Month: April
Year: 2022
Pages: 333-341

How to cite
Haydar KEPEKÇİ, Erman ASLAN; (2022), CFD Analysis of Convection Heat Transfer in Corrugated Channels for Different Inclination Angle. Sakarya University Journal of Science, 26(2), 333-341, DOI: 10.16984/saufenbilder.1069682
Access link
https://dergipark.org.tr/tr/journal/1115/issue/69580/1069682

New submission to SAUJS
http://dergipark.gov.tr/journal/1115/submission/start

Sakarya University Journal of Science 26(2), 333-341, 2022

CFD Analysis of Convection Heat Transfer in Corrugated Channels for Different Inclination Angle

Haydar KEPEKÇİ*[1], Erman ASLAN[2]

Abstract

Three different geometries have been used in this study, which investigated the effect of inclination angle on convective heat transfer in corrugated channels. The corrugated channel geometries used have inclination angles of 30°, 45°, and 60°. The finite volume method has been used in the study with numerical methods. k-ω, SST, and transition SST have been used as turbulence models. The mesh file used in the analysis consists of 192000 cells. The results obtained from the calculations using a corrugated channel with a 30° inclination angle have been compared with the experimental data. As a result of this comparison, the turbulence model to be used for this study has been determined as SST. SST turbulence model has been used in the analyzes made using a corrugated channel with 45° and 60° inclination angles and the results have been compared with each other. The Reynolds number ranges from 2225 to 7380. The Nusselt number and friction factor have been calculated using the data obtained as a result of the analysis. Based on the calculated values, it has been determined that the heat transfer increases as the angle of inclination increases in the corrugated channels. It has been also observed that the Nusselt number increased as the Reynolds number increased. It has been also seen that the analyzes for high Reynolds number gave results closer to the experimental data.

Keywords: Corrugated channel, inclination angle, heat transfer, turbulence models, Nusselt number.

1. INTRODUCTION

The amount of energy we use is increasing day by day due to the fact that technological devices are well-established in our lives. This increase in demand has led to an increase in energy costs. As a result of the home-office working system, which has become widespread with the Covid-19 pandemic, the use of air conditioning devices has also increased in order to provide thermal comfort in the building [1]. The use of these devices has been also reflected as a heavy burden on electricity bills. As a solution to this situation, the option of increasing the thermal performance of air conditioning devices that provide heat transfer has come to the fore. Heat exchangers have a wide area of use apart from air conditioning systems [2]. Examples of these are petroleum-chemical industries, refineries, food industries, and power plants. Traditional heat exchangers need to be

* Corresponding author: haydar.kepekci@nisantasi.edu.tr
[1] Nişantaşı University
ORCID: https://orcid.org/0000-0002-0037-8332
[2] Kocaeli University, Faculty of Engineering, Department of Mechanical Engineering
E-mail: erman.aslan@kocaeli.edu.tr
ORCID: https://orcid.org/0000-0001-8595-6092

redesigned in order to both reduce energy costs and save energy. One of the studies carried out in this context is to increase the use of corrugated channels [3]. The use of corrugated channels is a suitable method to increase thermal performance [4, 5].

The instability occurring in the thermal boundary layers arises when the fluid is flowing from the corrugated surfaces. In other words, corrugated channels change the modification of the flow by means of planes perpendicular to the main flow direction, making it turbulent. Thus, they significantly increase the heat transfer compared to straight channels. In recent years, many scientists have conducted experimental and numerical studies on the effect of corrugated channels on heat transfer. Tokgoz et al. investigated the effects of two different phase shifts of wavy channels on the flow hydrodynamics and the heat transfer rate for different Reynolds numbers. They used the PIV technique while observing turbulent flows and tracking flow velocities. They found that the cavity inlets in the corrugated channels create a vortex as it accelerates the flow movement and this increases the heat transfer. They conducted both numerical and experimental studies and found that the results they found in the two cases have been compatible with each other [6]. Aliabadi and Feizabadi investigated the hydrothermal performance of the flow using a square-section corrugated channel in their study. They compared the results of their initial calculations with the data in the literature and found that they have been suitable. They then tested each region of the corrugated channel separately and found that the sidewalls prevented the development of thermal boundary layers along with the flow. They assumed that the flow has been laminar in all calculations [7].

Ajeel et al. carried out numerical analyzes to investigate the effect of a corrugated channel on thermal performance in turbulent flows in the range of 10,000-30,000 Reynolds numbers. In their analysis, they assumed that there are SiO2 nanoparticles in the fluid medium. As a result, they found that the height-to-width ratio has a greater effect on increasing heat transfer than the pitch-length ratio [8]. Nayak and Weigand investigated the effect of corrugated channels on the mixing ratio using two different miscible liquids with different concentrations. As a result of their studies, they observed that the pressure change has a great effect on the regions that provide zero gradients throughout the fully developed regions. They also determined that a high convective zone should be created in order to increase the temperature of the liquids in the channel [9].

In their study, Ionescu and Neagu investigated the effect of the sinusoidal wavy corrugated channel model on heat transfer. In this study, a finite element method-based CFD program has been used. They kept the channel length and wavelength constant in their simulations. The modified lengths have been the width and amplitude of the channel. As a result, they have seen that the thickness of the lower wall has a great effect on the Nusselt Number in sinusoidal wavy corrugated channel geometry [10] Ahmed et al. investigated convective heat transfer numerically and experimentally by using nanofluids in trapezoidal, sinusoidal, and straight corrugated channels. The Reynolds number they used in their numerical analysis is in the range of 400-4,000 and they used the SIMPLE algorithm in the solutions. As a result, they found that the trapezoidal slotted channel provides the highest heat transfer increase, followed by the sinusoidal slotted channel and the straight slotted channel. They also found that the numerical results have been in good agreement with the experimental data [11].

Pehlivan et al. experimentally investigated the heat transfer rate using a sinusoidal slotted channel. In their study using different undulation angles, they accepted the Reynolds number between 1,500-8,000. They concluded that increasing the slotted angle accelerated the heat transfer [12]. In their study, Yin et al. investigated heat transfer and flow properties by using corrugated sinusoidal wavy channels for the different phase shifts between upper and lower wavy plates with the same diameter. During the calculations, the Reynolds number has been accepted as 2,000-10,000 and the Pr number as

0.696. As a result, they have seen that although the use of corrugated ducts increases the pressure loss, it will also increase the heat transfer due to its effect on the Nusselt number. They also found that the effect of phase shift on heat transfer is more pronounced in the high Re region of the slotted channels than in the low Re region [13]. Elshafei et al. experimentally investigated the convective heat transfer and pressure drop properties of flow in corrugated channels. Experiments have been carried out on channels with a constant groove ratio in the range of 3,220-9,420 Reynolds numbers. As a result, they found that the results of corrugated channel flow create a significant increase in heat transfer with the penalty for increased pressure drop. They also considered the effects of spacing and phase shift. They found that the friction factor increased with increasing channel spacing and phase shift. They noticed that the effect of gap changes on heat transfer has been more pronounced than phase shift change, especially at a high Reynolds number [14].

Ahmed et al. numerically investigated the forced convection heat transfer of a copper-water nanofluid in a trapezoidal corrugated channel. The momentum and energy equations they used have been discretized using the finite volume approach and they have been solved iteratively using the SIMPLE technique. As a result, they found that as the wavelength of the corrugated channel decreases, the average Nusselt number increases, and the pressure drop decreases [15]. Naphon conducted an experimental study to see the heat transfer and pressure drop in the corrugated channel under constant heat flux. Three channels with two opposing corrugated plates have been used during the experiments. The inclination angles of the channels, each of which has a height of 12.5 mm, have been chosen as 20°, 40° and 60°. Experiments have been made for the Reynolds number range of 500-1,400. As a result, he found that the corrugated surface has a significant effect on increasing the heat transfer and pressure drop due to the presence of recirculation zones [16].

The aim of this study is to determine the effect of inclination angle on convective heat transfer in corrugated channels. For this reason, numerical analyzes have been made using three different corrugated channel geometries and the results have been compared among themselves. First, numerical calculations have been made for the corrugated channel with a 30° inclination angle. During these calculations, different turbulence models have been used, namely k-ω, SST, and transition SST. The results obtained from these analyzes have been compared with the experimental data [17]. By determining the turbulence model that gives the closest result to the experimental data, analyzes have been made for corrugated channels with 45° and 60° inclination angles. Finally, the obtained results have been compared with each other and the effect of inclination angle on heat transfer has been investigated.

2. NUMERICAL METHOD

During this study, buoyancy forces have been not taken into account while performing numerical analysis. Geometry has been considered as two-dimensional while calculations have been made. Corrugated channels with different inclination angles have been drawn in the SolidWorks program and the mesh file created by dividing into grids has been created using the Pointwise program. This study has been carried out with numerical method and ANSYS Fluent, one of the most common computational fluid dynamics (CFD) programs in the market, has been used. The use of CFD analysis has been increasing in recent years. The reason for this is that it is cheaper and more practical than experimental studies. One of the most important parameters in all scientific studies is time [18]. The use of CFDs provides significant time savings. The most commonly used turbulence models in programs with CFD codes suitable for different flow characteristics are those based on Reynolds Average Navier Stokes [19]. There are basically two of these models, k-ω, and k-ε. The k-ε model gives more accurate results in regions where the boundary layer is weak, and the k-ω model in other regions. The SST model, which emerged as a combination of these two models, is frequently preferred among RANS-based methods [19]. While entering convergence criteria values, 10-8 is taken

for energy equations, while this value is determined as 10-6 for other equations. It is assumed that the turbulence intensity at the entrance of the channel is 4% and the mixing length is equal to 30% of the hydraulic diameter. These values have been obtained with experimental data.

2.1. General situation definition

The appearance of the symmetrical corrugated channel with different inclination angles used in this study is shown in Figure 1. 30°, 45°, and 60° have been selected as the inclination angle values. The a, b, and Hmin lengths of the channels used in the study have been taken from the experimental study as 5 [mm], 2.5 [mm], 5 [mm], respectively. The length S is obtained from the drawn channel geometries as 17.32 [mm] for 30^o, 10.231 [mm] for 45^o, and 5.77 [mm] for 60^o. The development of the flow in the channel and the temperature distributions have been observed and the effect of different inclination angles on increasing the heat transfer has been examined. During the study, the Reynolds number varies between 2,100 and 7,600. Prandtl number (Pr) has been accepted as 0.7 in all analyzes.

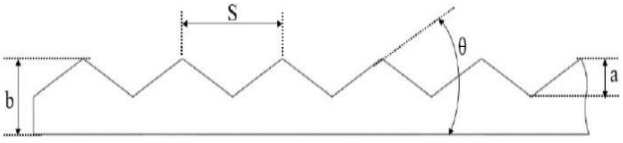

Figure 1 Corrugation channel with the parameters [20]

Maximum channel height is taken by,

$$H_{max} = 2b$$

The minimum channel height is described as,

$$H_{min} = 2(b - a)$$

2.2. Meshing

In order to be able to solve using the CFD program, it is necessary to create a mesh file by dividing the workpiece into grids [21]. More than one mesh file is created and analyzes are made using the same parameters. The results of the analyzes obtained are compared among themselves, and the file with less grid than those that give close results is selected and used in numerical analyzes using different parameters. This process is called mesh independence [21]. Mesh independence has been not performed in this study. The reason for this is that it is known that a mesh file containing 192,000 grid cells has been used in a similar study done before. Time is saved by not repeating the same process. It is necessary to pay attention to some parameters in the process of creating a mesh file. One of them is the y+ value. The y+, which means the mesh fineness in the area close to the wall, indicates the sensitivity of the created mesh file. As the sensitivity of the y+ value increases, the accuracy of the results obtained from the CFD analysis also increases [22]. In this study, the y+ value has been determined as 0.6. The small value of this value increased the sensitivity of the results of the analysis. A close view of the grid cells created in the mesh file is given in Figure 2.

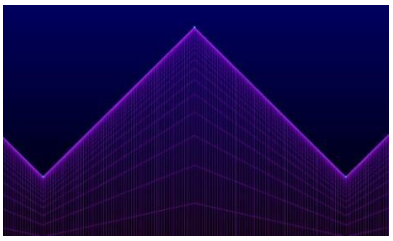

Figure 2 The close-up of mesh cells

2.3. Dimensionless Numbers

In this study, two different parameters have been selected and calculated in order to evaluate the effect of the peak angle of the corrugated channels on the heat transfer. These have been determined as Nusselt number and friction factors. The results obtained from the numerical analyzes have been compared with the experimental data. When the experimental setup has been examined, it has been observed that the flow in the corrugated channel became regular in the last three nodes. For this reason, the values used in calculating the Nusselt number and friction factor have been taken from those regions at the end of the numerical analysis.

The calculation of the Nusselt number (Nu) is given in Eq. 1;

$$Nu = \frac{h.D_h}{k} \quad (1)$$

k and h represent thermal conductivity and heat transfer coefficient, respectively [20].

The formula for the heat transfer coefficient (*h*) calculated by integrating the last three cycles of the channel is given in Eq. 2;

$$h = \frac{1}{3S}\int_0^S h_x d_x \quad (2)$$

The calculation of the friction factor (f) is given in Eq. 3;

$$f = -\frac{dP}{dx} D_h / \frac{1}{2}\rho {u_o}^2 \quad (3)$$

ρ and u_o represent density and velocity, respectively [20].

3. RESULTS

In Figure 3. the predictions of the axial velocity distribution of the calculations made with the SST turbulence model in three corrugated channel geometries are channels with (a) 60°, (b) 45° and (c) 30° inclination angles. During the calculations in which these figures have been taken, the velocity and Reynolds number have been accepted as 6.8 m/s and 7380, respectively. It is seen that the place where the flow fully develops is the cycle in the last parts of the channel. It has been determined that the flow in the corrugated channel with a 60° inclination angle is higher velocity than the flow in the other two-channel geometries. In the analyzes made, it has been seen that the corrugated channel geometry with a 45° inclination angle is also faster than the flow in the channel with a 30° inclination angle. In addition, it is seen that the turbulent region in the corrugated channel with an inclination angle of 60° is wider than the other channels. Therefore, the flow with the highest Nusselt number is obtained from the corrugated channel with a 60° inclination angle, followed by the flows in the corrugated channels with 45° and 30° inclination angles, respectively.

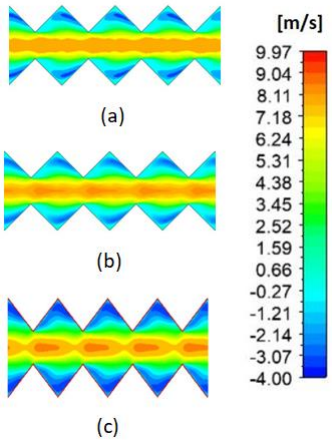

Figure. 3 Axial velocity by SST turbulence model for the corrugated channel (a) with a 60° inclination angle, (b) with a 45° inclination angle, (c) with a 30° inclination angle

In Fig. 4. the predictions of the temperature distribution of the calculations made with the SST turbulence model in three corrugated channel geometries are channels with (a) 60°, (b) 45°, and (c) 30° inclination angles. During the calculations in which these figures have been taken, the velocity and Reynolds number have been accepted as 6.8 m/s and 7380, respectively. It is seen that the place where the flow fully develops is the cycle in the last parts of the channel. The last sections of the corrugated channels are called the recirculation zone, and it is seen that the cold fluid coming from the channel mixes more intensely with the hot fluid near the boundary layer. This situation causes the highest temperature change values in the channels to be encountered at the wall edges. It is seen that the temperature gradients increase in the recirculation regions in parallel with the increase in the angle of inclination in the corrugated channels. These wall temperatures are among the factors that increase heat transfer. Therefore, the flow with the highest heat transfer efficiency has been seen in the corrugated channel with a 60° inclination angle, followed by the corrugated channel with a 45° and 30° inclination angle, respectively.

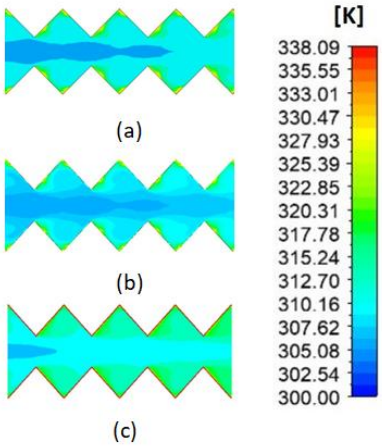

Figure 4 Temperature by SST turbulence model for the corrugated channel (a) with a 60° inclination angle, (b) with a 45° inclination angle, (c) with a 30° inclination angle

In order to compare the data obtained from this study with the experimental results (Aslan et al., 2016), the analyzes for the corrugated channel with a 30° inclination angle have been used. It has been researched which turbulence model would give the best results and it has been aimed to determine the model to be preferred in the next analysis. The turbulence models used in comparison with the experimental results have been determined as k-ω, SST, and transition SST. Nusselt number and friction factor values obtained from the numerical analysis results using these turbulence models have been compared with the experimental data and are given graphically in Figure 5 and Figure 6, respectively. In Figure 5, the Nusselt number increased in parallel with the Reynolds number. In addition, it has been determined that the results obtained from the analyzes using the high Reynolds number are more accurate than the analyzes using the low Reynolds number. This inference has been made by looking at the Reynolds values in Figure 5, where the Nusselt number obtained by calculating from the results of the numerical analysis approaches the experimental values. When the graph given in Figure 6 is examined, it is seen that the friction factor values obtained from the analyzes using different turbulence methods increase in parallel with the Reynolds number. It has been observed that the values obtained from the transition SST turbulence model have been much higher than the experimental data and the values obtained from the k-ω model have been much lower than the experimental data. It has been determined that the friction factor values obtained from the SST turbulence model are more successful in approaching the experimental data than other turbulence models. It has also been observed that numerical analyzes at high Reynolds numbers give more accurate results. In addition, both Figure 5 and Figure 6 show that the closest values to the experimental results have been obtained from the numerical analyzes using the SST turbulence model. For this reason, SST has been chosen as the turbulence model in the analyzes made for the corrugated channel with 45° and 60° inclination angles.

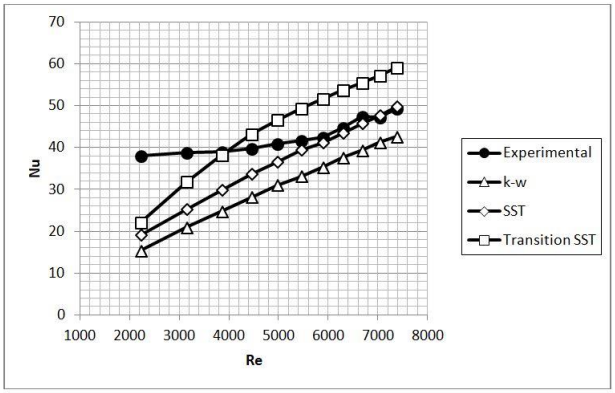

Figure 5 Comparison of Nusselt numbers from different turbulence methods

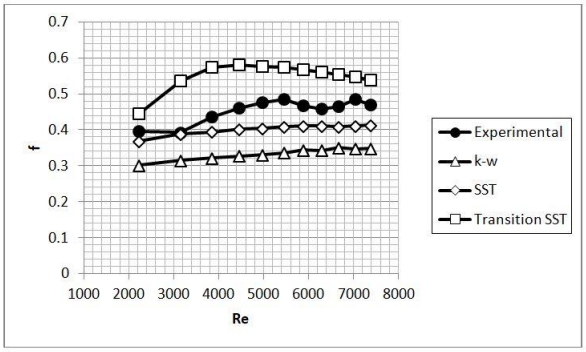

Figure 6 Comparison of friction factor from different turbulence methods

Figure 7 shows the Nusselt numbers obtained as a result of the calculations of corrugated channels with 30°, 45°, and 60° inclination angles using the SST turbulence method. According to this graph, the Nusselt number increases as the inclination angle increases in corrugated channels. In this case, it is concluded that the heat transfer is more efficient in channels with high inclination angles.

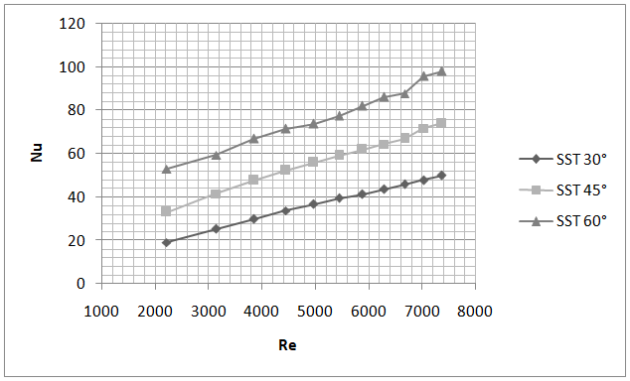

Figure 7 Comparison of Nusselt numbers from different inclination angles methods

In Figure 8, the friction factor values obtained as a result of the calculations of corrugated channels with 30°, 45°, and 60° inclination angles using the SST turbulence method are shown in the graph. According to this graph, the friction factor value decreases as the inclination angle increases in corrugated channels. In addition, in the analyzes made for high Reynolds number, it is seen that the friction factor value gives close results. This has been interpreted as the effect of inclination angle on the friction factor losing its importance when the velocity of the flow increases in corrugated channels.

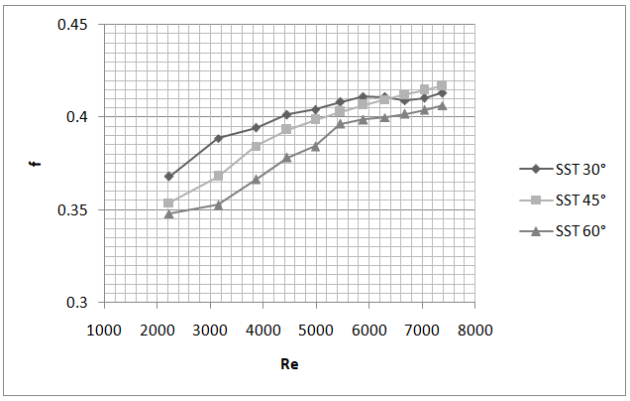

Figure 8 Comparison of friction factor from different inclination angles methods

4. CONCLUSIONS

In this study, numerical analyzes have been made by modeling corrugated channels with different inclination angles and the effect of inclination angle on heat transfer has been investigated. The inclination angles of the modeled corrugated channels have been determined as 30°, 45°, and 60°. Corrugated channel geometry with a 30° inclination angle has been drawn and analyzes have been made using three different turbulence models. These turbulence models have been chosen as k-ω, SST, and transition SST. They have been chosen because they are the most frequently used turbulence models in RANS-based studies in the literature. The Nusselt number and friction factor have been calculated using the data obtained from the analysis results. Calculated values have been compared with experimental data. As a result, it has been determined that the accuracy rate of the SST turbulence model is higher than other RANS based models. It has been decided to use the SST turbulence model in the analyzes of the corrugated channels with different inclination angles to be made from now on. Then, corrugated channel geometries with 45° and 60° inclination angles have been created and analyzes have been made using the SST turbulence model. Nusselt number and friction factor values have been calculated using the data obtained from the analyzes. The obtained values have been compared with each other. As a result of the study, the following information has been obtained;

- The inclination angle in corrugated channels is an option that can be used to increase heat transfer.
- If any numerical analysis is to be done for corrugated channels, the most suitable RANS-based turbulence model is SST.
- If the velocity of the flow is increased to increase the Reynolds number in corrugated channels, the Nusselt number will also increase and the heat transfer will increase.
- Increasing the angle of inclination in corrugated channels has a positive effect on heat transfer.
- As the inclination angle increases in the corrugated channels, the friction factor value decreases.

Many studies can be done on this subject by modifying the corrugated channel geometries. The next study will be calculations using

sinusoidal channels and comparison with the results of this study.

Funding

The authors have not received any financial support for the research, authorship, or publication of this study.

The Declaration of Conflict of Interest

No conflict of interest or common interest has been declared by the authors.

Authors' Contribution

The authors contributed equally to the study.

The Declaration of Ethics Committee Approval

This study does not require ethics committee permission or any special permission.

The Declaration of Research and Publication Ethics

The authors of the paper declare that they comply with the scientific, ethical, and quotation rules of SAUJS in all processes of the paper and that they do not make any falsification on the data collected. In addition, they declare that Sakarya University Journal of Science and its editorial board have no responsibility for any ethical violations that may be encountered and that this study has not been evaluated in any academic publication environment other than Sakarya University Journal of Science.

REFERENCES

[1] M. Miranda, P. Romero, V. Valero-Amora, J. Arranz, and I. Montero, "Ventilation conditions and their influence on thermal comfort in examination classrooms in times of COVID-19. A case study in a Spanish area with Mediterranean climate", International Journal of Hygiene and Environmental Health, vol.240, 113910, 2022.

[2] M. Astina, and M. Nugrah, "Numerical simulation of earth-air heat exchanger application for Indonesian simple house air conditioning system", Case Studies in Thermal Engineering, Vol.28, 101371, 2021.

[3] A. C. Benim, H. Chattapadhyay, and A. Nahavandi, "Computational Analysis of Turbulent Forced Convection in a Channel with a Triangular Prism", International Journal Thermal Sciences, vol. 50, no.10, pp. 1973-1983, 2011.

[4] I. Taymaz, E. Aslan, and A. C. Benim, "Numerical Investigation of Incompressible Fluid Flow and Heat Transfer across a Bluff Body in a Channel Flow", Thermal Sicences, vol.19, no.2, pp.537-547, 2015.

[5] H. Chattopadhyay, and A. C. Benim, "Turbulent Heat Transfer Over a Moving Surface Due to Impinging Slot Jets", Journal Heat Transfer – Transactions of the ASME, vol.133, no. 10, 104502, 2011.

[6] N. Tokgoz, T. Tunay, and B. Sahin, "Effect of corrugated channel phase shifts on flow structures and heat transfer rate", Experimental Thermal and Fluid Science, vol. 99, pp.374-391, 2018..

[7] M. Aliabadi, and A. Feizabadi, "Compound heat transfer enhancement of helical channel with corrugated wall structure", International Journal of Heat and Mass Transfer, vol. 146, 118858, 2020.

[8] R.K. Ajeel, W. Salim, and K. Hasnan, "Numerical investigations of heat transfer enhancement in a house shaped- corrugated channel: Combination of nanofluid and geometrical parameters", Thermal Science and Engineering Progress, Thermal Science and Engineering Progress, vol. 17, 100376, 2019.

[9] A. Nayak, and B. Weigand, "Mixing and heat transfer in micro/nano-channel due to charged corrugated surfaces", Applied

Thermal Engineering, vol. 170, 114979, 2020.

[10] V. Ionescu, and A. Neagu, "Modelling of fluid flow and heat transfer in a corrugated channel for heat exchanger applications", 11th International Conference Interdisciplinarity in Engineering, 5-6 October 2017, Tirgu-Mures, Romania.

[11] M. Ahmed, M. Yusoff, K. Ching and N. Shuaib, "Numerical and experimental investigations on the heat transfer enhancement in corrugated channels using SiO2-water nanofluid", Case Studies in Thermal Engineering, vol. 6, pp. 77-92, 2015.

[12] H. Pehlivan, I. Taymaz, Y. Islamoğlu, "Experimental study of forced convective heat transfer in a different arranged corrugated channel", International Communications in Heat and Mass Transfer, vol. 46, pp. 106-111, 2013.

[13] J. Yin, G. Yang, and Y. Li, "The Effects of Wavy Plate Phase Shift on Flow and Heat Transfer Characteristics in Corrugated Channel", Energy Procedia, vol. 14, pp. 1566 – 1573, 2012.

[14] E. Elshafei, M. Awad, E. El-Negiry, and A. Ali, "Heat transfer and pressure drop in corrugated channels", Energy, vol. 35, pp. 101–110, 2010.

[15] M. Ahmed, M. Yusoff, and N. Shuaib, "Effects of geometrical parameters on the flow and heat transfer characteristics in a trapezoidal-corrugated channel using nanofluid", International Communications in Heat and Mass Transfer, vol. 42, pp. 69–74, 2013.

[16] P. Naphon, "Laminar convective heat transfer and pressure drop in the corrugated channels", International Communications in Heat and Mass Transfer, vol. 34, pp. 62–71, 2007.

[17] E. Aslan, I. Taymaz, and Y. Islamoglu, "Finite volume simulation for convective heat transfer in wavy channels", Heat Mass Transfer, vol. 52, no. 3, pp. 483-497, 2016.

[18] H. Kepekci, E. Kosa, and C. Ezgi, "Modeling Study and Performance Investigation of a Thermoelectric Refrigerator", Engineer and Machinery, vol. 62, no. 705, pp. 715-730, 2021.

[19] H. Kepekci, B. Zafer, H. Guven, "Aeroacoustics Investigations of Unsteady 3D Airfoil for Different Turbulence Models Using Computational Fluid Dynamics Software", vol. 28, no. 10, pp. 7564-7573, 2019.

[20] E. Aslan, and H. Kepekci, "Investigation of Convective Heat Transfer and Friction Factor in Corrugated Channels with Different Inclination Angles Using Computational Fluid Dynamics", Journal of Advanced Thermal Science Research, vol.8, pp. 21-29, 2021.

[21] H. Kepekci, and A. Asma, "Comparative Analysis Of Heat Sink Performance Using Different Materials", American Journal of Engineering Research", vol. 9, no. 4, pp-204-210, 2020.

[22] H. Kepekci, "Comparative Numerical Aerodynamics Performance Analysis of NACA0015 and NACA4415 Airfoils", International Journal of Engineering,Science&Information Technology, vol. 2, no. 1, pp. 144-151, 2022.

SAKARYA ÜNİVERSİTESİ
FEN BİLİMLERİ ENSTİTÜSÜ DERGİSİ

Sakarya University Journal of Science
SAUJS

e-ISSN 2147-835X Period Bimonthly Founded 1997 Publisher Sakarya University
http://www.saujs.sakarya.edu.tr/

Title: Site Calibration of a Temperature-based Model for Estimating the Global Solar Radiation

Authors: Ceyda AKSOY TIRMIKÇI

Recieved: 2022-02-22 00:00:00

Accepted: 2022-03-11 00:00:00

Article Type: Research Article

Volume: 26
Issue: 2
Month: April
Year: 2022
Pages: 342-346

How to cite
Ceyda AKSOY TIRMIKÇI; (2022), Site Calibration of a Temperature-based Model for Estimating the Global Solar Radiation . Sakarya University Journal of Science, 26(2), 342-346, DOI: 10.16984/saufenbilder.1077449
Access link
https://dergipark.org.tr/tr/journal/1115/issue/69580/1077449

New submission to SAUJS
http://dergipark.gov.tr/journal/1115/submission/start

Sakarya University Journal of Science 26(2), 342-346, 2022

Site Calibration of a Temperature-based Model for Estimating the Global Solar Radiation

Ceyda AKSOY TIRMIKÇI*[1]

Abstract

In this paper, a commonly used global solar radiation (GSR) model is locally calibrated and tested for Kartepe, Kocaeli station. The coefficients of the model are calibrated for monthly and yearly by performing a regression analysis using the measured temperatures. Regression analysis results for both models provide that correlating the clearness index with the second degree of maximum temperature divided by minimum temperature gives the best accuracy for the selected location. Besides, the estimation results for each month indicate that the monthly calibrated coefficients provide very accurate results in terms of statistical errors. Moreover, seasonal calibration and yearly calibration of the model give less accurate predictions. The simple and accurate results by monthly calibrated models using this approach can be used in designing and evaluating solar energy applications in the absence of accurate sunshine data.

Keywords: Maximum temperature, minimum temperature, global solar radiation, regression, calibration

1. INTRODUCTION

Solar energy systems have become one of the best technical and economical solutions to meet increasing energy demand in many parts of the world in a sustainable, secure and clean way [1]. The first step in designing solar energy applications is to assess the availability by accurate solar radiation data. In current literature, there are many solar radiation models to estimate the total solar radiation on a tilted surface accurately [2]. However, solar radiation records are not always available due to high cost, and maintenance requirements [2, 3]. Therefore, there are various solar radiation models estimating solar radiation components from available measured meteorological variables [4-8]. These models are based on empirical correlations between sunshine fractions and commonly measured meteorological parameters including maximum temperature, minimum temperature, mean temperature and relative humidity.

Hargreaves and Samani suggested a very simple model using maximum temperature and minimum temperature to predict clearness index and global solar radiation on horizontal surfaces [8]. Several studies proposed modifications of the very simple model of Hargreaves and Samani. Bristow and Campbell introduced a model correlating clearness index with temperature difference exponentially [9]. Prieto et al. developed a location based model defining clearness index as a function of temperature difference and

* Corresponding author: caksoy@sakarya.edu.tr
[1] Sakarya University, Faculty of Engineering, Department of Electrical and Electronics Engineering
ORCID: https://orcid.org/0000-0003-0354-4022

minimum temperature [10]. Pandey and Katiyar proposed a new model expressing clearness index as a second degree function of the ratio between maximum temperature and minimum temperature [11].

In this paper, a commonly used temperature model proposed by Pandey and Katiyar [11] is selected to estimate global solar radiation, since air temperature measurement is available almost all over the world. The aim of this paper is to calibrate a simple temperature based model correlating clearness index with maximum and minimum temperatures for estimating monthly mean global solar radiation on horizontal surface with high accuracy. For this purpose, a common and simple model is selected from the literature and the coefficients of the model are calibrated by performing a regression analysis using the measured maximum and minimum temperatures of Kartepe, Kocaeli monthly, seasonal and yearly. Meteorological data of the location for each day of 2020 is used to determine the site calibrated coefficients. The modified model is tested in terms of common statistical indicators, Root Mean Square Error (RMSE) and Mean Absolute Percentage Error (MAPE). The results of the paper indicate that monthly specific calibration improves the accuracy of the model greatly, since the clearness index is dependent on the functional relationship between the maximum and minimum temperature variables.

2. METHODOLOGY

In this paper, a polynomial function using Tmax and Tmin variables is selected from the current literature to estimate clearness index for Kartepe, Kocaeli [11]:

$$K_t = a_1 + a_2 \frac{T_{max}}{T_{min}} + a3(\frac{Tmax}{Tmin})^2 \quad (1)$$

The clearness index, K_t, is the global radiation (H) divided by the extra-terrestrial radiation (H_0). The extra-terrestrial solar radiation is defined as follows [12-15]:

$$H_0 = \frac{24x3600}{\pi} x G_0 \quad (2)$$

$$G_0 = G_{sc} x \left(1 + 0.33 x cos \frac{360 x n_{day}}{365}\right) xk \quad (3)$$

$$k = (cos\varphi x cos\delta x sin w_s + \frac{\pi x w_s}{180} x sin\varphi x sin\delta) \quad (4)$$

where G_{sc}, n_{day}, ϕ, δ and w_s are the solar constant, the number of the day of the year, the latitude, solar declination and the sunrise hour angle for horizontal surface, respectively. G_{sc}, the total solar irradiation at the top of the atmosphere, is 1360.8 ± 0.5 W/m^2 [16].

The coefficients of Equation 1 are locally calibrated by performing regression analysis technique with daily measured maximum and minimum temperature values of August 2020. Then, the model is tested by using the measured solar radiation values of the same period in terms of Root Mean Square Error (RMSE) and Mean Absolute Percentage Error (MAPE). All local parameters are obtained from Meteoblue Weather History.

The RMSE is a commonly used measure determining the standard deviation of the estimation errors. The formula of the RMSE is as follows:

$$RMSE = \sqrt{(EV - MV)^2} \quad (5)$$

The MAPE is also a commonly used measure determining the estimation accuracy of a forecasting model. The formula of MAPE is as follows:

$$MAPE = \left|\frac{EV - MV}{MV}\right| \quad (6)$$

where EV and MV are estimated value and measured value respectively.

3. RESULTS AND DISCUSSION

Calibrated values of a_1, a_2 and a_3 in Equation 1 for each month are given in Table 1. According to the Table 1, clearness index of the selected location is correlated with the second degree of maximum temperature divided by minimum temperature. Table 2 indicates the measured temperature and radiation values at the location in August 2020. Estimated radiation and RMSE values using the

presented monthly temperature model are given in Table 3.

Table 1 Site-calibrated monthly coefficients

Month	a_1	a_2	a_3
January	0	0	0.031
February	0	0	0.0546
March	0	0	0.0855
April	0	0	0.0736
May	0	0	0.1358
June	0	0	0.2090
July	0	0	0.2803
August	0	0	0.256
September	0	0	0.2394
October	0	0	0.1761
November	0	0	0.0990
December	0	0	0.0991

Table 2 Monthly minimum and maximum temperatures (°C) and global solar irradiation on horizontal surface at Kartepe (kWh/m2.day) [17]

Month	Maximum Temperature	Minimum Temperature	Shortwave Radiation
January	9.762	2.81	1.532
February	13.51	4.55	2.646
March	15.44	6.65	3.456
April	17.42	6.37	5.257
May	23.54	11.893	5.853
June	27.502	16.697	6.574
July	28.611	19.954	6.499
August	30.356	19.247	6.411
September	28.864	19.131	4.466
October	25.144	14.525	3.210
November	15.967	7.263	2.105
December	14.913	7.514	1.4322

Table 3 Monthly model performance evaluation at Kartepe: global solar irradiation on horizontal surface at Kartepe (kWh/m2.day), RMSE (%) and MAPE(%)

Month	Estimated radiation	RMSE	MAPE
January	1.5313	7.462×10^{-4}	4.569×10^{-4}
February	2.6472	12×10^{-4}	4.535×10^{-4}
March	3.4556	3.793×10^{-4}	1.157×10^{-4}
April	5.2581	11×10^{-4}	2.092×10^{-4}
May	5.8546	16×10^{-4}	2.733×10^{-4}
June	6.5752	12×10^{-4}	1.825×10^{-4}
July	6.4987	2.973×10^{-4}	4.616×10^{-4}
August	6.4107	3.264×10^{-4}	4.679×10^{-4}
September	4.4653	7.354×10^{-4}	1.567×10^{-4}
October	3.2102	2.102×10^{-4}	6.230×10^{-4}
November	2.105	4.743×10^{-6}	0
December	1.4322	1.786×10^{-4}	0

Table 3 indicates that using the calibrated values for a specific location and a short period provides the highest accuracy. However, the coefficients depend on the functional relationship between maximum and minimum temperature variables and a_3 tends to rise in warmer periods.

Table 4 Seasonal model performance evaluation at Kartepe: global solar irradiation on horizontal surface at Kartepe (kWh/m2.day), RMSE (%) and MAPE(%)

Month	Estimated radiation	RMSE	MAPE
January	2.4599	0.9279	0.3772
February	2.4144	0.2316	0.0959
March	4.0975	0.6415	0.1566
April	7.2338	1.9768	0.2733
May	4.3625	1.4905	0.3417
June	7.7737	1.1997	0.1543
July	5.7290	0.7700	0.1344
August	6.1903	0.2207	0.0357
September	3.3406	1.1254	0.3369
October	3.2651	0.0551	0.0169
November	3.8081	1.7031	0.4472
December	0.7197	0.7125	0.9900

Table 5 Yearly model performance evaluation at Kartepe: global solar irradiation on horizontal surface at Kartepe (kWh/m2.day), RMSE (%) and MAPE(%)

Month	Estimated radiation	RMSE	MAPE
January	2.7060	1.1740	0.7663
February	7.6554	5.0094	1.8932
March	6.3933	2.9373	0.8499
April	11.2867	6.0297	1.1470
May	6.8067	1.2237	0.1629
June	4.9675	1.6066	0.2444
July	3.6609	2.8381	0.4367
August	3.9557	2.4553	0.3830
September	2.9451	1.5209	0.3406
October	2.8786	0.331	0.1032
November	3.3574	1.2524	0.5950
December	2.2819	0.8499	0.5933

Seasonal calibrated values of a_1, a_2 and a_3 in Equation 1 are 0, 0, 0.0498 for winter (December-February), 0, 0, 0.1012 for spring (March-May), 0,0, 0.2471 for summer (June-August) and 0, 0, 0.1791 for autumn (September-November). Calibrated values of a_1, a_2 and a_3 in Equation 1 for a year is obtained as 0, 0, 0.1579 respectively.

These results are coherent with monthly calibration results. Correlating the clearness index with the second degree of maximum temperature divided by minimum temperature gives the best estimations for the selected location.

Estimated radiation and statistical indicators using the presented seasonal and yearly temperature models are given in Table 5 and Table 6. Table 5 and Table 6 prove that the accuracy of the model decreases significantly with coefficients calibrated for a longer period. Since the ability of the model to estimate global solar radiation determines the design parameters of a solar energy application, sensitive calibrations for shorter periods are vital for temperature based models.

4. CONCLUSION

In this paper, a commonly used global solar radiation model is locally calibrated and tested for Kartepe, Kocaeli station. The coefficients are calibrated monthly, seasonal and yearly. Regression analysis results for both models provide that correlating the clearness index with the second degree of maximum temperature divided by minimum temperature gives the best accuracy for the selected location. Monthly calibrated models provide very high accurate results with RMSE and MAPE almost zero. However, the coefficients are highly dependent on the changes in maximum and minimum temperatures. Therefore, values of statistical indicators increase with seasonal and yearly models. In seasonal approach, RMSE is calculated between 0.0551 and 1.9768. MAPE of the estimated values by the same approach varies between 0.0169 and 0.9900. The accuracy decreases with yearly calibrated coefficients with RMSE from 0.331 to 6.0297 and MAPE from 0.1032 to 1.1470 in the same approach. The results prove that calibrating the models for short periods of time improves the accuracy and promises the best results for statistical indicators.

It is a fact that measurements of solar radiation and its components are not always available due to the high cost and maintenance requirements. Temperature based models are the best alternatives in the absence of sunshine data to estimate solar radiation and its components. However, the accuracy of these models depend on the functional relationships between temperature parameters. This paper proposes that monthly calibrated temperature coefficients of clearness index equations can be employed in the design and evaluation stages for any solar energy application.

Funding

The author has no received any financial support for the research, authorship or publication of this study.

The Declaration of Conflict of Interest/ Common Interest

No conflict of interest or common interest has been declared by the author.

Authors' Contribution

The author contributed 100%.

The Declaration of Ethics Committee Approval

This study does not require ethics committee permission or any special permission.

The Declaration of Research and Publication Ethics

The author of the paper declare that she complies with the scientific, ethical and quotation rules of SAUJS in all processes of the paper and that they do not make any falsification on the data collected. In addition, she declares that Sakarya University Journal of Science and its editorial board have no responsibility for any ethical violations that may be encountered, and that this study has not been evaluated in any academic publication environment other than Sakarya University Journal of Science."

REFERENCES

[1] IEA (2021), Renewables 2021, IEA, Paris https://www.iea.org/reports/renewables-2021.

[2] C. Aksoy Tırmıkçı and C. Yavuz, "Determining optimum tilt angles of solar surfaces in Sakarya, Turkey," Theor Appl Climatol, vol.133, pp.15–22, 2018.

[3] A.A. El-Sebaii, F.S. Al-Hazmi, A.A. Al-Ghamdi and S.J. Yaghmour, "Global, direct and diffuse solar radiation on horizontal and tilted surfaces in Jeddah, Saudi Arabia," Applied Energy, vol. 87, no.2, pp.568-576, 2010.

[4] S. Janjai, P. Pankaew and J. Laksanaboonsong, "A model for calculating hourly global solar radiation from satellite data in the tropics," Applied Energy, vol. 86, no. 9, pp. 1450-1457, 2009.

[5] Z. Jin, W. Yezheng and Y. Gang, "General formula for estimation of monthly average daily global solar radiation in China," Energy Conversion and Management, vol. 46, no. 2, pp. 257-268, 2005.

[6] M. Li, X. Tang, W. Wu and H. Liu, "General models for estimating daily global solar radiation for different solar radiation zones in mainland China," Energy Conversion and Management, vol. 70, pp. 139-148, 2013.

[7] E. Gasser, et al., "New Temperature-based Models for Predicting Global Solar Radiation," Applied Energy, vol. 179, pp. 437-450, 2016.

[8] G.H. Hargreaves and Z.A. Samani, "Estimating potential evapotranspiration," Journal of Irrigation and Drainage Engineering, vol.108 (IR3), pp. 223-230, 1982.

[9] K.L. Bristow and G.S. Campbell, "On the relationship between incoming solar radiation and daily maximum and minimum temperature," Agric For Meteorol; vol. 31, no. 2, pp.159–66, 1984.

[10] J.I. Prieto, J.C. Martínez-García, D. García, "Correlation between global solar irradiation and air temperature in Asturias, Spain," Sol Energy; vol. 83, no.7, pp.1076–85, 2009.

[11] C.K. Panday and A.K. Katiyar, "Temperature base correlation for the estimation of global solar radiation on horizontal surface," Int J Energy and Environment, vol. 1, no. 4, pp. 737–4, 2010.

[12] J.A. Duffie and W.A. Beckman, "Solar engineering of thermal processes," 3rd ed. New York: John Wiley & Son, 2006.

[13] P.I. Cooper, "The absorption of solar radiation in solar stills," Solar Energy, vol. 12, no. 3, pp. 333–46, 1969.

[15] M. Iqbal, "An introduction to solar radiation," New York, USA: Academic Press, 1983.

[16] G. Kopp, J.L. Lean JL, "A new, lower value of total solar irradiance: evidence and climate significance," Geophys Res Lett, vol. 38:L01706, 2011.

[17] Meteoblue Weather History Download Kartepe, available at https://www.meteoblue.com, accessed on 15.01.2022

SAKARYA ÜNİVERSİTESİ
FEN BİLİMLERİ ENSTİTÜSÜ DERGİSİ

Sakarya University Journal of Science
SAUJS

e-ISSN 2147-835X Period Bimonthly Founded 1997 Publisher Sakarya University
http://www.saujs.sakarya.edu.tr/

Title: Seismic Performance Evaluation and Retrofit of Liquid Storage Tanks- Case Study

Authors: Bülent ERKMEN

Recieved: 2021-09-20 00:00:00

Accepted: 2022-03-13 00:00:00

Article Type: Research Article

Volume: 26
Issue: 2
Month: April
Year: 2022
Pages: 347-356

How to cite
Bülent ERKMEN; (2022), Seismic Performance Evaluation and Retrofit of Liquid Storage Tanks- Case Study. Sakarya University Journal of Science, 26(2), 347-356, DOI: 10.16984/saufenbilder.997699
Access link
https://dergipark.org.tr/tr/journal/1115/issue/69580/997699

New submission to SAUJS
http://dergipark.gov.tr/journal/1115/submission/start

Sakarya University Journal of Science 26(2), 347-356, 2022

Seismic Performance Evaluation and Retrofit of Liquid Storage Tanks-Case Study

Bülent ERKMEN*[1]

Abstract

Seismic performance of existing liquid pentane storage tanks located in a tank farm in Turkey Kocaeli region, which is a high seismic region, is studied. The tanks are free-to-slide on their existing reinforced concrete foundation. The tanks seismic performance is evaluated based on the 2018-Turkish Building Seismic Code and API 650 provisions using three-dimensional (3D) finite element methods with nonlinear time-history analysis. The developed FE model for seismic performance assessment of the existing tanks includes tank-foundation dynamic interaction, tank supports uplifting, and sliding over the foundation. The study revealed poor and inadequate seismic performance for the existing tanks due to lack of tank foundation-anchorage. A practical seismic retrofit strategy is developed to anchor the tanks to the existing reinforced concrete foundation. Prefabricated and field-welding free steel split sleeves are developed for the tank anchorage. The retrofitted tank seismic performance is evaluated to verify the proposed retrofit strategy and its effects on tank seismic behavior. The base shear and uplift reactions for the retrofitted tank are monitored for the anchorage design. Tank top drift, which is an important seismic performance parameter for tank piping, and tank steel material yielding are also checked to verify adequacy of the proposed retrofit strategy.

Keywords: Liquid storage tanks, tank sliding, tank uplift, seismic

1. INTRODUCTION

This paper presents seismic performance evaluation of existing liquid pentane storage tanks located in a tank farm in Kocaeli region of Turkey and their seismic retrofit. The tank location is a high seismic region hit by the 1999 Kocaeli earthquake, which caused severe damage to the industrial facilities and liquid storage tanks as well as devastating fires in the region. Liquid-storage tanks are crucial part of the modern industrial facilities. Therefore, liquid-storage tanks filled with hazardous liquids such as oil, oil derived products, chemicals, petrochemical, and food processing liquids are in widespread. Failure of such tanks has frequently resulted in spillage of toxic material with disastrous effects and fires following explosions as occurred following the 1994 Northridge, the 1995 Kobe, 1999 Kocaeli, and the 2011 Eastern Japan earthquakes [1-3]. Therefore, when such tanks are located in earthquake prone regions, they should remain functional, or the damage should be at acceptable levels after earthquakes [4-6].

* Corresponding author: bulent.erkmen@ozyegin.edu.tr
[1] Özyeğin University, Faculty of Engineering, Department of Civil Engineering
ORCID: https://orcid.org/0000-0002-3980-3770

Liquid storage tanks seismic design provisions in current design codes such as API 650 [5], Turkish Code [6], and Eurocode 8 [7] are based on a mechanical spring-mass analogy developed by Graham and Rodriguez [8], Jacobsen [9], and Housner [10] for rigid tanks; and modified by Haroun and Housner [11] for flexible tanks. The mechanical model also known as spring-mass model shown in Figure 1 is based on liquid behavior under seismic loads. The part of the liquid located in the lower part of the tank, which is called impulsive component, is assumed to move with the tank under seismic loads. This component typically has natural period of vibration (T_i) in the range of 0.1 to 0.4 seconds [8, 8, 12]. The other part of the liquid located in the upper part of the tank is called convective component, and it is assumed to freely vibrate to form liquid sloshing in the tank during seismic loading. The convective component has longer natural period of vibration (T_c) between 3 and 10 seconds depending on the tank dimensions and liquid level [4, 5, 12].

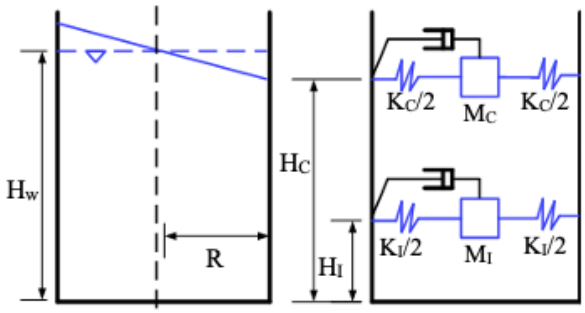

Figure 1 Spring-mass model for liquid storage tanks

Seismic behavior of liquid storage tanks is very complex due to liquid-structure dynamic interaction, liquid sloshing, and tank foundation interaction. The mechanical spring-mass tank model considerably simplifies computation of liquid storage tanks seismic behavior. Although this modelling approach is not sufficient to monitor change in the liquid level and liquid-structure interaction due to liquid sloshing, the approach is computationally cheap, simple to develop, and adequate for the main objective of this study [13-17].

The spring-mass model for the pentane tanks is developed using API 650 seismic provision [5]. The required parameters, which are shown in Figure 1, are the convective (M_C) and impulsive mass (M_I) values of the liquid, the elevations (H_I and H_C) at which they should be connected to the tank walls, and the spring constants for both masses. The damping for tanks has generally been assumed to be at the order of 0.5% for convective and 2-5% for impulsive modes.

This paper discusses seismic performance of liquid pentane tanks located in an industrial facility in Kocaeli region. The region is seismically active with large earthquakes, and the tank farm is in the vicinity of the North Anatolian fault. The tanks were post-installed on an existing concrete mat foundation, which was designed and provided to support various liquid storage tanks. Because the pentane tanks are post-installed, they are not anchored to the existing foundation. In other words, the tanks rest on the foundation, and they are free to slide and uplift. Seismic performance evaluation of the tanks showed that their seismic performance is not adequate due to tank structural damage resulting from tank sliding and uplifting. Therefore, a practical seismic retrofit strategy is developed to anchor the tanks to the existing reinforced concrete foundation. For this, prefabricated and field-welding free steel split sleeves are developed for the tank anchorage due to welding restrictions and explosion/fire risks at the facility. The study compares seismic performance of the tanks before and after the retrofitting. A simple and effective post anchorage detail is presented, which can be employed where such tanks need to be installed on existing foundations.

2. EXISTING AND UPGRADED PENTAN TANKS

A general view and dimensions of the pentane tanks are given in Figure 2. The tanks are vertical cylindrical type with a diameter of 382 cm and a total height of 1195 cm. The tanks are supported with six stand-supports, which are made of 36 cm diameter steel pipe with a wall thickness of 9.5 mm. The tank shell thickness is 10 mm for top end-dome and cylindrical part and 14 mm for the bottom end-dome. The steel grade used for the tanks is S235, which is one of the typical steel grades used for fabrication of liquid storage tanks.

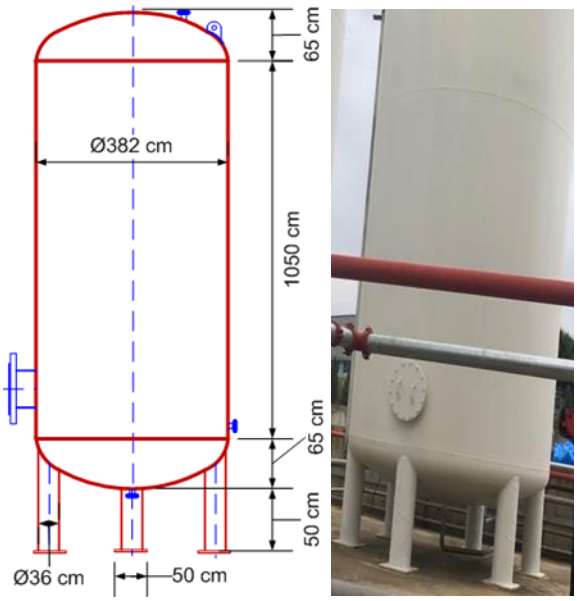

Figure 2 Dimension and overall view of pentane tank

The six stand-supports of the tanks are provided with a 20 mm thick 50 cm by 50 cm square base plate, but these plates are not anchored to the concrete foundation. In other words, the tanks rest on the foundation, and are free to slide and uplift from the foundation. In general, liquid storage tanks located in zones of high seismicity are recommended to be anchored if the ratio of safe operating height (H) to tank diameter (D) exceeds 2.0 to prevent tank uplift, overturning, and sliding [5, 12]. The pentane tanks are post-installed at the farm on an existing concrete foundation as a part of facility production expansion program. Therefore, anchorage of the tanks to the existing foundation was likely abandoned due to complications involved during expansion program.

Tanks seismic performance, which is discussed in the following sections, was found to be inadequate due to tank damage, large support uplift, sliding on the foundation, and tank overturning. Tank anchorage to the foundation was done through six stand-supports of the tank as shown in Figure 2. Each tank support is provided with a two-piece prefabricated steel split sleeves as shown in Figure 3. The sleeves are easy to fabricate and do field installation without requirement for field welding. The field welding is not permitted since it poses a risk of fire and explosion. Each sleeve is clamped to the tank stand-supports to transfer the shear and axial uplift forces. The split sleeves are connected to the reinforced concrete mat foundation through four Hilti M27 anchors. The anchors are connected to the foundation using Hilti HIT-RE 500 V4 injectable epoxy. The selected epoxy is heavy duty and suitable for seismic applications.

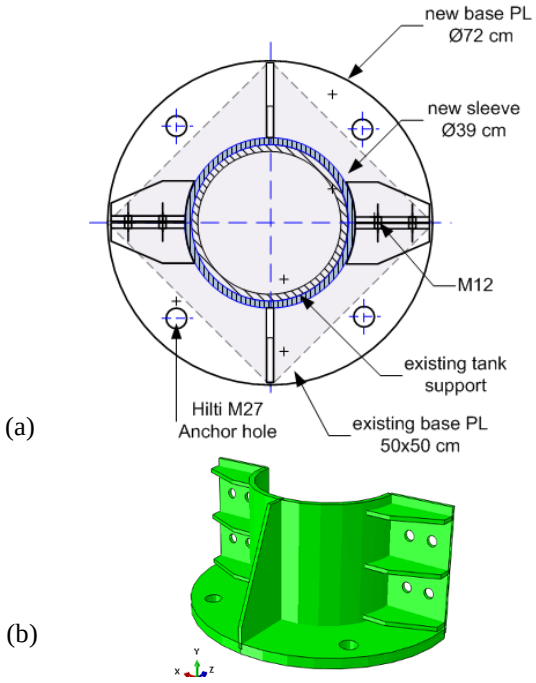

Figure 3 (a) Plane view and (b) 3D view of split sleeve

2.1. Site Seismicity and Selected Ground Motions

The tank farm is located in Kocaeli industrial region, which is a seismically active region with large earthquakes. The tank farm site has very tight layers of sand, gravel and hard clay based on the site soil report. Therefore, it is classified as site class ZC according to the 2018-Turkish Building Seismic Code (TBDY) [18]. The site has peak ground acceleration (PGA) of 0.556g and peak ground velocity of 40.7 cm/s per Turkey Earthquake Risk Maps (AFAD) [19] for earthquake level DD2, which has a 10% probability to be exceeded in 50 years. The site 5% damped design spectrum shown in Figure 4 has acceleration parameters for the short period (S_{DS}) equal to 1.614g and at period of 1 second (S_{D1}) equal to 0.551g per AFAD.

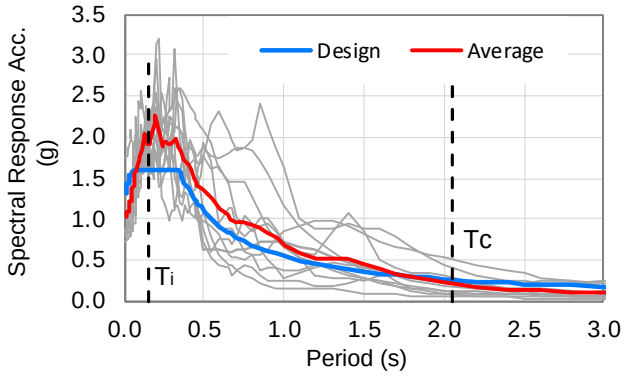

Figure 4 Design and average response spectrum

A set of 12 ground acceleration records given in Table 1 are selected from the Pacific Earthquake Engineering Research (PEER) Center database [20] to be used for nonlinear time history analyses of the tank. The number of records and selection are consistent with TBDY recommendations. The selected earthquake records include data from the tank location as well as other near-fault records since the farm is located in the vicinity of Main Marmara Fault. The selected ground motions are scaled to match the design spectrum for the site as shown in Figure 4. The ground motions are scaled so that their average spectrum will be above the design spectrum for period range between tank impulsive period T_i and liquid convective period T_c.

Table 1 Selected ground motions

Ground motion	Name	Year	Station	Dist.[(1)]
GM1	Helena Montana	1935	Car. College	2.9
GM2	Victoria Mexico	1980	Cerro Prieto	14.4
GM3	Morgan Hill	1984	Lake Dam	0.5
GM4	Duzce Turkey	1999	Lamont 375	3.9
GM5	Chi-chi Taiwan	1999	CHY074	6.2
GM6	Tottori Japan	2000	TTR007	11.3
GM7	Bam Iran	2003	Bam	1.7
GM8	Parkfield CA	2004	Cholame 4W	4.2
GM9	Big Bear	1992	Fire Sta #36	41.9
GM10	Joushua Tree CA	1992	Fire Sta #36	22.0
GM11	Duzce Turkey	1999	Irigm 498	3.6

(1) closest distance to earthquake generating fault in km.

3. TANK FINITE ELEMENT MODEL

Tank finite element (FE) model is developed using general purpose finite element program ABAQUS [21], which is selected for its computational efficiency for modelling nonlinear contact as well as its stability for nonlinear time history analysis. The FE model includes tank sliding and uplifting (separation) interactions with the foundation under dynamic loading. The model is developed based on the impulsive and convective liquid parameters given in Table 2. The required parameters for the liquid are computed using API 650 guidelines, and include mass, the distance between the bottom of the shell and the center of the lateral seismic forces, and periods of vibration for each liquid component.

Table 2 Tank modelling parameters

Parameter	Value
Operating liquid height	8.5 m
Liquid density	625 kg/m^3
Liquid mass	64366 kg
Impulsive liquid mass (M_I)	58073 kg
Convective liquid mass (M_C)	6293 kg
Impulsive mass height (H_I)	3.8 m
Convective mass height (H_C)	7.5 m
Impulsive liquid period (T_i)	0.15 sec
Convective liquid mass (T_c)	2.05 sec

The developed FE model is shown in Figure 5. The model includes 3D tank model, the six stand-supports and their square base plates, and the foundation to properly model tank-foundation contact interaction. The tank and foundation are modelled using S4R shell element, which is a 4-node general-purpose shell element with reduced integration. The element is suitable for large strain analyses of both thin and thick shells. Typical S235 steel material properties are assumed for the tank. The yield (f_y) and ultimate strengths (f_u) are taken as 235 MPa and 360 MPa, respectively. The Young's modulus and Poisson's ratio are taken as 210000 MPa and 0.3, respectively. The reinforced concrete foundation is assumed to be elastic with typical C30 concrete material properties.

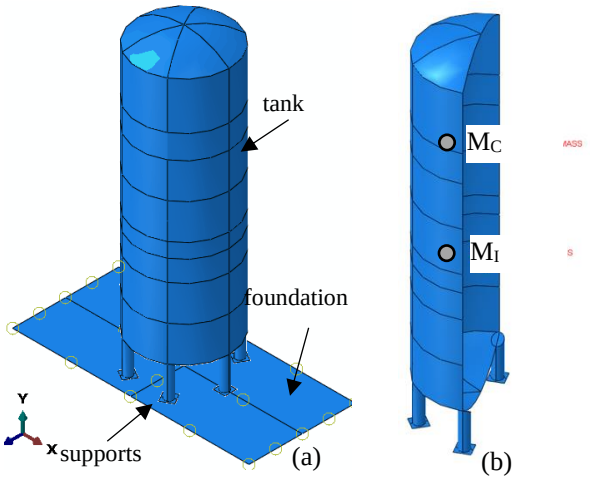

Figure 5 (a) FE model general view and (b) attachment of liquid masses

The impulsive and convective liquid masses are connected to the tank wall through elastic springs and coupling constraint (Figure 5b). For this purpose, two reference points were defined for each mass at the same point (H_I and H_C). The first reference point was connected to the tank shell using coupling constraint while the second reference point was assigned point mass and connected to the first reference point with the elastic spring. The spring stiffness was calculated for each mass to have the corresponding vibration periods T_i and T_c.

For boundary conditions, the reference points are allowed to move only in the direction of applied ground acceleration and restrained for other degrees of freedom. The tank foundation is assumed to be fixed for all displacement degrees of freedom except for the acceleration degree of freedom in the direction of earthquake records (i.e., global X-direction). The earthquake acceleration history is defined as the boundary condition for the tank foundation. The dynamic interaction between the tank base plates and its foundation is defined through contact formulation, which allows contact separation of surfaces. The static and dynamic friction coefficients between the two surfaces are taken as 0.57 [22].

Because tank liquid content is not modelled explicitly, the hydrodynamic pressure on the tank inner surface is modelled as initial pressure-loading as given in Figure 6. The gravity loads due to tanks self-weight and hydrodynamic pressure were applied to the model at a static analysis step, which was followed by the dynamic explicit time-history analysis step for earthquake loading. The vertical component of ground motions is considered as a static load acting in the opposite direction of the gravity. The vertical seismic acceleration is conservatively taken as $0.67S_{DS}$ per TBDY [18] while API 650 recommended acceleration value is $0.47S_{DS}$. The explicit dynamic analysis is selected for high nonlinearity due to tank sliding over the foundation and uplifting of tank supports. The whole model is meshed with shell elements, and a nominal mesh size of 25 cm is used for the tank and its foundation as shown in Figure 6b.

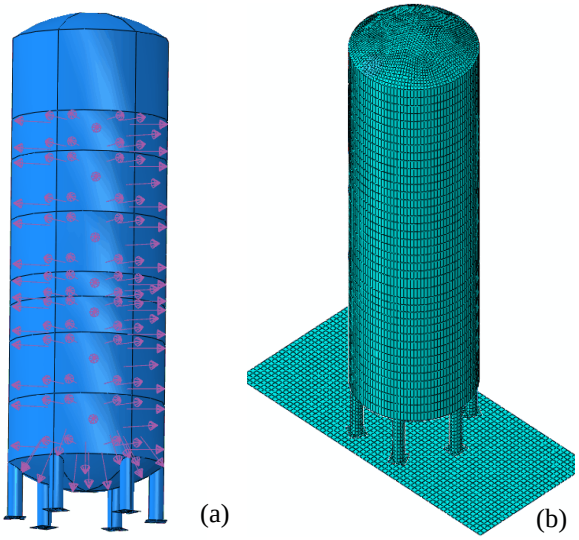

Figure 6 (a) Application of hydrodynamic pressures and (b) FE mesh

The seismic performance of the existing tanks is found to be inadequate mainly due to tank not having any foundation anchorage. Therefore, tank six stand-supports are anchored to the foundation through steel split sleeves as a part of the proposed retrofit scheme. The split-sleeves are fixed to the foundation with four Hilti M27 anchors and HIT-RE 500 V4 injectable epoxy. The same finite element model of the tank is used for the retrofitted tanks. However, the foundation is removed from the model since the retrofitted tanks are anchored to the foundation. In addition, the boundary condition of the tank supports is changed to pin-pin support. The new support condition is defined using a reference point for each support, and tank support base plate bottom surface is coupled to this reference point for all

degrees of freedom as shown in Figure 7. The earthquake acceleration history is applied to the six reference points at the same time.

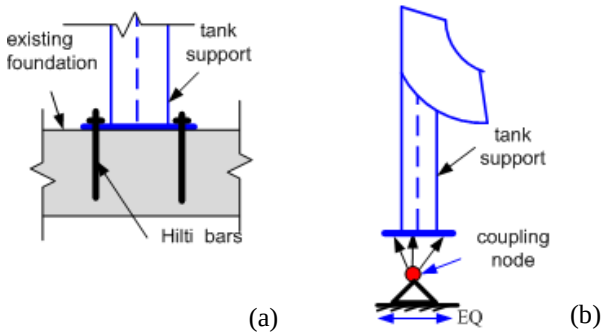

Figure 7 Retrofitted tank (a) foundation anchorage and (b) updated boundary condition

4. RESULTS AND DISCUSSIONS

The seismic performance evaluation of the tanks is based on time-history analyses performed using 12 scaled earthquake records. A summary of both existing and retrofitted tank seismic performance parameters is given in Table 3. The seismic performance of the tank is evaluated based on tank relative roof displacement, support uplift, tank overturning, retrofitted tank support reactions, and tank material damage.

Table 3 Summary of seismic performance

	Existing Tank		**Upgraded Tank**		
Ground motion	δ_{Roof} (mm)	Δ_{SPRT}[(2)] (mm)	δ_{Roof} (mm)	Support tension (kN)	Shear (kN)
GM1	263	64	57	331	92
GM2	x[(1)]	x	137	475	126
GM3	x	x	246	531	140
GM4	121	21	59	348	93
GM5	x	x	182	515	141
GM6	103	22	97	407	118
GM7	244	59	99	464	115
GM8	x	x	252	575	139
GM9	x	x	135	466	132
GM10	258	63	66	362	100
GM11	210	50	79	405	107
AVRG	200	47	128	444	118

[(1)] x shows tank failure due to tanks overturning.
[(2)] support maximum uplifting.

Because the existing tank is not anchored to the foundation, tank overturning occurred due to seismic loads for five earthquake records as given in Table 3. The main reason for the tank failure is the fact that tank supports are not anchored to the foundation and tank being free to slide over the foundation. Figure 8 shows tank displacements during earthquake loading. Tank supports uplifted from the foundation due to lateral seismic loads, and tank remained supported only by one or two supports as shown in Figure 8. The total seismic base shear is carried by these few supports, which bended as shown in Figure 8. At the locations where the supports are connected to the tank main body large material yielding and damage are observed as shown by the equivalent plastic strain (PEEQ) contours in Figure 9 due to bending of these supports.

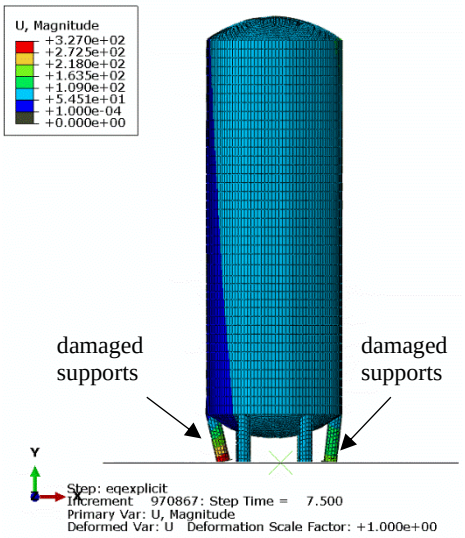

Figure 8 Tank support displacement and damage

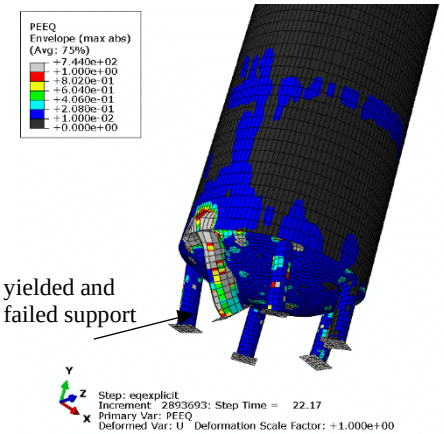

Figure 9 Tank support failure and material yielding

For the earthquake records that do not cause tank overturning failure, tank roof maximum relative displacement (δ_{Roof}) is between 103 mm and 263 mm with an average value of 200 mm. The average relative tank top displacement of 200 mm is still considered to be large to prevent piping

damage, which will cause liquid spillage after earthquakes. In addition, tank sliding over the foundation is another important performance criteria for tank piping connected to the foundation. For example, tank sliding over the foundation under GM9 is more than 1 m before its collapse due to overturning. In summary, it is concluded that the existing tanks need to be anchored to the foundation to limit their displacement, damage, and overturning failure.

Seismic evaluation of the tanks shows the need for seismic strengthening for their foundation anchorage. Tanks six stand-supports are anchored to the foundation using two-piece split sleeves and four M27 anchors with injectable epoxy. To determine design requirements for the anchorage system and its effects on tank seismic behavior, the nonlinear time-history analyses of the tank are repeated with the updated boundary conditions. The maximum support tension and shear reaction forces are given in Table 3. The maximum shear and tension reaction forces occurred at different supports. The maximum tension force is between 331 kN and 575 kN with an average value of 444 kN. The maximum shear force is between 92 kN and 141 kN with an average value of 118 kN. The tank anchorage system is designed for these average reaction forces.

The maximum support tension and shear reactions occurred under GM8 and GM5 earthquakes, respectively. Tank support tension and shear reactions time-history curves are given in Figure 10 and Figure 11, respectively. Anchoring the tank to the foundation improved its seismic performance by distributing the shear reaction force to all supports and limiting tank lateral displacements. Tank roof lateral displacement in the earthquake direction decreased significantly due to tank anchorage to the foundation. The displacement is between 57 mm and 252 mm with an average value of 128 mm as given in Table 3. These displacement values are more acceptable for tank piping to prevent piping failure, liquid content spillage, and fire during earthquakes.

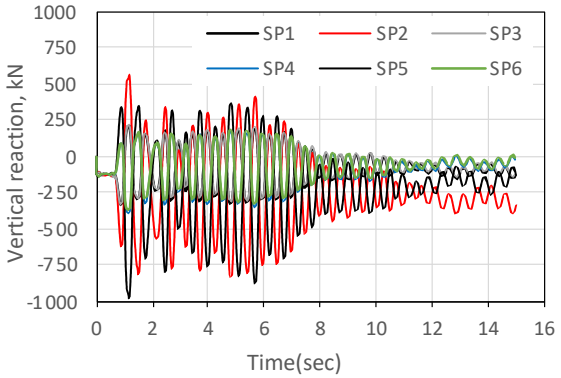

Figure 10 Supports vertical reaction history under GM8

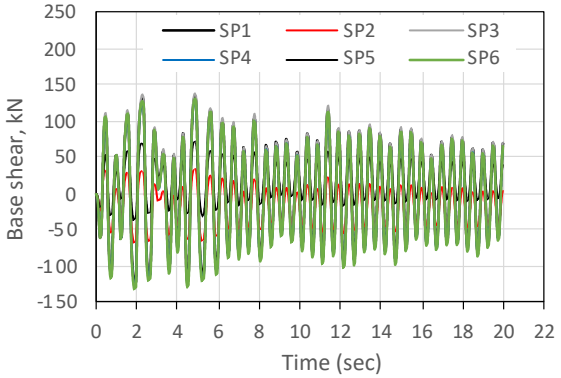

Figure 11 Supports shear reaction history under GM5

Figure 12 shows tank shell material yielding under GM8 earthquake, which creates the largest tension forces for the tank supports. The results show that tank main body and supports remain damage free (elastic) under the given earthquake. Tank bottom end-dome, where the supports are attached to the tank main body, experiences some material yielding. However, the equivalent plastic strain (i.e., PEEQ) values are less than 12%. In addition, the large values of PEEQ are only observed over a small area, where stress concentration occurs due to meshing and modelling in tank support and main body connection regions.

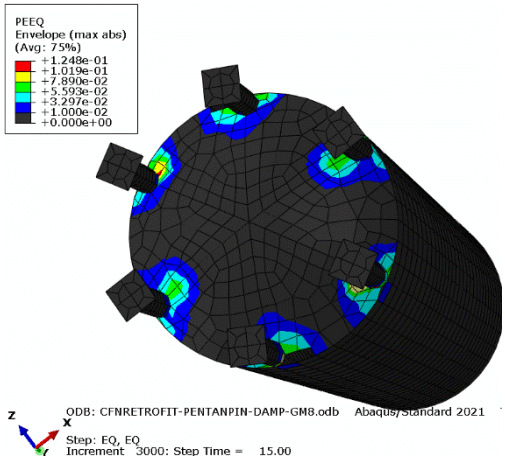

Figure 12 Anchored tank yielding and PEEQ contours

5. CONCLUSIONS

Seismic behavior of liquid pentane tanks located in a high seismic region of Turkey is studied using 3D nonlinear time-history analyses using 12 recorded ground motions. It is demonstrated that not having any tank anchorage-to-foundation has significant effects on tank seismic behavior including support uplift, tank sliding, material damage, and failure due to tank overturning. The tanks failed due to overturning for 5 ground motions out of 12 records selected for time-history analyses. In addition, the tanks experienced significant damage due to supports of the tank uplifting and sliding over the foundation.

A simple two-piece prefabricated steel split sleeve, which is easy to prefabricate and suitable for field installation without any field welding, is developed for tank foundation anchorage. The seismic design for the sleeve connection to the foundation is done by repeating the nonlinear time-history analyses of the tanks. The retrofitted tanks have significantly improved seismic behavior without any tank failure. Tank roof displacement decreased to 128 mm on average, which is tolerable for tank piping to remain intake after potential earthquakes. In addition, tank shell yielding is limited to a small area, where supports are connected to the tank main body. This study highlights the importance of seismic evaluation of existing liquid storage tanks, and presents a practical seismic retrofit strategy developed to anchor such tanks to existing reinforced concrete foundations.

Funding

The author has not received any financial support for the research, authorship or publication of this study.

The Declaration of Conflict of Interest/ Common Interest

No conflict of interest or common interest has been declared by the authors.

Authors' Contribution

The first author B. E. contributed 100%.

The Declaration of Ethics Committee Approval

This study does not require ethics committee permission or any special permission

The Declaration of Research and Publication Ethics

The authors of the paper declare that they comply with the scientific, ethical and quotation rules of SAUJS in all processes of the paper and that they do not make any falsification on the data collected. In addition, they declare that Sakarya University Journal of Science and its editorial board have no responsibility for any ethical violations that may be encountered, and that this study has not been evaluated in any academic publication environment other than Sakarya University Journal of Science.

REFERENCES

[1] NIST GCR 97-720, “A study of the performance of petroleum storage tanks during earthquakes, 1933-1995,” Building and Fire Research Laboratory, Gaithersburg, Maryland, 1997. [Online]. Available: https://nehrpsearch.nist.gov/static/files/NIST/PB99132896.pdf.

[2] J. Radnić, N. Grgić, M. S. Kusić, and A. Harapin, “Shake table testing of an open rectangular water tank with water sloshing,”

Journal of Fluids and Structures, vol. 81, pp. 97-115, 2018.

[3] M. Sivý, and M. Musil, "Seismic resistance of storage tanks containing liquid in accordance with principles of Eurocode 8 standard," Strojnícky časopis-Journal of Mechanical Engineering, vol. 66, no. 2, pp. 79-88, 2016.

[4] American Society of Civil Engineers (ASCE), "Guidelines for seismic evaluation and design of petrochemical facilities," ASCE, New York, NY, USA, 1998.

[5] API 650 Welded Tanks for Oil Storage, American Petroleum Institute Standard 11th Ed. 2007.

[6] Turkish Code for Seismic Design of Pipeline Systems and Liquid Storage Tanks Seismic [Online]. Available: https://www.resmigazete.gov.tr/eskiler/2021/03/20210307-1-1.pdf.

[7] P. Code, "Eurocode 8: Design of structures for earthquake resistance-part 1: general rules, seismic actions and rules for buildings." Brussels: European Committee for Standardization, 2005.

[8] E. W. Graham and A. M. Rodriguez, "The characteristics of fuel motion which affect airplane dynamics," Journal of Applied Mechanics, vol. 19, pp. 3881-3888, 1952.

[9] L. S. Jacobsen, "Impulsive hydrodynamics of fluid inside a cylindrical tank and of fluid surrounding a cylindrical pier," Bulletin of the Seismological Society of America, vol. 39, no.3, pp. 189-204, 1949

[10] G. W. Housner, "Dynamic Behavior Water Tanks," Bulletin of the Seismology Society of America, vol. 53, no.2, pp. 381-387, 1963.

[11] M.A. Haroun and G.W. Housner, "Dynamic characteristics of liquid storage tanks," Journal of Engineering Mechanics Division, ASCE, vol. 108, no.5, pp. 783-800, 1982.

[12] A. N. Oskouei and E. N. Naghani, "Mechanical behavior investigation for an atmospheric storage tank according to API 650 under loads using FEM," Journal of Current Research in Science, Vol. 2, no.5, pp. 664-672, 2014.

[13] D. Hernandez-Hernandez, T. Larkin, and N. Chouw, "Evaluation of the adequacy of a spring-mass model in analyses of liquid sloshing in anchored tanks," Earthquake Engineering & Structural Dynamics, vol. 50, no. 14, pp. 3916-3935, 2021.

[14] K. Bakalis and S. A. Karamanos, "Uplift mechanics of unanchored liquid storage tanks subjected to lateral earthquake loading," Thin-Walled Structures, vol 158, 2021.

[15] M. Kalantari, M. R. Nikoomanesh, and M. A. Goudarzi, "Applicability of mas-spring models for seismically isolated liquid storage tanks," Journal of Earthquake and Tsunami, vol. 12, no. 2, pp. 1950002, 2019.

[16] M. A. Goudarzi, and S. R. Sabbagh-Yazdi, "Numerical investigation on accuracy of mass spring models for cylindrical tanks under seismic excitation," Journal of Civil Engineering, vol. 7, no. 3, pp. 190-202, 2009.

[17] X. Yao, L. Meng, P. Chu, and L. Yao, "Modeling research and test verification of the seismic response of a multistage series liquid tank," Shock and Vibration, vol. 2021, 2021.

[18] *Turkish Seismic Earthquake Code (TBDY)*. [Online]. Available: https://www.resmigazete.gov.tr/eskiler/2018/03/20180318M1-2-1.pdf.

[19] The Disaster and Emergency Management Presidency (AFAD), "Turkey Earthquake Risk Maps," [Online]. Available: https://tdth.afad.gov.tr.

[20] PEER Strong Motion Database. [Online]. Available: http://peer.berkeley.edu/smcat/index.html.

[21] ABAQUS/Standard (2021). Dassault Systemes. [Online]. Available: https://www.3ds.com/products-services/simulia/products/abaqus/.

[22] B. G. Rabbat and H. G. Russell, “Friction coefficient of steel on concrete or grout,” Journal of Structural Engineering, vol. 111, no. 3, pp. 505-515, 1985.

SAKARYA ÜNİVERSİTESİ
FEN BİLİMLERİ ENSTİTÜSÜ DERGİSİ

Sakarya University Journal of Science
SAUJS

e-ISSN 2147-835X Period Bimonthly Founded 1997 Publisher Sakarya University
http://www.saujs.sakarya.edu.tr/

Title: GC-MS Analysis and Apoptotic Effect of Paliurus spina-christi Mill. Leaf and Flower Extracts against Breast Cancer Cells

Authors: Ferdi OGUZ, Çisil ÇAMLI PULAT, Süleyman İLHAN

Recieved: 2021-11-28 00:00:00

Accepted: 2022-03-14 00:00:00

Article Type: Research Article

Volume: 26
Issue: 2
Month: April
Year: 2022
Pages: 357-364

How to cite
Ferdi OGUZ, Çisil ÇAMLI PULAT, Süleyman İLHAN; (2022), GC-MS Analysis and Apoptotic Effect of Paliurus spina-christi Mill. Leaf and Flower Extracts against Breast Cancer Cells. Sakarya University Journal of Science, 26(2), 357-364, DOI: 10.16984/saufenbilder.1029351
Access link
https://dergipark.org.tr/tr/journal/1115/issue/69580/1029351

New submission to SAUJS
http://dergipark.gov.tr/journal/1115/submission/start

Sakarya University Journal of Science 26(2), 357-364, 2022

GC-MS Analysis and Apoptotic Effect of *Paliurus spina-christi* Mill. Leaf and Flower Extracts against Breast Cancer Cells

Ferdi OGUZ[1], Çisil ÇAMLI PULAT[1], Süleyman İLHAN*[1]

Abstract

In recent years, herbal medicines have become a significant novel source of treatment for various types of cancer, including breast cancer. Various investigations have declared that *Paliurus spina-christi* Mill. (PSC) shows antioxidant, antifungal, antimicrobial, and antibacterial properties, but its effect on cancer cells is unknown. This study purposed to evaluate the possible anti-cancer effects of the ethanolic extract of the PSC in human MCF-7 and MDA-MB-231 breast cancer cells. The leaf and flower extracts of PSC were prepared in ethanol and volatile compounds were determined by GC-MS analysis. The possible cytotoxic effects of extracts were evaluated via MTT assay. Apoptotic effect was examined using the PI Annexin V Apoptosis Detection Kit. Significant cytotoxic effects were detected after 72 h treatment of ethanolic leaf and flower extracts in MCF-7 cells but not in MDA-MB-231 cells. Both leaf and flower extracts of PSC induced apoptotic cell death in MCF-7 cells. On phytochemical screening, it was shown that the leaf extract of PSC contains pyrrolidine, 2-decenal, 2-undecanal, phytol, oleic acid, oleamide, squalane, vitamin E, and gamma-sitosterol and the flower extract contains pyrrolidine, 2-decenal, 2-undecenal, oleic acid, lupeol, and gamma-sitosterol. These data report that PSC leaf and flower extracts have cytotoxic and apoptotic effects in MCF-7 breast cancer cells. Moreover, this study can be considered an *in vitro* background for further *in vivo* cancer experiments.

Keywords: *Paliurus spina-christi*, breast cancer, anti-cancer, GC-MS, MCF-7.

1. INTRODUCTION

Breast cancer is both the most frequently diagnosed cancer in females and the second cause of cancer-related death in women [1]. Therefore, considering the limitations of present chemotherapeutic drugs such as various undesirable side effects and multi-drug resistance, novel treatment methods and agents are needed. In recent years, natural compounds have become a promising potential resource in cancer therapy [1-3]. Plants containing chemical compounds with therapeutic potential have a long history of use" in the treatment of various diseases. Most current anticancer drugs, such as taxol, vincristine, and vinblastine, originate from plants or their synthetic derivatives [4, 5]. *Paliurus spina-christi* Mill. (PSC), also defined as Jerusalem thorn or Christ's thorn, is generally

* Corresponding author: suleyman.ilhan@cbu.edu.tr
[1] Manisa Celal Bayar University, Faculty of Science and Literature, Department of Biology
E-mail: ferdioguz94@gmail.com, cisil.camli@cbu.edu.tr
ORCID: https://orcid.org/0000-0002-3123-8519, https://orcid.org/0000-0002-9641-7219, https://orcid.org/0000-0002-6584-3979

distributed in dry and rocky areas in the Mediterranean region and Asia [7]. The plant belongs to the Rhamnaceae family, which has five known species, and only PSC grows in the flora of Turkey. PSC is traditionally used as a diuretic, anti-rheumatic, tonic, hypocholesterolemic, anti-diarrheal. PSC fruit extract is also known to have an anti-diabetic effect [8]. The plant extract contains biologically active chemical compounds such as alkaloids, flavonoids, tannins, and sterols. These components in the PSC aqueous extract show antimicrobial, antibacterial, antifungal, hypoglycemic, and antioxidant properties. In addition, the fruits of the PSC generally are used as an anti-inflammatory in kidney stones, chest and face infections, and the leaves are usually used as a therapeutic against boil inflammation [6-8]. Based on all these significant biological activities of PSC, here we conducted the first study in the literature investigating the possible cytotoxic and apoptotic effects of the ethanolic extract of *Paliurus spina-christi* in human breast cancer cells. First, we characterized the extracts of leaves and flowers by gas chromatography–mass spectrometry (GC-MS) analysis. The possible cytotoxic effects were investigated via MTT assay and apoptotic effects of extracts were examined via flow cytometry.

2. MATERIALS AND METHODS

2.1. Preparation of PSC Extracts

Dried and washed plant material (*Paliurus spina-christi* Mill.) was purchased from a local company (Manisa, Turkey) and held at room temperature until used. The dried PSC flowers and leaves were powdered to homogeneous size with a homogenizer. Dried powder (2 gr) of the PSC leaf and flower were extracted separately in 50 ml ethanol (EtOH) at room temperature and ultrasonically extracted for 1 h and then filtration was performed with Whatman filter paper and stored at 4 °C until the experiments were carried out.

2.2. Cell Culture

MCF-7 and MDA-MB-231 cells were provided from Interlab Cell Line Collection (Genova, Italy). Human embryonic kidney cells (HEK-293) were provided from the American Type Cell Culture Collection (ATCC, USA). MCF-7 and MDA-MB-231 cells were grown in RPMI 1640 medium and human embryonic kidney cells were cultured in Eagle's Minimum Essential medium. Each medium included 10% heat-inactivated fetal bovine serum supplemented with 1% L-glutamine, and 1% penicillin-streptomycin. All cell lines were kept at 37 °C in a humidified atmosphere with 5% CO_2. The development and morphology of the cells were monitored daily with an inverted microscope.

2.3. Cytotoxicity Analysis

The cytotoxic effects of PSC leaf and flower extracts in MCF-7 and MDA-MB-231 cells were analyzed with MTT assay. Briefly, the breast cancer cells were placed at 10^4 cells per well in 100 µL media and increasing concentrations of PSC leaf and flower extracts (100, 250, 500, 750, 1000 µg/mL) were added to the cells in well-plate for 24, 48, and 72 h. After incubation periods, cells exposed to PSC leaf and flower extracts were subjected to 10 µL MTT and held at 37 °C for 4 h. Then, the solutions were withdrawn from wells and DMSO was implemented to the cells to dissolve formazan crystals. Lastly, the optical density of each well was evaluated at 570 nm wavelength with a spectrophotometer (TECAN Infinite 200 Pro).

2.4. Flow Cytometric Apoptosis Assay

PI Annexin V Apoptosis Detection Kit (BD, Biosciences) was utilized following the manufacturer's directions to verify the apoptotic effects of the PSC flower and leaf extracts. To determine early apoptotic cells, staining with Annexin V FITC is generally utilized in combination with a vital dye such as Propidium Iodide (PI). Viable cells externalize PI since they have undamaged membranes, while the membranes of dead cells are pervious to PI. Briefly, the cells were placed at 10^6 cells per well in a 6-well plate and were subjected to the most effective concentrations of PSC flower and leaf extracts for 72 h. Following the washing cells with cold PBS and resuspending in 1 mL of 1X

Binding Buffer, 5 µL of Annexin V FITC and 5 µL of PI were transferred to the solution. Then, the solution was shaken with vortex and maintained for 15 minutes at RT (25 °C) in the dark. Finally, 400 µl of 1X Binding Buffer was applied to each tube and the detection of apoptosis was evaluated utilizing flow cytometry. (BD Accuri C6 Flow Cytometer).

2.5. Detection of Volatile Components by GC-MS

Volatile compounds in the PSC flower and leaf extracts were qualitatively examined in electron ionization (EI) mode using an Agilent Technology 7890 Gas Chromatography (GC) Mass spectrometer (MS). The ethanol (EtOH) PSC extracts were centrifuged at 15.000 rpm for 10 min, and the supernatants were transported to the autosampler vial for GC-MS analysis. MS was registered at 70 eV ionization energy in full scan mode 35-550 amu range. The ionization source and transfer route temperatures were adjusted to 230 and 290 °C, respectively. The chromatographic pillar was an Agilent HP-5 MS capillary column (30 m x 0.25 mm i.d., 0.25 µm film thickness). The kiln temperature was launched at 40 °C with 2 min hold, then warmed to 300 °C at the rate of 5 °C min-1 and kept for 5 min. Helium gas was utilized as a carrier gas and the constant flow ratio was 1 mL min-1 and the injector temperature was adjusted as 220 °C. The PSC extracts were inserted in splitless mode (200:1) Evaluation of the mass spectrum of GC-MS was carried out utilizing the database of National Institute Standard and Technology (NIST).

2.6. Statistical Analysis

Statistical analysis was done via one-way analysis of variance (ANOVA) followed by a Dunnett's t-test using Graph Pad Prism 5. Values with a $p<0.05$ were considered statistically significant.

3. RESULTS

3.1. Volatile Components of PSC Extracts by GC-MS

The volatile component composition of PSC leaf and flower ethanolic extracts was identified by GC-MS analysis and the relative percentage amount of each component was measured by comparing the average peak area with the total areas. The analysis of PSC leaf extract volatile components exhibited a total of 27 defined components (Table 1) and the flower extract exhibited a total of 19 compounds (Table 2). On phytochemical screening, it was demonstrated that the leaf extract of PSC contains pyrrolidine, 2-Decanal, 2-Undecenal, phytol, oleic acid, oleamide, squalane, vitamin E, and gamma-sitosterol and the flower extract contains pyrrolidine, 2-Decanal, 2-Undecenal, oleic acid, lupeol, and gamma-sitosterol. Tables 1 and 2 display molecular formulas, similarity, and retention times of these components. Based on the present literature concerning components in GC-MS some compounds such as phytol, lupeol, gamma-sitosterol, oleamide, and squalane have been declared as anticancer agents.

3.2. Cytotoxic Effects of PSC Extracts on Breast Cancer Cells

To examine the efficacy of PSC leaf and flower extracts on the viability of human breast cancer cells, we exposed cells to increasing concentrations (100-1000 µg/mL) of PSC leaf and flower extracts for 24, 48, and 72 h and then MTT assay was carried out. As seen in Figure 1, PSC leaf extract did not have a significant cytotoxic effect on human breast cancer cells at 24 and 72 h ($p>0.05$), however, increasing PSC leaf extract concentrations inhibited the viability of MCF-7 and MDA-MB-231 cells at 48 h ($p<0.05$). As demonstrated in Figure 2, PSC flower extract suppressed the viability of MCF-7 breast cancer cells in a concentration- and time-dependent manner and the highest cytotoxic effect was obtained at 72 h. As shown in Figure 2, PSC flower extract showed no significant cytotoxic effect on MDA-MB-231 cells. Based on the MTT

viability assay, significant cytotoxic effects were observed after 72 h treatment of ethanolic leaf and flower extracts in MCF-7 cells but not in MDA-MB-231 cells.

Table 1 GC/MS analysis of ethanolic PSC leaf extract. The table lists the most common compounds in order of retention time (tR). The NIST database was used to interpret the mass spectrum of the GC-MS, which was expressed as % similarity

No	Source	Compound	tR (min)	Molecular formula	NIST match (similarity, %)
1	Leaf	Isopropoxycarbamic acid	5.431	C6H13NO3	71.31
2	Leaf	3-Amino-2-oxazolidinone	6.202	C3H6N2O2	80,62
3	Leaf	Pyrrolidine-Alpha	6.460	C4H5D4N	84.25
4	Leaf	Heptanal	8.377	C7H14O	92.86
5	Leaf	1,2-Cyclopentanedione	8.94	C5H6O2	89.72
6	Leaf	Octanal	10.997	C8H16O	95.17
7	Leaf	Formic acid	13.102	C9H18O2	94.48
8	Leaf	Nonanal	13.818	C9H18O	93.69
9	Leaf				
10	Leaf	2-Decenal	18.613	C10H18O	94.83
11	Leaf	Nonanoic acid	19.238	C9H18O2	97.09
12	Leaf	Cyclohexanone	20.072	C10H14O	78.54
13	Leaf	2-Undecenal	22.316	C13H18O2	93.38
14	Leaf	Trans-2-Dodecenoic acid	26.52	C12H22O2	80.41
15	Leaf	(-)-Loliolide	30.919	C11H16O3	81.67
16	Leaf	Hexadecanoic acid	34.72	C16H32O2	93.95
17	Leaf	Phytol	37.576	C20H40O	85.24
18	Leaf	Oleic Acid	37.999	C18H34O2	87.47
19	Leaf	Ethyl Oleate	38.507	C20H38O2	96.11
20	Leaf	9,12-Octadecadienoic acid	40.529	C18H32O2	75.72
21	Leaf	Oleamide	41.807	C18H35NO	84.53
22	Leaf	2,3-Dihydroxypropyl elaidate	46.866	C21H40O4	83.84
23	Leaf	13-Docosenamide	48.117	C22H43NO	95.27
24	Leaf	Squalene	48.784	C30H50	90.94
25	Leaf	Quercetin	49.715	C15H10O7	74.51
26	Leaf	Vitamin e	53.467	C29H50O2	90.27
27	Leaf	Gamma.-Sitosterol	57.456	C29H50O	73.85

Table 2 GC/MS analysis of ethanolic PSC flower extract. The table lists the most common compounds in order of retention time (tR). The NIST database was used to interpret the mass spectrum of the GC-MS, which was expressed as % similarity

No	Source	Compound	tR (min)	Molecular formula	NIST match (similarity, %)
1	Flower	Silane	5.410	C4H12O2Si	75.26
2	Flower	3-Amino-2-oxazolidinone	6.195	C3H6N2O2	80.46
3	Flower	Pyrrolidine-alpha	6.453	C4H5D4N	84
4	Flower	N Heptenal	8.377	C7H14O	92.53
5	Flower	Formic acid, octyl ester	13.13	C9H18O2	93.34
6	Flower	Nonanal	13.832	C9H18O	98
7	Flower	2-Decenal, (E)-	18.585	C10H18O	94.25
8	Flower	2-Undecenal	21.337	C11H20O	96.81
9	Flower	2H-Pyran-2-one	26.562	C12H22O2	80.23
10	Flower	1-Octadecanol	31.308	C18H38O	85.42
11	Flower	Hexadecanoic acid	34.740	C16H32O2	72.21
12	Flower	2,4(1H,3H)-Pyrimidinedione	35.387	C4H3N3O4	77.42
13	Flower	Oleic Acid	37.965	C18H34O2	72.04
14	Flower	Octadecanoic acid, ethyl ester	38.972	C20H40O2	83.17
15	Flower	Lupeol	43.551	C30H50O	79.26
16	Flower	2-Myristynoyl pantetheine	44.149	C25H44N2O5S	73.16
17	Flower	13-Docosenamide, (Z)-	48.151	C22H43NO	92.32
18	Flower	Butanoic acid	49.138	C24H34O6	78.15
19	Flower	Gamma.-Sitosterol	57.518	C29H50O	66.42

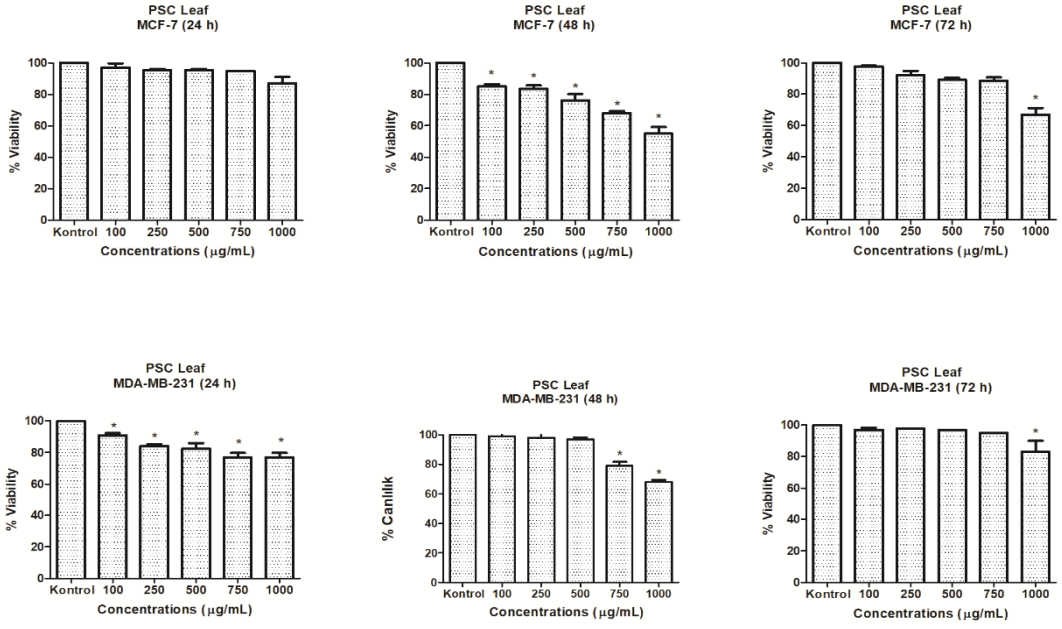

Figure 1 Effect of PSC leaf extract on the viability of MCF-7 and MDA-MB-231 breast cancer cells at 24, 48 and 72 h ($p<0.05$)

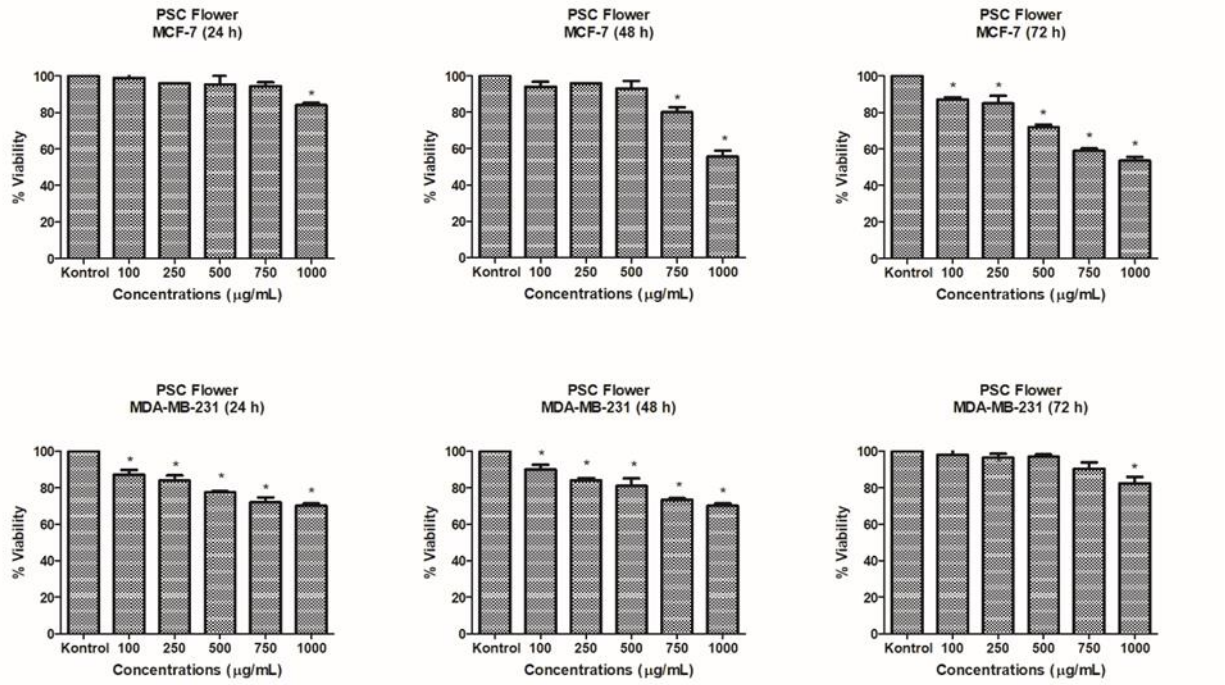

Figure 2 Effect of PSC flower extract on the viability of MCF-7 and MDA-MB-231 breast cancer cells at 24, 48 and 72 h ($p<0.05$)

3.3. Induction of Apoptosis by PSC Extracts in MCF-7 Breast Cancer Cells

To identify whether ethanolic PSC leaf and flower ethanolic extracts can trigger apoptosis in MCF-7 breast cancer cells, cells were exposed to 750 and 1000 µg/mL PSC extracts for 48 h. Then, we evaluated the potential apoptotic effect of PSC extracts on MCF-7 cells by flow cytometry using the PI Annexin V Apoptosis Detection Kit. Annexin V FITC has a high affinity to phosphatidylserine so Annexin V-FITC+/PI- cells specify early apoptotic cells and Annexin V-FITC+/PI+ cells specify late apoptotic cells. Based on a comparison of MCF-7 breast cancer cells exposed and not exposed to PSC flower and leaf extracts, dot plots of flow cytometric apoptosis analysis displayed the rate of early and late apoptosis. As shown in Figure 3, the percentage of early and late apoptotic cells in MCF-7 were 15.8% and 74.9% by 750 µg/mL PSC flower extract, respectively. The percentage of early apoptotic cells in MCF-7 breast cancer cells exposed to the PSC leaf extract was 0.2%, while the percentage of late apoptotic cells was 91.9% by 1000 µg/mL PSC flower extract, respectively. However, the rate of early apoptotic cells was 79% and the rate of late apoptotic cells was 0.8% in 750 µg/mL PSC flower extract treated MCF-7 breast cancer cells. The percentage of early and late apoptotic cells in MCF-7 breast cancer cells subjected to the 1000 µg/mL PSC leaf extract was 93.1% and 2.2%, respectively. These results revealed that both leaf and flower PSC extracts significantly induce apoptosis in MCF-7 breast cancer cells.

4. DISCUSSION

Multidisciplinary approaches such as surgery, adjuvant therapy, and radiotherapy are used in the treatment of breast cancer. In the effective treatment of breast cancer, maximum therapeutic effects and minimum undesirable effects such as recurrence, resistance, and toxic effects are aimed [12]. Plants have been widely used for therapeutic purposes in cancer treatment in recent years, due to their unique biological structures and the source of bioactive components [4].

Paliurus spina-christi Mill. (PSC) is a plant that grows in the Mediterranean region and Asia and has antimicrobial, antibacterial, antifungal, and

antioxidant properties [6-8]. PSC has attracted the attention of scientists in recent years due to these features. Takım et al. examined the inhibitory effect of PSC fruit against diabetes-stimulated inflammation caused by oxidative stress in vivo on diabetic rats. Researchers determined that PSC fruit extract has rich phenolic content and PSC fruit extracts showed a more effective antioxidant activity than standard antioxidants [9]. In another study, Takım et al. investigated the effects of PSC fruits on blood glucose, insulin, and glycated hemoglobin levels of streptozotocin-induced diabetic rats. They found that the groups that received insulin and PSC fruit extract had statistically lower blood sugar and glycosylated hemoglobin levels compared to the diabetic control group. Moreover, the outcomes of the investigation reported that the PSC fruit extract is rich in phenolic and mineral content [11]. Zor et al. analyzed the antigenotoxicity of compounds obtained from extracts of PSC fruits. The researchers examined the cytotoxicity and antigenotoxic efficiency of the components in Chinese hamster lung fibroblast (V79) cell lines. The IC_{50} values of catechin, gallocatechin, and rutin, which are components isolated from the PSC fruit extract, were calculated as 734 µg/mL, 220 µg/mL, and 1004 µg/mL, respectively. They found that the methanolic extract of PSC alone did not stimulate DNA single-stranded breaks, while catechins, gallocatechin, and rutin considerably decreased DNA damage caused by H_2O_2. Therefore, it is predicted that PSC fruits may be beneficial in the prevention of DNA damage-related disturbances [10]. Mosaddegh et al. investigated the effect of PSC fruit extract on lowering serum lipid content. The researchers administered streptozocin to male rats and then fed them a high cholesterol diet, and the rats were simultaneously exposed to various doses of PSC extract. Researchers analyzed serum levels of cholesterol, triglyceride, and HDL after 8 days and found that PSC extract decreased total

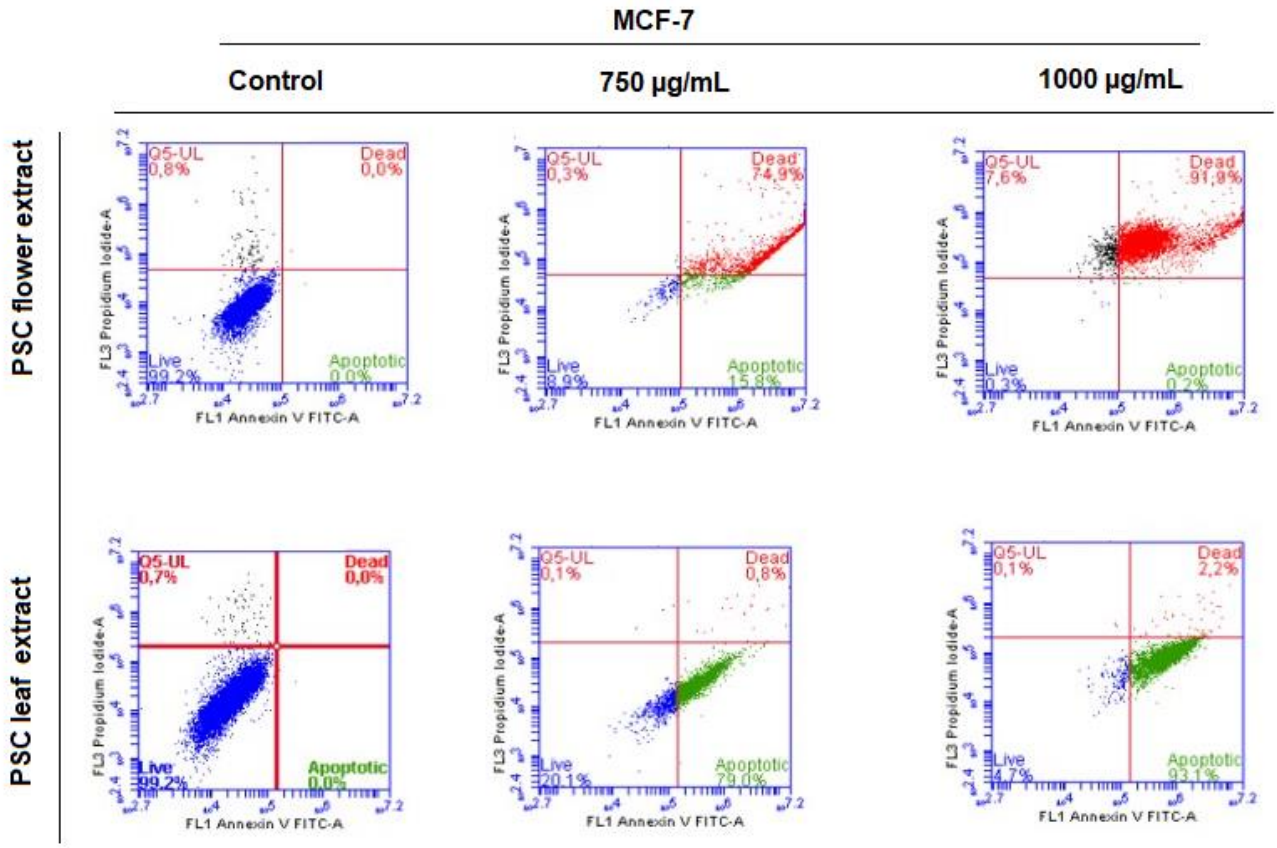

Figure 3 Apoptotic effects of PSC leaf and flower extract on MCF-7 cells at 48 h

cholesterol and triglyceride amount, but no significant increase was observed in HDL amount [13].

In the literature, antioxidant, antifungal, antimicrobial properties of PSC are known however its effects on cancer cells are not known [7]. Therefore, in this investigation, we purposed to investigate the possible anti-cancer effects of ethanolic extract of the PSC in human breast cancer cells. According to MTT analysis results, significant cytotoxic effects were observed in MCF-7 cells after 72 h of treatment of ethanolic leaf and flower extract, but not in MDA-MB-231 cells. This may be due to the different molecular phenotypes of the MCF-7 and MDA-MB-231 cell lines. MDA-MB-231 is an aggressive, invasive triple-negative breast cancer cell line as it lacks estrogen receptor, progesterone receptor expression, and HER2. MCF-7 cells are estrogen receptor-positive, progesterone receptor-positive, and HER2 negative [14]. Consistent with the MTT analysis results, flow cytometry data showed that both PSC leaf and flower extracts induced apoptosis in MCF-7 cells. We also performed GC-MS analysis to determine the volatile compound composition, and the results of the analysis detected the presence of active substances that may have anticancer potential in both leaf and flower extracts. These preliminary data showed that PSC is a potential herb to be used in the treatment against estrogen receptor-positive MCF-7 breast cancer cells. In the next stages, the active ingredients in the PSC extract can be purified and their effects on different cancer cells can be investigated individually or in combination.

5. CONCLUSION

Paliurus spina-christi Mill. has been used in folk medicine for its antimicrobial, antibacterial, antifungal, and antioxidant effects. Various in vitro studies have confirmed these effects of PSC extract, but to the best of our knowledge, the possible cytotoxic effect of ethanolic PSC extract on cancer cells had not been investigated before. This in vitro study reported that ethanolic PSC leaf and flower extracts have a significant cytotoxic effect on MCF-7 cells, but not in MDA-MB-231 cells. According to the results of flow cytometric analysis, PSC leaf and flower extracts also induced apoptosis in MCF-7 cells. GC-MS analysis results indicated the presence of active substances that may have anticancer effects in PSC leaf and flower extracts. These components in combination or separately may have behaved as an anticancer agent by inhibiting breast cancer cells. Therefore, there is a need for investigations in which the active ingredients in the PSC extract are purified and used on cancer cells individually or in combination.

Acknowledgements

The experiments in this paper were partially performed at Manisa Celal Bayar University (Turkey)- Applied Science and Research Center (DEFAM).

Funding

The authors have no received any financial support for the research, authorship or publication of this study.

The Declaration of Conflict of Interest/ Common Interest

No conflict of interest or common interest has been declared by the authors.

Authors' Contribution

Under this heading, the authors contributed equally to the study

The Declaration of Ethics Committee Approval

This study does not require ethics committee permission or any special permission. The Declaration of Research and Publication Ethics The authors of the paper declare that they comply with the scientific, ethical and quotation rules of SAUJS in all processes of the paper and that they do not make any falsification on the data collected. In addition, they declare that Sakarya University Journal of Science and its editorial board have no responsibility for any ethical violations that may be encountered, and that this study has not been evaluated in any academic

REFERENCES

[1] A. G. Waks and E. P. Winer, "Breast Cancer Treatment," *JAMA*, vol. 321, no. 3, p. 288, Jan. 2019.

[2] K. Barzaman *et al.*, "Breast cancer: Biology, biomarkers, and treatments," *Int. Immunopharmacol.*, vol. 84, no. April, 2020.

[3] K. L. Britt, J. Cuzick, and K. A. Phillips, "Key steps for effective breast cancer prevention," *Nat. Rev. Cancer*, vol. 20, no. 8, pp. 417–436, 2020.

[4] H. Atmaca, C. Camli, and S. Sert, "Ethanol Extract of Pinus nigra ssp. pallasiana var. şeneriana Inhibits Human Breast Cancer Cell Viability through Induction of Apoptosis," *Celal Bayar Üniversitesi Fen Bilim. Derg.*, vol. 14, no. 1, pp. 35–40, 2018.

[5] A. L. Risinger, F. J. Giles, and S. L. Mooberry, "Microtubule dynamics as a target in oncology," *Cancer Treat. Rev.*, vol. 35, no. 3, pp. 255–261, 2009.

[6] F. Farmani, M. Moein, A. Amanzadeh, H. M. Kandelous, Z. Ehsanpour, and M. Salimi, "Antiproliferative evaluation and apoptosis induction in MCF-7 cells by Ziziphus spina christi leaf extracts," *Asian Pacific J. Cancer Prev.*, vol. 17, no. 1, pp. 315–321, 2016.

[7] A. H. Brantner and Z. Males, "Quality assessment of Paliurus spina-christi extracts," *J. Ethnopharmacol.*, 1999.

[8] A. Şen, "Antioxidant and anti-inflammatory activity of fruit, leaf and branch extracts of Paliurus spina-christi P. Mill," *Marmara Pharm. J.*, vol. 22, no. 2, pp. 328–333, Apr. 2018.

[9] K. Takım and M. Işık, "Phytochemical Analysis of Paliurus spina-christi Fruit and Its Effects on Oxidative Stress and Antioxidant Enzymes in Streptozotocin-Induced Diabetic Rats," *Appl. Biochem. Biotechnol.*, vol. 191, no. 4, pp. 1353–1368, 2020.

[10] M. Zor, S. Aydin, N. D. Güner, N. Başaran, and A. A. Başaran, "Antigenotoxic properties of Paliurus spina-christi Mill fruits and their active compounds," *BMC Complement. Altern. Med.*, vol. 17, no. 1, pp. 1–10, 2017.

[11] K. Takım, "Bioactive component analysis and investigation of antidiabetic effect of Jerusalem thorn (Paliurus spina-christi) fruits in diabetic rats induced by streptozotocin," *J. Ethnopharmacol.*, vol. 264, no. August 2020, p. 113263, 2021.

[12] F. A. Fisusi and E. O. Akala, "Drug Combinations in Breast Cancer Therapy," *Pharm. Nanotechnol.*, vol. 7, no. 1, pp. 3–23, 2019.

[13] M. Mosaddegh, M. J. Khoshnood, M. Kamalinejad, and E. Alizadeh, "Study on the effect of paliurus spina-christi on cholesterol, triglyceride and hdl levels in diabetic male rats fed a high cholesterol diet," *Iran. J. Pharm. Res.*, vol. 3, no. 1, pp. 51–54, 2004.

[14] F. Ourique *et al.*, "DNA damage and inhibition of akt pathway in MCF-7 cells and ehrlich tumor in mice treated with 1,4-naphthoquinones in combination with ascorbate," *Oxid. Med. Cell. Longev.*, vol. 2015.

SAKARYA ÜNİVERSİTESİ
FEN BİLİMLERİ ENSTİTÜSÜ DERGİSİ

Sakarya University Journal of Science
SAUJS

e-ISSN 2147-835X Period Bimonthly Founded 1997 Publisher Sakarya University
http://www.saujs.sakarya.edu.tr/

Title: Early-breeding Season Movements of the Yelkouan Shearwater (Puffinus yelkouan, Acerbi, 1827) at the Dardanelles Strait

Authors: İbrahim UYSAL, Lider SİNAV, Yakut Can AŞIKOĞLU, Şafak ARSLAN

Recieved: 2021-12-28 00:00:00

Accepted: 2022-03-14 00:00:00

Article Type: Research Article

Volume: 26
Issue: 2
Month: April
Year: 2022
Pages: 365-374

How to cite
İbrahim UYSAL, Lider SİNAV, Yakut Can AŞIKOĞLU, Şafak ARSLAN; (2022), Early-breeding Season Movements of the Yelkouan Shearwater (Puffinus yelkouan, Acerbi, 1827) at the Dardanelles Strait. Sakarya University Journal of Science, 26(2), 365-374, DOI: 10.16984/saufenbilder.1049912
Access link
https://dergipark.org.tr/tr/journal/1115/issue/69580/1049912

New submission to SAUJS
http://dergipark.gov.tr/journal/1115/submission/start

Sakarya University Journal of Science 26(2), 365-374, 2022

Early-breeding Season Movements of the Yelkouan Shearwater (*Puffinus yelkouan,* Acerbi, 1827) at the Dardanelles Strait

İbrahim UYSAL*[1], Lider SİNAV[2], Yakut Can AŞIKOĞLU[3], Şafak ARSLAN[4]

Abstract

We aimed to make censuses of *Puffinus yelkouan* at the Dardanelles and to evaluate the movements at the Aegean and the Marmara Sea during the early breeding period. Field studies were carried out in the morning and afternoon for 40 days between 6 February and 22 March 2019. In the censuses, the highest number of birds, passing in both directions in a day was 78145 individuals; 56451 of them were counted in the direction of the Aegean Sea on 17 February, which is the highest number counted in one direction in a day. As a result, the number of birds crossing to the Aegean Sea through the Dardanelles in the afternoon is significantly higher than the number of birds crossing to the Aegean Sea in the morning. In the afternoon, the number of birds flying towards the Aegean Sea is significantly higher than the number of birds flying towards the Marmara Sea. Considering that the species visits the breeding colonies at night, this movement pattern could be related to the fact that the shearwater breeding population is predominantly found in the Aegean or in the Mediterranean Sea. In addition, some issues, such as how long the birds stay in these sea regions after flying to the Aegean Sea or the Marmara Sea, which route they follow or how the flocks mix require further investigation.

Keywords: Dardanelles, *Puffinus yelkouan*, breeding period, population census, movements

1. INTRODUCTION

Puffinus yelkouan species, which is included in the order of Procellariiformes, lives in the open seas outside the incubation period and almost all of its population is distributed in the Mediterranean, the Aegean and the Black Seas. According to the IUCN red list, it is reported to be in the status of vulnerable due to the decreasing trend of the population on a global scale. Fishing, illegal hunting, human-induced disturbance, light and noise pollution, increasing predator

* Corresponding author: uysalibrahim@comu.edu.tr
[1] Çanakkale Onsekiz Mart University, Çanakkale Health Services Vocational School, Department of Medical Services and Techniques
ORCID: https://orcid.org/0000-0002-7507-3322
[2] Hacettepe University, Faculty of Science
E-mail: lidersnv@gmail.com
ORCID: https://orcid.org/0000-0001-7938-8869
[3] Çanakkale Onsekiz Mart University, Graduate Education Institute Department of Biology
E-mail: yakutcanasikoglu@gmail.com
ORCID: https://orcid.org/0000-0001-9963-5732
[4] Birdlife Turkey
E-mail: safak.arslan@dogadernegi.org
ORCID: https://orcid.org/0000-0003-2282-5401

populations in breeding areas and habitat destruction are reported as the important factors in the decline in its population in recent years [1-7].

It has been reported that Yelkouan Shearwater individuals start to join the breeding colonies in November, mating takes place in February and lays eggs in March. Studies have shown that the young start to leave the nest in June and this process continues until July [8]. As breeding grounds, Yelkouan Shearwaters prefer hard-to-reach cavities under rock blocks, cavities they dig on soil surfaces, and sometimes human structures [9].

Islands, which contain suitable habitats for nest building, provide protection against external environmental conditions and predators, are preferred as breeding grounds [9-11]. Pair number in known breeding colonies reported; Italy (12,000–19,000 p.), Greece (7,000–10,000 p.), Malta (1,370-2,000 p.), France (627-1,044 p.), Croatia (300–500 p.), Tunisia (180–200 p.), Algeria (10–100 p.), Albania (1-10 p.), and Bulgaria (0–10 p.) [11].

In the studies carried out so far on the breeding areas of the species, it has been stated that most of the breeding population is concentrated in Malta, Italy, Greece, France, Croatia and Turkey, and there may be 10,815 to 53,574 breeding pairs in these areas [1]. Although it has been reported that a breeding colony is likely to exist in Turkey, a breeding site has not been determined yet [6, 12].

Radio-Telemetry studies carried out reveal that a large part of the population in the Mediterranean, which breed in Malta and France, migrate to the Black Sea to spend a few months outside the breeding period and are long-distance migrants [13-15]. In their study, Ortega and İsfendiyaroğlu [7] stated that the Black Sea is an important gathering area for the Yelkouan Shearwater populations in the Mediterranean, outside the breeding season.

Being a pelagic species, the activity of Yelkouan Shearwater in open sea is difficult to monitor from land. However, monitoring by boats causes problems in terms of cost and time. The areas where the water bodies narrow, such as the Dardanelles and the Bosphorus, are the most ideal points where the population can be monitored. As a matter of fact, in the observations made in the Bosphorus, it has been reported that over 90,000 Yelkouan individuals were counted in a short time. In the censuses made in the Bosphorus, it was reported that the lowest number of individuals was reached in September and October, and the highest number of individuals was reached in January and February [16].

The global population of Yelkouan Shearwater, a species endemic to the Mediterranean basin, is estimated at 15,337-30,519 pairs or 46,000-92,000 individuals [12, 17, 18]. Populations in known breeding colonies are either declining or have been poorly researched [19]. It has been reported that the global population will decrease by approximately 50% in 54 years (3 generations) if the decline in the population of the species included in the globally endangered Vulnerable species category continues at the current rate. Therefore, research priorities regarding the species have been reported as searching for new breeding colonies, monitoring the population in important breeding and bottleneck areas, assessing mortality rates and examining demographic parameters [12]. Considering the 75,000-90,000 individuals recorded during their pre-breeding mobility in the Bosphorus [16], more research is needed to confirm the breeding population sizes, especially in the Aegean Sea and Turkey.

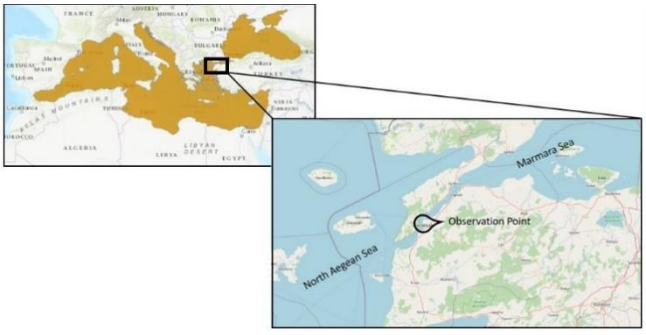

Figure 1 Distribution map of the Yelkouan Shearwater and the observation point in the Dardanelles

In the study, it was aimed to monitor and count the activity in the early breeding period in the Dardanelles Strait, which is one of the important

bottlenecks in terms of monitoring the population of the species, and to compare the activity in the direction of the Aegean Sea and the Marmara Sea during the early breeding period. In this respect, the data obtained from the study will provide the opportunity to compare the population censuses of the species to be made in the future, help guide international conservation efforts and contribute to the research of possible breeding colonies in Turkey.

2. MATERIAL AND METHOD

Monitoring studies were carried out between 06 February and 22 March 2019 for a total of 40 days. No monitoring studies were carried out on dates when visibility made it impossible to monitor due to heavy fog. For this reason, the entire 40-day follow-up study was carried out on the dates when visibility was appropriate. During the monitoring studies, at least two observers participated in the counts every day and the counts were continued between the hours of sunrise and sunset. Bourgeois et al. (2008a) reported that the copulation behaviour of the species takes place in February and they lay eggs in March (Bourgeois et al. 2008a). In this respect, observation studies were determined as February and March, taking into account the mating period of the species.

On observation days, there was only a break between 12:00 and 13:00 between sunrise and sunset. Binoculars, telescopes, telephoto lenses and cameras were used in the monitoring studies, and observation data (such as transit time, number of individuals, transit direction) were recorded in pre-prepared registration forms. Monitoring studies were carried out between the Çimenlik Castle and Kilitbahir Castle, which is the narrowest point of the Dardanelles with 1500 m, in order to minimize the losses (Observation point coordinate: UTM 35 N 448852 4444480, 5m) (Figure 1).

2.1. Statistical Analysis

The data used in statistical analysis are the morning and afternoon counts of 40 days. The data set consists of the number of Yelkouans passing through the Dardanelles in the direction of the Aegean and Marmara Seas, their transit times, date and direction of passage. The hypothesis in this research was established to test whether there is a significant difference between the number of Yelkouans crossing the Aegean and Marmara Seas. The normal distribution of the data was tested before the analyses were made. Since the sample size was less than 50 (n=40), Shapiro-Wilk Test was applied. As a result of the test, the p value ($p<0.05$) was found and it was accepted that the data were not normally distributed [20]. The log10 transformation was applied to the count data that did not comply with the normal distribution condition [21]. After the data transformation was completed, One Way ANOVA, Two Way ANOVA and interactions analysis were applied. With these tests, the numbers of Yelkouan moving between the Marmara and the Aegean Seas were examined in terms of time and direction, which are independent variables.

These tests are shown below;

- one.way<-aov(log10(tot_ind)~time, data=yelkouan)
- one.way<-aov(log10(tot_ind)~direction, data=yelkouan)
- two.way<-aov(log10(tot_ind)~time+direction, data=yelkouan)
- interactions<-aov(log10(tot_ind)~time*direction, data=yelkouan)

The dependent variable in the tests is the total number of individuals (tot_ind). The number of individuals in each Yelkouan flock were recorded separately. Time, which is one of the independent variables, was divided into two categories, namely morning and afternoon. The other independent variable was direction, and it was divided into two categories, the Marmara and the Aegean Sea. These tests were compared by looking at AICc values [22]. Binary interactions analysis with $\Delta AICc < 2$ was determined as the best explanatory analysis. Calculations to determine the AICc values were made using the 'AICcmodavg' package in the R program version 4.0.3 [23]. Then, Tukey HSD test was applied and the differences between the two groups were

compared (Table 1). It was found that the interactions between direction of passage and time of transition explained 98% (R^2 = 98) variability of the Yelkouan movements.

Table 1 Results of the Tukey HSD test (m=morning, a=afternoon, as=Aegean Sea, ms=Marmara Sea).

Comparisons	diff	lwr	upr	p-adj
m:as-a:as	-0.59	-0.85	-0.33	0.00
a:ms-a:as	-0.30	-0.57	-0.04	0.02
m:ms-a:as	-0.39	-0.65	-0.13	0.00
a:ms-m:as	0.28	0.02	0.54	0.03
m:ms-m:as	0.20	-0.06	0.45	0.20
m:ms-a:ms	-0.09	-0.35	0.17	0.82

3. RESULTS

Puffinus yelkouan species live in open seas except incubation period and almost all of its population is distributed in the Mediterranean and Black Seas. During the censuses in the Dardanelles during the early breeding period of the species, a total of 604956 individuals were counted in 892 passages during 40 days. 384678 of the crossings took place in the Aegean Sea direction and 220278 in the Marmara Sea direction. The highest counts made in one day in both directions were 78145 individuals (in the direction of the Marmara Sea: 24815 individuals, towards the Aegean Sea direction: 53330 individuals) on 26.02.2019 and a total of 57829 individuals on 17.02.2019 (in the direction of Marmara Sea: 1378 individuals, 56451 individuals in the Aegean Sea direction) realized with. On 17.02.2019, 56451 individuals counted towards the Aegean Sea became the highest number of individuals counted in a single direction in a day. The lowest number of individuals was counted on March 13 with a total of 3697 individuals. The maximum number of individuals in one hour was reached between February 26, 13:00-14:00 (4160 individuals towards the Aegean Sea 19423, towards the Marmara Sea). In the censuses made within the 40-day period, it was determined that the intensity of the activity was concentrated in the afternoon (13:00 and sunset hours) and towards the Aegean Sea. The distribution of morning and afternoon passes in February and March is given in Figure 2 and hourly observation records are given in Appendices 1.

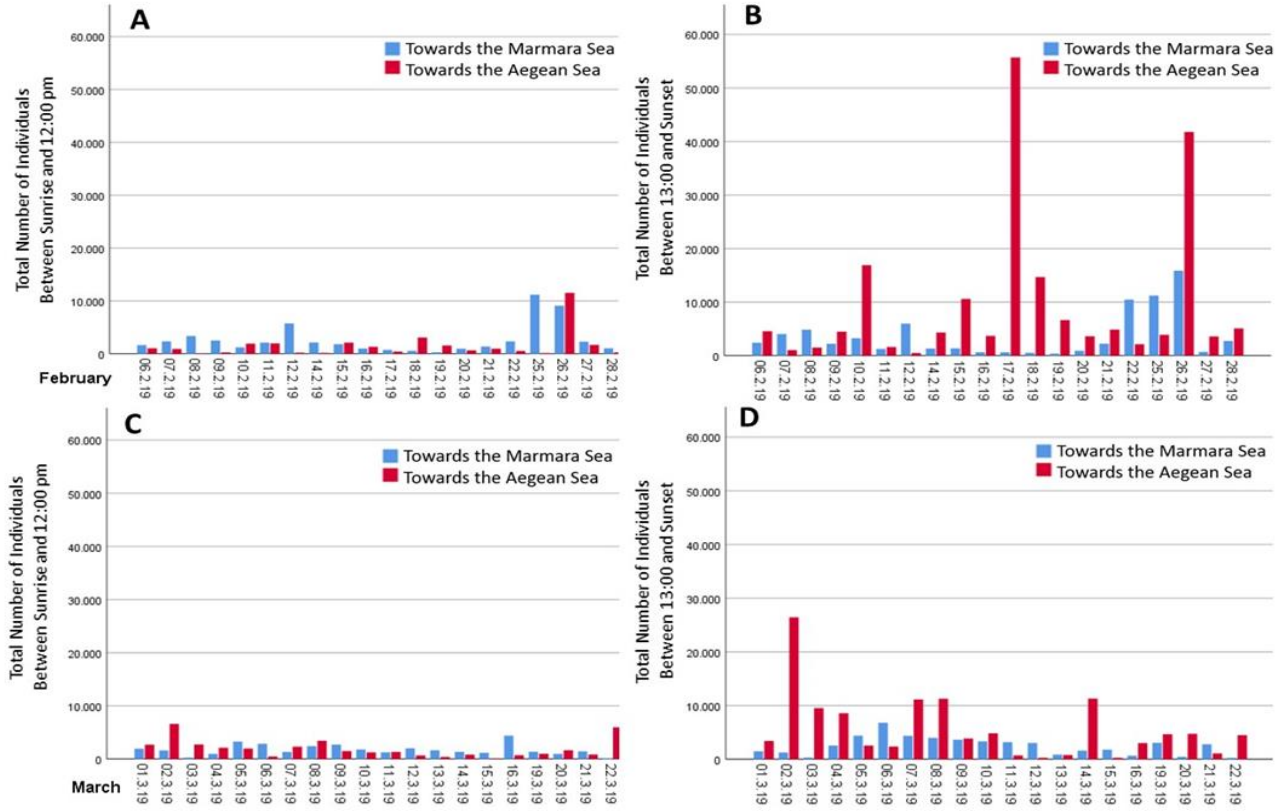

Figure 2 Number of individuals transiting (A: morning counts in February, B: afternoon counts in February, C: morning counts in March, D: afternoon counts in March

A significant ($p<0.001$) difference was found between the number of birds crossing the Aegean Sea in the morning and the number of birds crossing the Aegean Sea in the afternoon. In addition, a significant ($p<0.05$) difference was found between the number of birds crossing the Marmara Sea in the afternoon and the number of birds crossing the Aegean in the afternoon. In addition, a significant ($p<0.001$) difference was found between the number of birds crossing the Marmara Sea in the morning and the number of birds crossing the Aegean Sea in the afternoon. It was found that the number of birds crossing the Marmara Sea in the afternoon was significantly different from the number of birds crossing the Aegean Sea in the morning ($p <0.05$) (Figure 3).

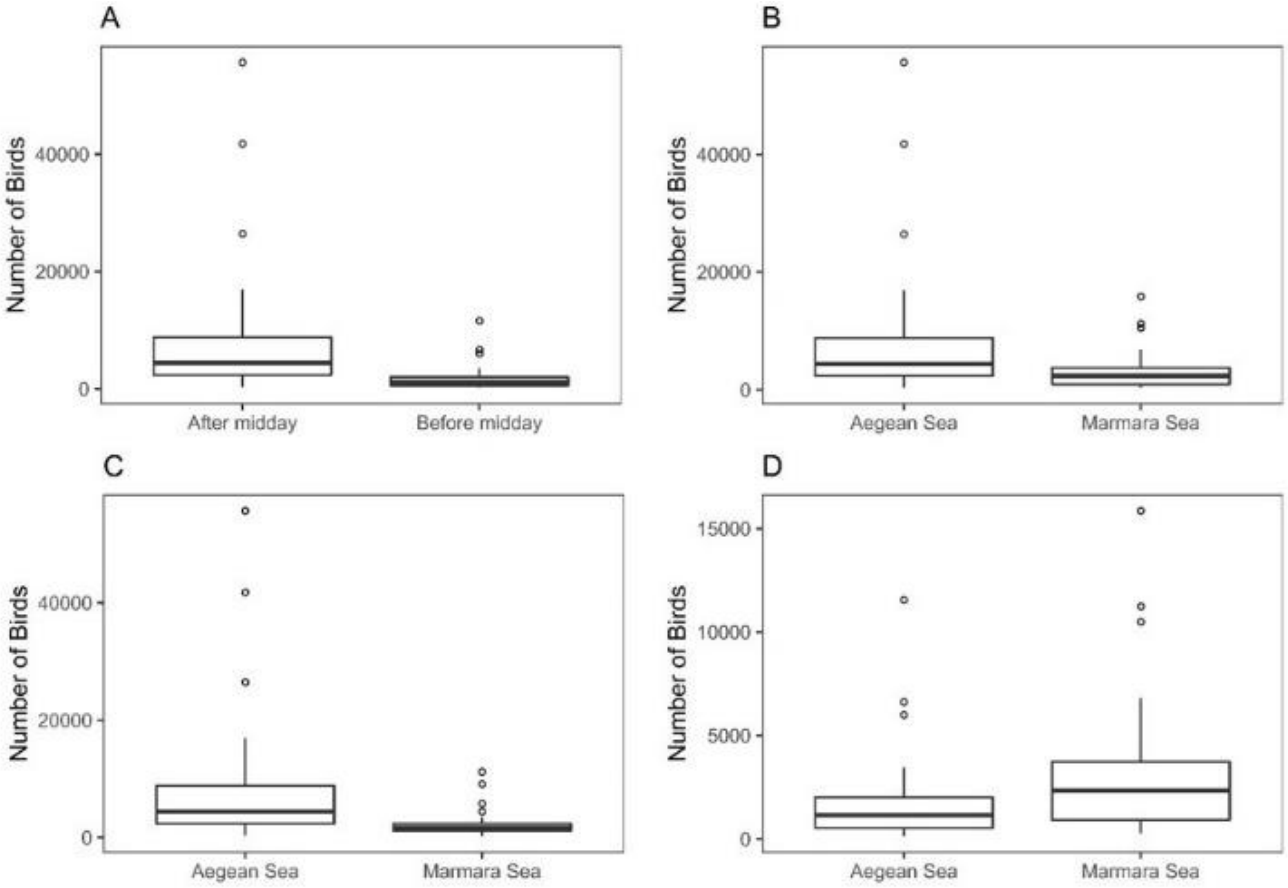

Figure 3. Tukey HSD test results

According to the results of the Tukey HSD test, the number of birds crossing from the Marmara Sea to the Aegean Sea through the Dardanelles in the afternoon is significantly higher than the number of birds crossing from the Marmara Sea to the Aegean Sea in the morning (Figure 3-A). In the afternoon, the number of birds flying towards the Aegean Sea is significantly higher than the number of birds flying towards the Marmara (Figure 3-B). The number of birds flying towards the Marmara Sea in the morning is significantly lower than the number of birds flying towards the Aegean Sea in the afternoon (Figure 3-C). The number of birds flying towards the Aegean Sea in the morning is significantly lower than the number of birds flying towards the Marmara Sea in the afternoon (Figure 3-D).

4. DISCUSSION AND CONCLUSION

This mobility direction and density during the breeding period shows that it would be appropriate to conduct monitoring in the Aegean Sea rather than the Marmara Sea in future studies to investigate the possible breeding colony.

It is reported that the populations of the Yelkouan species, which is endemic to the Mediterranean basin, in known breeding colonies are either in a decreasing trend or there is insufficient research

[19]. A reliable estimate of the population size of the species and repeat counts at regular intervals are essential, as the population tends to decline on a global scale.

Data from regular censuses provide information on conditions such as reduced successful reproduction or reduced adult survival that could result in a decline in numbers. However, at the stage of data collection, records must be recorded in a standard and reliable manner. Data obtained in this way can play a role in determining the success or failure of the conservation actions carried out [24]. In the censuses made in the Bosphorus in 2012, it was reported that nearly 90,000 individuals were counted within a few hours [16]. In the censuses made by us in the Dardanelles, these figures could not be reached. The maximum number of individuals in one hour was reached between 13:00 and 14:00 on February 26 (4160 in the direction of the Aegean Sea 19423, towards the Marmara Sea). The highest count in a day was recorded on February 26 with 78145 individuals. In order to interpret the data in a healthier way, simultaneous long-term counts should be made in the Istanbul and Çanakkale Straits.

In studies in which the mobility of the species is monitored using telemetry, it is seen that the population in France, Italy and Malta mostly migrate to the Eastern Mediterranean and Black Sea [13-15]. In addition, it is stated that the Black Sea is an important gathering area for the Yelkouan populations in the Mediterranean, outside the breeding season [7]. The Dardanelles Strait, where observation studies are carried out, is a very important point for monitoring the mobility of the species between the Black Sea and the Mediterranean.

The Yelkouan Shearwater global population size has been estimated at 46,000 to 92,000 individuals [18]. It has been reported that over 90,000 Yelkouan individuals were counted in a short time that they were flying through one direction in the observations made in the Bosphorus [16]. In the observation studies carried out by us in the Dardanelles, 78145 individuals were counted on the date when the total number of crossings to the Marmara Sea and the Aegean Sea directions was the highest (in the direction of Marmara Sea: 24815 individuals, in the direction of Aegean Sea: 53330 individuals). The distribution and the rate of mobility of the population outside the incubation period vary according to the nutrient abundance and meteorological conditions [25]. As a limitation of the study, the censuses made during the early breeding period should be evaluated by taking this issue into account. In addition, simultaneous censuses in bottlenecks where land censuses can be made can provide better data for comparison and to provide information about changes in the population of the species.

It is estimated that a large part of the breeding population is concentrated in Malta, Italy, Greece, France, Croatia and Turkey and there may be 10,815 to 53,574 breeding pairs in these areas [1]. Although it is likely to breed in Turkey, its breeding area has not been determined yet [12]. In order to investigate possible breeding sites of the species in the region, research studies should be conducted in areas containing suitable habitats for nest construction, such as cliffs and soil surfaces. However, in research studies that require intensive human resources, workforce and financial support, it is important to concentrate the areas to be researched with more probable areas. A pelagic species that makes long journeys in the sea during the breeding season, the Yelkouan travels an average of 428 km before returning to the colony to feed young [15]. In this respect, the records taken from the Dardanelles during the breeding period provided preliminary data for the investigation of a possible breeding colony.

Our findings showed that the number of birds that passed to the Aegean Sea in the afternoon was significantly higher than the number of birds that passed to the Aegean Sea in the morning. This may be related to the fact that the main breeding areas of the species are in the Aegean Sea region. In addition, the fact that the number of birds moving towards the Aegean Sea in the afternoon is significantly higher than the number of birds moving towards the Marmara Sea in the afternoon may be due to the fact that the main breeding areas are in the Aegean Sea. It is known that this species feeds in the open sea during the day and goes to

the land where there are colonies for breeding activities at night. However, the demographic characteristics of the birds counted in this study are not known. For this reason, it is difficult to explain comprehensively whether the movements of birds are for breeding purposes. The uncertainty of this situation cannot be investigated with this research method.

In addition, the fact that the number of birds flying towards the Marmara Sea in the morning is significantly lower than the number of birds flying towards the Aegean Sea in the afternoon suggests that this species may not be moving regularly between the two seas every day. Moreover, it is also among our findings that the number of birds flying towards the Aegean Sea in the morning is significantly lower than the number of birds flying towards the Marmara Sea in the afternoon. In addition, some issues, such as how long the birds stay in these sea regions after flying to the Aegean Sea or the Marmara Sea, which route they follow or how the flocks mix require further investigation. Extensive research would lead to a better understanding of the purpose of the bird's movements between the two seas and how the time spent in those two seas changes.

With the study, 40-day monitoring data was presented in February and March in the Dardanelles, which is one of the important bottlenecks in terms of monitoring the population of the species. In addition, in order to provide preliminary data in determining the probable breeding areas of the breeding population, which was also reported in previous studies where it could not be determined precisely in Turkey, a comparison of the movements in the Aegean Sea and the Marmara Sea during the early breeding period was made. In this respect, the data obtained from the study will provide the opportunity to compare the population censuses of the species to be made in the future, help guide international conservation efforts and contribute to the research of possible breeding colonies in Turkey.

5. GENERAL REQUIREMENTS

Acknowledgments

The authors also thank the bird watchers Pınar GÜNDOĞDU and Mehmet KAYA as well as who supported the field monitoring studies, for their contributions.

Funding

This work was supported by the Doğa Derneği (Bird Life Turkey).

The Declaration of Conflict of Interest/ Common Interest

No conflict of interest or common interest has been declared by the authors.

Authors' Contribution

The authors contributed equally to the study.

The Declaration of Ethics Committee Approval

This study does not require ethics committee permission or any special permission.

The Declaration of Research and Publication Ethics

The authors of the paper declare that they comply with the scientific, ethical and quotation rules of SAUJS in all processes of the paper and that they do not make any falsification on the data collected. In addition, they declare that Sakarya University Journal of Science and its editorial board have no responsibility for any ethical violations that may be encountered, and that this study has not been evaluated in any academic publication environment other than Sakarya University Journal of Science.

REFERENCES

[1] K. Bourgeois and E. Vidal, "The endemic Mediterranean yelkouan shearwater *Puffinus yelkouan*: distribution, threats and a plea for more data," Oryx, vol. 42, no. 2, pp. 187-94, 2008.

[2] J. J. Borg, H. Raine, A. Raine and N. Barbara, "Protecting Malta's wind chaser: the EU LIFE Yelkouan Shearwater project report," BirdLife Malta, EU LIFE Yelkouan Shearwater Project, Malta. 2010.

[3] S. Oppel, A. F. Raine, J. J. Borg, H. Raine, E. Bonnaud, K. Bourgeois and A. R. Breton, "Is the Yelkouan shearwater *Puffinus yelkouan* threatened by low adult survival probabilities?" Biol. Conserv, vol. 114, pp. 2255–2263, 2011.

[4] E. Bonnaud, G. Berger, K. Bourgeois, J. Legrand and E. Vidal, "Predation by cats could lead to the extinction of the Mediterranean endemic Yelkouan Shearwater *Puffinus yelkouan* at a major breeding site" Ibis, vol. 154, pp. 566–577. 2012.

[5] F. Micheli, B. S. Halpern, S. Walbridge, S. Ciriaco, F. Ferretti, S. Fraschetti, et al., "Cumulative human impacts on Mediterranean and Black Sea marine ecosystems: assessing current pressures and opportunities," PLoS One, vol. 8, no. 12, e79889, 2013.

[6] C. Carboneras, F. Jutglar and G. M. Kirwan, "Yelkouan Shearwater (*Puffinus yelkouan*), version 1.0. In Birds of the World" (J. del Hoyo, A. Elliott, J. Sargatal, D. A. Christie, and E. de Juana, Editors). Cornell Lab of Ornithology, Ithaca, NY, USA, 2020.

[7] M. P. Ortega and S. İsfendiyaroğlu, "Predicting foraging hotspots for Yelkouan Shearwater in the Black Sea" Deep-Sea Research, vol. 141, no. 2, pp. 237–247, 2017.

[8] K. Bourgeois, S. Dromzée, E. Vidal and J. Legrand, "Yelkouan shearwater *Puffinus yelkouan* presence and behaviour at colonies: not only a moonlight question" Comptes Rendus Biologies,vol. 331, pp. 88-97, 2008.

[9] K. Bourgeois and E. Vidal, "Yelkouan shearwater nest-cavity selection and breeding success" C. R. Biol., vol. 330, pp. 205–214, 2007.

[10] K. Bourgeois, E. Vidal, V. Comor, J. Legrand and S. Dromzée, "Colony-site selection drives management priorities for yelkouan shearwater populations" Journal of Wildlife Management, vol. 72, pp. 1188-1193, 2008.

[11] K. Bourgeois, S. Dromzée, E. Vidal, "Relationships between nest-cavity and mate selection, reproductive performance and fidelity in the Mediterranean endemic Yelkouan Shearwater *Puffinus yelkouan"* Acta Ornithologica, vol. 49, pp. 9-22, 2014.

[12] C. Carboneras, M. A. Derhè and I. Ramirez, "Update on the population status and distribution of Mediterranean shearwaters" Presented at the ACAP - 7th Meeting of the Advisory Committee At: La Rochelle, France, 6-10 May, 2013.

[13] T. Militão, K. Bourgeois, J. L. Roscales and J. González-Solís, "Individual migratory patterns of two threatened seabirds revealed using stable isotope and geolocation analyses" Divers. Distrib., vol. 19, no. 3, pp. 317–329, 2013.

[14] A. F. Raine, J. J. Borg, H. Raine and R. A. Phillips, "Migration strategies of the Yelkouan Shearwater *Puffinus yelkouan*" J. Ornithol., vol. 154, no. 2, pp. 411–422, 2012.

[15] C. Péron, D. Grémillet, A. Prudor, E. Pettex, C. Saraux, A. Soriano-Redondo, M. Authier and J. Fort, "Importance of coastal Marine Protected Areas for the conservation of pelagic seabirds: the case of Vulnerable yelkouan shearwaters in the Mediterranean Sea". Biol. Conserv., vol. 168, pp. 210–221, 2013.

[16] D. Şahin, E. Bacak, S. Bilgin, C. Atay, K. A. Boyla, J. Tavares, "Presence and behaviour of Yelkouan Shearwaters

Puffinus yelkouan at the Bosphorus" In:Yésou P, Baccetti N, Sultana J. (Eds), Ecology and Conservation of Mediterranean Seabirds. Presented at the 13th Medmaravis Pan-Mediterranean Symposium. Alghero (Sardinia), 14–17 Oct. 2011. Medmaravis, Alghero, pp. 54–57, 2011.

[17] P. Defos du Rau, K. Bourgeois, L. Ruffino, S. Dromzée, R. Ouni, A. Abiadh, R. Estève, J. P. Durand, L. Anselme, G. Faggio et al., "New assessment of the world largest colony of Scopoli's Shearwater Calonectris diomedea". In: Yésou, P.; Baccetti, N.; Sultana, J. (ed.), Ecology and Conservation of Mediterranean Seabirds and other bird species under the Barcelona Convention – Presented at the 13th Medmaravis Pan-Mediterranean Symposium. Alghero (Sardinia) 14-17 Oct. 2011, pp. 26–28. Medmaravis, Alghero, 2012.

[18] M. Derhé, Developing a population assessment for Yelkouan Shearwater *Puffinus yelkouan"* (Pp 65-73). In Yésou, P., Baccetti, N. & Sultana, J. (Eds.), Ecology and Conservation of Mediterranean Seabirds and other bird species under the Barcelona Convention-Presented at the 13th Medmaravis Pan–Mediterranean. Symposium. Alghero (Sardinia) 14-17 Oct. 2011. Medmaravis, Alghero, 2012.

[19] N. Piludi, E. Jenkins, J. Gulka and E. Kovacs, "First hand-rearing and translocation of Vulnerable yelkouan shearwaters, *Puffinus yelkouan*, in Malta" J. Wildlife Rehab., vol. 37, no. 3, pp. 7-14, 2018.

[20] M. Hayran and M. Hayran, "Sağlık Araştırmları için Temel İstatistik" Omerga Araştırma Organizasyon Eğitim Danışmanlık Ltd. Şti. Ankara, 2011.

[21] R. R. Sokal and F. J. Rohlf, "Biometry: the principles and practice of statistics in biological research", W.H. Freeman and Company, New York, 1995.

[22] K. P. Burnham, D. R. Anderson and K. P. Huyvaert, "AIC model selection and multimodel inference in behavioral ecology: some background, observations, and comparisons," Behavioral ecology and sociobiology, vol. 65, no. 1, pp. 23-35, 2011.

[23] M. J. Mazerolle, "Package 'AICcmodavg': Model Selection and Multimodel Inference Based on (Q)AIC(c)." Available at https://cran.r-project.org/web/packages/AICcmodavg/index.html, 2017.

[24] W. J. Sutherland, I. Newton and R. E. Green, "Birds Ecology and Conservation, a Handbook of Techniques" Oxford University Press, ISBN 0 19 852085 9, 2014.

[25] J. J. Borg, J. Sultana and C. Coleiro, "Pre-breeding Movements and Early Nest Visits by the Levantine Shearwater *Puffinus yelkouan* in Malta" II-Meril, vol. 30, pp. 20-23, 2002.

Appendices 1. Distribution of individual numbers according to observation dates and transit times (M: Marmara Sea, A: Aegean Sea)

Date	Total Individual	Toward the Marmara Sea	Toward the Aegean Sea	sunrise-08:59		09:00-09:59		10:00-10:59		11:00-11:59		13:00-13:59		14:00-14:59		15:00-15:59		16:00-16:59		17:00-17:59		18:00-sunset	
				M	A	M	A	M	A	M	A	M	A	M	A	M	A	M	A	M	A	M	A
06.2.2019	9695	4086	5609	15	109	189	310	530	369	913	253	370	1203	582	814	391	1353	483	820	288	196	325	182
07.2.2019	8352	6384	1968	173	90	821	376	678	295	661	158	912	487	440	199	832	220	730	107	815	31	322	5
08.2.2019	9912	8282	1630	226	39	1215	44	1058	21	883	9	838	245	420	287	724	200	992	411	912	290	978	84
09.2.2019	9492	4744	4748	472	49	1227	124	463	60	355	36	587	387	186	674	186	652	380	783	451	1138	437	845
10.2.2019	23308	4487	18821	376	40	310	453	113	656	428	770	470	4454	344	4770	379	3802	1080	1851	587	1625	400	400
11.2.2019	6979	3390	3589	492	252	477	722	431	412	730	583	249	273	296	472	180	439	355	270	121	83	59	83
12.2.2019	12466	11747	719	247	35	579	2	535	0	4390	184	1397	35	1320	47	867	160	964	104	908	120	540	32
14.2.2019	8013	3488	4525	178	39	271	36	456	6	1248	104	196	435	281	569	295	727	206	1191	74	855	283	563
15.2.2019	15886	3182	12704	165	126	438	173	678	1010	530	808	233	2335	371	4816	374	1241	179	731	191	1067	23	397
16.2.2019	6717	1704	5013	50	404	325	351	379	370	257	195	224	1014	79	847	43	806	36	555	50	201	199	270
17.2.2019	57829	1378	56451	99	198	269	103	232	107	151	15	138	13190	50	19370	48	12470	95	6662	179	3013	117	997
18.2.2019	18876	1102	17774	104	283	215	666	190	1329	55	800	14	2489	19	2708	65	2707	232	3312	108	2329	100	1151
19.2.2019	8919	698	8221	42	285	99	499	83	422	69	360	56	2199	13	1919	48	808	152	728	63	521	72	480
20.2.2019	6172	1886	4286	107	185	241	234	188	155	429	74	124	21	148	64	145	568	210	1495	214	1094	80	396
21.2.2019	9487	3634	5853	341	24	325	356	200	191	513	400	56	448	228	665	322	1426	587	1008	618	748	444	587
22.2.2019	15523	12820	2703	422	142	617	305	417	84	876	17	1703	338	2629	231	2189	384	1386	583	1828	512	753	107
25.2.2019	26461	22419	4042	0	0	375	4	2558	0	8246	144	4475	680	768	150	1722	407	2105	1054	1355	801	815	802
26.2.2019	78145	24815	53330	997	35	1746	913	1869	1070	4495	9529	4160	19423	4030	11242	3137	6822	1261	1349	1046	1687	2234	1260
27.2.2019	8373	3034	5339	360	340	860	515	600	493	473	340	294	388	84	1532	10	631	57	455	18	265	252	327
28.2.2019	9179	3801	5378	110	12	281	138	239	51	412	68	540	149	647	516	527	1093	387	1255	480	1384	178	712
01.3.2019	9543	3441	6102	456	216	446	901	605	875	449	705	571	792	214	24	256	156	197	552	107	968	140	913
02.3.2019	35943	2883	33060	117	285	492	594	294	398	719	5336	440	9292	318	5287	266	4138	181	3329	56	4176	0	225
03.3.2019	12824	584	12240	36	432	75	338	62	362	89	1595	68	2798	32	1028	30	1411	57	2061	34	1636	101	579
04.3.2019	13943	3223	10720	159	431	186	486	163	417	446	794	302	1608	379	1480	176	1542	386	1813	408	1494	918	655
05.3.2019	12215	7680	4535	478	339	756	758	938	451	1102	423	1335	362	1016	573	864	593	532	411	230	182	429	443
06.3.2019	12541	9672	2869	383	45	599	90	1001	163	878	190	1566	444	1833	502	1371	215	952	438	635	430	454	345
07.3.2019	19344	5703	13641	187	139	202	278	373	144	567	1769	638	1542	772	2059	895	2848	734	2072	758	1531	577	1096
08.3.2019	21144	6431	14713	182	521	211	676	844	824	1193	1426	1236	1582	818	2955	453	2042	548	2632	447	1059	499	996
09.3.2019	11736	6368	5368	230	284	225	525	323	420	1942	254	841	675	702	589	554	634	702	901	432	670	417	416
10.3.2019	11241	5147	6094	193	197	305	283	414	427	888	338	284	847	697	961	713	960	500	693	679	785	474	603
11.3.2019	6491	4432	2059	265	293	230	296	85	449	689	296	774	162	634	0	378	81	649	132	336	292	419	58
12.3.2019	6018	5072	946	437	100	319	113	172	97	1093	358	286	65	562	31	1148	83	670	10	298	71	87	18
13.3.2019	3697	2513	1184	512	208	345	40	404	80	371	57	233	197	84	61	55	83	143	175	140	164	226	119
14.3.2019	15103	2984	12119	412	176	353	91	265	468	324	91	310	346	280	1291	186	3175	263	3191	179	2152	412	1138
15.3.2019	3391	2968	423	398	34	237	27	254	24	281	57	276	46	203	11	219	41	351	36	300	54	449	93
16.3.2019	8833	5082	3751	764	565	859	60	1129	54	1653	40	143	596	116	424	60	467	200	528	77	607	81	410
19.3.2019	10093	4427	5666	331	22	324	27	332	18	383	928	135	416	333	941	863	1126	544	1066	317	747	865	375
20.3.2019	7817	1425	6392	317	448	176	220	167	845	301	125	117	1203	21	617	56	933	69	822	45	642	156	537
21.3.2019	6218	4250	1968	504	214	353	91	265	468	324	91	674	162	634	0	378	81	649	132	336	292	133	437
22.3.2019	10902	428	10474	25	1861	31	1292	15	1099	90	1735	2	813	38	1017	8	645	27	544	55	621	137	847

SAKARYA ÜNİVERSİTESİ
FEN BİLİMLERİ ENSTİTÜSÜ DERGİSİ

Sakarya University Journal of Science
SAUJS

e-ISSN 2147-835X Period Bimonthly Founded 1997 Publisher Sakarya University
http://www.saujs.sakarya.edu.tr/

Title: Aeroacoustic Simulation of an Owl Wing Cross-Section Using Computational Fluid Dynamics

Authors: Ferit YILDIZ, Sedat TOKGOZ

Recieved: 2021-07-09 00:00:00

Accepted: 2022-03-16 00:00:00

Article Type: Research Article

Volume: 26
Issue: 2
Month: April
Year: 2022
Pages: 375-387

How to cite
Ferit YILDIZ, Sedat TOKGOZ; (2022), Aeroacoustic Simulation of an Owl Wing Cross-Section Using Computational Fluid Dynamics. Sakarya University Journal of Science, 26(2), 375-387, DOI: 10.16984/saufenbilder.968701
Access link
https://dergipark.org.tr/tr/journal/1115/issue/69580/968701

New submission to SAUJS
http://dergipark.gov.tr/journal/1115/submission/start

Sakarya University Journal of Science 26(2), 375-387, 2022

Aeroacoustic Simulation of an Owl Wing Cross-Section Using Computational Fluid Dynamics

Ferit YILDIZ*[1], Sedat TOKGOZ[1]

Abstract

In this study, we aim to investigate the low noise flights of owls in terms of aerodynamics. The flow around cross-section of an owl wing, which is known for its nearly silent flight, is numerically analyzed using Computational Fluid Dynamics (CFD). The analysis are based on the parameters of angle of attack and the flight speed. The aerodynamic effects on the acoustic is compared in terms of vorticity and sound pressure level, where the frequency interval for the acoustic data is set to 0-7500Hz. It was seen that the vortical organisations around the airfoils are closely related to the acoustic results. The results show that the increase in both velocity and angle of attack affect the vorticity, thus lead to a rise in sound pressure level. It can be stated that the owl airfoil shape ensures a relatively silent flight.

Keywords: Aerodynamics, airfoil, biological flow, Computational Fluid Dynamics

1. INTRODUCTION

The noise of aircrafts is a significant problem for the environment. Different solutions for developing low-noise aircrafts are investigated in the industry. Consequently, one of the best application of these subjects probably lies in nature itself. Birds, which are responsible for the desire of flying, are analyzed for further improvements in aviation [1, 2]. As a result of this, various properties of birds were implemented into aircraft designs to achieve new improvements in terms of aerodynamic, as well assilent flight [3].

The wings of birds are adapted to operate over a wide range of flight styles, from the highly rigid geometries for gliding to the relatively flexible kinematics for flapping [4, 5]. These flight styles are extended further during take-off, landing, and manoeuvering while flying at high angles of attack and generating highly unsteady flows. In most of the cases, all of these occur in turbulent flow conditions. Not only the flight style, also the physical appearance/feature of the wings play a critical role in the flight itself. For example, they can vary from narrow to wide wings or from sharp to rounded forms [4, 6, 7] Compared to narrow wings, wide wings can help a bird to glide longer at low flight speeds. Furthermore, to carry the prey up in the air, larger and wider wings provide additional lift [8]. If we focus on owls, relatively large, broad, rounded wings, with a large surface area relative to their weight, are seen. This low wing-load (body mass × 9.81 ms-2 / both wing areas) allows them to fly easily, without much

* Corresponding author: ferit.yldz@hotmail.com
[1] Gebze Technical University
E-mail: sedattokgoz@gtu.edu.tr
ORCID: https://orcid.org/0000-0002-7450-846X, https://orcid.org/0000-0002-0836-2861

flapping. They can glide for long periods, even at low flight speeds [9, 10].

Owls are known for their silent flights. They are using their hearing system to sense prey, therefore they need to reduce flight noise. Flying slowly is one choice, but to provide enough lift at low-speed, the wing needs to be highly cambered [11]. In comparison to other similar birds, the owl wing cross-section profile shows a special camber and thickness distribution, which provides enough lift at low flight speed [12]. Considering this, together with the large wing area of owl wings, the special features (high camber, thinner profile towards trailing edge) are distributed throughout the whole wing, which makes the owl a nearly silent flying bird.

Neuhaus et al. [13] examined the flight noise of a tawny owl (Strix aluco) and a mallard duck, with and without the serrations on the leading edge. The recorded noise during flight reaches its most intense range between 200 and 1500 Hz. Furthermore, wind tunnel experiments show that the flow over the owl wing has a more laminar flow character compared to the flow over wing of the duck and has lower flight noise with the serrations on the leading edge Ito [14] investigated a NACA63-414 profile with different number of teeths as serrations and two Reynolds numbers ($2.1x10^4$ and $2.1x10^5$) to show the behavior of the flow at low and high speeds. By increasing the number of teeth on the wing, it is seen that the aerodynamic performance is improved in the low Reynolds number region, in turn, no significant changes are seen for the high Reynolds number region. Also, Mascha [15] mentioned the serrations on owl wings and identified the outstretched pennula (hair-like extensions of the feather) as a source of the mild wing layer of owls, which reduces the flight noise. Hertel [5] derived an explanation of how the velvet-like upper surface may prevent generated sound. He claimed that it acts as a kind of cushion so that it reduces the noise during flight.

Geyer et al. [16] performed wind tunnel and outdoor measurements to demonstrate the difference between the noise levels of the owl compared to the noise of non-silently flying birds. The outdoor experiment was carried out with an owl, flying over a microphone array. The wind tunnel measurements were performed with prepared wings (real wings of dead birds) of an owl, hawk, and kestrel at fifteen flight speeds between 5 m/s and 20 m/s at 0°, 8°, and 16° AOA. The outdoor flight noise was recorded between 500 Hz and 10 kHz frequencies. The results of both experiments show that the owls generate less noise (60dB) than the other birds (75-90dB) used in the studies. No major noise difference was measured at low-frequency level. But for mid and high-frequency range, the owl outperformed the other birds in case of silence.

In addition to the whole body or wing studies, investigations on 2D wing profiles can be found in the literature. Kondo et al. [17, 18] investigated the effect of the flow detachment around an airfoil (owl-like profile on the lift and drag coefficients using CFD. They concluded that the owl airfoil has a higher lift/drag ratio compared to NACA0002, NACA0012, and the Ishii airfoil. Anyoji et al. [19] performed experiments in the wind tunnel with an owl-like airfoil, where they visualized the flow and measured the lift and drag properties. Again, the high cambered airfoil (on the pressure side) showed a better lift/drag ratio compared to NACA0012.

It is shown in the literature that carrying out acoustic experiments with living animals are mostly difficult, whereas body part samples are also hard to find [6, 12, 16]. Since the owl is well known for its nearly silent flight, the scope of this work is to numerically investigate the owl wing cross-section in terms of aerodynamics and aeroacoustics to obtain faster, and reasonable acoustic results, compared to experiments. Properties like flight speed and Angle of Attack (AoA) were investigated to understand the flow behavior in relation to the reported silent flight characteristics. The connection between vortices and acoustics were examined to realize the noise generation of the owl flight.

2. NUMERICAL SET-UP AND DESIGN

In this section, the setup of the numerical analysis will be described, whereas a brief explanation about the design and meshing process will be

explained. All numerical analysis in this paper were performed using ANSYS Fluent software.

2.1. Computational Details

2.1.1. Turbulence Model

For simple cases of turbulent flow, equations can be solved directly, whereas, in complex turbulent flows, CFD simulations predict the outcome of turbulence with the help of turbulence models. These turbulence models are simplified equations that predict the statistical formation of turbulent flows [20]. In order to choose the most suitable turbulence model, the case which is going to be solved must be defined properly. Two common approaches can be seen in CFD, which are Large-eddy simulation (LES) and Reynolds-averaged Navier-Stokes (RANS). LES is a transient technique in which the large eddies are resolved directly, while small eddies are modeled. On the other hand, the RANS use the Navier-Stokes equations (as time-averaged) without filtration, while Reynolds stresses are solved directly [21]. Remaining turbulence models are based on these two approaches [22].

RANS and LES models have their pros and cons. In comparison to RANS models, LES is able to predict the vortex shedding and flow recirculation accurately. In contrast, LES has to be run for a sufficiently long flow-time to obtain a stable solution and can only be applied to 3D models. This leads to computational costs, which are higher than that of the steady RANS calculations. On the other hand, Detached-Eddy-Simulation (DES), which is a hybrid LES-RANS model. This model uses the RANS for the wall limited flows, whereas the LES for the far-field. The DES model requires more computational costs than RANS but requires less than LES [21, 22].

Spalart-Allmaras is a low Reynolds number turbulence model, which is developed for aerodynamic applications. This model has some weakness in computing shear flow, separated flow, or decaying turbulence, but it's advantageous in terms of convergence and stability [22]. For example X. Liu and X. Liu [23] used this model in the steady flow over an owl-wing-based airfoil for pressure and velocity coupling. The Spalart-Allmaras model has been shown to realize decent results for applications involving wall-restricted flows and boundary layers subjected to reverse pressure gradients [24]. Therefore, the Spalart-Allmaras was selected for the steady analysis as turbulence model. The DES, with Spalart-Allmaras as a submodel, was chosen for the transient cases, because of its capabilities of solving the wall-bounded and far-field flows better than RANS models. The submodel decision was made so that the analysis all have the same RANS model. In general, better vortex shedding and turbulence resolution was obtained compared to RANS, whereas computational costs were much less than LES.

2.1.2. Acoustic Model

There are different approaches to calculate the aeroacoustic field from flow field,where in Lighthill's acoustic analogy, Lighthill generated a wave equation by using the Navier-Stokes and continuity equations. This approach not only consists of the generated noise, but also includes the flow convection and the gradual dissipations by conduction and viscosity [25]. Unfortunately, Lighthill's analogy cannot describe kinematic effects, because refraction at shear- or boundary layers appear as sources. Several generalized wave equations have been derived after Lighthill, in the attempt to isolate those drawbacks, which could be stated as true sources of the sound [25, 26].

An essential part of aeroacoustics is the sound source characteristics. Consequently, it is important to understand the monopole, dipole, and quadrupole sources, which are very important to explain aerodynamically generated noise. The monopole is defined as a single, spherical sound source which radiates waves inward or outward. On the other hand, the dipole can be realized as two out of phase monopoles with the same strength, where the quadrupole is alike and consists of two out of phase dipoles [27]. This forms the basis to describe the relation between noise and flow. Both vortex and monopole have a direction, a strength and are based on velocity,

whereas they also can interact with each other and form new structures. While monopoles form new type of sources (dipole, quadrupole), the same situation occurs also in vortices, which can form complex structures by affecting one another.

ANSYS Fluent offers one acoustic source equation, the Ffowcs-Williams & Hawkings (FW-H) wave equation. In general, it takes the Lighthill's equation as a base, where a control surface is used to retain the monopole and dipole sources. Despite that, the effect of quadrupole sources, which are outside of the control surface, can be added with the Lighthill Tensor [26]. Combining this acoustic model with the DES turbulence model, the aeroacoustic behavior of the owl wing profile is described in terms of sound pressure (dB).

2.2. Design, Mesh, Numerical Setup, and Flow Conditions

2.2.1. Design

It is hard to define a standard 2D profile for avian wings, since they vary from bird to bird, from species to species. Different methods are used to define standard profiles for specific birds. In some studies, it is possible to find pairing approaches in which each bird's wing is associated with the most alike standard airfoil profile [28]. Others tried to scan a real wing and reproduce it in a computational environment. A 3D non-contact laser scanner[12], Projected pattern correlation technique [29], or a clinical tomography scanner are some of these kinds of methods [6].

For this study, the owl wing profile given by Liu et al. [12] is used as an airfoil profile (Figure 1) for the following CFD analysis. The owl profile is extracted from the cross-section at 40% of the wingspan.

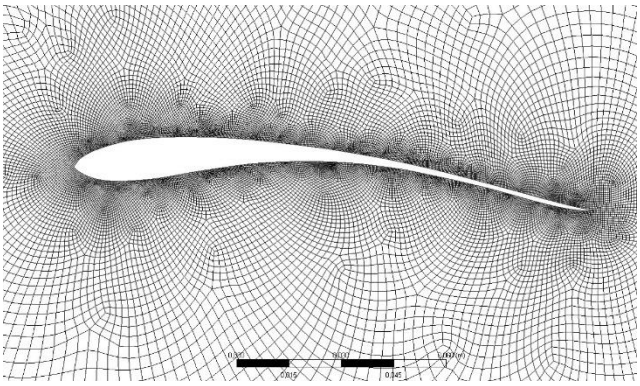

Figure 1 2D profile of an owl and the near-field mesh

2.2.2. Mesh

The mesh and the domain around the airfoil are shown in Figure 1 and Figure 2, respectively. The distances from the airfoils leading-edge to the upstream and downstream boundaries are 20x and 40x chords, respectively.

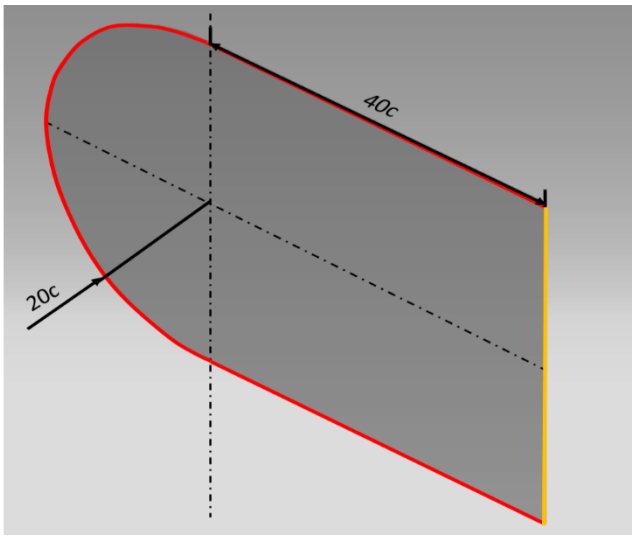

Figure 2 Domain of airfoil. Red line: inlet velocity boundary. Yellow line: pressure outlet boundary

The grid independency study shows five cases for possible meshing process (Table 1). The reference case is selected as case 4, where both near-field and far-field meshes are set as fine, relative to the first three cases. Since, the mesh around the airfoil had a poor resolution for case 1 and 2, the vortex shedding was affected in a negative way, which was the reason that these meshes were not suitable. On the other hand, case 3 had a finer

near-field mesh resolution, which was necessary for our study. It is found that the lower quality mesh in the far-field didn't affect the analysis in the near-field, since the main objective of this study was around the near-field. Due to limited computational resources, case 3 is determined as the optimal case instead of case 4 or case 5, where the mesh quality in the far-field is set between coarse and medium, whereas the near-field mesh quality is between medium and fine (case 3 in Table 1). The minimum grid size on the airfoil edge is 10^{-3}, while the average skewness is 0.13 and the average orthogonal quality is 0.97.

Table 1 Grid independency study

Case #	Nodes	Elements
1	9210	8934
2	18854	18557
3	26467	26501
4	31624	31231
5	39451	39070

2.2.3. Numerical Setup and Flow Conditions

According to Neuhaus et al. [13], the flight speed range of the owl is only about 6 to 10 m/s, where Mebs and Scherziger [9] stated that flight speeds of owls are in the range of 2.5 m/s to 7 m/s. Considering this, the maximum and minimum velocities investigated in this study are chosen as 2.5 m/s and 10 m/s. Additionally, 5 m/s is also selected to represent the medium speeds. Chord based Reynolds numbers are 2.6×10^4, 5.2×10^4, and 10.5×10^4. There is also a wide range of options for AOA, but 0°, 5°, and 10° were chosen according to gliding flight angles of owls [17, 18, 23, 30].

The same timestep number was selected for all cases to keep the same analyze period, which is important for studying the vortex shedding. For the vorticity results, the timestep is set to (Δt) 10^{-3}s, whereas an analysis for 2s is ensured. The numerical setup for the acoustic analysis depends on the Nyquist–Shannon sampling theorem. As stated by Sarradj et al. [31], at frequencies higher than 6.3 kHz the owl-generated noise couldn't be measured with microphones. Therefore, a max frequency of 7.5 kHz is considered sufficient for the acoustic analysis, which corresponds to a sampling frequency of 15 kHz. Here, a timestep value of $\Delta t = 6.6\times10^{-5}$s required, while the timestep number of 1.5×10^4 provides a flow time of 1s.

Vortex shedding is a significant mechanism which connects the aerodynamics and acoustics. The formation location, intensity and dimension (diameter) of different vortices lead to various sound pressure levels and noise locations in different frequency zones. Hereby, the vortices at specific instances should be analysed for this, which is the major reason of the unsteady incompressible flow analysis in this study [20, 22, 26].

Moreover, acoustic receivers are needed to be defined for the FW-H acoustic model. It is found in the literature that in wind tunnel measurements the receiver positions are located between 0.6-1 m from the airfoil, and distributed around the wing specimens at every 24 degrees [16, 32-34]. However, in numerical analysis, microphone distances and spacings are chord length based(e.g. 15x chord or 18x chord away from leading edge with 30° spacing) [23, 35]. In this study, the receiver placement is accomplished within a radius of 1.5 m from the leading-edge, which corresponds to 10 times the chord length, with an angular difference of 20˚ between the receivers. A total number of 18 receivers are placed around the airfoil as shown in Figure 3.

3. RESULTS

The results in this section are given in terms of vorticity and acoustic analysis for different freestream velocities and AoA's. The transient vorticity results are investigated in four equally spaced instant (0.5 seconds between steps). The results of the intermediate steps are not shown for simplicity. The acoustic analysis of the owl flightwas performed in terms of sound pressure level (dB).

3.1. Vorticity

In order to understand the effects of the freestream velocities and AoA's to the flow behaviour, a general look at the topology of the flow is required. The results in Figure 3a-d show that the flow is relatively smooth and the vortices are periodical. Positive vortices form at an early point (compared to Figure 3e-h and Figure 3i-l) at the leading-edge pressure side, whereas the suction side flow is smooth and mostly attached to the boundary layer. Moving to the 5 m/s case (Figure 3e-h), both the positive and negative vortices became larger relative to the 2.5 m/s case (Figure 3a-d). Here, the vortices on the suction side get bigger in diameter. Also at the trailing-edge, an interaction between the negative and positive vortices can be seen more clearly. Comparing the two cases (Figure 3a-d and Figure e-h) at each time step, the flow pattern looks quite similar, especially the positive vortex pattern. The 10 m/s (Figure 3i-l) results contain larger vortices compared to those two cases, which is expected for increased velocities. Positive-negative vortex interaction can be seen on both sides of the airfoil, while at the suction side near the trailing-edge positive vortices force the flow to separate from an earlier point of the airfoil surface compared to other two cases. Furthermore, interactions of vortices intensify in the downstream of the trailing-edge. Because of the special camber structure of the owl profile , it is expected that the positive (clockwise) vortex shedding starts at a point near the leading edge of the profile, especially at small AOA's e.g 0°.

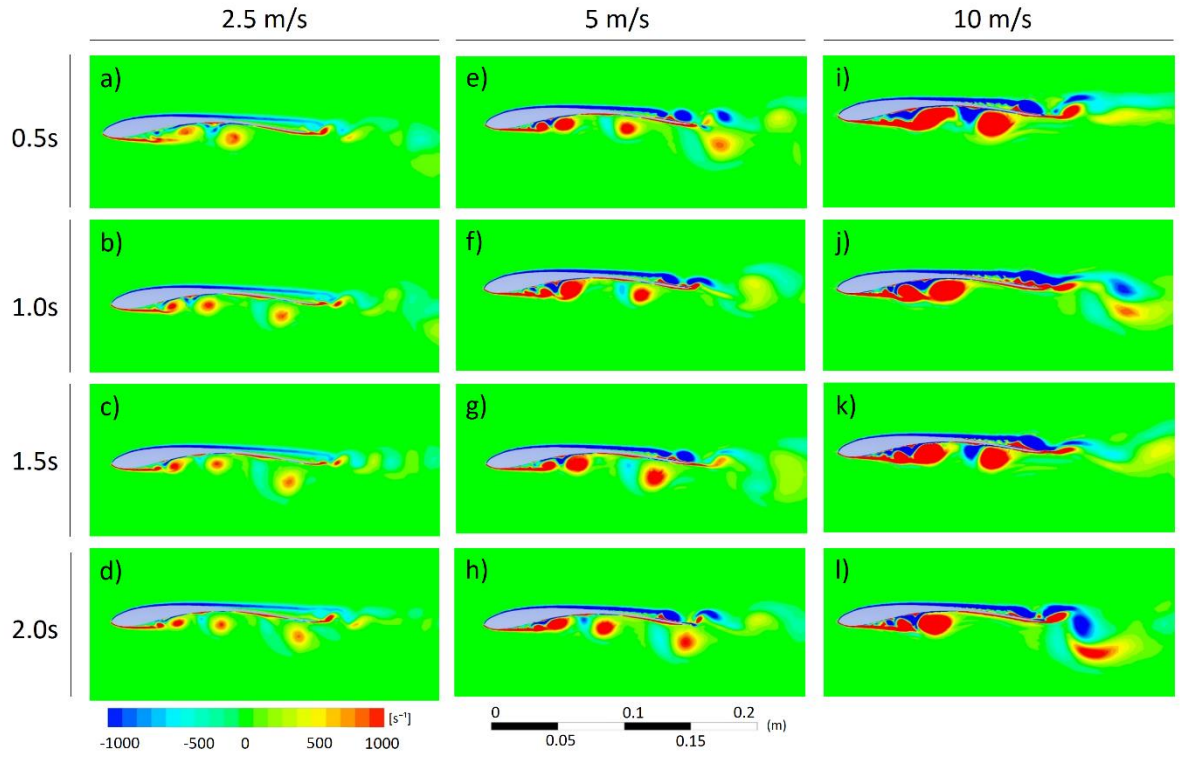

Figure 3 Vorticity distributions of AOA=0° for owl airfoil in four equally spaced instants

If we focus on the results of AoA=5° (Figure 4), the first point that stands out is the separation of the vortices at approximately the half chord length, whereas for the 0° AoA results (Figure 3) the separation point is closer to the trailing-edge (at approx. 75% of the chord). It can be concluded that this an outcome of the increase in AoA since the freestream velocity values didn't change. Another result of this change is that the negative vortices start to grow and get even larger than the positive vortices on the pressure side. For the 10 m/s case, at the suction side at 50% of the chord, the negative vortex grows over the positive vortex and traps it between the airfoil's surface. This indicates a separation bubble formation in the flow.

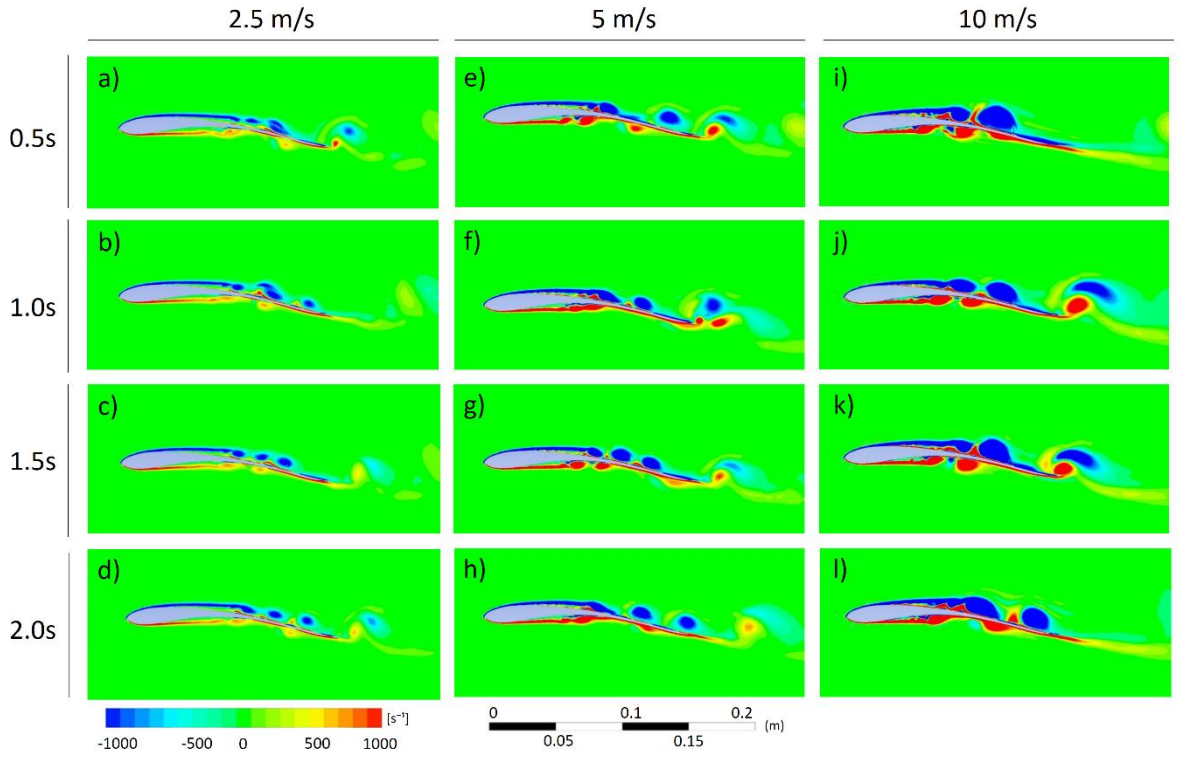

Figure 4 Vorticity distributions of AOA=5° for owl airfoil in four equally spaced instants

If we focus at the trailing-edge of the 5° case (Figure 4), the positive vortices on the pressure side initially move in a vertical direction, and then move in the downstream direction after interacting with the negative vortices. It can be due to the geometry of the owl airfoil's trailing-edge, which is sloping upward. Furthermore, different trailing edge geometries are seen in all three profiles. This leads to different interactions of vortices, which can affect the flow and the acoustic characteristics of each wing profile.

The results of AoA=10° cases are given in Figure 5. At this AoA the flow separate from an earlier point on the airfoil. The separation points of the negative vortices shift upstream to the leading-edge and reaches almost 25% of the chord length.. A similar effect is also seen in the 5° AoA cases (Figure 4).

In general, the 2.5 m/s cases (Figure 3) have small vortex shedding, while the 5 m/s and 10 m/s cases show rather greater vortex shedding. It is clearly seen that the airfoil is better adapted to the flow at 2.5 m/s. Because the flow stays attached at the pressure side at this velocity, which is the desired to produce lift more efficiently. Furthermore, it is also known that, in general the owls fly slower than other birds [9, 13].

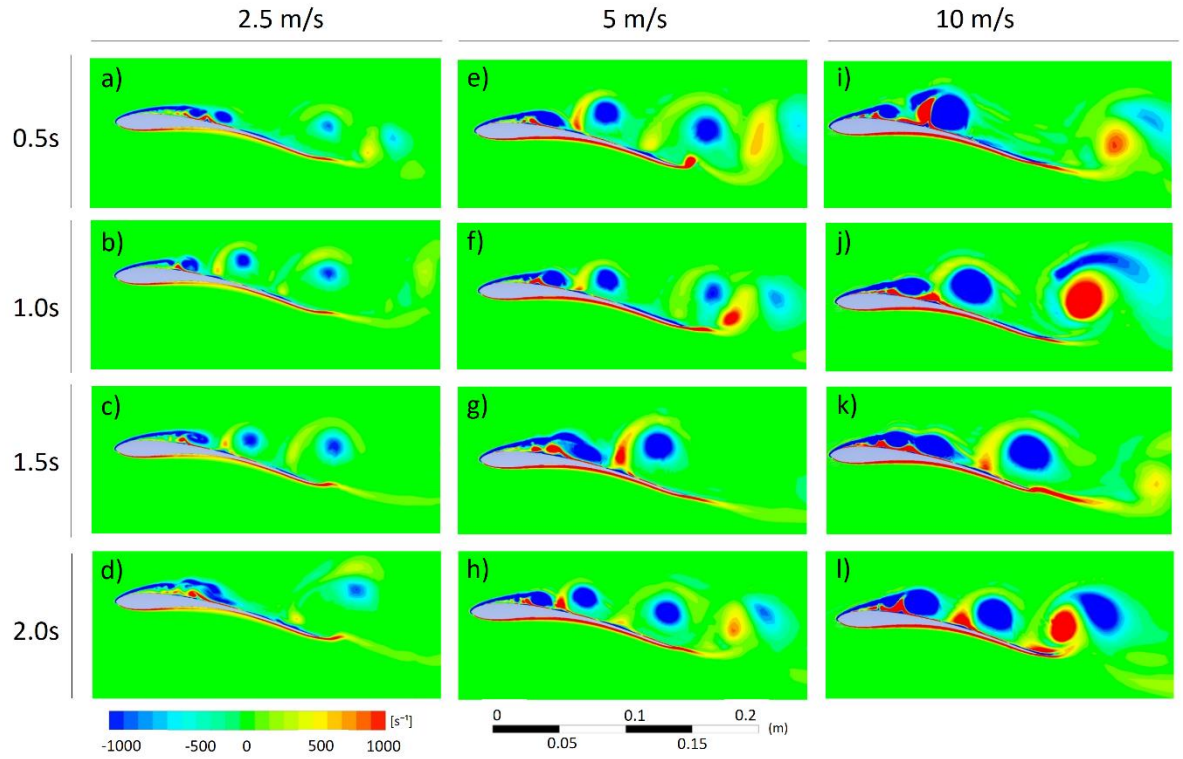

Figure 5 Vorticity distributions of AOA=10° for owl airfoil in four equally spaced instants

If we focus on the vortex dimensions, the diameter doubled from 2.5 m/s to 5 m/s, and almost tripled from 2.5 m/s to 10 m/s. Different from the other two cases, the 10° AOA results (Figure 5) demonstrate vortex interactions, which indicate the previously mentioned dipole and quadrupole sources. The image at 0.5s for the 10 m/s case (Figure 5i) is an example for dipoles, whereas image at 2.0s for the 10 m/s (Figure 5l) indicates a quadrupole. These sources are also seen in Figure 5e-h, while vortices with much smaller diameters are present in Figure 4e-h and Figure 4i-l.

3.2. Acoustic Results

In this section, the results of the acoustic analysis of the owl are investigated in terms of sound pressure level (dB). As mentioned in the previous chapter, the 5° (Figure 4e-l) and 10° (Figure 5e-l) cases are selected for aeroacoustic investigations. The aerodynamically generated noise is measured at the receivers, which are placed around the airfoil at a distance of 10 times the chord lengths (i.e. 1.5 m). The receivers are placed starting from the trailing-edge (0° receiver) and continues in a counter-clockwise direction with 20° increments (see Figure 7). First, similar to the literature [23, 31, 35] the acoustic data at the 0° receiver (Figure 6) is investigated to find the maximum sound pressure level in a range between 0-7500 Hz. After that, the maximum sound pressure level (SPL) is examined together with the remaining 17 receivers in a radar chart (Figure 7).

Following the approaches in the literature, the acoustic results in this section, are given relative to so-called “the reference acoustic pressure”. In the literature, it is defined as the threshold of hearing for humans and has a value of $2x10^{-5}$ Pa (=0 dB) [16, 36]. The negative sound pressure levels should be understood as values, which are below the reference acoustic pressure.

3.2.1. Sound Pressure Level

In Figure 6, the maximum SPL is located in a frequency interval of 20 - 120 Hz with a maximum SPL of 17dB for the case in Figure 4e-h. By increasing the velocity to 10 m/s, the SPL rises almost to 40dB for the same AoA. Here, the width of the SPL peak increases and propagates to a wider frequency range of 90 – 290 Hz. When

the AoA is increased to 10°, the effect of AoA on SPL can be clearly seen. The maximum SPL is around 25dB with a width of approximately 15-60 Hz for Figure 5e-h, and around 40dB at 40 – 170 Hz forFigure 5i-l.

At AoA=10°, the SPL decreases below the reference acoustic pressure level (RAPL) (i.e. 0 dB) around 2250 Hz. On the other hand, the SPL of the AoA=5° cases falls below the RAPL around 500 Hz. However, with these results, it is concluded that the acoustic advantage (silent flight) of the owl is reduced at AoA=10°, especially at 10 m/s freestream velocity. Furthermore, the maximum sound pressure values in all cases are seen at low frequencies. A possible explanation can be that the freestream velocity is not high enough to form high-frequency vortices or the AoA is too small to shed vortices in higher frequencies. Another notable point is seen in Figure 6b and Figure 6c cases, where the sound pressure levels are almost at the same level after 3000 Hz. This can be an outcome of the crosswise increase in the freestream velocity and the AoA (respectively for Figure 6b and 6c), which can affect the flow in the same way.

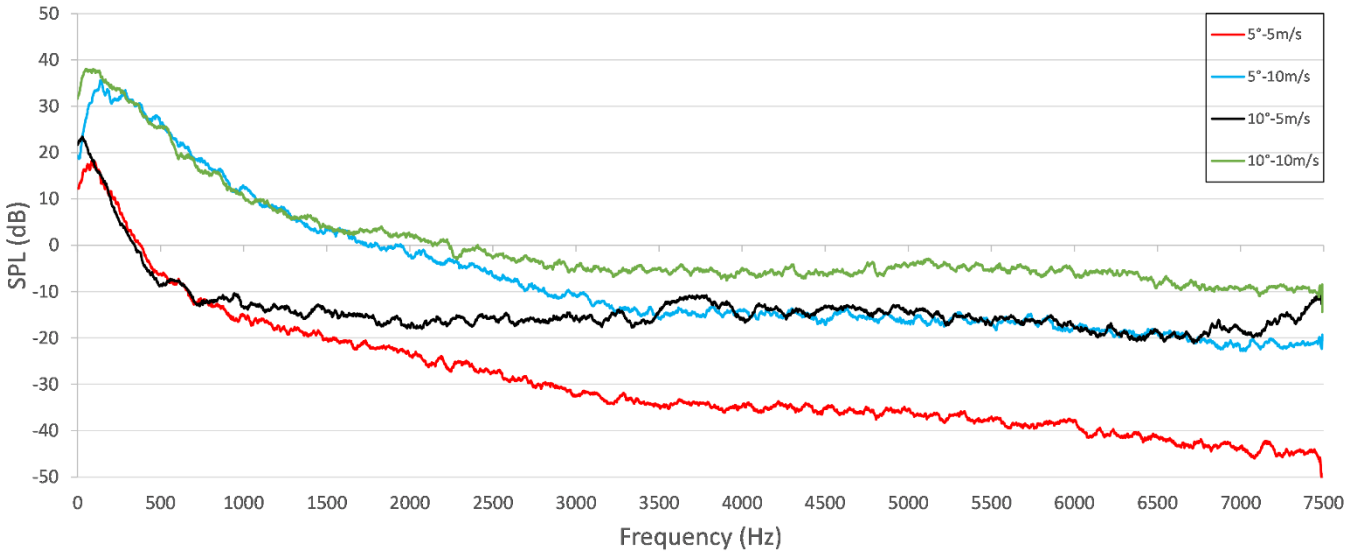

Figure 6 Sound pressure level between 0-7500 Hz for 5° and 10° AoA. Receiver is located at the trailing edge (0°). AoA=5° V=5 m/s (a) (red), AoA=5° V=10 m/s (b) (blue), AoA=10° V=5 m/s (c) (black), AoA=10° V=10 m/s (d) (green)

Liu et al. [23] found the maximum SPL (25-30 dB) at around 192 Hz for the similar owl airfoil in a numerical analysis (AoA=0°-9° and V= 7.5 m/s as boundary conditions), which verifies the results in this study. Also, the SPL distribution at 10 m/s freestream velocity for an owl airfoil obtained numerically by Li et al. [35] (23-40 dB) is similar to our results at the same velocity (i.e. 30-45 dB). The slight differences can be related to chord length, as Li et al. used 100 mm, whereas the chord length in our case is 150 mm. The experimental results in the study of Sarradj et al. [31] show that the maximum SPL for the owl and hawk is around 20 dB at regular flight speeds, which is comparable to our findings of 15-30 dB at 5 m/s. This can be compared with the 5 m/s data of this study because the flight speed range for the owl is around 2.5-10 m/s [9, 13].

In Figure 7 , the SPL distribution around the airfoil s are presented. The results are plotted for average SPL values at the receiver locations for the maximum frequency interval of the owl wing profile. These values are calculated to smooth out the fluctuating data at the maximum frequency interval and are referred to as overall sound pressure levels (OSPL) in this study. The maximum frequency intervals were mentioned in the previous section, where the range for Figure 7a is 20 – 120 Hz, for Figure 7b is 90 – 290 Hz, for Figure 7c is 15 – 70 Hz and for Figure 7d is 40 – 170 Hz.

For Figure 7a and Figure 7c cases, it can be said that the OSPL's lie between 26-28dB. With the increase of the velocity to 10 m/s, the OSPL increases to 45dB on average, which corresponds to an increase of approximately 15dB compared to the 5 m/s case. As an overview, between the receivers at 0°-340° (at trailing-edge pressure side region) and 140°-160° (at leading-edge suction side region), a same pattern of OSPL is noticed. A possible explanation can be that the vorticity characteristics at the leading and trailing edge have a similar effect on the sound pressure level. It is known that the flight speed range of the owl is around 2.5-10 m/s, which was also mentioned before in this study. Consequently, the OSPL behavior in 5 m/s freestream velocity conditions shows that the owl wing profile generates less noise compared to the 10 m/s conditions, regardless of the AoA.

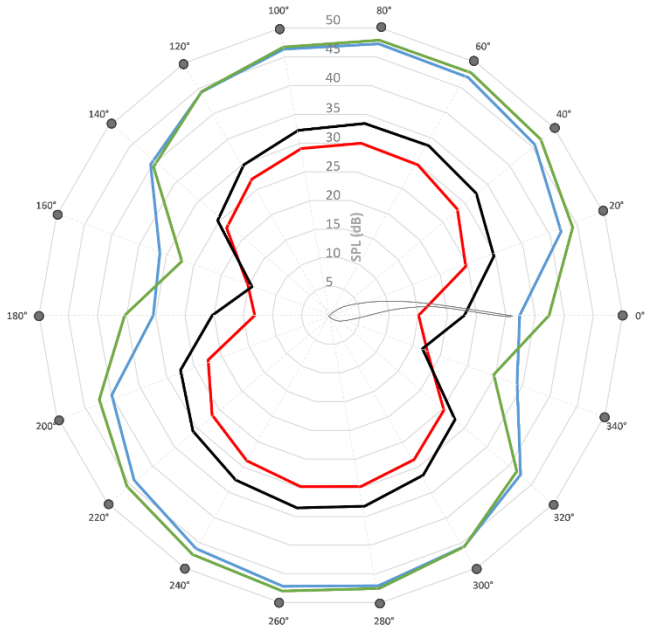

Figure 7 OSPL distribution around the owl airfoil. 5°AoA - 5 m/s (a)(red), 5°AOA - 10 m/s (b)(blue), 10°AOA - 5 m/s (c)(black), 10°AOA - 10 m/s (d)(green). Black dots represent the locations of the receivers. The frequency interval in the radar charts corresponds to the maximum SPL range. Airfoil is drawn to indicate the relative AoA with respect to the receivers. Therefore the chord length, and the distance between the leading edge of the airfoil and the receivers are not to scale

4. CONCLUSION

The objective of this study is to investigate the flow characteristics of the owl's wing profile, and its effect on the silent flight of the owls. For this purpose, typical values that describe the properties of the owl are chosen and analyzed with 2D computational fluid dynamics tools. In order to represent the gliding flight, freestream velocities are chosen as 2.5 m/s, 5 m/s, and 10 m/s, whereas the angle of attacks are taken as 0°, 5°, and 10°.

As a brief summary of both vorticity and acoustic results, it is seen that each investigated characteristic of the vortices have an impact on the SPL. The effect of the formation position of the vortices on the noise distribution can be seen in Figure 7. On the other hand, the vortex intensity and dimension have an influence on the SPL, whereas the vortex shedding (or occurrence frequency) is related to the frequency-dependent SPL (Figure 6). To understand the acoustic behavior of the owl wing profile, transient analyses are carried out over time. In general, the results show that all the cases with 2.5 m/s freestream velocity and 0° AoA have small vortices in the field, and almost no vortex interactions are observed. Since the vortices for 5 m/s and 10 m/s are larger and have more interaction between eachother, it is expected that the noise generation would be greater compared to 2.5 m/s. This can be seen in the vortex diameters, where it doubled from 2.5 m/s to 5 m/s, and almost tripled from 2.5 m/s to 10 m/s.

The results of the acoustic charachteristics of the owl airfoil show that in a frequency range between 0 – 2250 Hz, it generates the least noise at 5 m/s freestream velocity regardless of the AoA. The max SPL increases almost 80% from 5 m/s to 10 m/s, where the values share similarities with the literature. Investigations of the SPL distribution around the airfoil show that the owl has a similar sound distribution at the trailing-edge (at 0° and 340° receivers) and leading-edge (at 140° and 160° receivers). Thus, the flow behaviour at the leading and trailing edge are alike and affects the SPL in the same way. It is known that it has a flight speed range of 2.5-10 m/s ,

which explains why it generated more noise at 10 m/s freestream velocity conditions. Furthermore, the max SPL of the owl airfoil is located directly above and underneath the profile, whereas the min SPL is around the leading- and trailing-edge zone. In general, investigated flow characteristics around the owl wing profile are in agreement with the "nearly silent flight" observations of the owl.

Funding

The authors have no received any financial support for the research, authorship or publication of this study.

The Declaration of Conflict of Interest/ Common Interest

No conflict of interest or common interest has been declared by the authors.

Authors' Contribution

The first author contributed 60%, the second author 40%.

The Declaration of Ethics Committee Approval

This study does not require ethics committee permission or any special permission.

The Declaration of Research and Publication Ethics

The authors of the paper declare that they comply with the scientific, ethical and quotation rules of SAUJS in all processes of the paper and that they do not make any falsification on the data collected. In addition, they declare that Sakarya University Journal of Science and its editorial board have no responsibility for any ethical violations that may be encountered, and that this study has not been evaluated in any academic publication environment other than Sakarya University Journal of Science.

REFERENCES

[1] United States Civil Aeronautics Administration, "A Selected and Annotated Bibliography of Recent Air Age Education Textbooks," 1947.

[2] J. P. Fielding, Introduction to Aircraft Design. Cambridge University Press, 1999.

[3] K. P. Valavanis and G. J. Vachtsevanos, Handbook of unmanned aerial vehicles. Springer Netherlands, 2015.

[4] J. M. Forshaw, Encyclopaedia of Animals: Birds. Murdoch Books UK, 1991.

[5] H. Hertel, Struktur, Form, Bewegung. Mainz: Krauskopf-Verlag, 1963.

[6] T. Bachmann, G. Mühlenbruch, and H. Wagner, "The barn owl wing: an inspiration for silent flight in the aviation industry?," in Bioinspiration, Biomimetics, and Bioreplication, 2011, p. 79750N.

[7] J. del Hoyo, A. Elliott, and J. Sargatal, "Handbook of the Birds of the World. Ostrich to Ducks," Ostrich to Ducks. 1992.

[8] R. Sale, Falcons. Harper Collins UK, 2016.

[9] W. Scherzinger and T. Mebs, Die Eulen Europas. Franckh-Kosmos Verlag, 2000.

[10] H. N. Southern and H. Mikkola, "Owls of Europe," J. Anim. Ecol., 1984.

[11] C.-T. Edward L. and J. Roskam, Airplane Aerodynamics and Performance, 5th ed. DARcorporation, 1997.

[12] T. Liu, K. Kuykendoll, R. Rhew, and S. Jones, "Avian wing geometry and kinematics," AIAA J., 2006.

[13] W. Neuhaus, H. Bretting, and B. Schweizer, "Morphologische und Funktionelle Untersuchungen Über den Lautlosen Flug Der Eulen (Strix Aluco) im Vergleich zum Flug Der Enten (Anas Platyrhynchos)," Biol. Zent. Bl., 1973.

[14] S. Ito, "Aerodynamic influence of leading-edge serrations on an airfoil in a low Reynolds number: A study of an owl wing with leading edge serrations," J. Biomech. Sci. Eng., 2009.

[15] E. Mascha, "Über die Schwungfedern," Zeitschrift für wissenschaftliche Zool., no. 77, pp. 606–651, 1904.

[16] T. Geyer, E. Sarradj, and C. Fritzsche, "Measuring owl flight noise," in INTERNOISE 2014 - 43rd International Congress on Noise Control Engineering: Improving the World Through Noise Control, 2014.

[17] K. Kondo et al., "Analysis of Owl-like Airfoil Aerodynamics at Low Reynolds Number Flow," Trans. JAPAN Soc. Aeronaut. Sp. Sci. Aerosp. Technol. JAPAN, 2014.

[18] K. Kondo, H. Aono, T. Nonomura, A. Oyama, K. Fujii, and M. Yamamoto, "Large-eddy simulations of owl-like wing under low reynolds number conditions," in American Society of Mechanical Engineers, Fluids Engineering Division (Publication) FEDSM, 2013.

[19] M. Anyoji, S. Wakui, D. Hamada, and H. Aono, "Experimental Study of Owl-Like Airfoil Aerodynamics at Low Reynolds Numbers," J. Flow Control. Meas. & Vis., 2018.

[20] S. B. Pope, Turbulent Flows. Cambridge University Press, 2000.

[21] T. Bensow, R. E., Fureby, C., Liefvendahl, C. & Persson, "A Comparative Study of RANS, DES and LES," 26th ONR Symp. Nav. Hydrodyn., 2006.

[22] A. Fluent, "Ansys Fluent Theory Guide," ANSYS Inc., USA, 2013.

[23] X. Liu and X. Liu, "A Numerical Study of Aerodynamic Performance and Noise of a Bionic Airfoil Based on Owl Wing," Adv. Mech. Eng., 2014.

[24] P. R. Spalart and S. R. Allmaras, "One-equation turbulence model for aerodynamic flows," Rech. Aerosp., no. 1, pp. 5-21, 1994.

[25] M. J. Lighthill, "On sound generated aerodynamically I. General theory," Proc. R. Soc. London. Ser. A. Math. Phys. Sci., 1952.

[26] WILLIAMS JEF and HAWKINGS DL, "Sound Generation by Turbulence and Surfaces in Arbitrary Motion," Roy Soc London-Philosophical Trans Ser A, 1969.

[27] M. P. Norton and D. G. Karczub, Fundamentals of Noise and Vibration Analysis for Engineers. 2003.

[28] G. Tucker, V.; Parrot, "Aerodynamics of Gliding Flight in a Falcon and Other Birds," J. Exp. Biol., 1970.

[29] T. Wolf and R. Konrath, "Avian wing geometry and kinematics of a free-flying barn owl in flapping flight," Exp. Fluids, 2015.

[30] T. Geyer, E. Sarradj, and C. Fritzsche, "Silent owl flight: Comparative acoustic wind tunnel measurements on prepared wings," Acta Acust. united with Acust., 2013.

[31] E. Sarradj, C. Fritzsche, T. Geyer, and E. Gutmark, "Silent OWL flight: Bird flyover noise measurements," AIAA J., 2011.

[32] J. Kopania, "Acoustics Parameters the Wings of Various Species of Owls," Inter-Noise Noise-Con Congr. Conf. Proc., pp. 6841–7829, 2016.

[33] T. Geyer, E. Sarradj, and C. Fritzsche, "Measurement of the noise generation at the trailing edge of porous airfoils," Exp. Fluids, 2010.

[34] J. Vad, G. Koscsó, M. Gutermuth, Z. Kasza, T. Tábi, and T. Csörgo, "Study of the aero-acoustic and aerodynamic effects of soft coating upon airfoil," JSME Int. Journal, Ser. C Mech. Syst. Mach. Elem. Manuf., 2007.

[35] D. Li and X. Liu, "Aerodynamic performance and acoustic characteristics of bionic airfoil inspired by three-dimensional long-eared owl wing under low reynolds number," in Proceedings of the ASME Turbo Expo, 2016.

[36] H. Roeser, R. J.; Valente, Michael ; Hosford-Dunn, Audiology Diagnosis, 2nd ed. Thieme, 2007.

SAKARYA ÜNİVERSİTESİ
FEN BİLİMLERİ ENSTİTÜSÜ DERGİSİ

Sakarya University Journal of Science
SAUJS

e-ISSN 2147-835X Period Bimonthly Founded 1997 Publisher Sakarya University
http://www.saujs.sakarya.edu.tr/

Title: Quantum Reservoir Parameter Estimation via Fisher Information

Authors: Ufuk KORKMAZ, Deniz TÜRKPENÇE

Recieved: 2021-11-03 00:00:00

Accepted: 2022-03-21 00:00:00

Article Type: Research Article

Volume: 26
Issue: 2
Month: April
Year: 2022
Pages: 388-396

How to cite
Ufuk KORKMAZ, Deniz TÜRKPENÇE; (2022), Quantum Reservoir Parameter Estimation via Fisher Information. Sakarya University Journal of Science, 26(2), 388-396,
DOI: 10.16984/saufenbilder.1018716
Access link
https://dergipark.org.tr/tr/journal/1115/issue/69580/1018716

New submission to SAUJS
http://dergipark.gov.tr/journal/1115/submission/start

Sakarya University Journal of Science 26(2), 388-396, 2022

Quantum Reservoir Parameter Estimation via Fisher Information

Ufuk KORKMAZ*[1], Deniz TÜRKPENÇE[1]

Abstract

In this study, we show that as a result of weak interaction of different information environments structured with a single probe qubit, these environments can perform binary classification of the information they contain. In this way, we refer to these environments as quantum information baths because they consist of sequences of identical qubits in certain pure quantum states. A micro-maser like master equation has been developed to clearly describe the system dynamics analytically and the quantum states of different information reservoirs. The model can also be treated as a quantum neuron, due to the single-qubit probe that makes a binary decision depending on the reservoir parameters in its steady state. The numerical results of the repeated interaction process based on the divisibility and additivity of the quantum dynamic maps are compared with the analytical results. Besides being a single quantum classifier, the model we present can also serve as a basic unit of a quantum neural network within the framework of the dissipative model of quantum computing.

Keywords: Binary classification, information reservoir, collision model, quantum Fisher information

1. INTRODUCTION

Classification of data plays an important role in extremely important applications such as machine learning, medical diagnostics and pattern recognition. In recent studies, machine learning algorithms made within the scope of quantum framework present the advantages of quantum computing [1-7]. The standard circuit model of quantum computation relies on quantum registers in pure states. That is, the quantum register is a closed quantum system.

However, we propose a quantum processing task based on open quantum dynamics. Recent reports show that quantum baths can be evaluated as communication channels through which information is transmitted [8, 9]. These studies encourage us to examine the existence of quantum classifiers where their dynamics are not unitary.

In our study, we consider a two-level quantum system (probe qubit) weakly interacting with different quantum reservoirs carrying information content. We refer to these reservoirs information reservoirs as we assume they are identical qubit strings in pure states with specific information parameters. [10, 11]. The probe qubit is subject a dissipation process in the presence of information reservoirs [12], such as quantum reservoir engineering, where the steady state is a non-trivial

* Corresponding author: ufukkorkmaz@itu.edu.tr
[1] Istanbul Technical University, Faculty of Electrical and Electronics, Department of Electrical Engineering
E-mail: dturkpence@itu.edu.tr
ORCID: https://orcid.org/0000-0001-5836-5262, https://orcid.org/0000-0002-5182-374X

quantum state. We show that the steady state of the probe qubit acts as a quantum binary classifier as a result of interacting with various information environments. Using the mixing properties of quantum dynamic maps, we show that under some conditions the mixture of quantum dynamical maps can be natural data classifiers. Though it seems useless to use mixed states for quantum computation processing, it is shown that the dissipative model of quantum computing provides an alternative route for quantum computation. [14, 15].

For quantum thermodynamics or materials sciences, it is important to take advantage of quantum sources that exhibit non-linear response with respect to linear variation of dynamical parameters [16-18]. We construct our model by considering a single spin weakly connected to information reservoirs where reservoir induced non-linearity could be encountered. We then trace out the environmental states to calculate the reduced dynamics. Single spin magnetization as a steady-state response of reduced dynamics is an indication of merit. In the model, the input data represents information reservoirs connected to a single spin. The physics we use in this model is based on the complete positivity, additivity [19] and divisibility [20, 21] of quantum dynamical maps. As has been done in previous studies [7], [22], superconducting circuits can be shown as a physical model to apply the theoretical model with possible defects. We leave the activation and training tasks out of the scope of this study for our proposed classifier.

2. FRAMEWORK AND MODEL DYNAMICS

Perceptron is the simplest developed mathematical model for binary data classification. More precisely, the perceptron predicts binary decision output corresponding to a weighted sum of data instances as input. In general, the output is modulated by a rule, so-called activation function. For instance, a step function $f(y)$ where $y = \sum_i w_i x_i$ with x_i data instances and w_i corresponding weights [23] can be defined as output. By the behaviour of the step function, the output node returns $f(y) = +1$ for $y \geq 0$ and returns $f(y) = 0$ else. Activation functions can be selected from either linear or non-linear functions. However, nonlinear functions are attractive in multilayer neural network applications as they support back propagation. There have been studies based on the advantages of quantum computing using quantum perceptrons or neural network models [2, 3, 6, 24].

Our model is an open quantum system and we take advantage of dissipative processes for data classification. Such a system ρ is defined by

$$\frac{\partial \rho}{\partial t} = P_1 \mathcal{L}_t^{(1)} + \cdots + P_N \mathcal{L}_t^{(N)} \quad (1)$$

a weighted combination of generators representing the non-unitary evolutions induced by N distinct reservoirs. Here, the generators $\mathcal{L}_t^{(i)}$ are, in general, time-dependent and P_i are non-negative coefficients representing the probabilities of the probe qubit experiencing from the ith information reservoir. Note that, Eq. (1) represents the quantum equivalent of a classical perceptron model defined and represents a physical system as long as the weak coupling condition is satisfied, which ensures the additivity of the generators [19, 21, 25].

To this end, each generator will be represented by a completely positive trace-preserving (CPTP) quantum dynamical map

$$\Phi_t^{(i)} = Tr_{\mathcal{R}_i}\left[U_t\left(\rho_0 \otimes \rho_{\mathcal{R}_i}\right)U_t^{\dagger}\right] \quad (2)$$

where U_t is a unitary propagator acting both on the system and the environment and $\mathcal{R}_i$ represents the quantum state of the ith environment. In addition, if a dynamical map satisfying $\Phi_{t+s} = \Phi_t(\Phi_s[\rho])$ is completely positive (CP) for t and $s \geq 0$, this is referred to as a CP divisible map. It has been shown that CP divisibility ensures the additivity of quantum dynamical maps in the weak coupling condition where cross-correlations between distinct reservoirs are avoided [21, 26].

Therefore, we represent the open quantum dynamics of our model by using a weighted combination of quantum dynamical maps satisfying CP divisibility as

$$\Phi_t[\rho_0] = \sum_i P_i \, \Phi_t^{(i)}. \quad (3)$$

Note that, Eq. (3) can only be cast in place of Eq. (1) only if all the dynamical maps $\Phi_t^{(i)}$ in the summation is CP divisible.

Single qubit quantum information is parametrized by polar and azimuthal angles as $|\Psi(\theta,\emptyset)\rangle = \cos\frac{\theta}{2}|e\rangle + e^{i\emptyset}\sin\frac{\theta}{2}|g\rangle$ in the well-known Bloch sphere representation, here $|e\rangle \equiv |0\rangle$ and $|g\rangle \equiv |1\rangle$ stand for excited and ground states, respectively. Throughout of our study we take $\emptyset = 0$ fixed and parametrize 'quantum features' by θ. In our model, we treat the classifier as a schema that carries informational content to different reservoirs where the probe qubit is weakly coupled. We model the open quantum dynamics using a repeated interaction process [27]. The ancilla units in these models are identical. Ancilla units do not interact with each other and the dynamics of the repeated interactions are unitary with very small interaction time τ. Thanks to the standard formulation of the collision models, memoryless open quantum dynamics equivalent to the master equations is obtained. At the beginning, the ancillas $\mathcal{R}_i$, which are prepared identically, sequentially collide with system S in equal duration τ. The system plus reservoir $S\mathcal{R}$ state is initially assumed to be in a product state $\rho(0) = \rho_S(0)\bigotimes_i^N \rho_{\mathcal{R}_i}$ where $\rho(0) = |+\rangle\langle+|$ and $\rho_{\mathcal{R}} = |\Psi_\theta\rangle\langle\Psi_\theta|$. By choosing the initial system states as $|+\rangle = \frac{|e\rangle+|g\rangle}{\sqrt{2}}$, we initially provide a null magnetization. These identical qubit states $\mathcal{R}_i$ read as

$$\rho_{\mathcal{R}_i} = \bigotimes_{k=1}^N \rho_{i_k}(\theta,\emptyset). \quad (4)$$

In order to represent the additivity of quantum dynamical maps in terms of quantum collisional model, each dynamical map $\Phi_t^{(i)}$ in Eq. (3) can be rephrased as

$$\Phi_{n\tau}^{(i)}[\rho_0] = Tr_n\left[U_{0i_n}\cdots Tr_1\left[U_{0i_1}\left(\rho_0 \otimes \rho_{\mathcal{R}_{i_1}}\right)U_{0i_1}^\dagger\right]\otimes\cdots\rho_{\mathcal{R}_{i_n}}U_{0i_n}^\dagger\right] \quad (5)$$

by using the reduced dynamics where $n\tau$ is the time elapsed for n collisions. When the scheme above was repeated a sufficient number of times, the system state becomes identical to that of the reservoir state. Thus, the system reaches steady state where the process is referred to as 'quantum homogenization' [28]. From now on, we drop the index k for convenience.

We use the standard collision model where the bath of N qubits do not interact each other, so the open system evolution is Markovian analougus to the central spin model [29]. As shown in Figure 1, a cluster of Nqubits interacts randomly with the probe qubit. The total Hamiltonian reads $H = H_0 + H_{\mathcal{R}_i} + H_{int}$, where

$$H_0 + H_{\mathcal{R}_i} = \frac{\hbar w_0}{2}\sigma_0^z + \frac{\hbar w_b}{2}\sum_{i=1}^N \sigma_i^z. \quad (6)$$

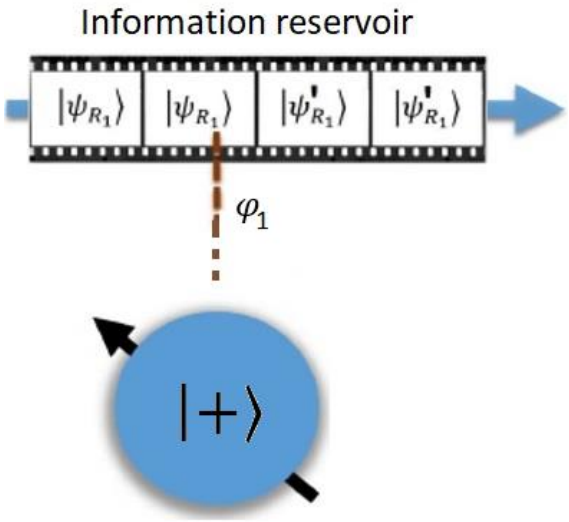

Figure 1 Statistically identical prepared cluster qubits interacts randomly with the probe qubit

Eq. (6) is the free Hamiltonian of the probe qubit and the N reservoir qubits, respectively. $\hbar$ is the reduced Planck constant. $\sigma_{0,i}^z = |e_{0,i}\rangle\langle e_{0,i}| - |g_{0,i}\rangle\langle g_{0,i}|$ are the Pauli z matrices for the probe and ith qubit, respectively. For simplicity, we assume that the system reservoir resonance is $w_0 = w_b$. We define interaction Hamiltonian as

$$H_{int} = \hbar\sum_{i=1}^N \varphi_i(\sigma_i^+\sigma_0^- + H.c.), \quad (7)$$

where φ_i is the coupling constant between the probe qubit and the ith reservoir qubits, $\sigma_i^+ = |e_i\rangle\langle g_i|$, $\sigma_i^- = |g_i\rangle\langle e_i|$ are the individual Pauli -

raising and -lowering operators. $\sigma_0^{\pm}$ are the Pauli matrices act on the probe qubit. The coupling strength is directly related to the $\varphi_i \propto P_i$ probability expressing the ith reservoir encounters. We derive a micromaser-like master equation based on repeated, random interactions. In this way, we establish the connection between the dynamic model of the study and real physical systems [17, 29-31]. In this article, open system evolution is Markovian. Because we used the standard collision model where the ancillas do not interact with each other. $U(\tau) = exp[-iH_{int}\tau/\hbar]$ are unitary propagators and describe the collisions between the system qubit and each ancilla.

$$U(\tau) = \mathbb{1} - i\tau\left(\sigma_0^+ J_{\varphi_i}^- + \sigma_0^- J_{\varphi_i}^+\right) - \frac{\tau^2}{2}\left(\sigma_0^+\sigma_0^- J_{\varphi_i}^- J_{\varphi_i}^+ + \sigma_0^-\sigma_0^+ J_{\varphi_i}^+ J_{\varphi_i}^-\right) \quad (8)$$

up to second order in τ. Here, $J_{\varphi_i}^{\pm} = \sum_{i=1}^{N} \varphi_i \sigma_i^{\pm}$ are the collective operators weighted by φ_i. The initial system is assumed to be factored $\rho(t) = \rho_0(t) \otimes \rho_{\mathcal{R}_i}$, assuming the reservoir states are reset to their initial state after each interaction. In the light of micro-maser theory, we explain random interactions with a Poisson process. The dynamics of the system is

$$\rho(t+\delta t) = r\delta t U(\tau)\rho(t)U^{\dagger}(\tau) + (1 - r\delta t)\rho(t) \quad (9)$$

in a time interval δt, where where $r\delta t$ is the probability of an interaction event at a rate r and $(1 - r\delta t)$ is the probability of occurring a non-interaction state. For the reduced dynamics of the probe qubit, the master equation is obtained as

$$\dot{\rho}_0(t) = Tr_{\mathcal{R}_i}[rU(\tau)\rho(t)U^{\dagger}(\tau) - r\rho(t)] \quad (10)$$

in the time limit $\delta t \to 0$ for $\dot{\rho}_0(t) = [\rho_0(t+\delta t) - \rho_0(t)]/\delta t$. After some adjustments, the master equation obtained for our model is

$$\dot{\rho}_0 = -i\left[H_{eff}, \rho\right] + \sum_{i=1}^{N} \varphi_i^2(\zeta^+ \mathcal{L}[\sigma_0^+] + \zeta^- \mathcal{L}[\sigma_0^-]) + \sum_{i<j}^{N'} \varphi_i\varphi_j(\zeta_s^+ \mathcal{L}_s[\sigma_0^-] + \zeta_s^- \mathcal{L}_s[\sigma_0^+]) \quad (11)$$

where $H_{eff} = r\tau \sum_i^N \varphi_i(\langle\sigma_i^-\rangle\sigma_0^+ + \langle\sigma_i^+\rangle\sigma_0^-)$ denotes the effective Hamiltonian describing a coherent drive on the probe qubit. $\langle\mathcal{O}_i\rangle = Tr\left[\mathcal{O}\rho_{\mathcal{R}_i}\right]$ are averages calculated over identical reservoir units. The superoperators here, respectively, $\mathcal{L}[o] \equiv 2o\rho o^{\dagger} - o^{\dagger}\rho o - \rho o o^{\dagger}$ is the standard Lindblad term and $\mathcal{L}_s[o] \equiv 2o\rho o$ describes a squeezing effect by the reservoir. Since the standard Linbladian coefficients $\zeta^{\pm} = \frac{r\tau^2}{2}\langle\sigma_i^{\pm}\sigma_i^{\mp}\rangle$ contain diagonal inputs and $\zeta_s^{\pm} = 2r\tau^2\langle\sigma_i^{\pm}\rangle\langle\sigma_j^{\pm}\rangle$ contain off-diagonal inputs, the Linbladian coefficients carry information corresponding to the different inputs of the density matrices of the reservoir units. $N' = N(N-1)/2$ are terms in the summation.

Let us express the density matrix of the probe qubit as $\rho(t) = p_e(t)|e\rangle\langle e| + p_g(t)|g\rangle\langle g| + (c(t)|e\rangle\langle g| + H.c.)$ in the standard basis. When we substitute these expressions in Eq. (11) as $\dot{\rho}_0$=0 and $c = c^* = 0$, the steady state equation is obtained as follows

$$\rho_0^{ss} = \frac{1}{\sum_i^N \varphi_i^2}\sum_{i=1}^{N} \varphi_i^2(\langle\sigma_i^+\sigma_i^-\rangle|e\rangle\langle e| + \langle\sigma_i^-\sigma_i^+\rangle|g\rangle\langle g| + [i\gamma_1^-(\langle\sigma_i^+\sigma_i^-\rangle - \langle\sigma_i^-\sigma_i^+\rangle)|e\rangle\langle g| + H.c.]) \quad (12)$$

where $\gamma_1^- = r\tau\sum_i^N \varphi_i\langle\sigma_i^-\rangle$. Eq. (12) reduces to

$$\rho_0^{ss} = (\langle\sigma_1^+\sigma_1^-\rangle|e\rangle\langle e| + \langle\sigma_1^-\sigma_1^+\rangle|g\rangle\langle g| + [i\gamma_1^-(\langle\sigma_1^+\sigma_1^-\rangle - \langle\sigma_1^-\sigma_1^+\rangle)|e\rangle\langle g| + H.c.]) \quad (13)$$

in the presence of a single (only $\varphi_1 \neq 0$) information reservoir. As clear above, the steady state density matrix involves the same diagonal terms as that of the reservoir density matrices of the reservoir units.

This result is typical for the steady state response of small quantum systems for dissipative interactions. However, the off-diagonal elements above depend on γ_1^-, which is a function of r. In other words, a complete implementation of a single information reservoir depends on the interaction statistics. That is, for Poisson interaction statistics $r\delta t \to 0$, off-diagonals will not appear in the steady state, while for regular statistics $r\delta t \to 1$, one obtains more data about the reservoir in the steady state with the inclusion of off-diagonal terms.

2.1. Fisher Information

As mentioned above, the probe qubit encodes the binary classification result in the steady state. A qubit can be represented as

$$\rho = \frac{1}{2}(\mathbb{1} + \boldsymbol{\omega}\cdot\boldsymbol{\sigma}) \tag{14}$$

in the Bloch representation where, $\mathbb{1}$ is the unit matrix, $\boldsymbol{\omega} = \left(\omega_x, \omega_y, \omega_z\right)^T$ is the Bloch vector and $\boldsymbol{\sigma} = \left(\sigma_x, \sigma_y, \sigma_z\right)$ denotes a vector whose components are the Pauli matrices. When the qubit undergoes a dissipation process with Pauli channels, this can be defined by a CPTP map

$$\varepsilon(\rho) = \frac{1}{2}\mathbb{1} + \frac{1}{2}(A\boldsymbol{\omega} + \boldsymbol{c})\cdot\boldsymbol{\sigma} \tag{15}$$

where A is a 3×3 transformation matrix with $A_{i,j} = \frac{1}{2}Tr\left[\sigma_i\varepsilon\left(\sigma_j\right)\right]$ real elements and $\boldsymbol{c}\,\epsilon\,R^3$ is a translation vector with $c_i = \frac{1}{2}Tr[\sigma_i\varepsilon(\mathbb{1})]$. Here, the transformation of the Bloch vector $\boldsymbol{\omega}$ is defined by an affine map $\varepsilon(\boldsymbol{\omega}) \coloneqq A\boldsymbol{\omega} + \boldsymbol{c}$.

An unknown parameter λ of a random variable can be estimated by Fisher information. The classical Fisher information for a discrete random variable reads

$$\mathcal{F}_\lambda = \sum_r p_r(\lambda)\left[\frac{\partial ln p_r(\lambda)}{\partial\lambda}\right]^2 \tag{16}$$

where $p_r(\lambda)$ is the probability of obtaining the result r conditioned on the parameter λ. Quantum Fisher information (QFI) can be quantified by the generalization of Eq. (16) as

$$\mathcal{F}_\lambda = Tr\left[\rho_\lambda L_\lambda^2\right] = Tr[(\partial_\lambda\rho_\lambda)L_\lambda] \tag{17}$$

where L_λ is the symmetric logarithmic derivative defined through $\partial_\lambda\rho_\lambda = \frac{1}{2}\{\rho_\lambda, L_\lambda\}$ [32].

Based on these expressions, for a general mixed state $\rho_\lambda = \sum_i p_i|\Psi_i\rangle\langle\Psi_i|$, QFI is defined by

$$\mathcal{F}_\lambda = \sum_i \frac{(\partial_\lambda p_i)^2}{p_i} + \sum_i p_i\mathcal{F}_{\lambda,i} - \sum_{i\neq j}\frac{8p_ip_j}{p_i+p_j}\left|\langle\Psi_i|\partial_\lambda\Psi_j\rangle\right|^2 \tag{18}$$

where $\{p_i\}$ are the eigenvalues of ρ and $\mathcal{F}_{\lambda,i}$ is the QFI for a pure state with

$$\mathcal{F}_{\lambda,i} = 4[\langle\partial_\lambda\Psi_i|\partial_\lambda\Psi_i\rangle - |\langle\Psi_i|\partial_\lambda\Psi_i\rangle|^2]. \tag{19}$$

In addition, a convenient formula specific to the two level system (TLS) was developed as follows [33]

$$\mathcal{F}_\lambda = Tr[(\partial_\lambda\rho)^2] + \frac{1}{det\rho_\lambda}Tr[(\rho_\lambda\partial_\lambda\rho_\lambda)^2]. \tag{20}$$

QFI can also be expressed in Bloch sphere representation under Pauli channels as [34]

$$\mathcal{F}_\lambda = |\partial_\lambda\,\varepsilon(\boldsymbol{\omega})|^2 + \frac{[\,\varepsilon(\boldsymbol{\omega})\cdot\partial_\lambda\,\varepsilon(\boldsymbol{\omega})]^2}{1-|\,\varepsilon(\boldsymbol{\omega})|^2}. \tag{21}$$

2.2. Numerical results for Fisher Information

The QuTIP package is used for numerical calculations [35]. It can define the density matrix for the information reservoir as follows

$$\rho_{\mathcal{R}_i} = \begin{bmatrix} \frac{1+\cos\theta_i}{2} & \frac{e^{-i\emptyset_i}}{2}\sin\theta_i \\ \frac{e^{i\emptyset_i}}{2}\sin\theta_i & \frac{1-\cos\theta_i}{2} \end{bmatrix} = \begin{bmatrix} \langle\sigma_i^+\sigma_i^-\rangle & \langle\sigma_i^-\rangle \\ \langle\sigma_i^+\rangle & \langle\sigma_i^-\sigma_i^+\rangle \end{bmatrix} \tag{22}$$

When we substitute the values in Eq. (22) in Eq. (12), $\varepsilon(\rho_0^{ss})$ is obtained according to the variables θ and $\emptyset$ as

$$\varepsilon(\rho_0^{ss}) = \frac{1}{2\sum_i^N\varphi_i^2}\sum_{i=1}^N(\varphi_i^2 + \varphi_i^2\cos\theta_i)|e\rangle\langle e| + \left(+\frac{ir\tau}{2\sum_i^N\varphi_i^2}\sum_{i,j=1}^N\varphi_i\,\varphi_j^2\sin\theta_i\cos\emptyset_i\cos\theta_j + \frac{r\tau}{2\sum_i^N\varphi_i^2}\sum_{i,j=1}^N\varphi_i\,\varphi_j^2\sin\theta_i\sin\emptyset_i\cos\theta_j\right)|e\rangle\langle g| + \left(-\frac{ir\tau}{2\sum_i^N\varphi_i^2}\sum_{i,j=1}^N\varphi_i\,\varphi_j^2\sin\theta_i\cos\emptyset_i\cos\theta_j + \frac{r\tau}{2\sum_i^N\varphi_i^2}\sum_{i,j=1}^N\varphi_i\,\varphi_j^2\sin\theta_i\sin\emptyset_i\cos\theta_j\right)|g\rangle\langle e| + \frac{1}{2\sum_i^N\varphi_i^2}\sum_{i=1}^N(\varphi_i^2 - \varphi_i^2\cos\theta_i)|g\rangle\langle g| \tag{23}$$

Substituting $\varepsilon(\rho_0^{ss})$ and Pauli matrices into Eq. (15),

$$\varepsilon(\rho_0^{ss}) = \frac{1}{2}\mathbb{1} + \frac{1}{2}\left(\varepsilon(\omega_x)\sigma_x + \varepsilon(\omega_y)\sigma_y + \varepsilon(\omega_z)\sigma_z\right) \quad (24)$$

we get

$$\varepsilon(\omega) = \begin{pmatrix}\omega_x\\ \omega_y\\ \omega_z\end{pmatrix} = \frac{1}{\sum_i^N \varphi_i^2}\begin{pmatrix} r\tau\sum_{i,j=1}^N \varphi_i\,\varphi_j^2 \sin\theta_i \sin\emptyset_i \cos\theta_j \\ -r\tau\sum_{i,j=1}^N \varphi_i\,\varphi_j^2 \sin\theta_i \cos\emptyset_i \cos\theta_j \\ \sum_{i=1}^N \varphi_i^2 \cos\theta_i \end{pmatrix} \quad (25)$$

Finally, when we substitute Eq. (25) in Eq. (21), the QFI ($\mathcal{F}_\theta$) is obtained in Bloch sphere notation.

Figure 2 shows the couplings are equal and fixed QFI is investigated for different reservoir states defined by the geometrical qubit parameters. In this case, the preferred parameter is the Bloch ball azimuthal angle θ to define to information reservoir states $|\Psi_\theta\rangle$.

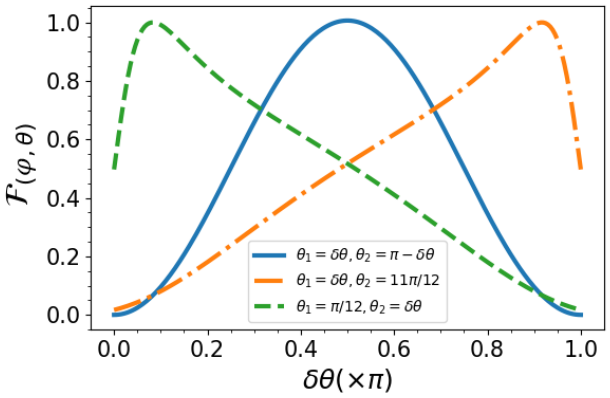

Figure 2 The variation of the QFI of the system qubit coupled to the two environments carrying different information contents parametrized by θ, where $\delta\theta$ is a fraction of θ with $\delta\theta = 1.0$. Coupling of the system to the reservoirs are fixed, equal and $\varphi_1 = \varphi_2 = 0.05$

While $t_r \sim 1 - 10ns$ is a single qubit reset time, current state-of-the art technology allows an energy dissipation on time scale $T_1 \sim 50 - 100\mu s$ [36]–[38]. We take $w_0 = w_b = 1\ GHz$ and is $k = 1 \times 10^3$ is number of successful. The interaction time is $\tau = 4ns$ corresponding to $\tau = 4$ when scaled w_0. The rate is $r = \frac{k}{T_1 w_0} = 0.2$.

Blue curve presents the QFI depicted against $\delta\theta$ which is a factor governs the variation of the Bloch ball azimuthal angle such as $\theta_1 = \delta\theta, \theta_2 = \pi - \delta\theta$ to the $|\Psi_{\theta_1}\rangle$ and $|\Psi_{\theta_2}\rangle$ reservoirs, respectively. For instance, when $\delta\theta = 0$; $\theta_1 = 0$ and $\theta_2 = \pi$. $\mathcal{F}_\theta$ is the maximum likelihood estimate when $\delta\theta = \pi/2$. This means that $\mathcal{F}_\theta$ has maximum information at $\delta\theta = \pi/2$.

The green curve represents the fixed state of the first environment represented by the azimuth angle $\theta_1 = 15^\circ$ and the variation of the state of the second environment parameterized by $\theta_2 = 1^\circ, 2^\circ, \cdots, 180^\circ$. Likewise, the orange curve represents the fixed state of the second environment represented by the azimuth angle $\theta_2 = 165^\circ$ and the variation of the state of the first environment parameterized by $\theta_1 = 1^\circ, 2^\circ, \cdots, 180^\circ$ (Figure 2). The shifts in the maximum information value of the $\mathcal{F}_\theta$ relative to the initial state of the information reservoirs are clearly visible. In this way, classification can be made as $\theta \leq \pi/2$ class1 and $\theta > \pi/2$ class2.

3. CONCLUSION

First, we derive a master equation, considering quantum reservoirs as information sources. Through this equation we have derived, we propose a classifier that makes a binary decision in its steady state depending on the coupling ratios and the parameters of the distinct, multiple, quantum information-carrying reservoirs. By specifying the classification according to the weighted sum of the amplitude parameters, the steady-state magnetization of the probe qubit is used as the classification tool. As a result, we analytically verify that a single probe qubit can classify it by reading the quantum information encoded in the reservoir qubits.

Second, the QFI is generalized for N reservoir states defined by the geometric qubit parameters. We then numerically obtain the QFI for $N = 2$ reservoir states. We also verify that quantum Fisher information can be used as a classification tool. In cases where quantum information tasks are based on dissipation, our results may contribute.

4. APPENDICES

Let's express Eq. (8) as follows

$$U(\tau) = \mathbb{1} - U_1 - U_2 \tag{A.1}$$

where $U_1 = i\tau\left(\sigma_0^+ J_{\varphi_i}^- + \sigma_0^- J_{\varphi_i}^+\right)$ and $U_2 = \frac{\tau^2}{2}\left(\sigma_0^+\sigma_0^- J_{\varphi_i}^- J_{\varphi_i}^+ + \sigma_0^-\sigma_0^+ J_{\varphi_i}^+ J_{\varphi_i}^-\right)$, respectively. If we substitute Eq. (A.1) in Eq. (10) and neglect the 3rd ($U_1(\tau)\rho(t)U_2^\dagger(\tau)$) and 4th ($U_2(\tau)\rho(t)U_2^\dagger(\tau)$) order terms, the following expression is obtained.

$$\dot{\rho}_0(t) = rTr_{\mathcal{R}_i}\big[U_1(\tau)\rho(t)U_1^\dagger(\tau) - U_1(\tau)\rho(t) - U_2(\tau)\rho(t) - \rho(t)U_1^\dagger(\tau) - \rho(t)U_2^\dagger(\tau)\big]. \tag{A.2}$$

Considering the cyclic and linearity properties of the trace operation, the explicit expression of the main equation (Eq. (A.2)) for the probe qubit is as follows when we trace the degrees of freedom of the information environments.

$$\begin{aligned}\dot{\rho}_0 = &-ir\tau[\textstyle\sum_i^N \varphi_i(\langle\sigma_i^-\rangle\sigma_0^+ + \langle\sigma_i^+\rangle\sigma_0^-), \rho] + \\ &\tfrac{r\tau^2}{2}\textstyle\sum_{i=1}^N \varphi_i^2(\langle\sigma_i^+\sigma_i^-\rangle\mathcal{L}[\sigma_0^+] + \\ &\langle\sigma_i^-\sigma_i^+\rangle\mathcal{L}[\sigma_0^-]) + \\ &2r\tau^2\textstyle\sum_{i<j}^{N'} \varphi_i\varphi_j\big(\langle\sigma_i^+\rangle\langle\sigma_j^-\rangle\,\mathcal{L}_s[\sigma_0^-] + \\ &\langle\sigma_i^-\rangle\langle\sigma_j^+\rangle\mathcal{L}_s[\sigma_0^+]\big)\end{aligned} \tag{A.3}$$

Funding

This study is supported by TÜBİTAK. Project Number: 120F353.

The Declaration of Conflict of Interest/ Common Interest

No conflict of interest or common interest has been declared by the authors.

Authors' Contribution

The authors contributed equally to the study.

The Declaration of Ethics Committee Approval

This study does not require ethics committee permission or any special permission.

The Declaration of Research and Publication Ethics

The authors of the paper declare that they comply with the scientific, ethical and quotation rules of SAUJS in all processes of the paper and that they do not make any falsification on the data collected. In addition, they declare that Sakarya University Journal of Science and its editorial board have no responsibility for any ethical violations that may be encountered, and that this study has not been evaluated in any academic publication environment other than Sakarya University Journal of Science.

REFERENCES

[1] P. Rebentrost, M. Mohseni, and S. Lloyd, 'Quantum Support Vector Machine for Big Data Classification', *Phys. Rev. Lett.*, vol. 113, no. 13, p. 130503, Sep. 2014.

[2] M. Schuld, I. Sinayskiy, and F. Petruccione, 'Simulating a perceptron on a quantum computer', *Physics Letters A*, vol. 379, no. 7, pp. 660–663, Mar. 2015.

[3] L. Banchi, N. Pancotti, and S. Bose, 'Quantum gate learning in qubit networks: Toffoli gate without time-dependent control', *npj Quantum Information*, vol. 2, no. 1, 2016.

[4] S. Lu *et al.*, 'Separability-entanglement classifier via machine learning', *Phys. Rev. A*, vol. 98, no. 1, p. 012315, Jul. 2018.

[5] S. Lloyd and C. Weedbrook, 'Quantum Generative Adversarial Learning', *Phys. Rev. Lett.*, vol. 121, no. 4, p. 040502, Jul. 2018.

[6] A. Y. Yamamoto, K. M. Sundqvist, P. Li, and H. R. Harris, 'Simulation of a Multidimensional Input Quantum Perceptron', *Quantum Inf Process*, vol. 17, no. 6, p. 128, Apr. 2018.

[7] D. Türkpençe, T. Ç. Akıncı, and S. Şeker, 'A steady state quantum classifier', *Physics*

Letters A, vol. 383, no. 13, pp. 1410–1418, Apr. 2019.

[8] R. Blume-Kohout and W. H. Zurek, 'A Simple Example of "Quantum Darwinism": Redundant Information Storage in Many-Spin Environments', *Found Phys*, vol. 35, no. 11, pp. 1857–1876, Nov. 2005.

[9] M. Zwolak and W. H. Zurek, 'Redundancy of einselected information in quantum Darwinism: The irrelevance of irrelevant environment bits', *Phys. Rev. A*, vol. 95, no. 3, p. 030101, Mar. 2017.

[10] S. Deffner, 'Information-driven current in a quantum Maxwell demon', *Phys. Rev. E*, vol. 88, no. 6, p. 062128, Dec. 2013.

[11] S. Deffner, 'Information-driven current in a quantum Maxwell demon', *Physical Review E*, vol. 88, no. 6, p. 062128, Dec. 2013.

[12] J. F. Poyatos, J. I. Cirac, and P. Zoller, 'Quantum Reservoir Engineering with Laser Cooled Trapped Ions', *Phys. Rev. Lett.*, vol. 77, no. 23, pp. 4728–4731, Dec. 1996.

[13] H.-P. Breuer, P. I. H.-P. Breuer, F. Petruccione, and S. of P. and A. P. F. Petruccione, *The Theory of Open Quantum Systems*. Oxford University Press, 2002.

[14] M. Siomau and S. Fritzsche, 'Quantum computing with mixed states', *Eur. Phys. J. D*, vol. 62, no. 3, p. 449, May 2011.

[15] F. Verstraete, M. M. Wolf, and J. Ignacio Cirac, 'Quantum computation and quantum-state engineering driven by dissipation', *Nature Phys*, vol. 5, no. 9, pp. 633–636, Sep. 2009.

[16] D. Turkpence, G. B. Akguc, A. Bek, and M. E. Tasgin, 'Engineering nonlinear response of nanomaterials using Fano resonances', *J. Opt.*, vol. 16, no. 10, p. 105009, Sep. 2014.

[17] D. Türkpençe and Ö. E. Müstecaplıoğlu, 'Quantum fuel with multilevel atomic coherence for ultrahigh specific work in a photonic Carnot engine', *Phys. Rev. E*, vol. 93, no. 1, p. 012145, Jan. 2016.

[18] D. Türkpençe, F. Altintas, M. Paternostro, and Ö. E. Müstecaplioğlu, 'A photonic Carnot engine powered by a spin-star network', *EPL (Europhysics Letters)*, vol. 117, no. 5, p. 50002, Mar. 2017.

[19] J. Kołodyński, J. B. Brask, M. Perarnau-Llobet, and B. Bylicka, 'Adding dynamical generators in quantum master equations', *Phys. Rev. A*, vol. 97, no. 6, p. 062124, Jun. 2018.

[20] M. M. Wolf and J. I. Cirac, 'Dividing Quantum Channels', *Commun. Math. Phys.*, vol. 279, no. 1, pp. 147–168, Apr. 2008.

[21] S. N. Filippov, J. Piilo, S. Maniscalco, and M. Ziman, 'Divisibility of quantum dynamical maps and collision models', *Phys. Rev. A*, vol. 96, no. 3, p. 032111, Sep. 2017.

[22] U. Korkmaz, D. Türkpençe, T. Ç. Akinci, and S. Şeker, 'A thermal quantum classifier', *Quantum Information and Computation*, vol. 20, no. 11–12, pp. 969–986, 2020.

[23] R. Hecht-Nielsen, 'Neurocomputing: picking the human brain', *IEEE Spectrum*, vol. 25, no. 3, pp. 36–41, Mar. 1988.

[24] M. Schuld and F. Petruccione, 'Quantum ensembles of quantum classifiers', *Sci Rep*, vol. 8, no. 1, p. 2772, Feb. 2018.

[25] M. T. Mitchison and M. B. Plenio, 'Non-additive dissipation in open quantum networks out of equilibrium', *New J. Phys.*, vol. 20, no. 3, p. 033005, Mar. 2018.

[26] J. Kołodyński, J. B. Brask, M. Perarnau-Llobet, and B. Bylicka, 'Adding dynamical generators in quantum master equations', *Physical Review A*, vol. 97, no. 6, p. 062124, Jun. 2018.

[27] L. Bruneau, A. Joye, and M. Merkli, 'Repeated interactions in open quantum systems', *J. Math. Phys.*, vol. 55, no. 7, p. 075204, Jul. 2014.

[28] V. Scarani, M. Ziman, P. Štelmachovič, N. Gisin, and V. Bužek, 'Thermalizing Quantum Machines: Dissipation and Entanglement', *Phys. Rev. Lett.*, vol. 88, no. 9, p. 097905, Feb. 2002.

[29] A. Manatuly, W. Niedenzu, R. Román-Ancheyta, B. Çakmak, Ö. E. Müstecaplıoğlu, and G. Kurizki, 'Collectively enhanced thermalization via multiqubit collisions', *Phys. Rev. E*, vol. 99, no. 4, p. 042145, Apr. 2019.

[30] J. D. Cresser, 'Quantum-field model of the injected atomic beam in the micromaser', *Phys. Rev. A*, vol. 46, no. 9, pp. 5913–5931, Nov. 1992.

[31] J.-Q. Liao, H. Dong, and C. P. Sun, 'Single-particle machine for quantum thermalization', *Phys. Rev. A*, vol. 81, no. 5, p. 052121, May 2010.

[32] C. W. Helstrom, 'Quantum detection and estimation theory', *J Stat Phys*, vol. 1, no. 2, pp. 231–252, Jun. 1969.

[33] J. Dittmann, 'Explicit formulae for the Bures metric', *J. Phys. A: Math. Gen.*, vol. 32, no. 14, pp. 2663–2670, Jan. 1999.

[34] W. Zhong, Z. Sun, J. Ma, X. Wang, and F. Nori, 'Fisher information under decoherence in Bloch representation', *Phys. Rev. A*, vol. 87, no. 2, p. 022337, Feb. 2013.

[35] J. R. Johansson, P. D. Nation, and F. Nori, 'QuTiP: An open-source Python framework for the dynamics of open quantum systems', *Computer Physics Communications*, vol. 183, no. 8, pp. 1760–1772, Aug. 2012.

[36] S. Filipp *et al.*, 'Multimode mediated qubit-qubit coupling and dark-state symmetries in circuit quantum electrodynamics', *Phys. Rev. A*, vol. 83, no. 6, p. 063827, Jun. 2011.

[37] X.-H. Deng, E. Barnes, and S. E. Economou, 'Robustness of error-suppressing entangling gates in cavity-coupled transmon qubits', *Phys. Rev. B*, vol. 96, no. 3, p. 035441, Jul. 2017.

[38] A. Blais, A. L. Grimsmo, S. M. Girvin, and A. Wallraff, 'Circuit quantum electrodynamics', *Rev. Mod. Phys.*, vol. 93, no. 2, p. 025005, May 2021.

SAKARYA ÜNİVERSİTESİ
FEN BİLİMLERİ ENSTİTÜSÜ DERGİSİ

Sakarya University Journal of Science
SAUJS

e-ISSN 2147-835X Period Bimonthly Founded 1997 Publisher Sakarya University
http://www.saujs.sakarya.edu.tr/

Title: Numerical Investigation of The Effect of Impeller Blade Angle for Stirred Tank

Authors: Dogan Engin ALNAK, Ferhat KOCA, Yeliz ALNAK

Recieved: 2021-09-07 00:00:00

Accepted: 2022-03-21 00:00:00

Article Type: Research Article

Volume: 26
Issue: 2
Month: April
Year: 2022
Pages: 397-409

How to cite
Dogan Engin ALNAK, Ferhat KOCA, Yeliz ALNAK; (2022), Numerical Investigation of The Effect of Impeller Blade Angle for Stirred Tank. Sakarya University Journal of Science, 26(2), 397-409, DOI: 10.16984/saufenbilder.992396
Access link
https://dergipark.org.tr/tr/journal/1115/issue/69580/992396

New submission to SAUJS
http://dergipark.gov.tr/journal/1115/submission/start

Sakarya University Journal of Science 26(2), 397-409, 2022

Numerical Investigation of The Effect of Impeller Blade Angle for Stirred Tank

Dogan Engin ALNAK*[1], Ferhat KOCA[1], Yeliz ALNAK[1]

Abstract

In this study, the most widely used Rushton turbine in the industry was discussed, and the effect of different blade angles on the mixture was investigated numerically. As a standard model, 6 bladed propellers were used and 4 baffles were placed in the stirred tank. The selected tank model is in the form of a flat bottom cylindrical container. Flow characteristics were obtained by giving angles (10°, 20°, 30°, 40°, 50°, 60°) to the propeller blades used in the straight model. The obtained results were compared with each other. In addition, analyzes were repeated at different rotation speeds (600 rpm, 750 rpm, 1000 rpm) for each model at each angle. ANSYS Fluent 18 commercial software, which is the most preferred CFD program in the literature, was used for this numerical study. The analyzes were provided in the standard k-epsilon (ε) turbulence model. The Multiple Reference Frame (MRF) approach was used to simulate impeller rotation. The velocity profiles obtained from the simulations have been shown to be in consistent with the experimental estimates and the results of previous studies. As a result, it has been revealed that the best mixing balance is provided by the impeller blade at 40 and 50 degrees.

Keywords: Stirred tank, agitator, propeller design, computational fluid mechanics, k-epsilon turbulence model.

1. INTRODUCTION

Mixing is the creation of two or more materials physically or chemically or both ways in order to increase the homogeneity of the mixture. The main purpose of mixing is to increase homogeneity. The devices performing this process are called agitator or mixer (stirred tank). The physical properties and mixing ratios of the materials are one of the most important factors affecting the mixing process. Since the existence of human beings, mixing processes have been continuously investigated and a standard has been tried to be established for the mixtures created. Stirred tanks consist of several pieces of equipment. These parts are a mixer, tank and power mechanism. Depending on the properties of the mixed materials, these tanks may require additional equipment. From past to present, stirred tanks have been diversified according to the physical conditions of the materials (solid, liquid, gas) and the difficulties encountered

* Corresponding author: dealnak@cumhuriyet.edu.tr
[1] Sivas Cumhuriyet University, Faculty of Technology, Department of Manufacturing Engineering, Department of Energy Systems
E-mail: ferhatkoca@cumhuriyet.edu.tr, ytas@cumhuriyet.edu.tr
ORCID: https://orcid.org/0000-0003-0126-1483, https://orcid.org/0000-0001-8849-5295, https://orcid.org/0000-0003-4383-3806

during use have been minimized. Therefore, stirred tanks attract the attention of researchers [1-9]. Naeeni and Pakzad simulated the mixture of liquid-liquid dispersion in their study. They simulated the mixing of water with crude oil by CFD in a tank using a standard Rushton Turbine. Four different types of crude oil and tap water were used in their study. They confirmed that the viscosity increases with the increase of the impeller speed, and the homogeneity increases with the decrease in the size of the droplets [10]. Farhad et al. investigated the effects of impeller type on mixing of high concentration mixtures. They used 3 different propeller types in the study; standard A310 propeller, PF3 propeller and 4 blade propeller. They showed that the most efficient propeller among them is the propeller with 4 blades. They emphasized that the mixture is more homogeneous, more efficient at the same power consumption and more effective in suspending solid particles [11]. Ameur et al. studied the flow patterns of the differences between radial impellers and a Rushton turbine in a cylindrical mixing tank of a viscous Newtonian liquid. They reported that the radial propeller was inefficient at low Re value, the jet became stronger with increasing Re value and thus improved axial circulation was provided. In the fully turbulent regime the radial impeller showed a stronger radial jet flow than the Rushton turbine. They also showed that the Rushton turbine provides a stronger tangential flow compared to the other radial propeller and that it is more efficient and increases the area with increased homogeneity [12]. Gu et al. made a numerical simulation of the new propeller designed by placing a rigid object with a hole between two propellers. In addition, they made comparisons with the models they placed without a rigid body in between and a rigid body without a hole. Of these new propellers designed by researching on various qualities, the one with a perforated rigid body was found to be more efficient, while the one without a hole was found to be more efficient than the system with two propellers [13]. González-Neria et al. compared the PIV and dynamic LES analysis of turbulent flow in a mixing tank mixed by a four-blade propeller with a v-groove. According to the results of the study, the v-grooved propeller showed a higher performance and provided a faster mixing [14]. Wadnerkar et al. conducted and investigated CFD simulation of solid liquid mixing tanks in low to dense solid loading systems. They used cylindrical, flat-bottomed tank with baffles and a six-bladed Rushton turbine. They performed simulations using the euler-euler multiphase model. They stated that there is maximum turbulence kinetic energy in the propeller region. They also stated that as the concentration of the solid increases, the turbulence disappears [15]. Qi et al. conducted a CFD simulation of the particle suspension in the stirred tank. They modeled a tank with baffles using a Smith türbine. k-ε and eulerian-eulerian turbulence model was employed. They saw a region where solid and liquid had low velocity due to the accumulation of solid particles at the bottom of the tank. They said that the effect of higher density and smaller diameter particles on suspension homogeneity is minimized when the particles are placed in a more viscous liquid [16]. Alcamo et al. modeled the turbulent flow in a tank without baffles using LES with Smagorinsky model. They used the standard Rushton turbine as the propeller and ANSYS-CFX 4.4 as the software. They showed that there was a pair of rear vortices known to exist in tanks with baffles and verified in tanks without baffles. They compared the results with the experimental data and showed that they were in consistent [17].

In this study, Rushton turbine stirred tank model with flat bottom, 4 baffles and standard 6 blades was considered. The main research topic is how Rushton turbine blade structure affects the mixing structure when it is inclined 10°, 20°, 30°, 40°, 50°, 60°. In addition, the effect of different angular speeds (600 rpm, 750 rpm and 1000 rpm) on flow characteristics was investigated for each inclined blade structure. ANSYS Fluent 18 commercial software, which is the most preferred CFD program in the literature, was used for the numerical study. The analyzes were provided in the standard k-epsilon (ε) turbulence model. The Multiple Reference Frame (MRF) approach is used to simulate impeller rotation.

2. NUMERICAL WORK AND MATHEMATICAL FORMULAS

The stirred tank configuration used for simulation in this study is same as Torotwa and Ji [18] as shown in Figure 1. The shaft holding the impellers had a diameter of 0.012 m and were positioned concentric to the axis of the tank. Baffles were included in the set-up to prevent the liquid from spinning as a single body. The outline of the experimental tank and the dimensions of the agitation components are shown in Figure 1 and Table 1 respectively.

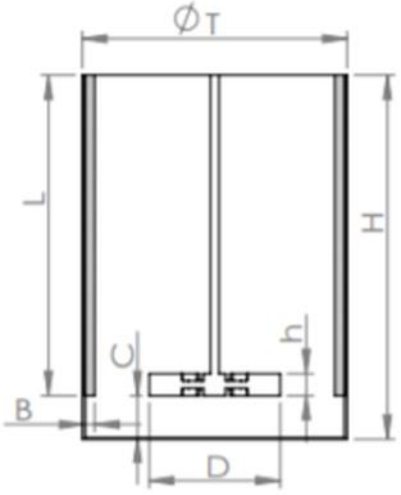

Figure 1 Diagram of the numerical set-up

Table 1 Dimensions of the strirred tank

Parameter	Symbol	Value (mm)
Tank diameter	T	360
Tank height	H	500
Impeller diameter	D=T/2	180
Impeller blade height	H	10
Baffle length	L	440
Baffle width	B=D/12	15
Impeller clearance	C=D/3	60

The Multiple Reference Frame (MRF) motion technique was used to simulation of impeller rotation. In this method, the flow in the impeller region is solved in a rotating framework while the outer region is solved in a stationary reference frame. The boundary of the inner rotating region was positioned from C = 60 mm (where C is the axial distance from the bottom of the vessel) with D = 180 mm. The Enhanced Wall Treatment function was chosen to enhance the solution by giving advantage for selected RPM (600, 750, 1000) and fine meshes. The simulation was performed using CFD software Ansys Fluent 18 solver where a control-volume-based technique was used to convert the general scalar transport equations to algebraic equations and then solved numerically using the pressure-based solver with segregated algorithm. Simulations were performed using the "COUPLED" scheme to model the Pressure-Velocity coupling, the "PRESTO! (Pressure Staggering Option)" to model the pressure and the "Second Order Upwind" scheme for the momentum, turbulent kinetic energy and turbulent dissipation rate. A maximum convergence criterion of 10-6 was set for the simulation and the case was conducted steady. The total simulation time for each case was around 30 h and residual target of 10-4 was reached within 5000 iterations. Flow behavior inside stirred tank is solved by discretized governing equations. The governing equations are the Navier–Stokes equations, which solve the mass and momentum conservation equations and provide solution for flow variables such as velocity and pressure. The continuity or mass conservation equation is given by

Continuity equation

$$\frac{\partial \bar{u}}{\partial x}+\frac{\partial \bar{v}}{\partial y}+\frac{\partial \bar{w}}{\partial z}=0 \tag{1}$$

Momentum equation

x direction momentum equation

$$\left[\bar{u}\frac{\partial \bar{u}}{\partial x}+\frac{\partial \overline{(u')^2}}{\partial x}\right]+\left[\bar{v}\frac{\partial \bar{u}}{\partial y}+\frac{\partial \overline{(u'v')}}{\partial y}\right]+\left[\bar{w}\frac{\partial \bar{u}}{\partial z}+\frac{\partial \overline{u'w'}}{\partial z}\right]=-\frac{1}{\rho}\frac{\partial \bar{p}}{\partial x}+\nu\left(\frac{\partial^2 \bar{u}}{\partial x^2}+\frac{\partial^2 \bar{u}}{\partial y^2}+\frac{\partial^2 \bar{u}}{\partial z^2}\right) \tag{2}$$

y direction momentum equation

$$\left[\bar{u}\frac{\partial \bar{v}}{\partial x}+\frac{\partial \overline{(v')^2}}{\partial x}\right]+\left[\bar{v}\frac{\partial \bar{v}}{\partial y}+\frac{\partial \overline{(v'v')}}{\partial y}\right]+\left[\bar{w}\frac{\partial \bar{v}}{\partial z}+\frac{\partial \overline{v'w'}}{\partial z}\right]=-\frac{1}{\rho}\frac{\partial \bar{p}}{\partial y}+\nu\left(\frac{\partial^2 \bar{v}}{\partial x^2}+\frac{\partial^2 \bar{v}}{\partial y^2}+\frac{\partial^2 \bar{v}}{\partial z^2}\right) \tag{3}$$

z direction momentum equation

$$\left[\bar{u}\frac{\partial\bar{w}}{\partial x}+\frac{\partial\overline{(w')^2}}{\partial x}\right]+\left[\bar{v}\frac{\partial\bar{w}}{\partial y}+\frac{\partial\overline{(w'v')}}{\partial y}\right]+\left[\bar{w}\frac{\partial\bar{w}}{\partial z}+\frac{\partial\overline{w'w'}}{\partial z}\right]=-\frac{1}{\rho}\frac{\partial\bar{p}}{\partial z}+\nu\left(\frac{\partial^2\bar{w}}{\partial x^2}+\frac{\partial^2\bar{w}}{\partial y^2}+\frac{\partial^2\bar{w}}{\partial z^2}\right) \quad (4)$$

Simulation was employed using realizable Reynolds-Averaged Navier-Stokes (RANS) k–ε model for single-phase. The reason for applying the RANS-based solution model is its advantageous use in terms of computer hardware, human effort and computation time compared to DNS or LES models. The fluid in the tank was assumed to be homogeneous and incompressible, and that the various components of the fluid had the same velocity distribution, pressure and flow pattern. The realizable k-ε model was used to specify the characteristics of turbulence and determine the basis of flow phenomena by the following equations.

The steady flow turbulance kinetic energy equation

$$\frac{\partial(\rho uk')}{\partial x}+\frac{\partial(\rho vk')}{\partial y}+\frac{\partial(\rho wk')}{\partial z}=\frac{\partial}{\partial x}\left(\frac{\mu_t}{\sigma_k}\frac{\partial k'}{\partial x}\right)+\frac{\partial}{\partial y}\left(\frac{\mu_t}{\sigma_k}\frac{\partial k'}{\partial y}\right)+\frac{\partial}{\partial z}\left(\frac{\mu_t}{\sigma_k}\frac{\partial k'}{\partial z}\right)+\mu_t\phi-\rho\varepsilon \quad (5)$$

Turbulance viscosity

$$\mu_t=C_{\mu'}\rho\frac{k'^2}{\varepsilon} \quad (6)$$

the k-ε turbulance model used in the present study, ε indicates turbulance distribution while k' and ϕ show turbulance kinetic energy and viscous dissipation term, respectively.

Turbulance kinetic energy

$$k'=\frac{1}{2}\left(\overline{u'^2}+\overline{v'^2}+\overline{w'^2}\right) \quad (7)$$

Viscous dissipation term

$$\phi=2\mu\left[\left(\frac{\partial u}{\partial x}\right)^2+\left(\frac{\partial v}{\partial y}\right)^2\right]+\mu\left(\frac{\partial v}{\partial x}+\frac{\partial u}{\partial y}\right)^2 \quad (8)$$

Turbulence kinetic energy disappearance equation

$$\frac{\partial(\rho u\varepsilon)}{\partial x}+\frac{\partial(\rho v\varepsilon)}{\partial y}+\frac{\partial(\rho w\varepsilon)}{\partial z}=\frac{\partial}{\partial x}\left(\frac{\mu_t}{\sigma_\varepsilon}\frac{\partial\varepsilon}{\partial x}\right)+\frac{\partial}{\partial y}\left(\frac{\mu_t}{\sigma_\varepsilon}\frac{\partial\varepsilon}{\partial y}\right)+\frac{\partial}{\partial z}\left(\frac{\mu_t}{\sigma_\varepsilon}\frac{\partial\varepsilon}{\partial z}\right)+C_{1\varepsilon}\mu_t\frac{\varepsilon}{k'}\phi-C_{2\varepsilon}\rho\frac{\varepsilon^2}{k'} \quad (9)$$

C_μ, $C_{1\varepsilon}$, $C_{2\varepsilon}$, σ_k and σ_ε that are model constants are typical default values used in the standard k-ε turbulence model [19]. The values of these constants have provided by numerous data fitting iterations for many turbulent flows.

3. MODELS

In the study, numerical studies were carried out using the Rushton turbine model. 6 propeller blades were used in the main model, which was determined as straight model, and 4 baffles were placed in the stirred tank. The selected tank model is in the form of a flat bottom cylindrical container. The results were obtained by giving angles (10°, 20°, 30°, 40°, 50°, 60°) to the propeller blades used in the flat model. The obtained results were compared with each other. These results at different rotation speeds (600 rpm, 750 rpm, 1000 rpm) were repeated for the model at each angle created. Models are shown in Figure 2.

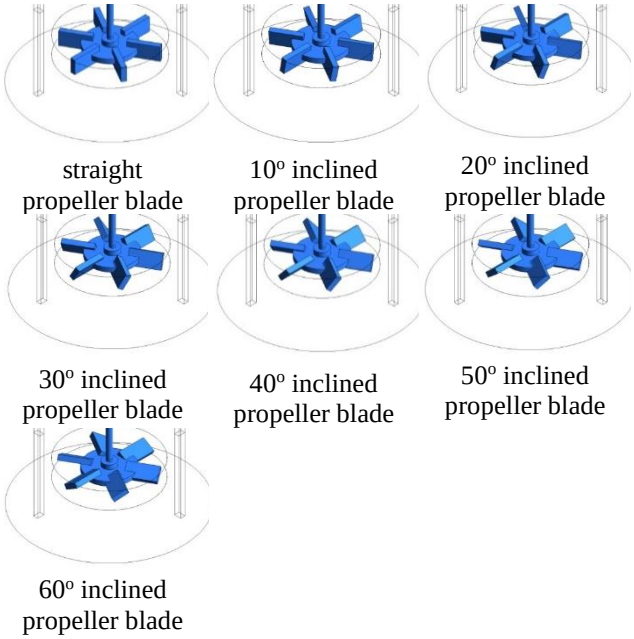

Figure 2 View of the propeller models used in the study

4. MESH STRUCTURE

Hybrid mesh structure is used in the study. The total mesh number of the model was chosen as 922973 pieces. 4 different mesh numbers counted for mesh independence were determined as reference. Evaluated mesh numbers and evaluation parameter (pressure) variation are given in Table 2.In the comparison of these reference mesh numbers, when the selected mesh number was exceeded, no change was observed in the results.

Tablo 2 Pressure variation according to the number of mesh elements

Element Nu.	**510363**	**751655**	**922973**	**1205030**
P (Pa)	7850	7920	8000	8010

The mesh structure of the model is shown in Figure 3. A 20-layer mesh structure was applied on the wing surfaces, baffle surfaces and tank interior surfaces, where the fluid's non-slip condition occurs and where the most interaction occurs, and a finer mesh is formed in the areas close to these surfaces. The applied mesh structures were analyzed in the same and approximate number of elements in all models.

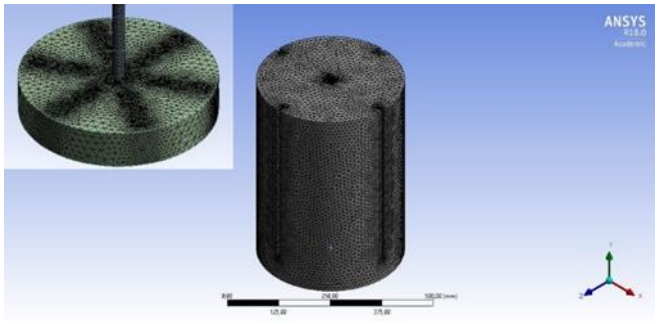

Figure 3 Structural view of mesh structure

Before the mixing simulations, it is also necessary to confirm the validity of the CFD model used in this work for stirred tank systems. The predicted results were verified by the numerical data of Duan et al. As seen from Figure 4, the predicted radial and axial profiles of azimuthally-averaged velocity components of the liquid is close to the numerical data of Duan et al. [20] respectively. The present study curve shown with the dotted line is in consistent with the work of Duan et al. shown straight line.

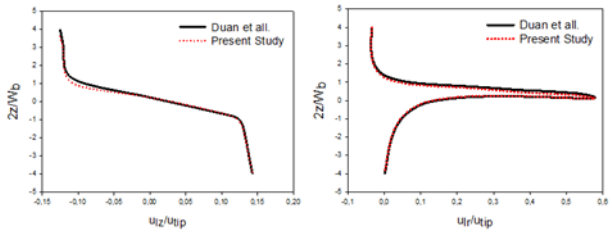

Figure 4 Comparison numerical datas with the study of Duan et al. [20]

5. RESULT

Numerical results were obtained at 600 rpm, 750 rpm and 1000 rpm turbine rotation speeds for different blade angles. Turbulence kinetic energy distributions and velocity vectors obtained for the propellers rotated at 600 rpm are given in Figure 5 for straight blade, 10° inclined blade, 20° inclined blade, 30° inclined blade, 40° inclined blade, 50° inclined blade and 60° inclined blade, respectively.

When these figures are examined, it is seen that the turbulence kinetic energy values are high at the blade tips. The formation of turbulence and flow eddies behind the blades causes the flow not to occur in those regions or to occur partially. Therefore, in these regions where the flow decreases, the decrease in inertia forces and the coincidence of the reverse flow reflected from the wall due to the effect of the baffles increased the turbulent kinetic energy. In addition, it is clearly seen in these figures that the turbulent kinetic energy is higher in the regions close to the propeller blades. Also in this rotation speed (600 rpm), although the highest instantaneous changes of turbulence kinetic energies are observed in straight blade compared to other structures, it can be observed the highest value at the models with inclination of 40° and 50° throughout the tank. In general, it is seen that the impeller with the lowest turbulence kinetic energy throughout the tank are 10° and 60° inclined blades. When the figures are examined, it is obvious that there are regions where the flow of change consisting of velocity vectors accelerates, the vicinity of the blades and the regions close to the tank walls. The reason for this event is the increase in the pressure applied to the blade with the swirling movements on the flow created by the blades, and also the points where the opposite flows hitting the tank walls

intersect with the flows from the blade. It is observed that the velocity vectors make eddies around the blades. The reason for this is the swirling movements created by the blades on the flow, and the points where the opposite flows which hit the tank walls, intersect with the flows from the blade, with the increase of the pressure applied to the blade.

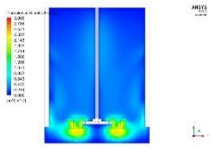
straight propeller blade (TKE)

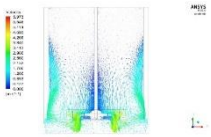
straight propeller blade (velocity vectors)

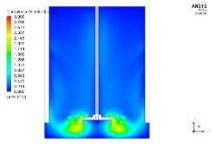
10º inclined propeller blade (TKE)

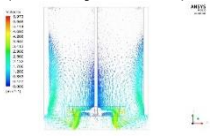
10º inclined propeller blade (velocity vectors)

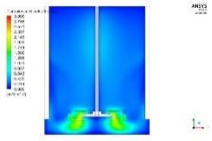
20º inclined propeller blade (TKE)

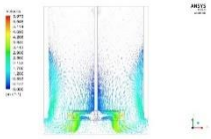
20º inclined propeller blade (velocity vectors)

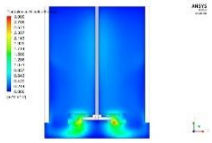
30º inclined propeller blade (TKE)

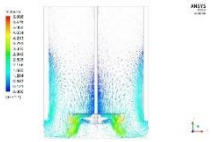
30º inclined propeller blade (velocity vectors)

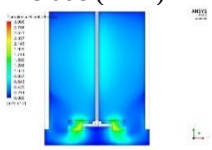
40º inclined propeller blade (TKE)

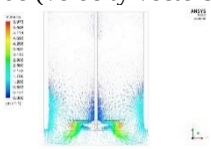
40º inclined propeller blade (velocity vectors)

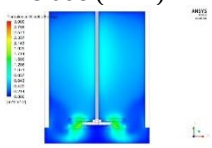
50º inclined propeller blade (TKE)

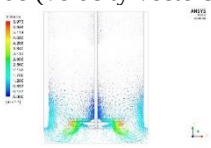
50º inclined propeller blade (velocity vectors)

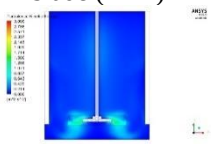
60º inclined propeller blade (TKE)

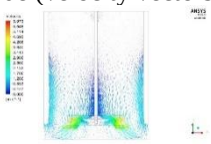
60º inclined propeller blade (velocity vectors)

Figure 5 Model blades at 600 rpm (a) turbulence kinetic energy distribution (b) velocity vectors

Turbulence kinetic energy distributions and velocity vectors obtained for the propellers rotated at 750 rpm are given in Figure 6 for straight blade, 10° inclined blade, 20° inclined blade, 30° inclined blade, 40° inclined blade, 50° inclined blade and 60° inclined blade, respectively. When these figures are examined, it is seen that turbulence kinetic energy values are high at the blade tips, as in the visuals examined at 600 rpm. Vortex movements around the wing can be seen from the results where turbulent kinetic energy and velocities are high. It is observed that the flow changes direction due to the vortex movements in the regions between the blade and the tank bottom. According to the data obtained, it is seen that the maximum turbulence kinetic energy at 600 rpm increased from 3000 m2/s2 to 6000 m2/s2 at 750 rpm. Likewise, looking at the velocity vectors, it was observed that the maximum speed increased from 5,973 m/s to 15,071 m/s. It can be said that, with the increase in speed, the mixture achieves better results and therefore the mixture becomes more homogeneous compared to the mixes at 600 rpm.

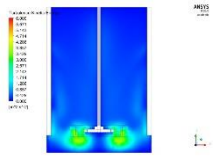
straight propeller blade (TKE)

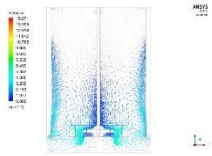
straight propeller blade (velocity vectors)

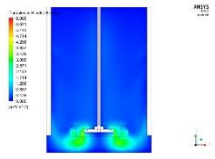
10º inclined propeller blade (TKE)

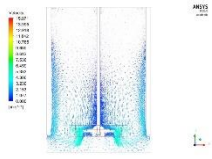
10º inclined propeller blade (velocity vectors)

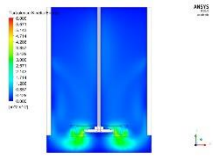
20º inclined propeller blade (TKE)

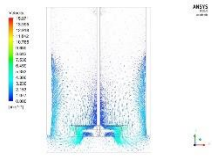
20º inclined propeller blade (velocity vectors)

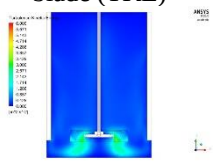
30º inclined propeller blade (TKE)

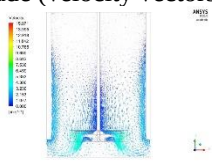
30º inclined propeller blade (velocity vectors)

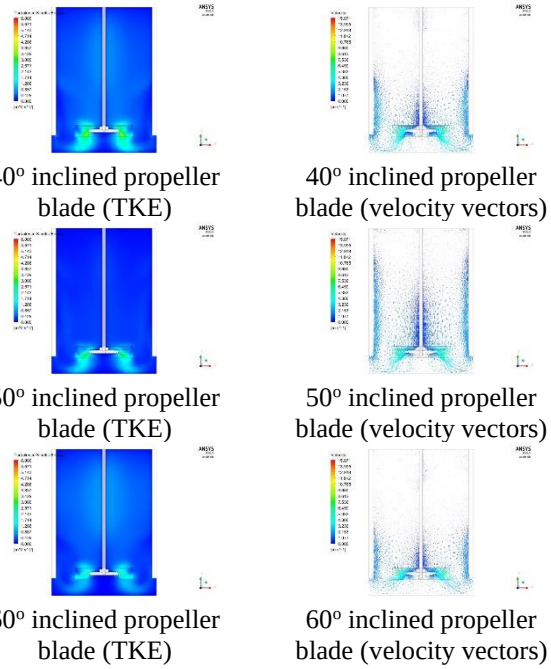

Figure 6 Model blades at 750 rpm (a) turbulence kinetic energy distribution (b) velocity vectors

Turbulence kinetic energy distributions and velocity vectors obtained for the propellers rotated at 1000 rpm are given in Figure 7 for straight blade, 10° inclined blade, 20° inclined blade, 30° inclined blade, 40° inclined blade, 50° inclined blade and 60° inclined blade, respectively. When these figures are examined, it is seen that turbulence kinetic energy values are high at the blade tips, as in the visuals examined in 600 and 750 rpm. According to the data obtained, it is seen that the maximum turbulence kinetic energy reaches 9000 m2/s2 at 1000 rpm. Looking at the velocity vectors, it was observed that the maximum velocity increased to 20000 m/s. It is more possible to say that the mixture is better with the increase in impeller speed by looking at the values of turbulence kinetic energy and flow velocities obtained. As with other impeller speed, turbulence kinetic energy is observed to be highest in 40° and 50° inclined blade while the lowest levels in the straight and 10° inclined blade throughout the tank.

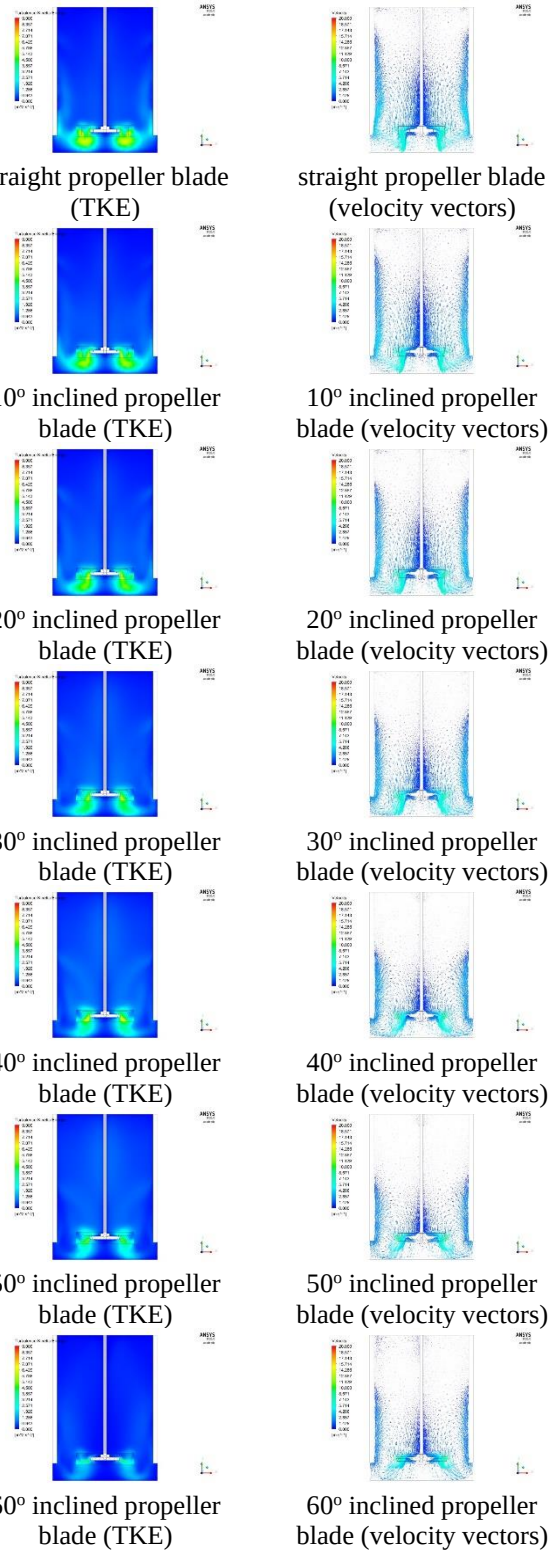

Figure 7 Model blades at 1000 rpm (a) turbulence kinetic energy distribution (b) velocity vectors

The results obtained were compared according to the pressure, turbulence kinetic energy and velocity vectors with respect to the x and y plane. The results for comparison are the data taken from the x and y plane as shown in Figure 8.

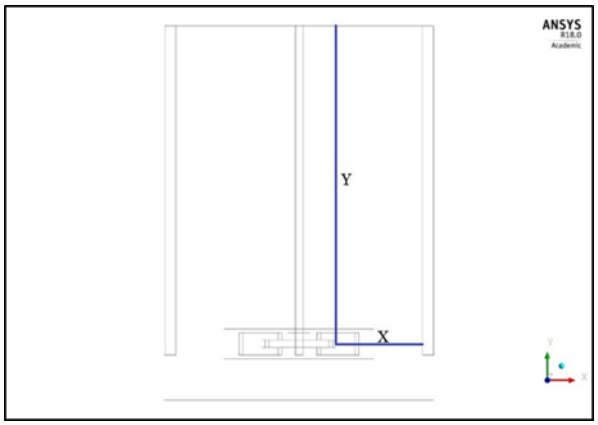

Figure 8 View of the x and y plane evaluated for comparison.

The comparison of the pressure, turbulence kinetic energy and velocity graphs of different propeller models at 600 rpm, respectively, with reference to the x and y plane in Figure 8, is shown in Figure 9. When looked at the x-plane of the pressure graphs in Figure 9a, it was observed that the pressure towards the tank surfaces increased.

Similarly, when the y-plane pressure graphs are examined in Figure 9a, the curves including the pressure created by the straight blade follow a linear path in all blade types. While the pressure of the straight blade towards the upper point of the tank is around 8 kPa, this pressure value decreases as the angle of the other wings increases. The high pressure increases the power consumed for mixing, therefore the highest power consumption requirement was seen in the flat blade here. It is clearly seen from the pressure graphs that at the 60° inclined propeller blade where the pressure is the lowest, lower power consumption will occur.

The change of turbulence kinetic energy along the x and y axis is given in Figure 9b. It is seen that the turbulent kinetic energy decreases from the center to the edges on the x axis. In the y plane, it can be said that the turbulence kinetic energy towards the upper surface of the tank is stable up to a certain level except for the blades inclined 40° and 50°. However, it is possible to say that the 40° and 50° inclined blades generally increase the turbulence kinetic energy in the tank at this point and reach higher levels compared to all other blade models. This increase in kinetic energy shows that turbulence is greater throughout the tank, and therefore blades with 40° and 50° inclinations provide a more homogeneous mixture than straight and other inclined blades. The opposite situation occurs with 10° and 60° inclined blades.

Velocity graphs in x and y axes for 600 rpm are given in Figure 9c. In the x-plane, there was a drop after the effects of the turbulence created behind the blades, and a sudden increase immediately after the fall due to the effect of baffles and reserve flows returning from the tank walls. In the y plane towards the top of the tank; It is seen that the flow velocities in 10 ° inclined and straight blades are higher than the other blades.

The comparison of the pressure, turbulence kinetic energy and velocity graphs of different propeller models at 750 rpm, respectively, with reference to the x and y plane in Figure 8, is shown in Figure 10. The graphics are like at 600 rpm, but the values have increased.

The comparison of the pressure, turbulence kinetic energy and velocity graphs of different propeller models at 1000 rpm, respectively, with reference to the x and y plane in Figure 8, is shown in Figure 11. The graphics are like at 600 rpm and 750 rpm, but the values have increased.

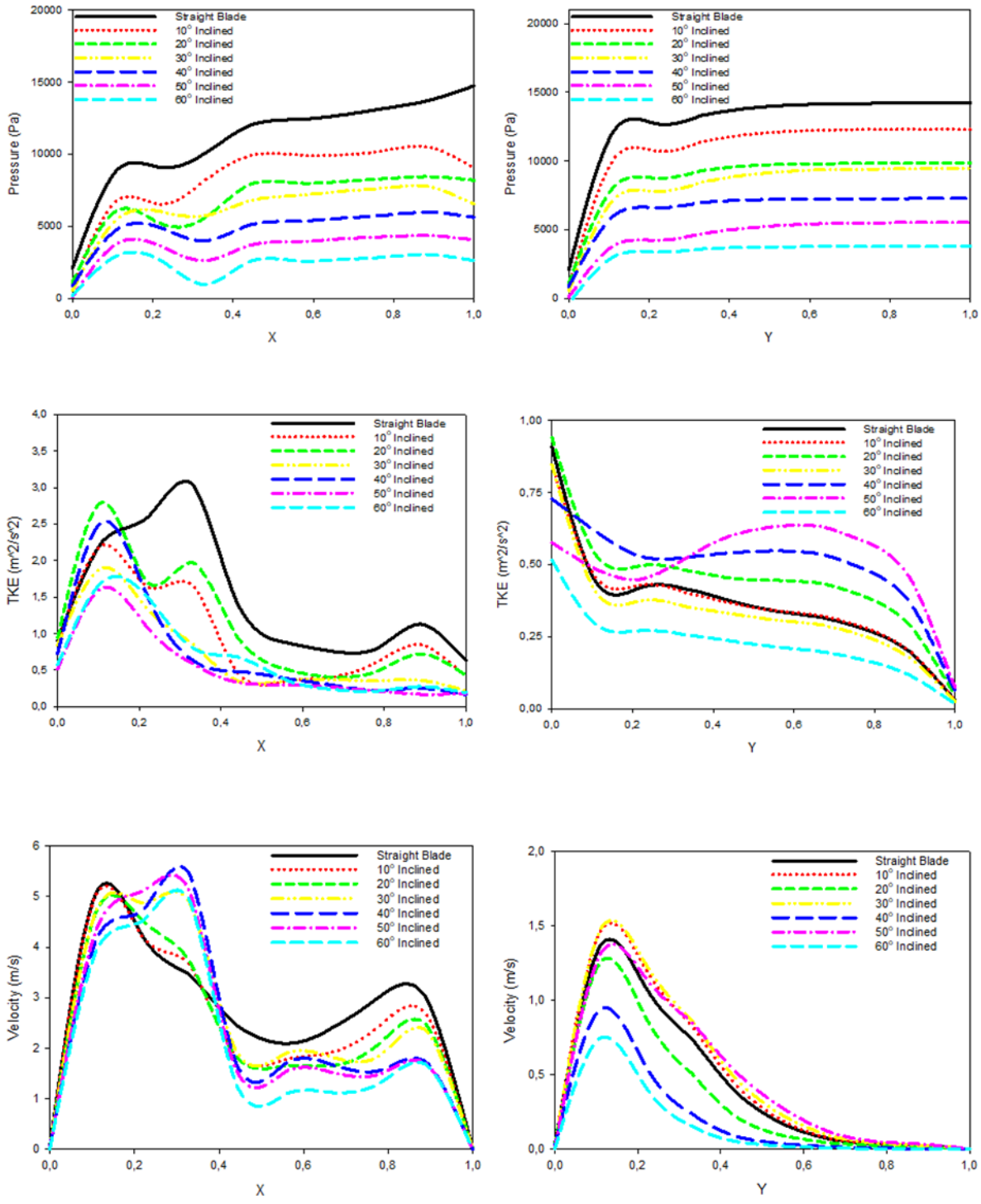

Figure 9 Comparison of a) pressure b) TKE c) velocity graphs in the x and y plane at 600 rpm

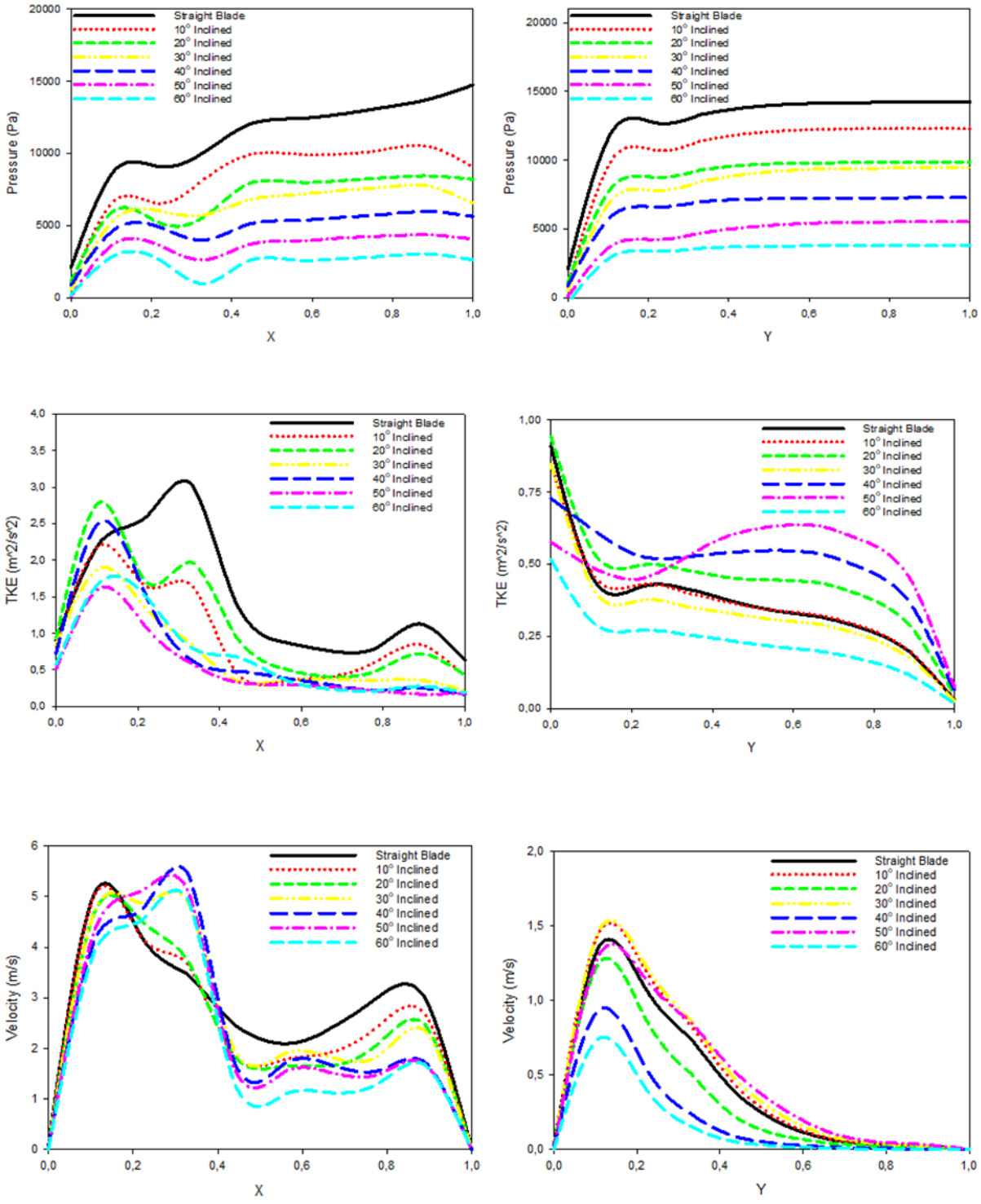

Figure 10 Comparison of a) pressure b) TKE c) velocity graphs in the x and y plane at 750 rpm

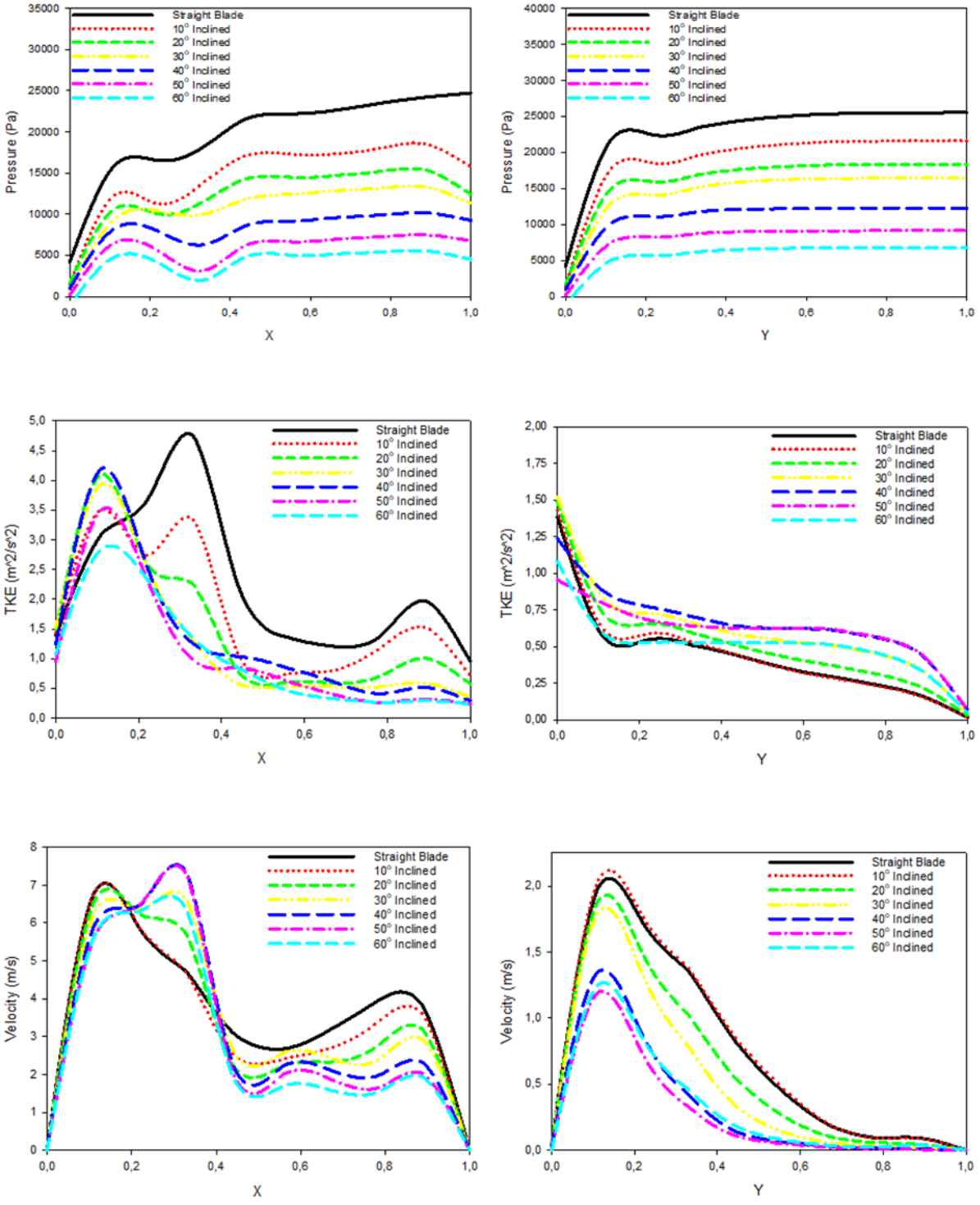

Figure 11 Comparison of a) pressure b) TKE c) velocity graphs in the x and y plane at 1000 rpm

6. CONCLUSİON

In this study, propeller blade types with straight, 10° inclined, 20° inclined, 30° inclined, 40° inclined, 50° inclined and 60° inclined were analyzed numerically.

As a result of the investigation of all the case, it was concluded that the increase in the impeller rotation speed increased the power consumption according to the pressure graphs, but on the other hand, it increased the homogeneity according to the turbulence kinetic energy values. It can be the most accurate result to decide by looking at the material to be used, the power requirement and

the place in the application for the selection of the most suitable rotation speeds.

All of the results showed that increasing the angle of inclination reduced power consumption. The power consumption required by the blades can be listed as high to low straight, 10° inclined, 20° inclined, 30° inclined, 40° inclined, 50° inclined and 60° inclined blades. However, the most effective blade profiles in order to ensure mixture homogeneity have come to the fore as 40° and 50° inclined blades with higher turbulence kinetic energy.

The comparison was made by considering all blade structures and all rotation speeds, the highest turbulence kinetic energy change was seen on the blade 40° inclined in the x and y axis. Although it is concluded that the lowest pressure and therefore the least power consumption are in the blade inclined at 60°, it has been revealed that the turbulent kinetic energy changes cannot provide a homogeneous mixture. However, by comparing the pressure changes, kinetic energy changes and flow rates together, it was concluded that the ideal model was the propeller blade 40° and 50° inclined.

Nomenclature (Word Style TS Strong)

b Baffle width (m)

D Impeller diameter (m)

H Impeller distance from bottom of vessel (m)

g Acceleration due to gravity (m/s-2)

H Total liquid depth (m)

k Turbulent kinetic energy (m2/s-2)

L Length of blades on impeller (m)

m Rotating domain height (m)

M Rotating domain diameter (m)

n Impeller speed (s-1)

p Pressure (N.m-2)

s Clearance of baffle from wall (m)

T Inside diameter of stirred tank (m)

u Flow velocity in rotating frame (m/s-1)

v Flow velocity (m/s-1)

W Width of blades on impeller (m)

x, y, z Cartesian coordinates

Greek Symbols

μ Dynamic viscosity (m2/s-1)

ω Angular velocity (rad/s-1)

Funding

There is no financial support.

Declaration of Competıng Interests

The authors declare no competing financial interests.

REFERENCES

[1] J. Scully and P. Frawley, “Computational Fluid Dynamics Analysis of the Suspension of Nonspherical Particles in a Stirred Tank,” Ind. Eng. Chem. Res., vol. 50, pp. 2331–2342, 2011.

[2] F. Laurenzi, M. Coroneo, G. Montante, A. Paglianti, and F. Magelli, “Experimental and computational analysis of immiscible liquid – liquid dispersions in stirred vessels,” Chem. Eng. Res. Des., vol. 7, no. October 2008, pp. 507–514, 2009.

[3] E. S. Szalai, P. Arratia, K. Johnson, and F. J. Muzzio, “Mixing analysis in a tank stirred with Ekato Intermig J impellers,” Chem. Eng. Sci., vol. 59, pp. 3793–3805, 2004.

[4] C. P. K. Dagadu, Z. Stegowski, B. J. A. Y. Sogbey, and S. Y. Adzaklo, “Mixing Analysis in a Stirred Tank Using Computational Fluid Dynamics,” J. Appl.

Math. Phys., vol. 3, no. June, pp. 637–642, 2015.

[5] V. I. Bykov and S. B. Tsybenova, "Parametric Analysis of the Continuous Stirred Tank Reactor Model," Theor. Found. Chem. Eng., vol. 37, no. 1, pp. 59–69, 2003.

[6] S. K. Naeeni and L. Pakzad, "Chemical Engineering Research and Design Experimental and numerical investigation on mixing of dilute oil in water dispersions in a stirred tank," Chem. Eng. Res. Des., vol. 147, pp. 493–509, 2019.

[7] S. Hosseini, D. Patel, F. Ein-mozaffari, and M. Mehrvar, "Study of Solid - Liquid Mixing in Agitated Tanks through Computational Fluid Dynamics Modeling," Ind. Eng. Chem. Res., vol. 49, pp. 4426–4435, 2010.

[8] J. Aubin, D. F. Fletcher, and C. Xuereb, "Modeling turbulent flow in stirred tanks with CFD : the influence of the modeling approach , turbulence model and numerical scheme," Exp. Therm. Fluid Sci., vol. 28, no. 2004, pp. 431–445, 2006.

[9] C. A. Coulaloglou and T. L, L, "Description Of Interaction Processes In Agitated Liquid-Liquid Dispersions," Chem. Eng. Sci., vol. 32, pp. 1289–1297, 1977.

[10] S. K. Naeeni and L. Pakzad, "Droplet size distribution and mixing hydrodynamics in a liquid – liquid stirred tank by CFD modeling," Int. J. Multiph. Flow, vol. 120, 2019.

[11] A. Kazemzadeh, F. Ein-mozaffari, and A. Lohi, "Particuology Effect of impeller type on mixing of highly concentrated slurries of large particles," Particuology, vol. 50, pp. 88–99, 2020.

[12] H. Ameur, Y. Kamla, and D. Sahel, "Data on the agitation of a viscous Newtonian fl uid by radial impellers in a cylindrical tank," Data Br., vol. 15, pp. 752–756, 2017.

[13] D. Gu, Z. Liu, Z. Xie, J. Li, C. Tao, and Y. Wang, "Numerical simulation of solid-liquid suspension in a stirred tank with a dual punched rigid-flexible impeller," Adv. Powder Technol., vol. 28, no. 10, pp. 2723–2734, 2017.

[14] I. González-neria et al., "PIV and dynamic LES of the turbulent stream and mixing induced by a V- grooved blade axial agitator," Chem. Eng. J., vol. 374, no. June, pp. 1138–1152, 2019.

[15] D. Wadnerkar, R. P. Utikar, M. O. Tade, and V. K. Pareek, "CFD simulation of solid – liquid stirred tanks," Adv. Powder Technol., vol. 23, pp. 445–453, 2012.

[16] N. Qi, H. Zhang, K. Zhang, G. Xu, and Y. Yang, "CFD simulation of particle suspension in a stirred tank," Particuology, vol. 11, no. 3, pp. 317–326, 2013.

[17] R. Alcamo, G. Micale, F. Grisafi, A. Brucato, and M. Ciofalo, "Large-eddy simulation of turbulent flow in an unbaffled stirred tank driven by a Rushton turbine," Chem. Eng. Sci., vol. 60, pp. 2303–2316, 2005.

[18] C. J. Ian Torotwa, "A Study of the Mixing Performance of Different Impeller Designs in Stirred Vessels Using Computational Fluid Dynamics," Designs, vol. 2, no. 10, 2018.

[19] Fluent Inc. Lebanon, FLUENT User's Guide. Netherland, 2003.

[20] X. Duan, X. Feng, C. Peng, C. Yang, and Z. Mao, "Numerical simulation of micro-mixing in gas – liquid and solid – liquid stirred tanks with the coupled CFD-E-model," Chinese J. Chem. Eng., vol. 28, no. 9, pp. 2235–2247, 2020.

SAKARYA ÜNİVERSİTESİ
FEN BİLİMLERİ ENSTİTÜSÜ DERGİSİ

Sakarya University Journal of Science
SAUJS

e-ISSN 2147-835X Period Bimonthly Founded 1997 Publisher Sakarya University
http://www.saujs.sakarya.edu.tr/

Title: Performance of Gas-phase Toluene by Adsorption onto Activated Carbon Prepared from Robinia pseudoacacia L. as Lignocellulosic Material

Authors: Kaan IŞINKARALAR

Recieved: 2021-12-30 00:00:00

Accepted: 2022-04-05 00:00:00

Article Type: Research Article

Volume: 26
Issue: 2
Month: April
Year: 2022
Pages: 410-420

How to cite
Kaan IŞINKARALAR; (2022), Performance of Gas-phase Toluene by Adsorption onto Activated Carbon Prepared from Robinia pseudoacacia L. as Lignocellulosic Material. Sakarya University Journal of Science, 26(2), 410-420, DOI: 10.16984/saufenbilder.1051342
Access link
https://dergipark.org.tr/tr/journal/1115/issue/69580/1051342

New submission to SAUJS
http://dergipark.gov.tr/journal/1115/submission/start

Sakarya University Journal of Science 26(2), 410-420, 2022

Performance of Gas-phase Toluene by Adsorption onto Activated Carbon Prepared from *Robinia pseudoacacia* L. as Lignocellulosic Material

Kaan IŞINKARALAR*[1]

Abstract

The main target of this study was to eliminate gas-phase toluene with activated carbon from indoor air. The activated carbons were prepared from *Robinia pseudoacacia* L. biomass under different conditions. The change in surface functional groups of the activated carbon biomass raw material produced by pyrolysis in the absence of oxygen at 500–900 °C and activation by potassium hydroxide (KOH). The highest surface area of 1271.3 m^2/g gives reason for its external porous surface. The surface porosity and the graphite properties of the prepared KN_xACs were detected by scanning electron microscope (SEM). The amount of adsorbed toluene (C_7H_8) was determined using a gas chromatograph-mass spectrometry with a thermal desorber system (TD–GC–MS) on the KN_xAC surface. The toluene adsorption capacity was reached 111 mg/g at 25 °C and 1000 ppm. As a result, the study revealed that the prepared $KN_{24}AC$ from the *Robinia pseudoacacia* L. biomass has the best adsorption capacity of gas-phase toluene from indoor air.

Keywords: Activated carbon, lignocellulosic material, indoor air quality, toluene removal

1. INTRODUCTION

Volatile organic compounds (VOCs) have high vapor pressure easily releasable to indoor air [1-3]. Toluene (C_7H_8) is commonly found in indoor air as VOC, affecting human health [4-6]. It is prevalent in the synthesis of chemicals, petroleum refining, wood goods, and several industries' activities [7-9]. The gas-phase toluene can cause several problems, such as photochemical smog in the winter season, adverse effects on plants, and human diseases (respiratory, nervous, etc.) [10-13]. The availability of toluene in industrial air is less than 265.76 ppm, although many industrial processes cause to limit the excess of this value [14]. World Health Organization (WHO) reported that the concentration of toluene should not exceed 53.15-106.3 ppm due to adverse effects on human health. According to the Bureau of Indian Standards (BIS) should be 200 ppm for the threshold limit of intake. On average, an employee is exposed to approximately 200 ppm for 8 hours a day in offices, industries, etc. Therefore, removing gas-phase toluene from indoor air is crucial to block its adverse impact on indoor air quality [15-18].

There are various methods in use to remove gaseous pollutants, such as physical (absorption and adsorption), chemical (scrubbing and oxidation), and biological (bio-filter and bio-scrubbing) ways [19-21]. Among them,

* Corresponding author: kisinkaralar@kastamonu.edu.tr
[1] Kastamonu University, Faculty of Engineering and Architecture, Department of Environmental Engineering
ORCID: https://orcid.org/0000-0003-1850-7515

adsorption has been widely used to remove VOCs from the air [22-24]. The advantages of adsorption are included low operational cost, easy accessibility of used materials, sometimes reusability, and high removal efficiency [25]. In particular, the performance of adsorption can easily increase the efficiency with adsorbate structure and properties [26]. The most widely used adsorbate is activated carbon with numerous pore sizes (including micro and macropores) [27]. Carbon-based adsorbents' efficiency and success in removing VOCs have made them more familiar and preferable materials [28]. The most distinctive feature of a high affinity is the result of the interaction of the non-polar adsorbent and the adsorbate [29]. For the adsorption process to work with high efficiency, it aims to develop the raw material and production method of the adsorbent. Thanks to this, it has an important place in the adsorption of gases due to obtaining a high surface area and improving the micropore volume.

Lignocellulosic materials such as *Tamarix hispida, Diplotaxis harra, Glebionis coronaria* L., apricot kernels, date palm seed, and coconut shells are plentiful, and many investigations have been used to prepare activated carbon [30-35]. Many raw materials have been employed to manufacture diverse materials due to their lignocellulosic biomass [36-38]. The *Robinia pseudoacacia* L. (Fabaceae) was preferred because it is widely spread in warm climates and the wet forests zone of Anatolia, Türkiye. This plant's fresh form is beneficial for many disorders since it contains polyholosides, phonolic, nitrogenous, sesquiterpenes, steroids, lipids, and minerals [39]. Also, this plant is abundant in the environment as a lignocellulosic waste.

The purpose of the paper was to use activated carbon from *Robinia pseudoacacia* L. biomass as lignocellulosic waste to eliminate gas-phase toluene with various concentrations. The produced activated carbons were also determined physicochemical properties. The removal efficiency of different concentrations of toluene, which is commonly found in the outdoor and indoor environment, with carbon-based adsorbent was investigated.

2. MATERIAL AND METHOD

2.1. Materials

All used chemicals were analytical grade, potassium hydroxide (KOH from Merck, Germany), toluene (C_7H_8, >99.9% from Sigma–Aldrich), BTEX standard solution (Ultra Scientific brand Aromatic Hydrocarbons Mixture DWM-550-1). The chemicals used in the study were used without any purification process and without allowing them to deteriorate in their pure form. The precise weighing of the samples was accomplished by Adam PW 21, England.

2.2. Production of the KN_xAC

The stems of *Robinia pseudoacacia* L. were used as a precursor for activated carbon. It was collected from Kastamonu, Türkiye, in September 2021 and dried for two months at room temperature until not damp. After the drying process, these plants were cut into very small particles (range of 1-4 cm). They were sent to ball-milling and sieved for 63-250 μm fine powder. KOH impregnated all samples in the ratio of 0.5:1, 1:1, 2:1, 3:1, and 4:1 w/w for 24 h at room temperature. They were washed with deionized water until pH was neutral to remove any remaining chemicals.

The neutral samples were dried at 105°C overnight and stored in a desiccator for characterization. The temperature ranges studied in the carbonization process are between 500-900 ^oC for 1.5 h under nitrogen gas (N_2) using a reactor which was put raw material ($W_{raw\ material}$) in high-temperature resistant steel material. The produced ($W_{produced}$) activated carbons were coded in Table 1 and calculated its yield percentage in Equation (1).

$$Yield\ of\ AC = \left(\frac{W_{produced}}{W_{raw\ material}}\right) x100 \quad (1)$$

Table 1 Identifications of KNACs

Sample ID	Impregnation ratio wt%	Activation temperature °C
KN_1AC	0.5:1	500
KN_2AC	0.5:1	600
KN_3AC	0.5:1	700
KN_4AC	0.5:1	800
KN_5AC	0.5:1	900
KN_6AC	1:1	500
KN_7AC	1:1	600
KN_8AC	1:1	700
KN_9AC	1:1	800
$KN_{10}AC$	1:1	900
$KN_{11}AC$	2:1	500
$KN_{12}AC$	2:1	600
$KN_{13}AC$	2:1	700
$KN_{14}AC$	2:1	800
$KN_{15}AC$	2:1	900
$KN_{17}AC$	3:1	600
$KN_{18}AC$	3:1	700
$KN_{19}AC$	3:1	800
$KN_{20}AC$	3:1	900
$KN_{21}AC$	4:1	500
$KN_{22}AC$	4:1	600
$KN_{23}AC$	4:1	700
$KN_{24}AC$	4:1	800
$KN_{25}AC$	4:1	900

2.3. Characterization of KNAC

The KN_xAC samples were taken from the desiccator. They carried out surface area and pore size distribution by the Brunauer–Emmett–Teller (BET) method using Quantachrome Autosorb automated gas sorption analyzer (NOVA 2200e). All characterization processes were applied to KN_xAC samples and raw material.

2.4. Gas-phase Toluene Adsorption Experiment

The experimental setup for gas-phase toluene adsorption was operated with KN_xACs. Air vacuum pump widely used in gas experiments (SKC The AirChek XR5000), a gas flow meter for a flow rate adjustment, Tenax TA sorbent in tubes for accumulation of toluene, and a reactor from quartz reactor, which the filled KN_xACs. Before the experiments, the system with different volumes was run uninterruptedly to determine the initial conditions (C_o). These experiments were made under steady humidity and temperature conditions as 20% RH and 25 °C, respectively. It was operated with 10, 50, 100, 150, 300, 600, 800 and 1000 ppm for 30 – 60 - 90 - 120 - 150 - 180 - 210 - 240 min. Adsorption samples were collected, sealed, transported, and placed according to the US. Environmental Protection Agency Method TO-17 [40]. The percentage of toluene removal was calculated by Equation 2 which C_o is the initial concentration, C_e is the equilibrium concentration (ppm).

$$Removal\ \% = \frac{C_o - C_e}{C_o} x100 \quad (2)$$

2.5. TD-GC-MS Analysis

The gas-phase toluene concentration was measured using thermal desorption-gas chromatography-mass spectrometry (TD-GC/MS). It is the addition of gas chromatography, which provides desorption of toluene heated by an inert carrier gas stream and injection or transfer to a carrier with selected ion monitoring (SIM) mode. Agilent 6890N Network Gas Chromatograph and Agilent 5975 Series Markes Unity-2 TD were used in experimental apparatus with Tenax TA sorbent tube. The calibration is based on the seven standards as 10, 20, 40, 60, 80, 100, and 200 ng/µl for 1 µl of each concentration by TD-GC/MS to establish the calibration curves. The gas column was a DB-1 series J&W 123-1063 (60 m × 0.32 mm ID × 1.0 µm, Agilent Technologies, Santa Clara, CA, USA). The injected sample volume was 1 µl the detector temperature was operated at 250°C. 40 ml/min hydrogen (H_2) gas and 20 psi pure helium (He) gas. The utilized temperature program began at 35°C min and then increased to 300°C with a rate of 5°C/min for 30 min. Each sampling tube was consecutively used with three sorbent tubes for the average value.

3. RESULTS

According to the American Society for Testing and Materials (ASTM), *Robinia pseudoacacia* L. as raw material made volatile matter, moisture,

and ash analysis by standards E872-82, E871–82 D1102–84 [41-43].

3.1. Yield of KN_xAC

One of the first targets aimed at producing activated carbon is to obtain as much activated carbon as possible from the raw material. Therefore, two factors to be considered during the production phase are the pyrolysis time and the carbonization temperature. These effects can keep the high or low product of KN_xACs. The activated carbon production performance at 500 °C was found at 39.78%, while carbonization temperature increased to 900 °C was obtained at 21.45% after the process result.

3.2. Characterization of KN_xAC

High porosity and BET surface area are required for a successfully activated carbon, measured with NOVA Touch LX4 nitrogen adsorption-desorption analysis (Quantachrome Instruments, South San Francisco, CA, USA). Also, KN_xACs were coded from $KN_{1\text{-}25}AC$ according to the several impregnation ratios of KOH. The cellulose, hemicellulose, and lignin content of the biomass was found in Table 2.

Table 2 Cellulose, Hemicellulose, and Lignin content (wt%)

Cellulose wt%	Hemicellulose wt%	Lignin wt%
25.2	31.3	30.9

The composition of *Robinia pseudoacacia* L. biomass is given in Table 3.

Table 3 Composition of *Robinia pseudoacacia* L. biomass

Ash %	Moisture %	Volatile %	Fix C %	C %	H %	N %	O %
1.3	11.88	82.7	4.28	36.21	9.13	6.55	34.93

The highest surface area was obtained with 4:1 KOH at 800 °C coded as $KN_{24}AC$ (1271.3 m^2/g). Also, $KN_{19}AC$, $KN_{20}AC$, and $KN_{25}AC$ were found in high surface areas of 1142.7, 1067.5, and 1202.8 m^2/g, respectively. They were chosen for micro and total pore volume in Table 4.

Table 4 The pore structure of KN_xAC.

Samples	S_{BET} (m^2/g)	V_{micro} (cm^3/g)	V_{total} (cm^3/g)
$KN_{19}AC$	1142.7	0.151	0.355
$KN_{20}AC$	1067.5	0.122	0.274
$KN_{24}AC$	1271.3	0.303	0.377
$KN_{25}AC$	1202.8	0.281	0.317

The surface morphology of *Robinia pseudoacacia* L. biomass and $KN_{24}AC$ were present with solid residue and chemicals by SEM. Their surface area was calculated by the BET method [44]. As the carbonization process temperature increases, other compounds in the activated carbon structure are eliminated because of the pore formation. However, it is seen that the disinformation in the form becomes after a specific temperature in Figure 1.

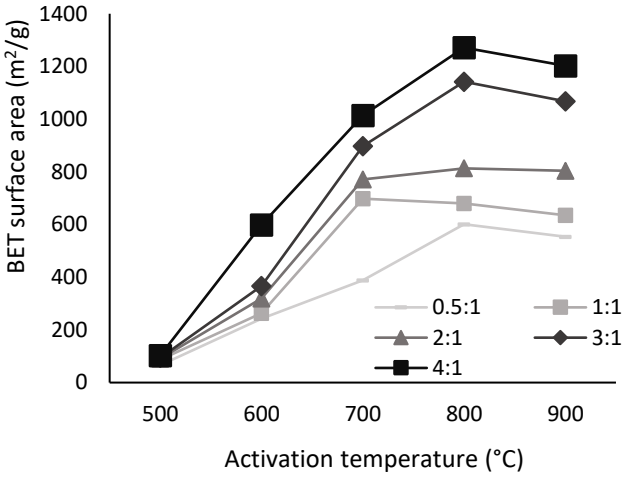

Figure 1 S_{BET} values of $KN_{24}AC$

Scanning Electron Microscopy (SEM) graphs were described in the *Robinia pseudoacacia* L. biomass and $KN_{24}AC$. The striking point is the existence of irregular structures and inhomogeneous order in the SEM microimages. The surface of raw material is smooth and has no porosity, although after the activating process has been seen. Also, their pore size has increased and become more regular in Figure 2.

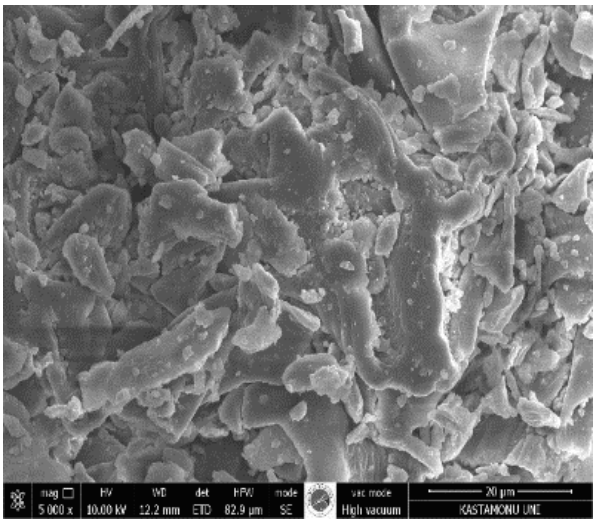

(a)

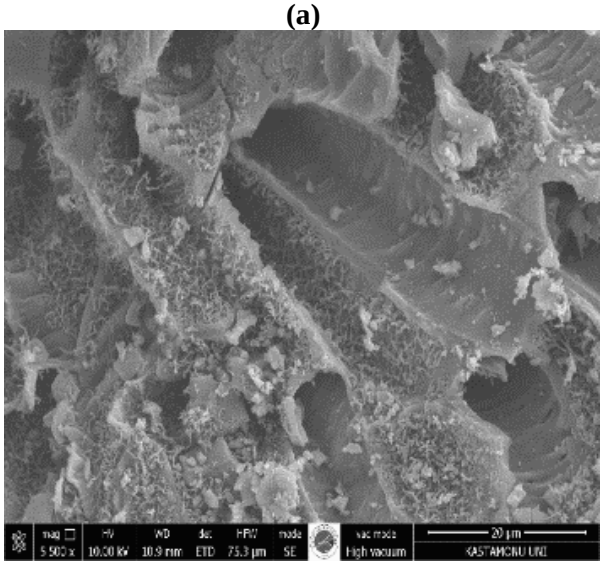

(b)

Figure 2 SEM micrographs at 20 nm (a: Raw biomass, b: $KN_{24}AC$)

3.3. Adsorption of Toluene

According to the IUPAC classification, the adsorption behavior of KN24AC was analyzed by N2 adsorption-desorption analysis that exhibited type IV isotherm at 77 K. It indicates the presence of mesopores sizes between 2 and 50 nm or 20 and 500 Å. To determine the initial conditions of the experimental setup was operated multiple times without adding activated carbon to the system. There are several reasons for this, the most important of which is that toluene molecules are high-speed and active. It was run empty because the desire to cling to the wall and pipes of the reactor was high. The efficiency of adsorbents varies depending on initial concentration and contact time. The adsorption capacity of an adsorbent is the milligrams of adsorbate per 1 gram of KNxACs. The highest surface area was obtained with $KN_{24}AC$, although $KN_{19}AC$, $KN_{20}AC$, and $KN_{25}AC$ were used in the toluene capture test. Before the test conditions, it was waited for about 30 minutes for the system to steady-state conditions.

3.3.1. Initial Concentration

The initial concentrations used in the study were determined as 10, 50, 100, 150, 300, 600, 800, and 1000 ppm, which are levels that can be commonly found indoors. At test conditions with 10 ppm was 4 mg/g, 111 mg/g was obtained at 1000 ppm. There is a difference in saturation value of activated carbon at low concentration (10 ppm) and high concentration (1000 ppm) in Figure 3.

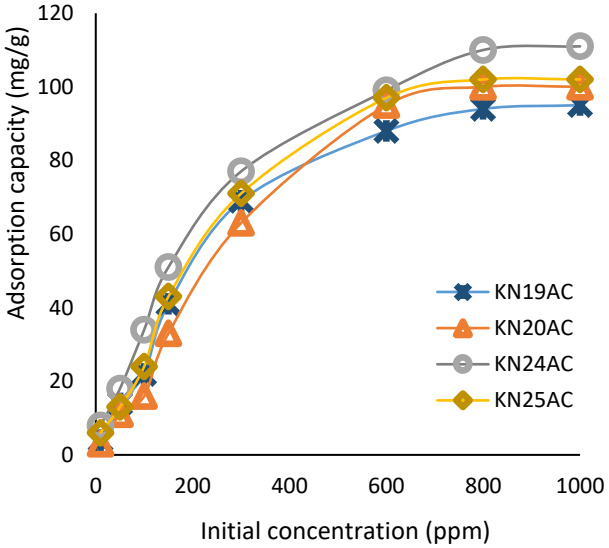

Figure 3 The plots of initial concentration gas-phase toluene according to types of KN_xACs

3.3.2. Experimental Time

The effect of contact time was examined until 240 min on the toluene adsorption study. Each measurement was made at 30-minute intervals. The retention time of toluene gas in activated carbon was fast until the 120th minute. Then, it showed a decreasing trend until the 180th minute and reached the saturation value between 180-240 in Figure 4.

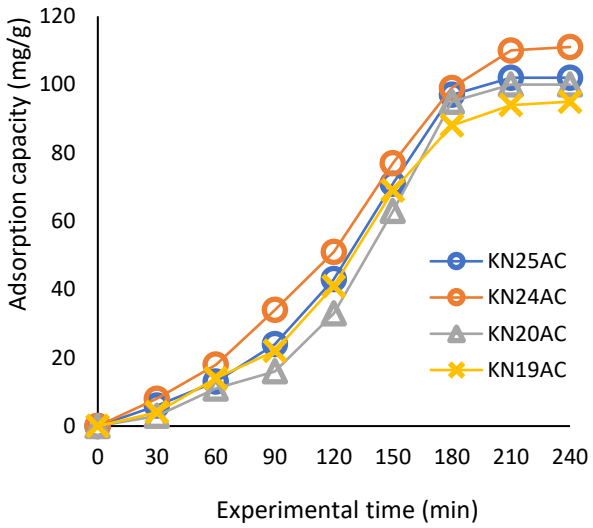

Figure 4 Variation of toluene adsorption capacity for experimental time

The binding rate, shape, and desire of toluene are directly affected by the arrangement of its molecules. The adsorbate speed was affected by plugged pores, so the bond of speed toluene molecules was decreased during the adsorption. As the pores fill, the toluene molecules need more time. The maximum adsorption capacity of gas-phase toluene was reached 111 mg/g in 1000 ppm for 240 min.

4. DISCUSSION

The performance of KN_xACs was executed with several initial concentrations between 10 and 1000 ppm at room temperature. Raw material impregnated with KOH and carbonized at 800 ºC. The holding capacity of toluene molecules is higher in experiments due to the BET surface area of $KN_{24}AC$ being highly increased. The $KN_{24}AC$ was compared to other studies that the surface area seems tolerable for a lignocellulosic-based activated carbon [45]. Freitas et al. [37] were produced activated carbon derived from coconut shells (S_{BET}: 560 m^2/g, V_{micro}: 0.19 cm^3/g) and were exhibited surface areas. Also, they were analyzed commercial activated carbon and compared it with produced activated carbon (S_{BET}: 799 m^2/g, V_{micro}: 0.24 cm^3/g). Chung et al. [46] were used lignocellulosic waste materials such as *Acacia mangium* wood sawdust, coconut shell, sugarcane bagasse, and lignin-rich (S_{BET}: 307.92-937.43 m^2/g). They were analyzed through BET, EDS, TPD-NH_3, SEM, and FTIR. According to this study, the $KN_{24}AC$ was demonstrated high surface area and micropore volume as 1271.3 m^2/g and 0.303 cm^3/g, respectively. Various pollutants were also removed with the produced activated carbons [47]. Adsorption capacities varied according to pollutant type and ambient conditions. Andrade et al. [48] were investigated VOC removal by activated carbon from mango fruit shells. The adsorption capacity was found at 472 mg/g at 30 °C and 363 mg/g at 50 °C for acetone gaseous. Shen and Zhang [29] were prepared with N-doped porous carbon from co-hydrothermal carbonization (co-HTC) of lignocellulose via KOH at 700 °C. It has 1396.5 m^2/g, and an adsorption capacity was 394.2 mg/g for toluene removal. Anjum et al. [49] were modified activated carbon with benign oxidizing agents and were searched for physicochemical properties for BTX removal in aqueous. The ACs were used 0.01-1 g, different temperature ranges (25-45 °C). They found contact time, adsorbent amount, initial concentration, temperature, and pH important factors for removing benzene as 260.78 mg/g. Vikrant et al. [50] used a metal-organic framework and referenced activated carbon to compare adsorption capacity. They were reported that the high degree of M199 was 94.8 mg/g, although activated carbon was reached 93.5 mg/g in the treatment of gaseous pollutants. He et al. [51] were produced with lignin-based pitch extracted from black liquor and were found to have a high surface area of 3652 m^2/g. This high-powered activated carbon was obtained at 1244.9 mg/g to capture gaseous benzene under 5000 ppm.

Generally, the variety and duration of chemical activation have been changed for high surface area in studies. The carbon and lignin contents of biomass were effectively used. Also, different molecular sizes and affinities were effective in toluene, which is desired to be removed. Adsorption studies were performed in a batch, continuous, and sequential reactor. However, these studies were tested in simultaneous high concentration indoor air. It is seen that the adsorbed amount decreases as it increases with reactor size. Thus, the material and experimental

setup are important for adsorption capacity and behavior.

5. CONCLUSION

The lignocellulosic biomass can be used as the raw material for activated carbon preparation. It is a valuable material for the removal of toluene from indoor air. Also, it is a substantial treatment in air pollution control. The lignocellulosic biomass can be regarded as ample agricultural or woodsy waste. An effort was made to obtain the optimum surface and micropore volume with the carbonization at the optimum temperature. It seems more appropriate to investigate the evaluation of optimum conditions with different conditions and activation agents. The carbon content of the raw material is an important factor in the production of activated carbon. In this study, the highest yield of activated carbon was carbonization at 800 °C and 90 min via KOH (4:1), resulting in activated carbon with a maximum total specific surface area of 1271.3 m^2/g. Temperature value has increased the adsorbent's performance through some groups (such as hydroxyl, ethers, and aromatic compounds). Toluene is an air pollutant released from various sources, deteriorating indoor air quality. It can be carcinogenic for human health when it is excessive. Toluene removal is a very significant issue that has been widely used in various industries and industries. The aim of the study was successfully performed with $KN_{24}AC$, which was used as a filter for toluene removal from indoor air. As a result of the success of KNAC produced in the study in toluene gas, which is among the volatile compounds, its application to other volatile compounds is seen as a very reasonable and inexpensive method. Investigating the total removal of other VOCs on an industrial scale and conducting kinetic studies will be a pioneer for other researchers.

Funding

There is no financial support and commercial support.

The Declaration of Conflict of Interest/ Common Interest

No conflict of interest or common interest has been declared by the authors.

Authors' Contribution

The authors contributed equally to the study

The Declaration of Ethics Committee Approval

This study does not require ethics committee permission or any special permission"

The Declaration of Research and Publication Ethics

The authors of the paper declare that they comply with the scientific, ethical and quotation rules of SAUJS in all processes of the paper and that they do not make any falsification on the data collected. In addition, they declare that Sakarya University Journal of Science and its editorial board have no responsibility for any ethical violations that may be encountered, and that this study has not been evaluated in any academic publication environment other than Sakarya University Journal of Science.

REFERENCES

[1] H. M. Shin, T. E. McKone and D. H. Bennett, Contribution of low vapor pressure-volatile organic compounds (LVP-VOCs) from consumer products to ozone formation in urban atmospheres, Atmospheric Environment, vol. 108, pp. 98-106, 2015.

[2] F. Qu, L. Zhu, & K. Yang, Adsorption behaviors of volatile organic compounds (VOCs) on porous clay heterostructures (PCH), Journal of hazardous materials, vol. 170, no. 1, pp. 7-12, 2009.

[3] G. R. Parmar, & N. N. Rao, Emerging control technologies for volatile organic compounds. Critical Reviews in

Environmental Science and Technology, vol. 39, no. 1, pp. 41-78, 2008.

[4] I. Dhada, M. Sharma, & P. K. Nagar, Quantification and human health risk assessment of by-products of photo catalytic oxidation of ethylbenzene, xylene and toluene in indoor air of analytical laboratories. Journal of hazardous materials, vol. 316, pp. 1-10, 2016.

[5] O. Isinkaralar, K. Isinkaralar, A. Ekizler and C. Ilkdogan, Changes in the amounts of CO_2 and particulate matter in Kastamonu Province depending on weather conditions and locations. Journal of Chemical, Biological and Physical Sciences, vol. 7, no. 3, pp. 643-650, 2017.

[6] H. X. Fu, & X. H. Liu, Review of the impact of liquid desiccant dehumidification on indoor air quality. Building and Environment, vol. 116, pp. 158-172, 2017.

[7] H. BHuang, & D. Ye, Combination of photocatalysis downstream the non-thermal plasma reactor for oxidation of gas-phase toluene. Journal of hazardous materials, vol. 171, no. 1-3, pp. 535-541, 2009.

[8] N. Shinohara, Y. Okazaki, A. Mizukoshi, & S. Wakamatsu, Exposure to benzene, toluene, ethylbenzene, xylene, formaldehyde, and acetaldehyde in and around gas stations in Japan. Chemosphere, vol. 222, pp. 923-931, 2019.

[9] N. Barros, M. Carvalho, C. Silva, T. Fontes, J. C. Prata, A. Sousa, & M. C. Manso, Environmental and biological monitoring of benzene, toluene, ethylbenzene and xylene (BTEX) exposure in residents living near gas stations. Journal of toxicology and environmental health, Part A, vol. 82, no. 9, pp. 550-563, 2019.

[10] R. Fan, J. Li, L. Chen, Z. Xu, D. He, Y. Zhou, ... & J. Li, Biomass fuels and coke plants are important sources of human exposure to polycyclic aromatic hydrocarbons, benzene and toluene. Environmental research, vol. 135, pp. 1-8, 2014.

[11] S. V. Dozein, M. Masrournia, Z. Es'haghi, & M. R. Bozorgmehr, Determination of benzene, toluene, ethylbenzene, and p-xylene with headspace-hollow fiber solid-phase microextraction-gas chromatography in wastewater and Buxus leaves, employing a chemometric approach. Chemical Papers, pp. 1-12, 2021.

[12] M. E. Meek, & P. K. L. Chan, Toluene: evaluation of risks to human health from environmental exposure in Canada. Journal of Environmental Science & Health Part C, vol. 12, no. 2, pp. 507-515, 1994.

[13] P. Rashnuodi, B. F. Dehaghi, H. A. Rangkooy, A. Amiri, & S. M. Poor, Evaluation of airborne exposure to volatile organic compounds of benzene, toluene, xylene, and ethylbenzene and its relationship to biological contact index in the workers of a petrochemical plant in the west of Iran. Environmental Monitoring and Assessment, vol. 193, no. 2, pp. 1-10, 2021.

[14] M. Kumar, B. S. Giri, K. H. Kim, R. P. Singh, E. R. Rene, M. E. López,... & R. S. Singh, Performance of a biofilter with compost and activated carbon based packing material for gas-phase toluene removal under extremely high loading rates. Bioresource technology, vol. 285, pp. 121317, 2019.

[15] K. Singh, R. S. Singh, B. N. Rai, & S. N. Upadhyay, Biofiltration of toluene using wood charcoal as the biofilter media. Bioresource Technology, vol. 101, no. 11, pp. 3947-3951, 2010.

[16] H. Ukai, T. Kawai, O. Inoue, Y. Maejima, Y. Fukui, F. Ohashi,... & M. Ikeda, Comparative evaluation of biomarkers of occupational exposure to toluene. International archives of occupational and environmental health, vol. 81, no. 1, pp. 81-93, 2007.

[17] K. Grob, C. Frauenfelder, & A. Artho, Uptake by foods of tetrachloroethylene, trichloroethylene, toluene, and benzene from air. Zeitschrift für Lebensmittel-Untersuchung und Forschung, vol. 191, no. 6, pp. 435-441, 1990.

[18] C. Treesubsuntorn, and P. Thiravetyan, Botanical biofilter for indoor toluene removal and reduction of carbon dioxide emission under low light intensity by using mixed C3 and CAM plants. Journal of Cleaner Production, vol. 194, pp. 94-100, 2018.

[19] K. Corey, and L. Zappa, Odor Control' ABC's: How to Compare and Evaluate Odor Control Technologies. Global Environmental Solutions, Inc., 2018.

[20] S. Fujii, H. Cha, N. Kagi, H. Miyamura, & Y. S. Kim, Effects on air pollutant removal by plant absorption and adsorption. Building and Environment, vol. 40, no. 1, pp. 105-112, 2005.

[21] G. Soreanu, M. Dixon, and A. Darlington, Botanical biofiltration of indoor gaseous pollutants–A mini-review. Chemical engineering journal, vol. 229, pp. 585-594, 2013.

[22] M. Wen, G. Li, H. Liu, J. Chen, T. An, and H. Yamashita, Metal–organic framework-based nanomaterials for adsorption and photocatalytic degradation of gaseous pollutants: recent progress and challenges. Environmental Science: Nano, vol. 6, no. 4, pp. 1006-1025, 2019.

[23] W. Ghoma, H. Sevik and K. Isinkaralar, Using indoor plants as biomonitors for detection of toxic metals by tobacco smoke. Air Quality, Atmosphere & Health, 2022.

[24] Q. Chen, F. Liu, and J. Mo, Vertical macro-channel modification of a flexible adsorption board with in-situ thermal regeneration for indoor gas purification to increase effective adsorption capacity. Environmental Research, vol. 192, pp. 110218, 2021.

[25] J. Loipersböck, G. Weber, R. Rauch, and H. Hofbauer, Developing an adsorption-based gas cleaning system for a dual fluidized bed gasification process. Biomass Conversion and Biorefinery, vol. 11, no. 1, pp. 85-94, 2021.

[26] V. Presser, J. McDonough, S. H. Yeon, and Y. Gogotsi, Effect of pore size on carbon dioxide sorption by carbide derived carbon. Energy & Environmental Science, vol. 4, no. 8, pp. 3059-3066, 2011.

[27] Y. H. Tan, J. A. Davis, K. Fujikawa, N. V. Ganesh, A. V. Demchenko, and K. J. Stine, Surface area and pore size characteristics of nanoporous gold subjected to thermal, mechanical, or surface modification studied using gas adsorption isotherms, cyclic voltammetry, thermogravimetric analysis, and scanning electron microscopy. Journal of materials chemistry, vol. 22, no. 14, pp. 6733-6745, 2012.

[28] Y. Wang, L. Liu, and H. Cheng, Gas Adsorption Characterization of Pore Structure of Organic-rich Shale: Insights into Contribution of Organic Matter to Shale Pore Network. Natural Resources Research, vol. 30, no. 3, pp. 2377-2395, 2021.

[29] C. Zhang, J. Wu, R. Wang, E. Ma, L. Wu, J. Bai, & J. Wang, Study of the toluene absorption capacity and mechanism of ionic liquids using COSMO-RS prediction and experimental verification. Green Energy & Environment, vol. 6, no. 3, pp. 339-349, 2021.

[30] Z. M. Yunus, N. Othman, Al-A. Gheethi, R. Hamdan, and N. N. Ruslan, Adsorption of heavy metals from mining effluents using honeydew peels activated carbon; isotherm, kinetic and column studies. Journal of Dispersion Science and Technology, vol. 42, no. 5, pp. 715-729, 2021.

[31] M. A. E. S. El-Hashemy and N. F. Alotaibi, Purification of benzene-laden air by static adsorption of benzene onto activated carbon prepared from Diplotaxis acris biomass. Biomass Conversion and Biorefinery, pp. 1-15, 2021.

[32] A. Aziz, M. N. Nasehir Khan, M. F. Mohamad Yusop, E. Mohd Johan Jaya, M. A. Tamar Jaya, and M. A. Ahmad, Single-Stage Microwave-Assisted Coconut-Shell-Based Activated Carbon for Removal of Dichlorodiphenyltrichloroethane (DDT) from Aqueous Solution: Optimization and Batch Studies. International Journal of Chemical Engineering, 2021.

[33] C. Djilani, R. Zaghdoudi, F. Djazi, B. Bouchekima, A. Lallam, A. Modarressi and M. Rogalski, Adsorption of dyes on activated carbon prepared from apricot stones and commercial activated carbon. Journal of the Taiwan Institute of Chemical Engineers, vol. 53, pp. 112-121, 2015.

[34] K. Isinkaralar, G. Gullu and A. Turkyilmaz, Experimental study of formaldehyde and BTEX adsorption onto activated carbon from lignocellulosic biomass. Biomass Conversion and Biorefinery, 2022.

[35] C. Bouchelta, M. S. Medjram, O. Bertrand, and J. P. Bellat, Preparation and characterization of activated carbon from date stones by physical activation with steam. Journal of Analytical and Applied Pyrolysis, vol. 82, no. 1, pp. 70-77, 2008.

[36] K. Isinkaralar, Theoretical removal study of gas BTEX onto activated carbon produced from Digitalis purpurea L. biomass. Biomass Conversion and Biorefinery, 2022.

[37] J. V. Freitas, F. G. Nogueira, and C. S. Farinas, Coconut shell activated carbon as an alternative adsorbent of inhibitors from lignocellulosic biomass pretreatment. Industrial Crops and Products, vol. 137, pp. 16-23, 2019.

[38] K. Isinkaralar, Production and Characterization of Activated Carbon Using with *Althaea officinalis* L. as a Lignocellulosic Waste, 2021 International Congress on Scientific Advances, pp. 926-927, 2021.

[39] Q. Bu, H. Lei, S. Ren, L. Wang, J. Holladay, Q. Zhang, ... & R. Ruan, Phenol and phenolics from lignocellulosic biomass by catalytic microwave pyrolysis. Bioresource technology, vol. 102, no. 13, pp. 7004-7007, 2011.

[40] U.S. Environmental Protection Agency (EPA). Compendium Method TO-17: Determination of Volatile Organic Compounds in Ambient Air Using Active Sampling onto Sorbent Tubes; EPA: Washington, DC, USA, pp. 1–53, 1999.

[41] ASTM International, E872-82 Standard test method for volatile matter in the analysis of particulate wood fuels. Am Soc Mater Test Int., 2019.

[42] ASTM International E871–82 Standard test method for moisture analysis of particulate wood fuels. Am Soc Mater Test Int. 2019.

[43] ASTM International D1102–84 Standard test method for ash in wood. Am Soc Mater Test Int. 2021.

[44] S. Brunauer, P. H. Emmett and E. Teller, Adsorption of gases in multimolecular layers. Journal of the American chemical society, vol. 60, no. 2, 309-319. 1938.

[45] N. M. Nor, L. C. Lau, K. T. Lee, and A. R. Mohamed, Synthesis of activated carbon from lignocellulosic biomass and its applications in air pollution control—a review. Journal of Environmental Chemical Engineering, vol. 1, no. 4, pp. 658-666, 2013.

[46] N. H. Chung, N. T. Que, N. T. Thanh, and G. T. P. Ly, Comparative study on the conversion of Acacia mangium wood sawdust-derived xylose-containing acid

hydrolysate to furfural by sulfonated solid catalysts prepared from different lignocellulosic biomass residues. Wood Science and Technology, pp. 1-21, 2021.

[47] R. V. P. Antero, A. C. F. Alves, S. B. de Oliveira, S. A. Ojala, and S. S. Brum, Challenges and alternatives for the adequacy of hydrothermal carbonization of lignocellulosic biomass in cleaner production systems: A review. Journal of Cleaner Production, vol. 252, pp. 119899, 2020.

[48] R. C. de Andrade, R. S. G. Menezes, R. A. Fiuza-Jr, and H. M. C. Andrade, Activated carbon microspheres derived from hydrothermally treated mango seed shells for acetone vapor removal. Carbon Letters, pp. 1-15, 2020.

[49] H. Anjum, K. Johari, N. Gnanasundaram, A. Appusamy, and M. Thanabalan, Impact of surface modification on adsorptive removal of BTX onto activated carbon. Journal of Molecular Liquids, vol. 280, pp. 238-251, 2019.

[50] K. Vikrant, C. J. Na, S. A. Younis, K. H. Kim, and S. Kumar, Evidence for superiority of conventional adsorbents in the sorptive removal of gaseous benzene under real-world conditions: Test of activated carbon against novel metal-organic frameworks. Journal of Cleaner Production, vol. 235, pp. 1090-1102, 2019.

[51] S. He, G. Shi, H. Xiao, G. Sun, Y. Shi, G. Chen, ... & X. Yang, Self S-doping activated carbon derived from lignin-based pitch for removal of gaseous benzene. Chemical Engineering Journal, vol. 410, pp. 128286, 2021.

SAKARYA ÜNİVERSİTESİ
FEN BİLİMLERİ ENSTİTÜSÜ DERGİSİ

Sakarya University Journal of Science
SAUJS

e-ISSN 2147-835X Period Bimonthly Founded 1997 Publisher Sakarya University
http://www.saujs.sakarya.edu.tr/

Title: The Variation of the Linewidths and Amplitudes of sub-Doppler Resonances of 87Rb D2 Line with Laser Beam Intensity

Authors: Ersoy ŞAHİN

Recieved: 2022-02-10 00:00:00

Accepted: 2022-04-06 00:00:00

Article Type: Research Article

Volume: 26
Issue: 2
Month: April
Year: 2022
Pages: 421-428

How to cite
Ersoy ŞAHİN; (2022), The Variation of the Linewidths and Amplitudes of sub-Doppler Resonances of 87Rb D2 Line with Laser Beam Intensity. Sakarya University Journal of Science, 26(2), 421-428, DOI: 10.16984/saufenbilder.1071289
Access link
https://dergipark.org.tr/tr/journal/1115/issue/69580/1071289

New submission to SAUJS
http://dergipark.gov.tr/journal/1115/submission/start

Sakarya University Journal of Science 26(2), 421-428, 2022

The Variation of the Linewidths and Amplitudes of Sub-Doppler Resonances of ^{87}Rb D_2 Line with Laser Beam Intensity

Ersoy ŞAHİN*[1]

Abstract

The sub-Doppler resonances linewidths and amplitudes depend on the laser beam intensity. The effect of laser beam intensity on the resonance linewidths and amplitudes obtained from different energy transitions of atoms varies from resonance to resonance. The effect of laser beam intensity on resonance linewidths and amplitudes is of great importance for diode laser frequency stability applications. It needs to be determined by measuring. The effect of the laser beam intensity on the linewidths and amplitudes of sub-Doppler resonances were measured by laser heterodyne spectroscopy using the linearly polarized frequency stabilized extended cavity diode lasers. The measurements are compatible with the theory and the uncertainty of the measurements are fewer than 1.6 MHz and 0.3 mV for linewidths and amplitudes, respectively.

Keywords: Sub-Doppler resonance, linewidth, amplitude, saturation absorption spectroscopy, laser frequency stability

1. INTRODUCTION

Sub-Doppler resonances are detected by the saturation spectroscopy method [1, 2]. Derivative signals obtained from saturation resonances by different spectroscopic methods are used to establish the frequency stability of lasers [3-6]. The level of frequency stability that the laser will reach depends on the linewidth and amplitude of the saturation resonance used as a reference, and high-frequency stability levels can only be achieved by using derivative signals obtained from resonances with narrow linewidth and high amplitude [7, 8]. Linewidth and amplitude of saturation resonances depend on the polarization of the laser beam, the laser beam intensity, the diameter of the laser beam, and the ambient temperature parameters where the atoms are located [9-11]. The effect of laser beam intensity on the linewidths and amplitude of the hyperfine resonances of the ^{87}Rb D_2 line have not been measured. The polarization and the diameter of the laser beam on the linewidths and amplitude of the hyperfine resonances of the ^{87}Rb D_2 have been studied [9, 10]. Laser beam intensity increases the linewidth of the saturation resonance (saturation broadening) and causes a light shift of the resonance frequency [12, 13]. It is of great importance for applications that the laser beam intensity should be at a value that will both expand the resonance linewidth at the minimum level and shift the resonance frequency the least [14-18].

In this study, the effect of the laser beam intensity on the linewidths and amplitudes of the

* Corresponding author: ersoy.sahin@tubitak.gov.tr
[1] TÜBİTAK National Metrology Institute (TÜBİTAK UME)
ORCID: https://orcid.org/0000-0002-0609-2079

$F=1\rightarrow F'=0,1,2$ and $F=2\rightarrow F'=1,2,3$ hyperfine resonances of ^{87}Rb D_2 line were measured. The linearly polarized counter-propagated pumping and probe beams were used for creating and detecting the resonances respectively. During the measurements, the laser beam intensity of the probe beam was constant, and the pumping beam was changed. The saturation resonances were recorded by using the computer-controlled lock-in amplifier, digital multimeter, and frequency counter. The variation of the saturation resonances linewidths and amplitudes with laser beam intensity was investigated by statistical analysis of the measurements.

2. MEASUREMENT METHOD

The variation of the linewidths and amplitudes of the sub-Doppler resonances of ^{87}Rb D_2 energy transitions with laser beam intensity were determined by using two extended cavity diode recording (L_{rec}) and reference (L_{ref}) lasers with a linewidth of less than 150 kHz and operating at a wavelength of 780 nm. The measurement setup is in Figure 1 and it is the experimental setup used in the previous study. [19]. For creating and detecting the resonances, counter-propagated pumping and probe laser beams with diameters of 3 mm obtained from the L_{rec} were used. The two optical paths were obtained by splitting the beam of the L_{rec} laser with a beam splitter (BS_1). To get rid of the back reflection from the optics to the L_{rec} laser, an optical isolator (OI) was placed in front of the laser. By using the beam splitter (BS_3), the first optical path was divided into two parts and some part of it was used for the beat frequency measurements with a reference laser while the other part was sent to the temperature-controlled Fabry-Perot interferometer with the usage of a mirror (M_4) for creating a transmission resonance of the interferometer. The beam expander (BE) was used to enlarge the laser beam of the second optical path and the diaphragm (D) was used for adjusting the beam diameter of the L_{rec} laser to 3 mm. The counter-propagated pumping and probe laser beams were obtained by using the polarizing beam splitter (PBS). The laser beam reflected from the polarizing beam splitter was used for optical pumping (pumping beam), and the transmitted beam (probe beam) was used to detect resonances. By using the beam splitter (BS_2) and mirror (M_3), the reference laser beam constituted for removing background signal coming from the probe laser beam on the differential photodetector (DFD). For generating linear polarized parallel pumping and probe laser beams, the half-wave ($\lambda/2$) plate was used for adjusting the angle of the pumping beam polarization that was 90^o different linearly polarized to the probe laser beam. The intensity of the pumping laser beam was changed with a neutral density filter (ND_2), whereas the probe laser was kept constant at 0.1 mW/cm^2 usage of the neutral density filter (ND_1).

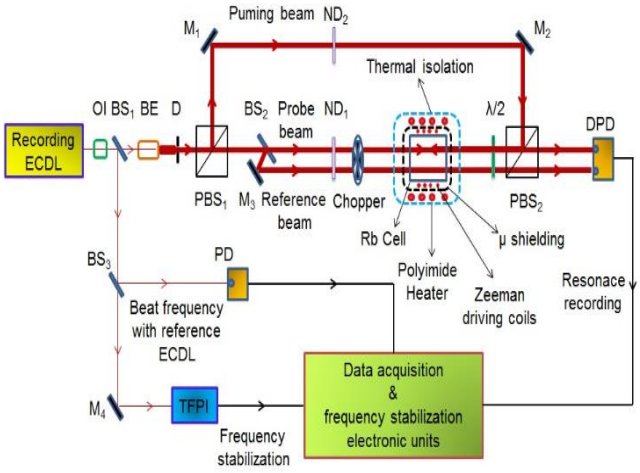

Figure 1 Measurement setup

The pumping and probe laser beams were optically superimposed inside a cylindrical glass cell with a length of 5 cm and a diameter of 3 cm, in which there is enriched Rb atoms. To ensure that the linewidth and amplitude of the resonances are not affected by the external magnetic field and ambient temperature, the Rb glass cell was magnetically shielded by wrapping two layers with Mu-metal, and temperature stability was achieved with polyamide heaters wrapped on the shielding. The magnetic field was measured less than 1 μT inside the shielding, the Rb glass cell temperature was kept stable at 22.5 ^oC from peak to peak at 5 mK [20]. To perform precise and repeatable measurements, both lasers were frequency stabilized.

The frequency stability of the L_{rec} laser was done by applying the first derivative of the transmission

resonance of the temperature-controlled Fabry-Perot interferometer to both the laser current and the piezoelectric transducer as feedback. Neither the piezoelectric transducer nor the current of the L_{rec} laser was modulated because the frequency modulation [21], which must be applied to obtain the derivative of the transmission resonance, increases the linewidths of the saturation resonances and also causes fluctuations in their amplitudes. The derivation of the transmission resonances were obtained by modulating and demodulating the Fabry-Perot interferometer's piezoelectric transducer by using the locking amplifier sinus signal. The L_{ref} laser frequency was stabilized by using the third derivative of saturation resonances of ^{87}Rb as a feedback signal. The feedback signal was applied both to the current and piezoelectric transducer of the laser. The derivative signal of the saturation resonances were obtained by modulation of the L_{ref} laser current with the sinus signal and demodulation from the lock-in amplifier. The beat frequency between the two lasers (laser heterodyne spectroscopy) was detected via a fast photodetector and recorded over a computer-controlled frequency counter to perform the frequency scale of the measurements [22]. The L_{rec} frequency was scanned with the sawtooth signal applied to the piezoelectric transducer of the Fabry-Perot interferometer from the signal generator, and the $F=1\rightarrow F'=0,1,2$ and $F=2\rightarrow F'=1,2,3$ hyperfine resonances of the ^{87}Rb transition line were recorded by using a computer-controlled lock-in amplifier and digital multimeter. The variation of resonance linewidths and amplitudes with laser beam intensity was investigated by statistical analysis of repeated measurements. Each value of laser intensity in the graphs of resonance linewidths and amplitudes is the mean value of the resonances that have been recorded five times in consecutive, and the standard deviation around the mean value is given with uncertainty bars as k=1.

3. LINEWIDTH AND AMPLITUDE MEASUREMENTS OF HYPERFINE RESONANCES OF ^{87}Rb D_2 LINE

The energy level diagram of ^{87}Rb is indicated in Figure 2. The fine structure is a result of the coupling between the orbital angular momentum **L** of the outer electron and its spin angular momentum **S**. The total electron angular momentum is given by **J** = **L** + **S**. For ground state L = 0 and S = 1/2, so J =1/2 and for the first excited state L = 1, so J = 1/2 or J = 3/2. According to the value of J, the transition split into two parts D_1 line ($5^2S_{1/2} \rightarrow 5^2P_{1/2}$, 794 nm) and D_2 line ($5^2S_{1/2} \rightarrow 5^2P_{3/2}$, 780 nm). The hyperfine structure is a result of the coupling of **J** with the total nuclear angular momentum **I**. The total atomic angular momentum F is then given by **F** = **J** + **I**. For the ground state, J = 1/2 and I = 3/2, so F = 1 or F = 2. For the excited state of the D_2 line, F can take the values 0, 1, 2, and 3 [23].

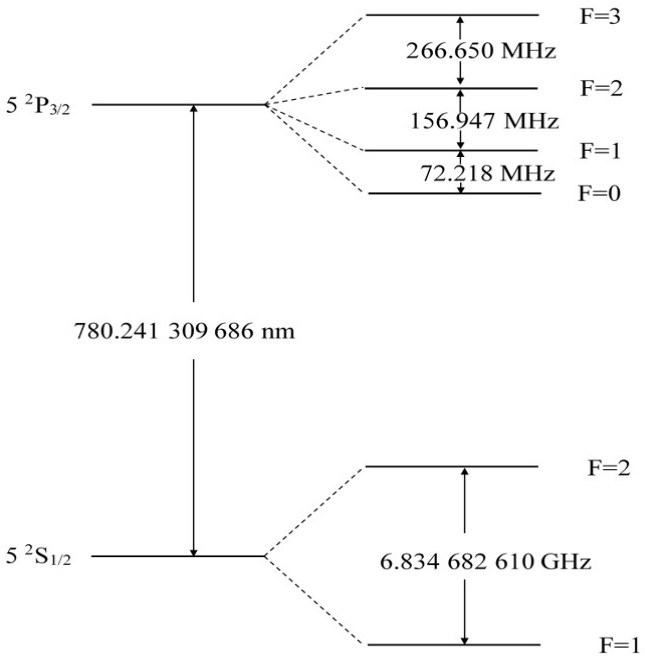

Figure 2 The fine and hyperfine structure energy levels of ^{87}Rb D_2 line

Figure 3 shows the variation of the $F=1\rightarrow F'=0,1,2$ and $F=2\rightarrow F'=1,2,3$ hyperfine resonances of the ^{87}Rb D_2 line with pumping laser beam intensity. The left column of the figure is the spectrum of $F=1\rightarrow F'=0,1,2$, and the recorded crossover (CO) resonances in the case of pumping laser beam intensity (a) 1.19, (b) 2.39 and (c) 3.98 mW/cm^2.

The spectrum of F=2→F/=1,2,3, and crossover resonances recorded at (I) 0.4, (II) 1.59, and (III) 3.58 mW/cm^2 values of pumping laser beam intensity is in the right column of Figure 3.

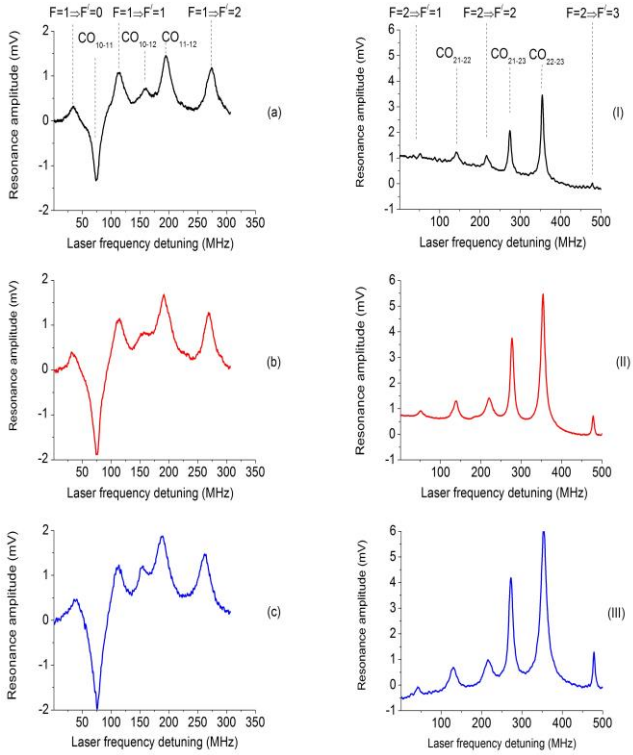

Figure 3 The effect of the laser beam intensity on linewidths and amplitudes of F=1→F/=0,1,2, F=2→F/=1,2,3, and crossover resonances

3.1. Variation of Linewidths Hyperfine Resonances of ^{87}Rb D_2 Line with Pumping Laser Beam Intensity

The variation of linewidths of F=1→F/=0,1,2, and crossover resonances with pumping laser beam intensity is shown in Figure 4. As can be seen from Figure 4, the full half-maximum linewidths (FWHM) of the CO_{11-12}, CO_{10-11}, and F=1→F/=2 resonances have expanded with increasing pumping laser beam intensity. The linewidths of the F=1→F/=0 and F=1→F/=1 resonances have broadened to 2.4 and 3.2 mW/cm^2 laser beam intensity values respectively and then began to narrow. Since the CO_{10-12} crossover resonance signal could not be detected from sufficient signal amplitude, the variation of the pumping laser beam intensity on the resonance linewidth could not be analyzed.

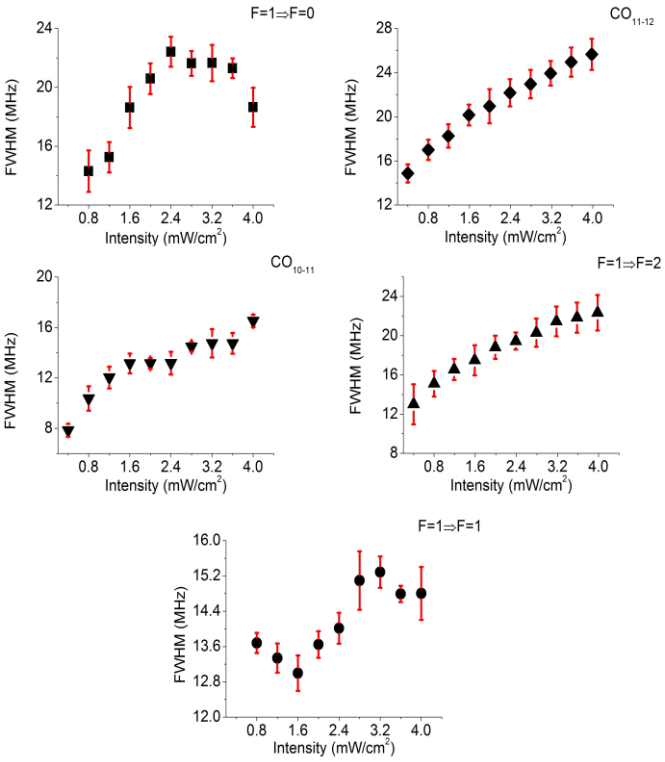

Figure 4 Variation of linewidths of F=1→F/=0,1,2, and crossover resonances with laser beam intensity

Figure 5 shows the variation of linewidths of F=2→F/=1,2,3, and crossover resonances with pumping laser beam intensity. The linewidths of CO_{22-23}, CO_{21-23}, and F=2→F/=3 transition resonances broadened with the increase of pumping laser beam intensity. The linewidth of CO_{21-22} and F=2→F/=2 transition resonances broadened up to the laser beam intensity value of 0.8 mW/cm^2, after this value, despite the increase in the laser beam intensity value, there is no visible broadening in the linewidth. Since F=2→F/=1 resonance amplitude could not be detected in the signal amplitude to be analyzed, the analysis of the linewidth could not be performed.

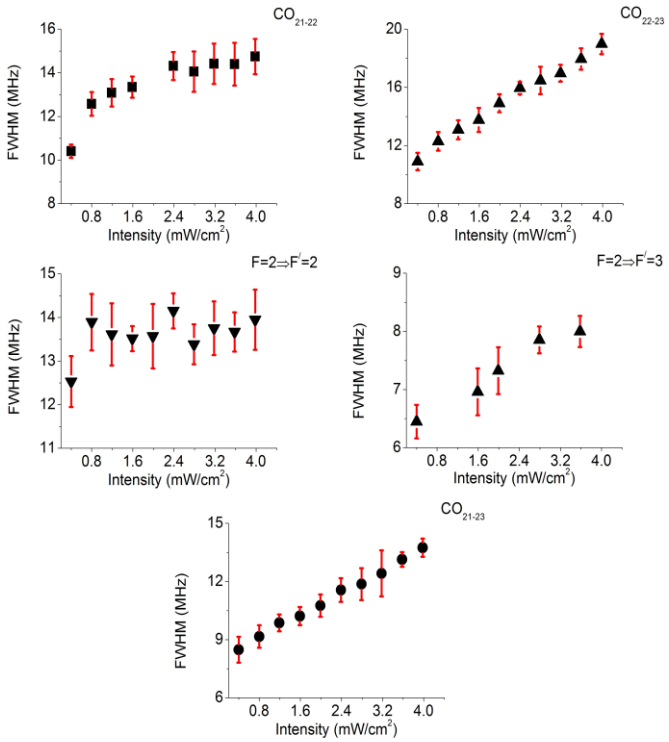

Figure 5 Variation of linewidths of F=2→F/=1,2,3, and crossover resonances with laser beam intensity

The linewidth measurements of the saturation resonances are in agreement with the theory. The expansion of the laser beam intensity on the resonance linewidth is expressed

$$\Gamma' = \Gamma.[1 + (\frac{I}{I_{sat}})]^{1/2}$$

by the equation where Γ is the natural linewidth of the resonance defined by the lifetime of the atoms at the upper energy level, and I_{Sat} is the saturation intensity value [12]. The lifetime of the ^{87}Rb atoms at the F=2→F/=3 transition at the F/=3 level is 26.24 ns (6.065 MHz), I_{Sat} =2.5 mW/cm^2 for linearly polarized laser beam [23]. According to the equation, if the laser radiation intensity I=0.4 mW/cm^2, the line broadening of the laser beam intensity on the resonance linewidth Γ/=6.5 MHz is calculated. This value is in agreement with the measured value for the line width of the F=2→F/=3 saturation resonance and is within the measurement uncertainty (Figure 5).

3.2. Variation of Amplitudes of Hyperfine Resonances of ^{87}Rb D_2 Line with Pumping Laser Beam Intensity

The variation of amplitudes of F=1→F/=0,1,2, F=2→F/=1,2,3, and crossover resonances with pumping laser beam intensity is given in Figures 6 and 7. Except for the F=2→F/=3 resonance, the amplitudes of the resonances increase up to the laser beam intensity value of 1.8 mW/cm^2. After this value, there are no increase in resonance amplitudes and there are saturated. The amplitude of the F=2→F/=3 resonance increases as the laser beam intensity increases. $CO_{10\text{-}12}$ and F=2→F/=1 resonances could not be analyzed because their amplitudes could not be detected in the signal amplitude to be analyzed.

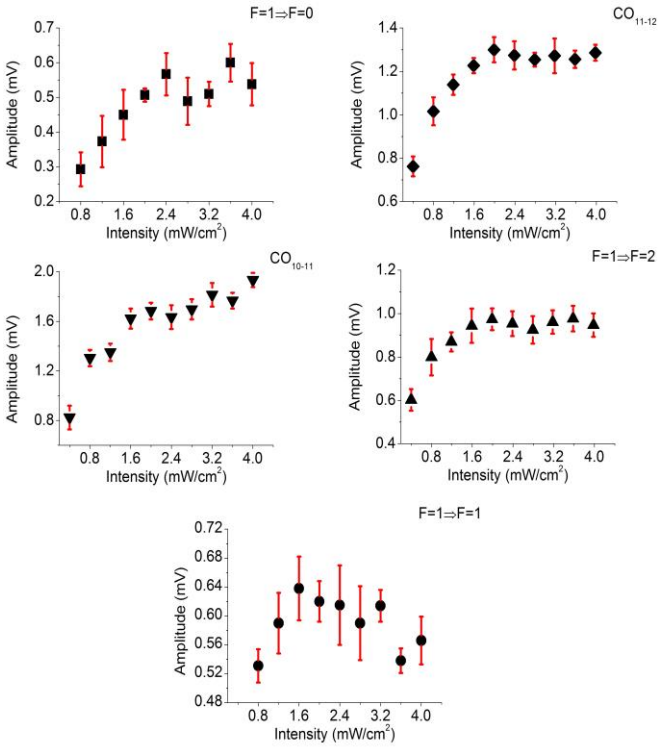

Figure 6 Variation of amplitudes of F=1→F/=0,1,2, and crossover resonances with laser beam intensity

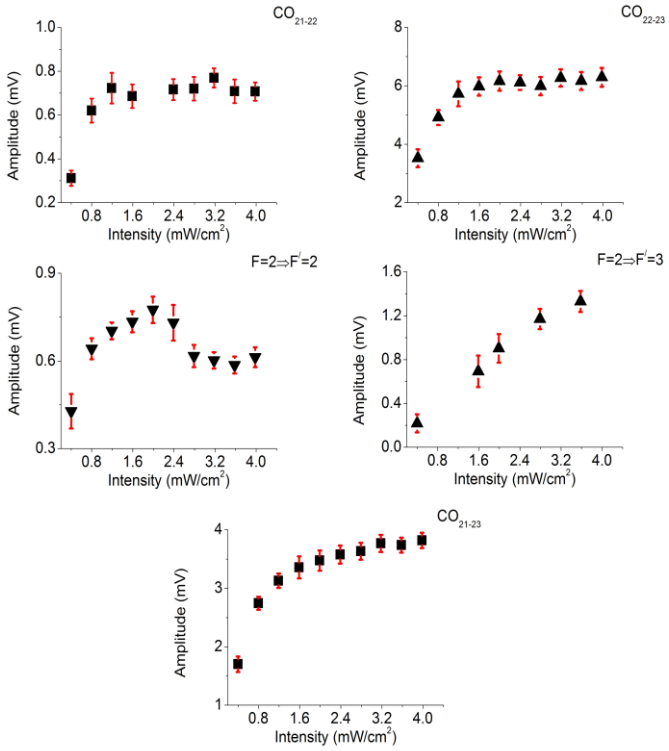

Figure 7 Variation of amplitudes of F=2→F/=1,2,3, and crossover resonances with laser beam intensity

4. CONCLUSION

The variation of the sub-Doppler resonance linewidths and amplitudes of ^{87}Rb D_2 energy transition line with the laser beam intensity was measured with linearly polarized laser beam precisely by using the laser heterodyne spectroscopy method. To perform the measurements sensitively and accurately, frequency stabilized extended cavity diode lasers, temperature-controlled magnetically shielded ^{87}Rb cell, and temperature-controlled Fabry-Perot interferometer were used. For each of the sub-Doppler saturation resonances, it was investigated at which value the pumping laser beam intensity had the narrowest linewidth and the highest resonance amplitude, and values consistent with the theory were measured. The uncertainty of the measurements is fewer than 1.6 MHz and 0.3 mV for linewidths and amplitudes, respectively. The measurements made are important in terms of laser frequency stability studies and laser applications requirements.

Acknowledgments

I thank the reviewers, editors, or secretaries that contributed to the article.

Funding

The author has no received any financial support for the research, authorship or publication of this study.

The Declaration of Conflict of Interest/ Common Interest

No conflict of interest or common interest has been declared by the author.

Authors' Contribution

The author contributed 100% to preparing the article.

The Declaration of Ethics Committee Approval

This study does not require ethics committee permission or any special permission.

The Declaration of Research and Publication Ethics

The author of the paper declare that they comply with the scientific, ethical and quotation rules of SAUJS in all processes of the paper and that I do not make any falsification on the data collected. In addition, I declare that Sakarya University Journal of Science and its editorial board have no responsibility for any ethical violations that may be encountered, and that this study has not been evaluated in any academic publication environment other than Sakarya University Journal of Science.

REFERENCES

[1] M. Himsworth, and T. Freegarde, “Rubidium pump-probe spectroscopy: Comparison between ab initio theory and experiment,” Physical Review A, vol. 81, pp. 023423, 2010.

[2] W. Demtröder, Laser Spectroscopy Basic concepts and Instrumention, second enlarged ed., Springer, Verlag Berlin Heidelberg, 1996.

[3] U. Tanaka, and T. Yabuzaki, "Frequency Stabilization of Diode Laser Using External Cavity and Doppler-Free Atomic Spectra," Japanese Journal of Applied Physics, vol. 33, pp. 1614-1622, 1994.

[4] S. Pustelny, V. Schultze, and D. Budker, "Dichroic atomic vapor laser lock with multi-gigahertz stabilization range," Review of Scientific Instruments, vol. 87, pp. 063107, 2016.

[5] S. Chakrabarti, B. Ray, and P:N. Ghosh, "Velocity selective optical pumping and repumping effects with counter and copropagating laser radiations for D_2 lines of rubidium," The European Physical Journal D, vol. 42, pp. 359–368, 2007.

[6] M.L. Harris, C.S. Adams, S.L. Cornish, I.C. McLeod, E. Tarleton, and I.G. Hughes, "Polarization spectroscopy in rubidium and cesium," Physical Review A, vol. 73, pp. 062509, 2006.

[7] G.P. Barwood, P.Gill, Laser stabilization for precision measurements, C. Guo, S.C. Singh (Eds.), Handbook of Laser Technology and Applications: Laser Applications: Medical, Metrology and Communication (Volume Four), CRC Press, Boca Rotan, pp.111-126, 2021.

[8] C. Affolderbach, G. Mileti, D. Slavov, C. Andreeva, S. Cartaleva, "Comparision of Simple and Compact Doppler and Sub-Doppler Laser Frequency Stabilisation", Proceedings of the 18 th European Frequency and Time Forum, pp. 375-379, 2004.

[9] S. Nakayama, "Theoretical Analysis of Rb and Cs D_2 Lines in Doppler-Free Spectroscopic Techniques with Optical Pumping," Japanese Journal of Applied Physics, vol. 24, 1985.

[10] G. Moon, and H.R. Noh, "Observation of nonstationary effects in saturation spectroscopy," Optics Communications, vol. 281, pp. 294-298, 2008.

[11] N.T. Hanaboonrungroch, P. Buranasiri, P. Limsuwan, and W. Yindeesuk, "Effect of temperature on the absorption of rubidium vapor cell D_2 line studied by two-photon absorption spectroscopy," Nonlinear Optics and its Applications, 106841V, 2018.

[12] D.A. Smith, and I.G. Hughes, "The role of hyperfine pumping in multilevel systems exhibiting saturated absorption," American Journal of Physics, vol. 72, pp.631-637, 2004.

[13] E. Şahin, "780 nm Lazer Dalgaboyu Standardı Mutlak frekans ve Kararlılığı Ölçümleri," Ölçümbilim Sempozyumu ve Sergisi, pp. 45-49, 2019.

[14] T. J. Quinn, "Practical realization of the definition of the meter, including recommended radiations of other optical frequency standards (2001)," Metrologia, vol. 40, pp. 103-133, 2003.

[15] J. Kitching, "Chip-scale atomic devices," Applied Physics Reviews, vol. 5, pp. 031302, 2018.

[16] S. Micalizio, F.Levi, C.E. Calosso, M. Gozzelino, and A. Godone, "A pulsed-Laser Rb atomic frequency standard for GNSS applications," GPS Solutions, vol. 25, 2021.

[17] K. Numata, J.R. Chen, S.T. Wu, J.B. Abshire, and M.A. Krainak, "Frequency stabilization of distributed-feedback laser diodes at 1572 nm for lidar measurements of atmospheric carbon dioxide," Applied Optics, vol. 50, pp. 1047-1056, 2017.

[18] Y. Ovchinnikov, and M. Giuseppe, "Accurate rubidium atomic fountain frequency standard," Metrologia, vol. 48, pp. 87-100, 2011.

[19] E. Şahin, "Unmodulated diode laser stabilized by the Zeeman modulation technique," Applied Physics B, vol. 127, 148, 2021.

[20] Y. Deniz, A. Gedik, E. Şahin, N. Ekren, Y. Baba, "Lazer Dalgaboyu Standardı Atomik Gaz Sıcaklık Elektronik Kontrol Ünitesi Tasarımı ve Ölçüm Sonuçları," Ölçümbilim Sempozyumu ve Sergisi, pp.59-64, 2019.

[21] G.C. Bjorklund, M.D. Levenson, W. Lenth, and C. Ortiz, "Frequency modulation (FM) spectroscopy Theory of lineshapes and signal-to-noise analysis," Applied Physics B, vol. 32, pp. 145–152, 1983.

[22] J.A.R. Griffith, "Laser heterodyne spectroscopy," Philosophical Transactions of the Royal Society of London. Series A, Mathematical and Physical Sciences, pp. 563-571, 1982.

[23] D.A. Steck, "Rubidium 87 D Line Data," https://steck.us/alkalidata/rubidium87numbers.1.6.pdf, 21 December 2021.

SAKARYA ÜNİVERSİTESİ
FEN BİLİMLERİ ENSTİTÜSÜ DERGİSİ

Sakarya University Journal of Science
SAUJS

e-ISSN 2147-835X Period Bimonthly Founded 1997 Publisher Sakarya University
http://www.saujs.sakarya.edu.tr/

Title: Metabolism Determination by Soft Computing Methods From Breath Molecules

Authors: Sedat METLEK, Hatice AKMAN, Ismail BAYRAKLI

Recieved: 2021-04-12 00:00:00

Accepted: 2022-04-08 00:00:00

Article Type: Research Article

Volume: 26
Issue: 2
Month: April
Year: 2022
Pages: 429-437

How to cite
Sedat METLEK, Hatice AKMAN, Ismail BAYRAKLI; (2022), Metabolism Determination by Soft Computing Methods From Breath Molecules. Sakarya University Journal of Science, 26(2), 429-437, DOI: 10.16984/saufenbilder.911990
Access link
https://dergipark.org.tr/tr/journal/1115/issue/69580/911990

New submission to SAUJS
http://dergipark.gov.tr/journal/1115/submission/start

Sakarya University Journal of Science 26(2), 429-437, 2022

Metabolism Determination by Soft Computing Methods From Breath Molecules

Sedat METLEK[1], Hatice AKMAN*[2], Ismail BAYRAKLI[3]

Abstract

The breath analysis is a non-invasive risk-free and painless method used to diagnose specific diseases. Since the breath analysis method is a new study field than the other methods, there are many unsettled standards and unknown parameters. Numerous complex metabolisms are constantly working in the human body. Therefore, there are numerous unknown molecular relationships. ANN can produce solutions in these unexplained situations.

In our pilot study, breath of 19 healthy people has been analyzed. The TD / GC-MS method, which is an analytical method of breath analysis, has been used to detect molecules in the breaths. Using soft computing methods to the results of the 19 breath samples, the relation between fermentation and carbon hydrate metabolism has been associated with breath analysis technique. The results indicated that, there can be a relationship between these metabolisms. There must be done more studies for the exact results.

Keywords: Breath Analysis, Artificial Neural Network, acetone, hexanal, butanol.

1. INTRODUCTION

Breath analysis method gains importance day by day in the diagnosis of diseases and in monitoring the health status of the patient. Breath molecules are exhault by the different and unknown metabolisms. The present study has been done to understand the relationship between molecules from lipid metabolism and lipid peroxidation metabolism. Acetone and butanol molecules are the products of lipid metabolism and hexanal is known as the product of the lipid peroxidation metabolism.

Acetone is an organic compound that is one of three ketone bodies together with acetoacetate and 3-β-hydroxybutyrate. These bodies are produced in the liver (Figure 1). Acetone is produced in two ways: by acetoacetate decarboxylation and by isopropanol dehydration. Acetone is produced by the spontaneous decarboxylation of acetoacetate

* Corresponding author: haticeakman@isparta.edu.tr
[1] Burdur Mehmet Akif Ersoy University, Vocational School of Technical Sciences
E-mail: sedatmetlek@mehmetakif.edu.tr
ORCID: https://orcid.org/0000-0002-0393-9908
[2] Isparta University of Applied Sciences, Faculty of Technology, Department of Biomedical Engineering
ORCID: https://orcid.org/0000-0002-8906-2122
[3] Aksaray University, Faculty of Engineering, Department of Electrical-Electronics Engineering
E-mail: ismailbayrakli@aksaray.edu.tr
ORCID: https://orcid.org/0000-0002-4512-8783

[1]. Acetone cannot be converted into acetyl-CoA [2] again and is therefore excreted with urine and breath. In the literature, acetone sources and formation ways are summarised in detail [3] The brain usually uses glucose necessarily as an energy source. However, when carbohydrates are limited with starvation, the brain cannot use glucose anymore. With the change of metabolism, the brain obtains ketone bodies from fats instead of carbohydrates, which are the main energy source. The fats taken generally dissolve into acetyl-CoA molecules by β-oxidation in the liver, then, produce energy through adenosine triphosphate (ATP) production by entering the cycle of the tricarboxylic acid (TCA). Acetyl-CoA, which is required for the biosynthesis of ketone bodies, is an important intermediate product in the energy metabolism. In the case of fasting, the tissues increase the fatty acid oxidation to meet the energy requirement, and as a result of this, a part of the excess acetyl-CoA is incorporated into the ketone body biosynthesis. The liver lacks the necessary enzymes to degrade ketone bodies. β-hydroxybutyrate and acetoacetate participate in the circulation through tissues such as the brain and muscle. Thus, the brain is able to utilise ketones, which are the main oxidative substrates for cerebral metabolism, through fasting or high fat/low carbohydrate uptake. Due to fasting, the ketones pass through the blood-brain barrier with an easy diffusion with the monocarboxylate transporter. With fasting, the brain monocarboxylate transporter levels get better. Neurons and glial cells separate β-hydroxybutyrate and acetoacetate into the acetyl-CoA fragment. (β-hydroxybutyrate dehydrogenase and 3 oxoacid CoA-transferase) Acetyl-CoA molecules can be considered to enter the Krebs Cycle and produce energy [4, 5]. In the brain, ketone bodies are an essential source of energy during fasting or strenuous exercise. In the brain, ketone bodies are an essential source of energy during fasting or strenuous exercise. The studies indicated that breath acetone can be used for the ketogenic state during fasting [6-9].

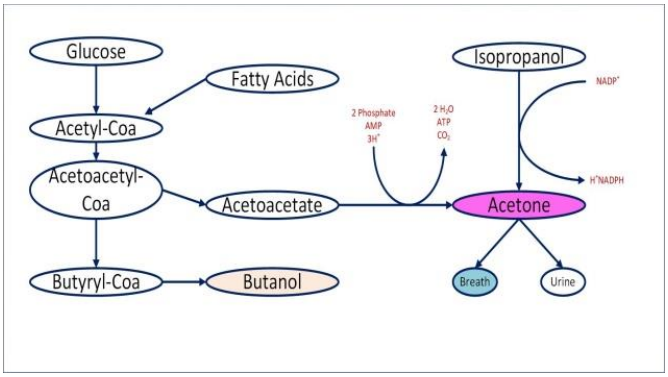

Figure 1 Biochemical pathways of acetone and butanol [10, 11]

Butanol can be produced from the microbial fermentation of carbohydrates such as glucose, for example, clostridium acetobutylicum [10]. This process has been metabolised to produce acetone and butanol from carbohydrates for various applications by means of acetone-butanol fermentation. Butyryl-CoA produced from acetoacetyl-CoA is converted to butanol in this process. Butanol was detected in human breath samples [12]. Filipiak et al. [13], analysed VOCs released by streptococcus pneumonia and haemophilus influenza cultures using the GC-MS method and found butanol at slightly high concentrations in both bacterial cultures. Kushch et al. [14], compared the breaths of smokers with those of non-smokers and found that the butanol molecule was not a significant biomarker for smokers. However, the butanol molecule was found at a significantly higher concentration in the breaths of lung cancer patients compared to the healthy control group.

There is not enough information about how the butanol molecule is formed and its effects on the cellular system. Some studies have shown the effects of acetone and butanol as anti-inflammatory agents [15, 16].

During lipid peroxidation, along with the increase in the formation of reactive oxygen species (ROS) that cause the increase in oxidative stress and neurotoxicity in the brain, an increase in lipid peroxidation markers as hexanal [17]. Lipid peroxidation metabolism is shown in Figure 2. Hexanal lipid peroxidation during lipid peroxidation is the molecule that occurs in the breath as a biomarker [18-22].

At the first stage of lipid peroxidation, lipid radical is formed by removing an H atom containing an electron from conjugated double bonds in fatty acids. The lipid radical forms the lipid peroxide radical (LOOH) by reacting with oxygen. LOOH degradation occurs with the ion catalysis of the transition metals. The cell membrane and organelle lipid peroxidation can be stimulated by free radicals and increases in the presence of transition metals. The formation of the hydroxyl radical ($OH^{\cdot}$) from hydrogen peroxide (H_2O_2) can initiate a chain reaction. As a result of these reactions, aldehydes (e.g. hexanal) emerge as end products [23]. The lipid peroxidation metabolism progressing without enzymes is a very harmful chain reaction. In these reactions, the membrane structure is directly damaged and the produced reactive aldehydes indirectly damage other cell components. This can cause many diseases [24], [25].

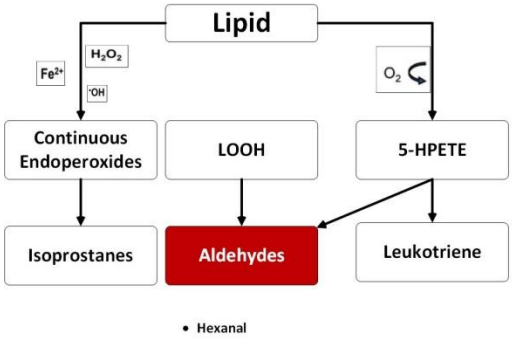

Figure 2 Lipid peroxidation metabolism [26]

2. MATERIAL METHOD

2.1. Breath Collection

Breath of 19 healty people has been collected via tubes from markes and translated to TENAX-TA 200 cartridge stored at the $4C^0$ to preserve VOCs (Figure 3). The information of the people breath collected from are shown at the Table 1.

Figure 3 Breath collection tube and cartage

Table 1 Breath Samples Collected Group

Gender (male/female)	10/9
Age (years)	Between 21 and 43 years Average: 28,8 years Standard Deviation (SD): 7,3
BMI (kg m^{-2})	Between 21 and 25,2 Average :23,2 SD: 1,5

2.2. GC-MS/TD Method

In conjunction with MS, GC is commonly used for breath analysis. In this study, TD - GCMS was used for analysis of breath acetone hexanal and butanol levels (Agilent Technologies 7890A 5975C). VOCs are thermally decomposed by thermal decomposers injected into GC / MS. Conditions for thermal decomposer are shown in Table 2.

The undifferentiated (non-split) mode has been applied to the TD system. GC / MS injector temperature was set to 250 ° C and the flow rate was set to 20 psi. The column oven temperature was raised to 180 ° C by keeping it at 60 ° C for 4 minutes and then increasing it by 20 ° C per minute. After holding at 180 ° C for 15 minutes, the temperature was raised again to 215 ° C at a rate of 4 ° C / min. It was held at this temperature for 20 minutes. In addition, the column oven was heated up to 240 ° C at 4 ° C per minute. It was held at this temperature for 35 minutes. Analytes were then injected into a DB-5 non-polar capillary column of 30 m length and 0.25 mm inner diameter. Selective ion tracking / imaging (SIM) mode was used to obtain lower detection limits. SIM mode allows us to get much more effective results in full scan mode. Helium gas (99.999%)

was used as a carrier in the analytical column with a flow of about 20 psi. Ionization of individual compounds was accomplished by electron impact ionization at 70 eV.

Table 2 Thermal desorption unit settings

Pre-desorption settings	
Split on in standby	
Flow path temperature	200°C
Minimum transporter pressure	5 psi
Pre-purification time	1 min
Tube / sample desorption settings	
Tube desorption time	5 min
Tube desorption temperature	250°C
Trap Settings	
Pre-trap fire purge	Minimum 1 min of trap flow
Trap low	−10°C
Trap heating rate	Maximum
Trap fixation / minute	3 min
Split	Open
Trap maximum	300°C

2.3. ANN

Artificial neural networks (ANN) are computer programs that are developed on the basis of the human brain, which are mainly connected to each other and which perform parallel and distributed information processing, each of which performs its own processing [27]

Examples related to the operations to be made to artificial neural networks are given. Thus, ANN can collect relevant information, make generalizations, and then decide on those samples using information learned in comparison with samples that have never been seen. Due to these learning and generalization features, artificial neural networks now find wide application in many scientific fields and demonstrate their ability to solve complex problems successfully [28].

ANN can be applied to many fields such as control and system identification, image and voice recognition, prediction and estimation, failure analysis, medicine, communication, traffic, production management [29].

There are also many different types of ANN developed for linear and non-linear systems such as perceptron neural networks, multi-layered artificial neural networks (MLF-ANN), and ADALINE / MADALINE. Since the nonlinear data are used in the study, the MLF-ANN structure of ANN is preferred.

2.3.1. Multi-layered Artificial Neural

Networks (MLF-ANN)

It is a structure developed for systems without linear solution. The MLF-ANN is a model in which the inputs are entered during the training phase and outputs are expected to be generated for these inputs.

Generated output based on network input [30]. The Multilayer Network structure is shown in Figure 4. The layer that the incoming information is transmitted to the hidden layer is the input layer. The hidden can be one or more. Here, the information received at the input layer is processed. On the output layer, the output values are calculated for each input against the information received from the hidden layer.

2.3.2. Feedback

Feedback in Artificial Neural Networks is done when the output of at least one neuron enters itself or other neurons and obtain error is usually made.

The feedback can be between neurons in a layer as well as between neurons in a layer. With this structure, feedback-driven ANN shows a non-linear dynamic behavior. Therefore, the feedbacks with different structures and behavior can be obtained according to the shape of the artificial neural networks.

Figure 4. below shows an ANN structure with three layers and feedback to the input layer.

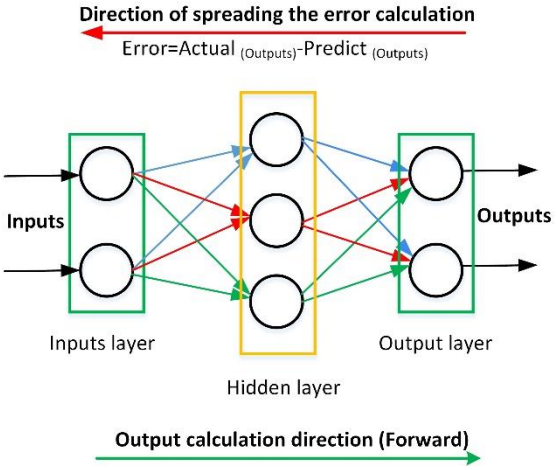

Figure 4 Feedback Neural Network

2.3.3. Back Propagation Algorithms

The backpropagation algorithm finds the error signal between the inputs and outputs, and the weights are updated with this error signal. The error e(t) is the difference between the actual output t(t) and the output of the neural network y(t) [31].

$$e(t) = t(t) - y(t); \quad t = 1,..,m \tag{1}$$

The backpropagation algorithm spreads the effects of the e(t) function on all weights on the network. Thus, the total error value is the lowest.

$$TH = \frac{1}{2}\sum_m E^2 \tag{2}$$

In Equation 2, TH represents the Total Error value. m is the output layer m. it is the element. Equation 2 shows that if the TH value is reduced in any experiment, the system error will decrease.

Methods that re-update the weight values on the network based on the decrease in system error and to support this decrease are used. The training process is based entirely on this update process.

With this algorithm xi. For input, the wji (t) change in weights between the i and j times processing elements is calculated. This expression is given in Equation 3.

$$\Delta w_{ji}(t) = \eta\delta_j x_i + \alpha\Delta w_{ji}(t-1) \tag{3}$$

In Equation 3, η is the learning coefficient, α is the momentum coefficient, and δj is a factor of any j-neuron at the intermediate or output level. For the output stage, this factor is given as follows.

$$\delta_j = \frac{\partial f}{\partial net_j}(y_j^{(t)} - y_j) \tag{4}$$

Where $y_j^{(t)}$ is the target output of the j processor element. For the Process Elements (PE) in the hidden layers (Process Elements - Neurons), this factor is expressed as in Equation 5.

$$\delta_j = \left(\frac{\partial f}{\partial net_j}\right)\sum w_{qi}\delta_q \tag{5}$$

Since there is no target output for neurons in hidden layers, Equation 5 is used instead of Equation 4. Depending on this situation, starting at the output layer, δj factor is calculated for neurons in all layers. The weights are then updated for all links based on the form in Equation 3. The activation function to be used in the backpropagation algorithm should have several important properties.

The activation function must be a continuous, derivative-derived function that does not degrade in a uniform manner. The reason for this preference is that the derivation of this function is easy. In general, the function is expected to lie between the minimum and maximum asymptotes [32].

In our study, the breathing of 19 healthy persons was examined. The TD / GC-MS method, which is an analytical method of breath analysis, has been used to detect molecules in the breaths. Breath samples taken from 19 individuals are shown in Table 3 and structure of prepared MLF-ANN Model is created.

Table 3 Inputs and outputs used in Feedback Multilayer Artificial Neural Network

	Inputs		**Outputs**
	Hexanal (ppb)	Acetone (ppb)	Butanol
1	0,62	92	0,18
2	2,02	97	0,57
3	1,13	97	0,25

4	2,23	114	0,63
5	8,22	119	0,67
6	5,55	148	1,26
7	1,11	148	1,12
8	5,69	199	0,25
9	0,98	210	0,89
10	2,56	216	0,36
11	6,56	219	0,36
12	0,85	243	1,25
13	1,62	267	0,44
14	0,82	305	0,3
15	2,5	305	0,56
16	1,99	307	1,51
17	1,25	309	0,75
18	1,92	317	0,56
19	5,05	772	0,28

MATLAB 2017a version was used to process the data. The structure of the prepared model is shown in Figure 5. In this structure Hexanal and Aceton were taken as input and Butanol was taken as output. Thirteen of the data in the Table 1 are used for training (70%), 3 data (15%) for testing, and 3 data (15%) for validation.

Levenberg-Marquart, Bayesian Regularization and Scaled Conjugate Gradient functions were tested for training. The results obtained are shown in Table 4. Mean squared error values are used to evaluate the performance of the system.

When Table 4 and Figures 5,6,7 examined, it is seen that the Bayesian Regularization method gives better results in training and test results in two-input, 10 hidden-layer and one output system than the other two methods.

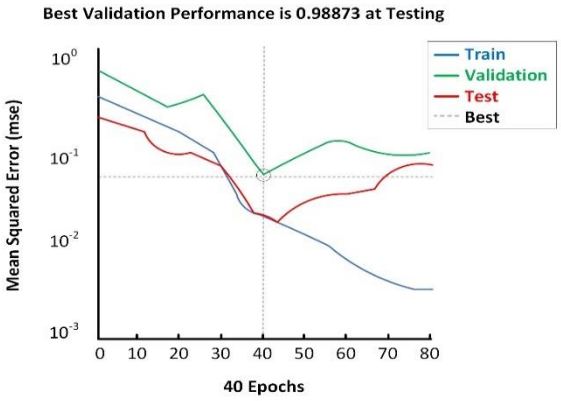

Figure 5 Levenberg-Marquart

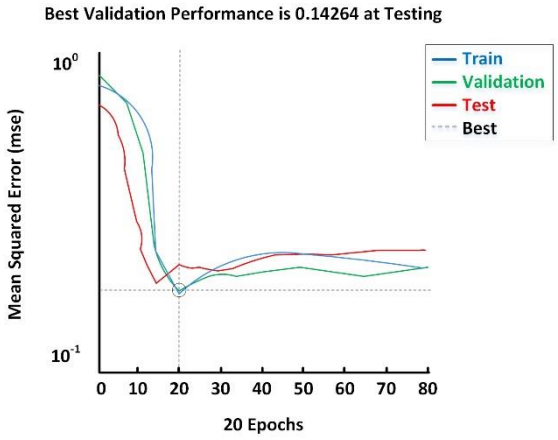

Figure 6 Bayesian Regularization

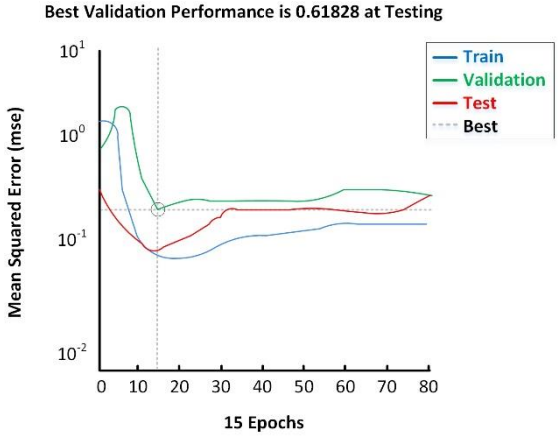

Figure 7 Scaled Conjugate Gradient

Table 4 Results Obtained from Feedback Model Neural Network Model

		Samples	Number of neurons in hidden layer	Iterations	Mean Squared Error (MSE)
Levenberg-Marquart	Training	13	10	40	0,80314
	Validation	3	10	40	0,64211
	Testing	3	10	40	0,98873
Bayesian Regularization	Training	13	10	20	0,12345
	Validation	3	10	20	0,13708
	Testing	3	10	20	0,14294
Scaled Conjugate Gradient	Training	13	10	15	0,73701
	Validation	3	10	15	0,70095
	Testing	3	10	15	0,61828

Despite the small number of data used in the study, high accuracy was obtained in the training and testing processes as the data completely covered the research subject.

3. CONCLUSIONS

Hexanal and acetone is the end product of the carbon hydrate metabolism and can be detected from breath. Butanol is the end product of the carbon hydrate fermentation. Many complex metabolisms occur in the body and there are lots of undefined metabolisms. This pilot study is done to understand the indeterminate metabolisms' products. This is a preliminary study to discover metabolism, and can be a method to diagnose diseases but more data is needed. Hexanal and Acetone are defined as input and Butanol as a output at the model which is prepared by using feedback artificial neural network method which is a flexible calculation method. The prepared ANN model is also an example of human metabolism. According to this pilot study there can be a relationship between fermentation and carbon hydrate metabolism.

An association is established between these non-linear data. It is a preliminary study of what chemicals will enter the human metabolism in the future and which components will result in a reaction. If there are more and more data from human metabolism, they can be explained more clearly in relation to each other. As a result, the personalized ANN model can be obtained. Thus, according to certain chemical results to be taken from the person, the anomalies of the person's body can be determined much more quickly and accurately.

The Declaration of Research and Publication Ethics

In the writing process of this study, international scientific, ethical and citation rules were followed, and no falsification was made on the collected data. Sakarya University Journal of Science and its editorial board have no responsibility for all ethical violations. All responsibility belongs to the responsible author and this study has not been evaluated in any academic publication environment other than Sakarya University Journal of Science.

The Declaration of Ethics Committee Approval

The authors declare that this document does not require an ethics committee approval or any special permission. B

The Declaration of Conflict of Interest/ Common Interest

No conflict of interest or common interest has been declared by the authors.

Authors' Contribution

Sedat Metlek: Artificial Neural Network Design, Writing

Hatice Akman: Breath Analysis, Writing

İsmail Bayraklı: Breath Analysis

REFERENCES

[1] A. Prabhakar,A. Quach,D. Wang,H. Zhang, M. Terrera, and D. Jackemeyer "Breath acetone as biomarker for lipid oxidation and early ketone detection," Glob. J. Obesity, Diabetes Metab. Syndr., vol. 1, no. 1, pp. 12–19, 2014.

[2] W. Li, Y. Liu, X. Lu, Y. Huang, Y. Liu., and S. Cheng, "A cross-sectional study of breath acetone based on diabetic metabolic disorders," J. Breath Res., vol. 9, no. 1, p. 16005, 2015.

[3] Z. Wang and C. Wang, "Is breath acetone a biomarker of diabetes? A historical review on breath acetone measurements," J. Breath Res., vol. 7, no. 3, p. 37109, 2013.

[4] S. A. Masino and J. M. Rho, "Mechanisms of ketogenic diet action," Epilepsia, vol. 51, no.. 5, p. 85, 2010.

[5] J. W. Wheless, "History of the ketogenic diet," in Epilepsia, 2008, vol. 49, no. SUPPL. 8, pp. 3–5.

[6] C. N. Tassopoulos, D. Barnett, and T. R. Fraser, "Breath-acetone and blood-sugar measurements in diabetes," Lancet, vol. 293, no. 7609, pp. 1282–1286, 1969.

[7] O. E. Owen, V. E. Trapp, C. L. Skutches, M. A. Mozzoli, R. D. Hoeldtke, G. Boden, and G. A.Reichard,., "Acetone metabolism during diabetic ketoacidosis," Diabetes, vol. 31, no. 3, pp. 242–248, 1982.

[8] D. Smith, P. Spanel, and S. Davies, "Trace gases in breath of healthy volunteers when fasting and after a protein-calorie meal: a preliminary study," J. Appl. Physiol., vol. 87, no. 5, pp. 1584–1588, 1999.

[9] M. Righettoni, A. Schmid, A. Amann, and S. E. Pratsinis, "Correlations between blood glucose and breath components from portable gas sensors and PTR-TOF-MS," J. Breath Res., vol. 7, no. 3, p. 37110, 2013.

[10] D. T. Jones and D. R. Woods, "Acetone-butanol fermentation revisited.," Microbiol. Rev., vol. 50, no. 4, p. 484, 1986.

[11] C. C. Pamela, A. H. Richard, and R. F. Denise, "Lippincotts illustrated reviews biochemistry." Lippincott Williams and Wilkins, Philadelphia, 2005.

[12] M. Libardoni, P. Stevens, J. H. Waite, and R. Sacks, "Analysis of human breath samples with a multi-bed sorption trap and comprehensive two-dimensional gas chromatography (GC× GC)," J. Chromatogr. B, vol. 842, no. 1, pp. 13–21, 2006.

[13] W. Filipiak, A.Sponring, M. Baur, C. Ager, A.Filipiak, H. Wiesenhofer, M. Nagl, J. Troppmair, and A. Amann, "Characterization of volatile metabolites taken up by or released from Streptococcus pneumoniae and Haemophilus influenzae by using GC-MS," Microbiology, vol. 158, no. 12, pp. 3044–3053, 2012.

[14] I. Kushch K. Schwarz, L. Schwentner, B. Baumann, A. Dzien, and Smith D.., "Compounds enhanced in a mass spectrometric profile of smokers' exhaled breath versus non-smokers as determined in a pilot study using PTR-MS," J. Breath Res., vol. 2, no. 2, p. 26002, 2008.

[15] J.-E. Huh B.-K. Seo, Y.-H. Baek, S. Lee, J.-D. Lee, D.-Y. Choi, D.-S. Park., "Standardized butanol fraction of WIN-34B suppresses cartilage destruction via inhibited production of matrix metalloproteinase and inflammatory mediator in osteoarthritis human cartilage explants culture and chondrocytes," BMC Complement. Altern. Med., vol. 12, no. 1, p. 1, 2012.

[16] M. Gupta, S. Sasmal, and A. Mukherjee, "Therapeutic effects of acetone extract of saraca asoca seeds on rats with adjuvant-induced arthritis via attenuating inflammatory responses," ISRN Rheumatol., vol. 2014, 2014.

[17] R. Paul, A. Choudhury, and A. Borah, "Cholesterol - A putative endogenous contributor towards Parkinson's disease," Neurochemistry International, vol. 90. pp. 125–133, 2015.

[18] C. J. Dillard and A. L. Tappel, "Lipid peroxidation products in biological tissues," Free Radic. Biol. Med., vol. 7, no. 2, pp. 193–196, 1989.

[19] H. Orhan, "Analyses of representative biomarkers of exposure and effect by chromatographic, mass spectrometric, and nuclear magnetic resonance techniques: method development and application in life sciences," J. Sep. Sci., vol. 30, no. 2, pp. 149–174, 2007.

[20] H. Esterbauer, R. J. Schaur, and H. Zollner, "Chemistry and biochemistry of 4-hydroxynonenal, malondialdehyde, and related aldehydes," Free Radic. Biol. Med., vol. 11, no. 1, pp. 81–128, 1991.

[21] W. A Pryor, B. Das, and D. F. Church, "The ozonation of unsaturated fatty acids: aldehydes and hydrogen peroxide as

products and possible mediators of ozone toxicity.," Chem. Res. Toxicol., vol. 4, no. 3, pp. 341–348, 1991.

[22] M. Kinter, "Analytical technologies for lipid oxidation products analysis," J. Chromatogr. B Biomed. Sci. Appl., vol. 671, no. 1, pp. 223–236, 1995.

[23] S. Demirci, S. Kutluhan, M. Naziroğlu, and A. C. Uğuz, V. A. Yürekli, and K. Demirci, "Effects of selenium and topiramate on cytosolic Ca2+ influx and oxidative stress in neuronal PC12 cells," Neurochem. Res., vol. 38, no. 1, pp. 90–97, 2013.

[24] D. E. Stanley, "Tietz Textbook of Clinical Chemistry," JAMA J. Am. Med. Assoc., vol. 282, no. 3, pp. 283–283, 1999.

[25] İ. Akkuş, "Serbest radikaller ve fizyopatolojik etkileri". Mimoza yayınları, 1995.

[26] A. Higdon, A. R. Diers, J. Y. Oh, A. Landar, and V. M. Darley-Usmar, "Cell signalling by reactive lipid species: new concepts and molecular mechanisms.," Biochem. J., vol. 442, no. 3, pp. 453–64, 2012.

[27] Ç. Elmas, "Yapay Sinir Ağları" Kuram, Mimari, Eğitim, Uygulama, Seçkin Yayıncılık, Ankara, 2003.

[28] H. Ergezer, M. Dikmen and E. Özdemir, "Yapay Sinir Ağları ve Tanıma Sistemleri" - PiVOLKA, vol 2, no. 6, pp. 14-17, 2003.

[29] H. Pirim, "Yapay Zeka". Journal of Yaşar University, pp. 81-93, 2006.

[30] İ, Gör, "Çok Katmanlı Algılayıcı Yapay Sinir Ağı ile Lineer Diferansiyel Denklem Sisteminin Çözümü". 18. Akademik Bilişim Konferansı, 30 Ocak-5 Şubat 2016, Adnan Menderes Üniversitesi, Aydın, 2016.

[31] K. Görgülü,, E. Arpaz, and Ö. Uysal,. Investigation of the effects of blasting design parameters and rock properties on blast-induced ground vibrations. Arab J Geosci., vol. 8, no. 4269, 2015.

[32] A.G. Yüksek, H. Bircan, M. Zontul, O. Kaynar, "Sivas İlinde Yapay Sinir Ağları İle Hava Kalitesi Modelinin Oluşturulması Üzerine Bir Uygulama", C.Ü. İktisadi ve İdari Bilimler Dergisi, vol. 8, no. 7, 2007.